Schwarze Löcher als Astronomische Objekte

Zusammenfassung zur kumulativen Habilitation

Jörn Wilms
Institut für Astronomie und Astrophysik, Abteilung Astronomie

5. Mai 2002

Inhaltsverzeichnis

1 Einführung **5**
- 1.1 Warum Schwarze Löcher? . . . 5
- 1.2 Auswahl der Veröffentlichungen . . . 6

2 Sternentwicklung zum Schwarzen Loch **7**
- 2.1 Entwicklung von Einzelsternen . . . 7
- 2.2 Entwicklung von Doppelsternsystemen . . . 11
- 2.3 Kompakte Objekte . . . 13
- 2.4 Massenbestimmung . . . 14

3 Röntgenstrahlung stellarer Schwarzer Löcher **18**
- 3.1 Astronomische Energieerzeugungsmechanismen . . . 18
- 3.2 Akkretion . . . 19
- 3.3 Meßmethoden der Röntgenastronomie . . . 21
- 3.4 Physik galaktischer Schwarzer Löcher . . . 23
  - 3.4.1 Breitbandspektren im Röntgenbereich . . . 23
  - 3.4.2 Hard State: Einzelbeobachtungen . . . 24
  - 3.4.3 Zustandsänderungen und Soft State . . . 31

4 Röntgenstrahlung supermassiver Schwarzer Löcher **33**
- 4.1 Aktive Galaxien . . . 33
- 4.2 Die Existenz Schwarzer Löcher in Aktiven Galaxien . . . 36
- 4.3 Röntgenbeobachtungen Aktiver Galaxien . . . 36

5 Zusammenfassung und Ausblick **40**

A Wilms et al. (1999): Low-Luminosity States of the Black Hole Candidate GX 339−4. I. ASCA and Simultaneous RXTE/Radio Observations **45**

B Nowak et al. (1999): Low-Luminosity States of the Black Hole Candidate GX 339−4. II. Timing Analysis **63**

C Nowak et al. (2001): A Good Long Look at the Black Hole Candidates LMC X-1 and LMC X-3 **77**

D Wilms et al. (2001): Discovery of Recurring Soft to Hard State Transitions in LMC X-3 **89**

E Nowak & Wilms (1999): On the Enigmatic X-ray Source V1408 Aql (=4U 1957+11) **105**

F Wilms, Allen, & McCray (2000): On the Absorption of X-rays in the Interstellar Medium **117**

G Wilms, Speith, & Reynolds (1998): Broad Iron Lines in Active Galactic Nuclei **129**

H Wilms et al. (2001): XMM-EPIC Observation of MCG−6-30-15 **141**

KAPITEL 1

Einführung

1.1 Warum Schwarze Löcher?

Schwarze Löcher sind Körper, die so kompakt sind, daß ihre Entweichgeschwindigkeit größer als die Lichtgeschwindigkeit ist. Erste physikalische Überlegungen über die Existenz Schwarzer Löcher gehen über 200 Jahre zurück (Michell, 1784; Laplace, 1796), diese Überlegungen hatten jedoch rein hypothetischen Charakter. Erst nachdem sich die Erkenntnis durchsetzte, daß Gravitation durch die Allgemeinen Relativitätstheorie beschrieben werden muß, wurde erkannt, daß die Existenz Schwarzer Löcher eine direkte Vorhersage dieser Theorie ist (Schwarzschild, 1916).

Schwarze Löcher sind prinzipiell sehr einfache physikalische Objekte – sie sind durch die Angabe ihrer Masse, ihres Drehimpulses und ihrer Ladung vollständig charakterisiert. Im Fall nichtrotierender Schwarzer Löcher ("Schwarzschild Schwarz-Löcher") ist der charakteristische Radius des Schwarzen Loches, der Schwarzschild Radius, R_s, gegeben durch

$$R_\mathrm{s} = 2\,\frac{GM}{c^2} = 3\,\mathrm{km}\,\frac{M}{\mathrm{M}_\odot} \tag{1.1}$$

Der Potentialtopf eines Schwarzen Lochs ist also sehr tief. Daher kann, wenn Material in diesen Potentialtopf gebracht wird, eine sehr große Energiemenge freigesetzt werden. Dieser Prozeß der sogenannten Akkretion spielt in der Astrophysik neben der Kernfusion eine herausragende Rolle als Energiequelle. Supermassive Schwarze Löcher mit Massen $M \sim 10^{6\ldots8}\,\mathrm{M}_\odot$ in den Zentren Aktiver Galaxien stellen dann auch die stärksten dauerhaften Energiequellen in unserem Universum dar. Hier kann in einem Volumen, das dem unseres Sonnensystems entspricht, mehr Energie erzeugt werden, als in der restlichen Galaxie. Mit Temperaturen von einigen Milliarden Kelvin ist die Umgebung Schwarzer Löcher auch einer der heißesten Orte im ganzen Universum.

Diese nicht mehr mit normaler Intuition verständlichenn Phänomene machen die Untersuchung Schwarzer Löcher und anderer kompakter Objekte wie der Neutronensterne zu einem sehr dankbaren wissenschaftlichen Arbeitsfeld. Auch wenn Schwarze Löcher als astronomische Realität seit mehr als 30 Jahren bekannt sind und dadurch der prinzipielle Aufbau dieser astronomischen Objekte einigermaßen zugänglich ist, so sind doch sehr viele der an ihnen beobachteten Phänomene immer noch nicht verstanden.

In dieser kumulativen Habilitationsarbeit soll versucht werden, einen Überblick über den momentanen Stand der Untersuchungen an galaktischen und extragalaktischen Schwarzen Löcher im Licht meiner Untersuchungen der letzten Jahre zu geben. Das einführende Kapitel 2 zeigt auf, wie aus normalen Sternen im Rahmen unseres heutigen Verständnisses der Sternentwicklung stellare Schwarze Löcher entstehen können und bettet so das hier behandelte Forschungsgebiet in den größeren Rahmen der stellaren Astrophysik ein. Ferner werden in Kapitel 2 Methoden der optischen Astronomie dargestellt, mit denen festgestellt werden kann, ob es sich bei einem beobachteten Objekt um ein Schwarzes Loch handelt. Ferner wird ein Überblick über die bekannten stellaren Schwarzen Löcher gegeben. In den folgenden Kapiteln 3 und 4 fasse ich dann meine Untersuchungen an stellaren Schwarzen Löchern und Aktiven Galaxien zusammen. Ziel dieser Untersuchungen ist es insbesondere, mit Hilfe röntgenastronomischer Methoden Modelle für die Akkretion von Materie auf das kompakte Objekt zu überprüfen. Daher wird in Kapitel 3 zunächst ein Überblick über

die heute diskutierten Akkretionsmechanismen gegeben. Ob und wie zwischen diesen Mechanismen unterschieden werden kann, wird dann unter Zuhilfenahme der Veröffentlichungen im Anhang erläutert. Kapitel 4 widmet sich dem Phänomen der breiten Eisenlinien, die in der Region starker Gravitation nahe supermassiver Schwarzer Löcher in Aktiven Galaxien entstehen. Mit derartigen Beobachtungen wird versucht, Vorhersagen der Allgemeinen Relativitätstheorie durch Messungen zu überprüfen. Im letzten Kapitel dieser Arbeit soll schließlich versucht werden, einen Ausblick auf die Zukunft des Forschungsgebiets der astronomischen Schwarzen Löcher für die nächsten Jahre zu geben.

1.2 Auswahl der Veröffentlichungen

Der Anhang dieser Arbeit enthält eine Auswahl meiner Veröffentlichungen, mit deren Hilfe in den folgenden Kapiteln gezeigt wird, mit welchen Beobachtungsmethoden und theoretischen Überlegungen versucht wird, die Beobachtungen galaktischer Schwarzer Löcher im Rahmen physikalischer Überlegungen zu interpretieren. Die Arbeiten im Anhang umfassen daher (referierte) Veröffentlichungen zum Thema galaktischer Schwarzer Löcher sowie Untersuchungen zu supermassiven Schwarzen Löchern in Aktiven Galaxien. Ebenfalls Teil des Anhangs ist eine Veröffentlichung über die Absorption von Röntgenstrahlung im Interstellaren Medium als Arbeit auf einem interessanten Forschungsgebiet, in dem Atomphysik, die Astrophysik des Interstellaren Mediums und die Hochenergieastrophysik ineinander greifen.

Weitere Veröffentlichungen über Schwarze Löcher und insbesondere akkretierende Neutronensterne wurden nicht in diese Arbeit selbst aufgenommen, um den Rahmen dieser Habilitationsschrift nicht zu sprengen. Dennoch bitte ich, sie als Teil der Habilitationsleistungen zu zählen. Sie liegen daher dieser Arbeit als gesonderte Nachdrucke bei. Weitere, insbesondere nichtreferierte, Veröffentlichungen sind in der vollständigen Liste meiner wissenschaftlichen Veröffentlichungen enthalten, die ebenfalls beiliegt. Die überwiegende Zahl meiner referierten und nichtreferierten Veröffentlichungen ist im World Wide Web unter `http://astro.uni-tuebingen.de/~wilms/vita/` im Volltext einsehbar. Daher habe ich auf eine Anlage der nichtreferierten Veröffentlichungen verzichtet.

Wie es insbesondere in der beobachtenden Astronomie üblich ist, sind alle meine Arbeiten in Kollaboration mit anderen Wissenschaftlern und Wissenschaftlerinnen entstanden. Auf dem Gebiet der Schwarzen Löcher sind dies in Tübingen insbesondere Dipl. Phys. Katja Pottschmidt, Lic. math. Sara Benlloch und Prof. Dr. Rüdiger Staubert. International ist von überragender Bedeutung die Zusammenarbeit mit Dr. Michael A. Nowak (JILA und University of Colorado, Boulder, jetzt Massachusetts Institute of Technology), in der ein überwiegender Teil der im Anhang abgedruckten Arbeiten entstanden ist, sowie mit Dr. William A. Heindl (University of California at San Diego), Prof. Dr. James B. Dove (Metropolitan State College of Denver), Prof. Dr. Mitchell C. Begelman (JILA und University of Colorado, Boulder) und Prof. Dr. Christopher Reynolds (JILA, jetzt University of Maryland at College Park). Bei den Verweisen auf meine Veröffentlichungen habe ich versucht, der Forderung der Habilitationsordnung der Fakultät für Physik Rechnung zu tragen und die Schwerpunkte auf meinen konkreten Anteil an diesen Veröffentlichungen zu legen. Dies ist nicht immer einfach, da aufgrund der engen Kollaboration viele Ideen gemeinsamen Diskussionen entsprungen sind und nur noch schwer zu rekonstruieren ist, wer der Urheber oder die Urheberin jeder bestimmten Idee war. Grundsätzlich ist mein Anteil bei allen der im Anhang abgedruckten Veröffentlichungen mit $\gtrsim 50\%$ anzusetzen, wobei die Erst- oder Zweitautorenschaft im Normalfall *keine* Gewichtung dieses Anteils zuläßt.

KAPITEL 2

Sternentwicklung zum Schwarzen Loch

In diesem Kapitel soll ein Überblick über die verschiedenen Phasen der Sternentwicklung gegeben werden, die zur Entstehung kompakter Objekte, also von weißen Zwergen, Neutronensternen oder Schwarzen Löchern führen. Abschnitt 2.1 führt in die Entwicklung von Einzelsternen ein, die dann in Abschnitt 2.2 auf Doppelsternsysteme erweitert wird. Abschnitt 2.3 faßt die physikalischen Eigenschaften kompakter Objekte zusammen. Es zeigt, daß aufgrund der Masse eine eindeutige Klassifikation möglich ist. Daher wird im letzten Abschnitt dieses Kapitels, Abschnitt 2.4, die Methode der astronomischen Massenbestimmung mit Hilfe der optischen Spektroskopie vorgestellt. Aus Platzgründen kann hier nur ein kurzer Abriß dieses Forschungsgebiets mit vielen Vereinfachungen gegeben werden, zur Vertiefung sei auf die sehr umfangreiche Literatur verwiesen (Kippenhahn & Weigert, 1990; Iben, 1991; Hansen & Kawaler, 1994; Verbunt & van den Heuvel, 1995; Wallerstein et al., 1997; Verbunt, 2001). Detaillierte neue Modellrechnungen für Sterne mit Massen $< 9\,\mathrm{M}_\odot$ finden sich zum Beispiel bei Dominguez et al. (1999), einen Überblick über noch massereichere Sterne geben Vanbeveren, de Loore & Van Rensbergen (1998).

2.1 Entwicklung von Einzelsternen

Sterne entstehen durch Kontraktion von Wolken im Interstellaren Medium, die hauptsächlich aus Wasserstoff, Helium und einigen Gewichtsprozent schwererer Elemente ("Metalle" im astronomischen Sprachgebrauch) bestehen. Wenn ein Teil dieser Wolke gravitativ instabil wird, das heißt, wenn der Gravitationsdruck nicht mehr durch thermischen Druck oder Magnetfelder ausgeglichen werden kann, dann zieht sich die Gaswolke zusammen, heizt sich auf und zerfällt in einzelne Fragmente. Wird die Temperatur im Inneren eines der weiter kontrahierenden Fragmente so heiß, daß Wasserstofffusion möglich wird, dann kann die Kontraktion gestoppt werden und ein Stern entsteht. Die weitere Entwicklung des Sterns ist über weite Teile seines Lebens dadurch bestimmt, daß er sich im hydrostatischen Gleichgewicht befindet, das heißt in seinem Inneren herrscht ein Gleichgewicht zwischen dem nach innen gerichteten Druck aufgrund der Eigengravitation des Sternmaterials und dem diesem entgegengerichteten thermischen Gasdruck.

Die weitere Beschreibung der Sternentwicklung kann am besten anhand des sogenannten Hertzsprung-Russell-Diagramms dargelegt werden. In diesem Diagramm, das nach seinen beiden Entdeckern benannt ist, wird die absolute Helligkeit eines Sterns über der Farbe des Sterns aufgetragen (Abb. 2.1). Hierbei ist die absolute Helligkeit in der Astronomie definiert als die Helligkeit, in der ein Stern erscheinen würde, wenn er aus einer Entfernung von 10 pc ($\sim$32 Lichtjahre) beobachtet werden würde. Die Helligkeit wird dabei häufig in der logarithmischen Intensitätsskala der sogenannten "Magnituden" angegeben, die definiert sind durch

$$m - m_0 = -2.5 \log \frac{I}{I_0} \tag{2.1}$$

Hier sind m die Magnitude des Sterns, I die gemessene Intensität, I_0 eine Referenzintensität und m_0 die dieser Referenzintensität entsprechende Magnitude. Hellere Sterne haben eine kleinere Magnitude. Die Sonne hat eine scheinbare Helligkeit von $\sim -26\,\mathrm{mag}$, Sirius als hellster Stern $\sim -1.8\,\mathrm{mag}$. Die schwächsten mit bloßem Auge unter Normalbedingungen in Tübingen sichtbaren Sterne haben $\sim 4\,\mathrm{mag}$. Für die Beobachtung in einem bestimmten Wellenlängenbereich, der zum Beispiel durch einen Filter oder die spektrale Empfindlichkeitskurve der Meßapparatur definiert ist, gelten entsprechende Formeln, der Filter wird durch Anhängen

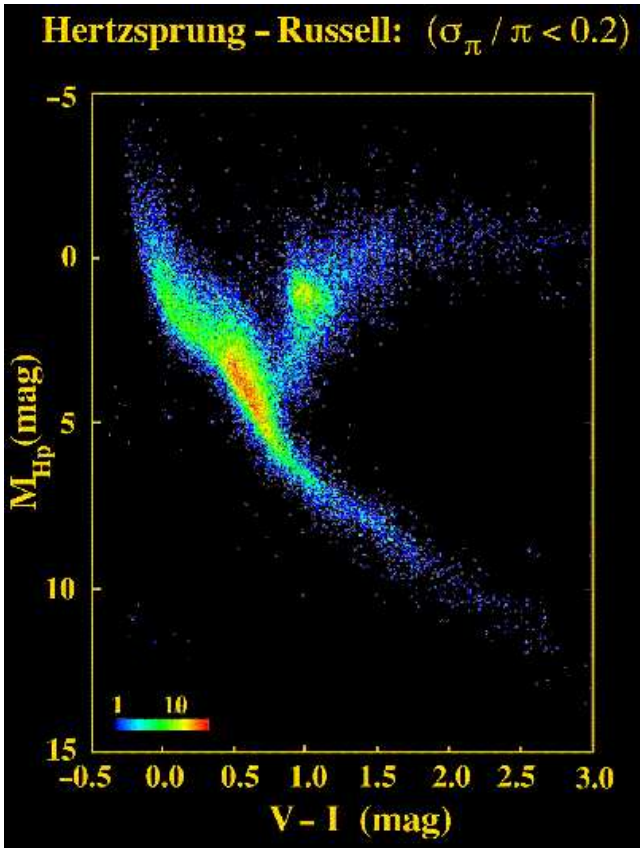

Abbildung 2.1: Hertzsprung-Russell Diagramm von ∼41500 nahen Sternen, deren Parallaxe π mit einer relativen Genauigkeit von $\sigma_\pi/\pi < 0.2$ gemessen werden konnte. Die Zahl der Sterne in einem Diagrammbereich von $0.1\,\mathrm{mag} \times 0.1\,\mathrm{mag}$ ist farbig codiert, die Strukturen parallel zur y-Achse sind durch die Genauigkeit der Messung der "Farbe" V − I bedingt (Perryman et al., 1995, siehe auch `http://astro.estec.esa.nl/Hipparcos/TOUR/hrdiagram3.html`).

eines Suffix an das m gekennzeichnet. Die Referenzintensität wird so definiert, daß Sterne vom Spektraltyp A0 in jedem Spektralband einen Farbindex von 0 haben.

Unter der "Farbe" eines Sterns versteht man in der Astronomie die Differenz der Sternhelligkeiten in zwei verschiedenen Wellenlängenbereichen. Da das Spektrum eines Sterns genähert einem Schwarzkörperspektrum entspricht, ist diese Differenz ein gutes Maß für die Temperatur des Sterns. Abbildung 2.1 stellt das beste gemessene Hertzsprung-Russell Diagramm für ∼41500 Sterne in der Sonnennähe dar, wie es vom europäischen Astrometrie-Satelliten HIPPARCOS gemessen wurde (Perryman et al., 1995). Es umfaßt einen Farbbereich von $m_\mathrm{V} - m_\mathrm{I} \equiv \mathrm{V} - \mathrm{I}$ von -0.5 bis 3.0, was einem Temperaturbereich von einigen 10000 K bis ∼1000 K entspricht[1] und einen Helligkeitsbereich von $M = 15\,\mathrm{mag}$ bis $M = -5\,\mathrm{mag}$. Die Sonne hat eine Leuchtkraft von $\mathrm{L}_\odot = 4 \times 10^{26}\,\mathrm{W}$, eine absolute Helligkeit von $M_\mathrm{V} = 4.8\,\mathrm{mag}$ und $\mathrm{V} - \mathrm{I} = 0.86$. Der typische Leuchtkraftbereich der Sterne reicht von $\sim 10^{-4}\,\mathrm{L}_\odot$ bis $\sim 10^5\,\mathrm{L}_\odot$.

Das sich diagonal durch das Hertzsprung-Russell-Diagramm ziehende Band heißt die "Hauptreihe". Sterne, die sich auf der Hauptreihe befinden (sogenannte Hauptreihensterne), erzeugen ihre Energie durch die Fusion von Wasserstoff zu Helium. Die Hauptreihe ist eine Massensequenz, das heißt, der Ort auf der Hauptreihe, auf dem sich ein Stern befindet, ist von seiner Masse abhängig. Diese wird normalerweise in Sonnenmassen, $\mathrm{M}_\odot$, gemessen, $1\,\mathrm{M}_\odot = 2 \times 10^{30}\,\mathrm{kg}$.

Sterne mit Massen $< 1.5\,\mathrm{M}_\odot$ bevölkern die "untere Hauptreihe", bei niedrigen Temperaturen von einigen 1000 K und dementsprechend kleinen Leuchtkräften. In ihrem Inneren dominiert bei moderaten Temperaturen von einigen 10^6 K das pp-Brennen. Da die Energieerzeugungsrate des pp-Brennens, ϵ_pp, nur schwach temperaturabhängig ist, $\epsilon_\mathrm{pp} \propto T^{4\ldots6}$ (Rolfs & Rodney, 1988), wird über einen vergleichsweise großen Bereich des Sterninneren Energie erzeugt. Damit kann die entstandene Energie radiativ transportiert werden. Die äußere Hülle dieser Sterne ist hingegen konvektiv instabil, d.h. Sterne auf der unteren Hauptreihe haben einen radiativen Kern und eine konvektive Hülle.

Oberhalb $1.5\,\mathrm{M}_\odot$ ist die Kerntemperatur so hoch, daß die Fusion von Wasserstoff zu Helium über den sogenannten CNO-Zyklus abläuft. Hier ist die Energieerzeugungsrate $\epsilon_\mathrm{CNO} \propto T^{18}$ (Hansen & Kawaler,

[1] V und I sind zwei der an Bord von HIPPARCOS vorhandenen Filter für die Intensitätsmessung.

Tabelle 2.1: Endstadien der Sternentwicklung in Abhängigkeit der Anfangsmasse; WD: Weißer Zwerg, NS: Neutronenstern, BH: Schwarzes Loch (nach Verbunt & van den Heuvel, 1995, Tab. 11.2).

	Endstadium	
Anfangsmasse	Einzelstern	Doppelstern
$< 3\,\mathrm{M}_\odot$	CO WD	He WD
3–8 $\mathrm{M}_\odot$	CO WD	CO WD
8–11 $\mathrm{M}_\odot$	O-Ne-Mg WD	O-Ne-Mg WD oder NS
11–40 $\mathrm{M}_\odot$	NS	NS
$> 40\,\mathrm{M}_\odot$	BH	BH

1994, Gl. 6.76), d.h. sehr stark temperaturabhängig. Daher sind diese Objekte in ihrem Inneren konvektiv instabil, so daß die Kernzone permanent durchmischt wird. In den äußeren Zonen dieser Sterne wird hingegen das Schwarzschild-Kriterium für Konvektion nicht erfüllt, d.h. der Energietransport in der äußeren Hülle findet durch Strahlung statt (siehe Hansen & Kawaler, 1994, Kap. 5, für eine Definition der Schwarzschild-Kriterien). Sterne auf der "oberen Hauptreihe" haben daher einen konvektiven Kern und eine radiative Hülle.

Rechnungen zeigen, daß diese Hauptreihenstruktur eines Sterns so lange bestehen bleibt, bis ungefähr 10% des anfänglich im Stern vorhandenen Wasserstoffs in Helium umgewandelt ist. Die Verweildauer eines Sterns auf der Hauptreihe, die "nukleare Zeitskala", ist damit ungefähr

$$\tau_\mathrm{n} \sim \frac{\eta_\mathrm{pp} \cdot 0.1 M c^2}{L} \sim 10^{10}\,\mathrm{Jahre} \cdot \frac{M}{\mathrm{M}_\odot} \cdot \left(\frac{L}{\mathrm{L}_\odot}\right)^{-1} \tag{2.2}$$

wo $\eta_\mathrm{pp} = 0.007$ die Effizienz des Wasserstoffbrennens ist, die sich aus dem Massendefekt von Deuterium im Vergleich zu zwei Protonen herleitet. Massearme Sterne, mit $M \lesssim \mathrm{M}_\odot$ und $L \lesssim \mathrm{L}_\odot$, haben daher eine sehr lange Verweildauer von einigen Milliarden Jahren auf der unteren Hauptreihe, während Sterne hoher Masse nur wesentlich kürzer auf der Hauptreihe verbleiben können. Für einen Stern auf der oberen Hauptreihe kann die Verweildauer weniger als 10^6 Jahre betragen.

Ist der Wasserstoff im Kern verbraucht, dann kann kein thermischer Druck mehr entgegen dem Gravitationsdruck aufgebracht werden und der Kern kontrahiert. Dabei heizt sich das Gas auf. Bei Kerntemperaturen oberhalb $\sim 10^8\,\mathrm{K}$ wird die Schwelle für die Fusion von Helium zu Kohlenstoff und Sauerstoff erreicht und der Stern erreicht ein weiteres Mal einen Gleichgewichtszustand. Bei dieser Kontraktion des Kerns dehnt sich der äußere Teil des Sterns stark aus – aufgrund der größeren Energieerzeugungsrate im Kern muß mehr Energie abgestrahlt werden, was bei hydrostatischer Struktur des Sterns nur bei einer größeren Sternoberfläche möglich ist. Im Hertzsprung-Russell-Diagramm wandert der Stern daher nach oben rechts, in den Bereich der sogenannten "Roten Riesen". Diese Zone ist neben der Hauptreihe die zweite stark bevölkerte Zone im Hertzsprung-Russell-Diagramm. Da die "Mutation" vom Hauptreihenstern zum Roten Riesen sehr schnell vonstatten geht, hat das Hertzsprung-Russell-Diagramm eine Lücke zwischen der Hauptreihe und der Zone der Roten Riesen (Abbildung 2.1), die Hertzsprung-Lücke.

Das weitere Leben eines Sterns nach dem Ende des Heliumbrennens hängt von seiner anfänglichen Masse auf der Hauptreihe, M_ZAMS (von "Zero Age Main Sequence", Alter-Null Hauptreihe), ab. Im folgenden werden die verschiedenen Wege zu den Endstadien Weißer Zwerg, Neutronenstern oder Schwarzes Loch genauer beschrieben. In Tab. 2.1 sind die verschiedenen möglichen Endstadien der Sternentwicklung in Abhängigkeit von M_ZAMS zusammengefaßt.

In masseärmeren Sternen ist nach dem Erlöschen des Heliumbrennens das Kernmaterial entartet. In diesem Fall kann im Sterninneren der Druck ausreichend groß sein, daß der Stern nicht weit genug kontrahiert, um die nächste Stufe der Kernfusion zu zünden. Ein solcher Stern kann daher keine weitere Energie erzeugen, sondern einfach die in ihm verbliebene thermische Energie abstrahlen und langsam abkühlen. Bevor der Stern erlöscht, kann er einen großen Teil der äußeren Hülle durch einen Sternwind abstoßen, so daß am Ende des

Lebens nur noch der Kern beobachtbar ist. Die Zusammensetzung dieses "weißen Zwergs" (white dwarf, WD) hängt von der Anfangsmasse des Sterns ab: Bei massenarmen Sternen ($M_{\mathrm{ZAMS}} \lesssim 3\,\mathrm{M}_\odot$) erlischt das Kernbrennen schon nach dem Heliumbrennen, Sterne höherer Masse können noch bis zum Kohlenstoff oder eventuell sogar bis zum Neon fusionieren.

Bei massereichen Sternen mit $M_{\mathrm{ZAMS}} \gtrsim 10\,\mathrm{M}_\odot$ setzen sich die Brennzyklen nach dem Heliumbrennen fort: Ist das Helium im Kern aufgebraucht, dann kann Kohlenstofffusion einsetzen, danach Sauerstoffbrennen, und so weiter, bis schließlich nach der Fusion von Eisen während des Siliziumbrennens durch Fusion keine weitere Energie mehr freigesetzt werden kann. Am Schluß hat der Stern einen "zwiebelschalenförmigen" Aufbau, mit einem Eisenkern, dann einer Siliziumschale, usw., bis zur Heliumschale und schließlich außen einer Wasserstoffhülle. Da der relative Energiegewinn pro Kernbrennstufe immer geringer wird, während die abgestrahlte Leuchtkraft des Sterns zunimmt, verringert sich nach Gl. (2.2) auch die nukleare Zeitskala immer weiter, bis sie beim Siliziumbrennen nur noch wenige Stunden bis Tage beträgt.

Ist auch diese Quelle erloschen, dann fällt der Stern in sich zusammen. Wie schon beim Beginn des Heliumbrennens verdichten sich dabei die inneren Regionen des Sterns stark und heizen sich stark auf. Da durch Fusion keine weitere Energie aufgebracht werden kann, kann der Kollaps allerdings nicht weiter aufgehalten werden. Das Sterninnere verdichtet auf Dichten im Bereich von $10^{10\ldots12}\,\mathrm{g\,cm^{-3}}$ (Arnett, 1996). Die Fermienergie der Elektronen ist hier so hoch, daß durch Elektroneneinfang die Atomkerne desintegrieren ("Neutronisierung"). In diesem Stadium wird der Druck im Sterninnern hauptsächlich durch relativistische Elektronen und Neutrinos aufgebracht. Erst wenn Dichten vergleichbar der Kerndichte erreicht werden ($\rho \sim 10^{14}\,\mathrm{g\,cm^{-3}}$), kann der weitere Zusammenbruch des Sterns aufgehalten werden, da die Nukleonen so dicht zusammengepresst werden, daß die starke Wechselwirkung repulsiv wird (Arnett, 1996). Der hauptsächlich aus Neutronen bestehende Kern des Sterns hat zu diesem Zeitpunkt eine Masse von $\sim$0.5 $\mathrm{M}_\odot$ und einen Radius von $\sim$10 km. Er bildet für die von außen mit Überschallgeschwindigkeit einfallende normale Materie eine quasi inkompressible Oberfläche, von der das einfallende Material abprallt. Der Rückstoß dieses Materials führt zur Bildung eines stehenden Schocks bei einer Höhe von $\sim$100 km oberhalb des Kerns (Bruenn, De Nisco & Mezzacappa, 2001). Material "regnet" durch diesen Schock auf die Oberfläche des Neutronenkerns. Wahrscheinlich aufgrund des Drucks der bei der Neutronisierung entstandenen Neutrinos, die nicht aus dem Stern entweichen können, da das akkretierende Material optisch dick für Neutrinos wird, wird dann nach einigen Millisekunden der Sternkollaps in eine Explosion umgewandelt, bei der der größte Teil der Hülle des Sterns abgestoßen wird. Der explodierende Stern wird als Supernova vom Typ Ib oder II sichtbar (siehe Filippenko, 1997, und die darin angegebene Literatur für Details zur Klassifikation der Supernovae). Bei einer solchen Supernovaexplosion wird eine sehr große Energiemenge innerhalb kürzester Zeit freigesetzt: Supernovae haben typischerweise Helligkeiten im Bereich einiger $10^{10}\,\mathrm{L}_\odot$ im optischen Spektralbereich, d.h. sie sind heller als die Helligkeit einer typischen Spiralgalaxie wie unserer Milchstraße. Der innere, aus Neutronen bestehende Kern des Sterns bleibt nach dieser Explosion als "Neutronenstern" erhalten, er hat theoretischen Rechnungen zufolge eine Masse von etwas über 1 $\mathrm{M}_\odot$.

Am Ende einer Supernova muß allerdings nicht immer ein Neutronenstern entstanden sein. Beim Kollaps der äußeren Hülle kann der Druck auf den Neutronenstern so groß sein, daß auch er nicht mehr stabil ist. Da es sich bei Kernmaterie um das stabilste zur Zeit in der Physik bekannte Material handelt, geht man davon aus, daß sich dieser Kollaps bis ins Unendliche fortsetzen wird. Es bildet sich ein Schwarzes Loch. Die genaue Massengrenze, oberhalb derer sich in Supernovae Schwarze Löcher bilden können, hängt stark von der bislang noch nicht mit ausreichender Genauigkeit verstandenen Zustandsgleichung für Kernmaterial ab. Ferner kann mit heute verfügbaren Computern auch die Supernovaexplosion nur unter sehr vereinfachten Annahmen (z.B. Rotationssymmetrie, keine Magnetfelder, vereinfachte Annahmen über die Rotation des Sterns, vereinfachte Zustandsgleichung, Vernachlässigung relativistischer Effekte, ...) berechnet werden. Eine Zusammenfassung dieser Annahmen geben Bruenn, De Nisco & Mezzacappa (2001). Daher kann aus theoretischen Berechnungen die genaue Grenze für M_{ZAMS}, oberhalb derer bei Supernovae ein Schwarzes Loch entsteht, nicht erhalten werden.

Außer aus Supernovaberechnungen wird daher versucht, durch die Erklärung der Existenz beobachteter Neutronensterne die Grenzmasse für die Supernovaentstehung einzuengen. So folgern zum Beispiel Wellstein & Langer (1999) aus der Existenz eines Neutronensterns im System Wray 977/GX 301$-$2 eine obere Grenze

für die Entstehung eines Neutronensterns von $M_{\mathrm{ZAMS}} = 13 \ldots 21\,\mathrm{M}_\odot$, während andere Autoren $M_{\mathrm{ZAMS}} = 20 \ldots 50\,\mathrm{M}_\odot$ (Ergma & van den Heuvel, 1998) beziehungsweise $M_{\mathrm{ZAMS}} \gtrsim 18\,\mathrm{M}_\odot$ (Brown et al., 1999) angeben.

Die große Ungenauigkeit dieser Grenzmassen für die Schwarzlochentstehung ist nicht nur durch die Ungenauigkeit der Supernova-Simulationen bedingt, die in diese Abschätzungen nicht eingehen, sondern hauptsächlich durch die Ungenauigkeiten in unserem Verständnis der Sternentwicklung, hauptsächlich im Bereich der Modellierung des sehr starken Massenverlusts von Sternen mit $M_{\mathrm{ZAMS}} \gtrsim 20\,\mathrm{M}_\odot$ und im Bereich der Modellierung der Durchmischungsprozesse in den konvektiven Zonen der Sterne.

Annahmen über den Sternwind sind wichtig, weil die Gesamtmasse eines Sterns die Entwicklungszeitskalen und sein Äußeres maßgeblich beeinflußt. Sternwinde sind sehr dynamische Phänomene, die bis heute nur grob verstanden sind. Die für die Schwarzlochentstehung so wichtigen massereiche Sterne haben so hohe Leuchtkräfte, daß der Strahlungsdruck in den äußeren Zonen der Atmosphäre ausreicht, das Atmosphärengas über die Entweichgeschwindigkeit an der Sternoberfläche zu beschleunigen. Zur Computersimulation solcher Winde müssen dreidimensionale strahlungshydrodynamische Rechnungen durchgeführt werden, für die heute weder die Computerleistung existiert, noch sind die für diese Rechnungen notwendigen Atomdaten hochionisierter Metalle bekannt. Daher gehen in die Sternentwicklungsrechnungen notwendigerweise Näherungen ein. Beispielsweise kann je nach angenommener Massenverlustrate ein Stern mit $60\,\mathrm{M}_\odot$ Hauptreihenmasse vor seiner Supernovaexplosion eine Masse zwischen $4.5\,\mathrm{M}_\odot$ und $\gtrsim 30\,\mathrm{M}_\odot$ haben (Woosley, Langer & Weaver, 1993), und damit in der Explosion entweder einen Neutronenstern oder ein schwarzes Loch erzeugen.

Kentnisse über die Konvektion sind notwendig, weil die Konvektion verschiedene Zonen des Sterns durchmischt und so zum Beispiel Wasserstoff aus Zonen, in denen vorher keine Fusion stattgefunden hat, in wasserstoffbrennende Zonen des Kerns transportieren kann. Dies verändert die chemische Struktur des Sterns und damit seine Entwicklung. Stellare Konvektion ist ebenfalls ein aktuelles astrophysikalisches Forschungsgebiet. Auch hier setzt wieder die Verfügbarkeit ausreichend guter Simulationsrechnungen mit dreidimensionaler Magnetohydrodynamik die Grenzen. Daher wird in Sternentwicklungsrechnungen üblicherweise mit verschiedenen "Mischungswegtheorien" gearbeitet, bei denen die Konvektion nur sehr genähert dargestellt wird (Hansen & Kawaler, 1994, Kap. 5). In diesen Theorien setzt Konvektion "schlagartig" ein, sobald das Schwarzschild-Kriterium erfüllt wird. Genauso prompt wird das Sterninnere wieder als rein radiativ angesehen, wenn das Schwarzschild-Kriterium nicht mehr erfüllt wird. Da das konvektive Material aus Impulserhaltungsgründen nicht prompt gestoppt werden kann, wird es aber offensichtlich noch etwas in eine Zone "überschießen", die dem Schwarzschild-Kriterium nach eigentlich schon radiativ sein sollte. Theorien des "convective overshoot" versuchen, diese Zone mit mehr oder weniger ad hoc Annahmen zu modellieren, eine wirklich befriedigende Lösung ist hier aber auch noch nicht in Sicht (siehe Schröder, Pols & Eggleton 1997 und Young et al. 2001 für neuere Diskussionen zu diesem Thema). Daß eine solche wirklich notwendig ist, um die Entwicklung von einem Hauptreihenstern zu einem Weißen Zwerg, Neutronenstern oder Schwarzen Loch zu verstehen, sei daran illustriert, daß die Untergrenze für die Vorgängersterne von Neutronensternen von $8\,\mathrm{M}_\odot$ auf $6\,\mathrm{M}_\odot$ sinkt, wenn "overshoot" berücksichtigt wird (Verbunt & van den Heuvel, 1995).

Dennoch: Trotz all dieser Unsicherheiten der Sternentwicklung scheint es keinen Ausweg zu geben, daß eine gewisse Zahl an Sternen am Ende ihres Lebens ein Schwarzes Loch bildet. Ziel der Untersuchungen an Schwarzen Löchern ist es, die an ihnen beobachteten Phänomene zu verstehen. Dazu gehört insbesondere auch, zu verstehen, wie die Schwarzen Löcher mit ihrer Umgebung wechselwirken und es gehört letztendlich auch dazu, zu verstehen, wie die Schwarzen Löcher entstanden sind.

2.2 Entwicklung von Doppelsternsystemen

Alle beobachteten Schwarzlochkandidaten in der Milchstraße sind Mitglieder von Doppelsternsystemen. Dies ist teilweise ein Auswahleffekt, da Schwarze Löcher und Neutronensterne als Röntgendoppelsterne eine hohe Leuchtkraft haben und dadurch einfacher beobachtbar sind als alleinstehende Neutronensterne oder Schwarze Löcher (Kap. 3). Ferner sind ungefähr 50% aller Sterne Doppel- oder Mehrfachsysteme, so daß ein gewisser Anteil an Schwarzen Löchern in Doppelsternsystemen grundsätzlich zu erwarten ist. Je nach Massenverhältnis der Sterne verläuft die Entwicklung eines Doppelsternsystems stark unterschiedlich. Als Beispiel für die

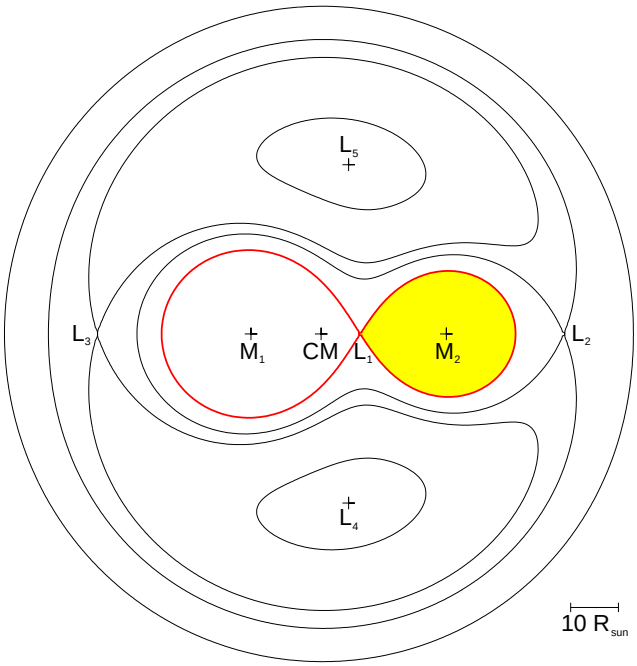

Abbildung 2.2: Roche-Potential mit Lagrange-Punkten L_1, L_2, ... , L_5, für Massen $M_1 = 18\,\mathrm{M}_\odot$ und $M_2 = 10\,\mathrm{M}_\odot$. CM ist der Massenschwerpunkt des Systems.

Doppelsternentwicklung soll im Folgenden die Entwicklung eines Doppelsternsystems in einen sogenannten High-Mass X-ray Binary beschrieben werden, da dieser Klasse einige der später behandelten Objekte angehören. Für weitere Entwicklungswege siehe die am Anfang dieses Kapitels angegebene Literatur, insbesondere Verbunt & van den Heuvel (1995) und Verbunt (2001).

Unterschiede zur Entwicklung von Einzelsternen sind bei Doppelsternsystemen dann zu erwarten, wenn die beiden Sterne einander so nahe sind, daß ihre Gezeitenwechselwirkung einen Einfluß bekommt. Bei diesen engen Doppelsternsystemen kann davon ausgegangen werden, daß sich die Rotationszeit der Sterne aufgrund von Gezeitenwechselwirkungen der Umlaufszeit angleicht und die Umlaufbahn um den gemeinsamen Schwerpunkt kreisförmig wird (siehe Tassoul, 1978, Kapitel 2). Zur Berechnung von Bewegungen in einem solchen System ist es angebracht, ein Bezugssystem zu wählen, das mit den Sternen rotiert. Das effektive Potential in diesem Bezugssystem setzt sich aus den Gravitationspotentialen der Einzelsterne (die als Punktmassen angenommen werden können) und einem zusätzlichen Term zusammen, der die Zentrifugalkraft beschreibt: (z.B. Frank, King & Raine, 1992, Gl. 4.5)

$$\Phi_{\mathrm{R}}(\mathbf{r}) = -\frac{GM_1}{|\mathbf{r}-\mathbf{r_1}|} - \frac{GM_2}{|\mathbf{r}-\mathbf{r_2}|} - \frac{(\boldsymbol{\omega}\times\mathbf{r})^2}{2} \tag{2.3}$$

Abbildung 2.2 zeigt die Äquipotentiallinien dieses sogenannten Roche-Potentials. Die ausgezeichnete Äquipotentiallinie, die die Form einer Sanduhr hat und beide Punktmassen umläuft, definiert die sogenannte Roche-Fläche. Innerhalb der jeweiligen Roche-Volumina ist Material an den jeweiligen Stern gebunden. In Abbildung 2.2 sind zusätzlich noch die Sattelpunkte des Roche-Potentials eingezeichnet, die sogenannten Lagrange-Punkte. Von besonderem Interesse wird noch der "innere Lagrange-Punkt", L_1, sein, der beim Berührungspunkt der Roche-Flächen der Einzelsterne auf der Symmetrielinie des Systems liegt.

Bei vielen Doppelsternsystemen ist der anfängliche Abstand der Sterne so groß, daß sie während ihres Hauptreihenstadiums wesentlich kleiner als ihre Roche-Volumina sind. Während dieser Phasen ist ihre Entwicklung identisch zu der von Einzelsternen. Dies ändert sich jedoch beim Verlassen der Hauptreihe. Hier dehnt ein Stern sein Volumen auf dem Weg zum Roten Riesen Stadium stark aus, so daß er das Roche-Volumen erreichen kann. Ist dies der Fall, dann fließt Material auf den Begleiter über[2]. Da die Entwicklungszeitskalen mit höherer Masse kürzer sind, wird Material immer vom Stern größerer Masse auf den kleinerer Masse

[2]Der hier besprochene Fall ist der sogenannte "Case B", der für die später behandelten Objekte relevant ist. Findet der Massenüberfluß schon auf der Hauptreihe statt, so ist das ein "Case A"-Entwicklungsszenario. "Case C" ist dementsprechend die Entwicklung eines Doppelsternsystems, wenn der erste Massenübertrag erst nach dem Erreichen des Roten Riesen Stadiums stattfindet (Verbunt, 2001).

übergehen. Aufgrund der Drehimpulserhaltung wächst dabei der Abstand der beiden Sterne stark an. Am Ende dieser ersten Phase des Masseübertrags hat der ursprünglich massereichere Stern einen Großteil seiner Masse verloren. Der verbleibende Heliumkern dieses Sterns entwickelt sich weiter und explodiert schließlich in einer Supernova. Bei dieser Explosion kann das System auseinandergerissen werden. Ist dies nicht der Fall, enthält das Doppelsternsystem nach der Explosion einen Neutronenstern oder ein Schwarzes Loch, das von einem massereichen Hauptreihenstern umkreist wird. Im Laufe der weiteren Entwicklung des Systems wird der ursprünglich masseärmere Stern sich ebenfalls ausdehnen. Füllt er sein Roche Lobe aus, dann kann Material über den inneren Lagrange-Punkt auf seinen kompakten Begleiter fallen und das System wird als Röntgendoppelstern sichtbar (Kapitel 3).

Modifikationen dieses Szenarios sind sehr wahrscheinlich. Wie in Abschnitt 2.1 dargestellt wurde, haben massereiche Sterne starke Sternwinde. Daher wird anstelle des oben vorgestellten konservativen Masseübertrags im Doppelsternsystem, bei dem die Gesamtmasse des Systems und der Gesamtdrehimpuls erhalten bleiben, ein Teil der Masse und des Drehimpulses durch einen Sternwind das System verlassen. Ferner kann im Fall stärkerer Winde ein Masseübertrag auch dann stattfinden, wenn ein Stern sein Roche-Volumen noch nicht vollständig ausfüllt. In beiden Fällen verläuft die detaillierte Entwicklung eines Systems unterschiedlich von der oben dargestellten. Tabelle 2.1 listet die wahrscheinlichen Endstadien für typische "Case B" Szenarien auf.

2.3 Kompakte Objekte

Trotz aller Unsicherheiten in der Sternentwicklung können den Erläuterungen in Abschnitt 2.1 zufolge als Endstadium drei verschiedene Arten von Objekten entstehen: Weiße Zwerge, Neutronensterne und schwarze Löcher. Diese Objektarten werden häufig unter dem Überbegriff "kompakte Objekte" zusammengefaßt, das heißt, sie sind Objekte stellarer Masse mit Radien, die klein sind im Vergleich zu normalen Sternen.

Kompakte Objekte können aus physikalischen Gründen nur innerhalb bestimmter Massengrenzen existieren, das heißt, daß sie häufig durch eine Massenbestimmung klar identifiziert werden können:

Weiße Zwerge werden durch den Druck entarteter Elektronen stabilisiert. Mit mittleren Dichten von $\rho \sim 10^{5\ldots6}\,\mathrm{g\,cm^{-3}}$ haben sie typische Radien, die vergleichbar mit dem Erdradius sind. Oberhalb einer Grenzmasse von $1.44\,\mathrm{M_\odot}$, der Chandrasekhar-Grenze (Chandrasekhar, 1931), können weiße Zwerge nicht existieren, da dann die Elektronen relativistisch entarten und kein Gleichgewicht mehr zwischen der Gravitation und dem Elektronendruck existiert.

Neutronensterne können oberhalb der Chandrasekhar-Grenze existieren, weil sie durch Wechselwirkungen zwischen den Neutronen stabilisiert werden. Ihre typische Dichte liegt in der Nähe der von Kernmaterial, $\rho \sim 10^{13} \ldots 10^{16}\,\mathrm{g\,cm^{-3}}$, ihre Radien sind im Bereich von $\sim$10 km. Der Aufbau der Neutronensterne ist wenig verstanden, weil er stark von der Zustandsgleichung für Kernmaterie abhängt, die noch nicht ausreichend gut bekannt ist (Shapiro & Teukolsky, 1983, Kapitel 8). Diese Unsicherheit bedingt auch die obere Massengrenze für Neutronensterne, die je nach Zustandsgleichung zwischen $\sim 2\,\mathrm{M_\odot}$und $\sim 3\,\mathrm{M_\odot}$liegt. Die maximale Obergrenze für Neutronensterne wird für die steifste Zustandsgleichung erreicht, die einem Kausalitätsargument von Oppenheimer & Volkoff (1939) folgend dann erreicht wird, wenn die Schallgeschwindigkeit im Neutronenstern gleich der Lichtgeschwindigkeit ist. Diese Oppenheimer-Volkoff Grenze liegt bei $M_{\mathrm{OV}} = 3.2\,\mathrm{M_\odot}$ (Rhoades & Ruffini, 1974, unter der Annahme einer "matching density" von $\rho_0 = 4.6 \times 10^{14}\,\mathrm{g\,cm^{-3}}$, d.h. unter der Annahme, daß die Zustandsgleichung von Kernmaterie bis zu einer Dichte von ρ_0 verstanden ist), neuere Untersuchungen von Kalogera & Baym (1996) ergeben $M_{\mathrm{OV}} = 2.9\,\mathrm{M_\odot}$ ($\rho_0 = 5.4 \times 10^{14}\,\mathrm{g\,cm^{-3}}$) bzw. $M_{\mathrm{OV}} = 2.6\,\mathrm{M_\odot}$ (Olson, 2001, Mittelwert für verschiedene Zustandsgleichungen).

Schwarze Löcher sind damit alle die kompakten Objekte, die oberhalb der Oppenheimer-Volkoff-Grenze beobachtet werden[3]. Ihre Größe kann durch den Schwarzschild-Radius, das heißt durch den Radius des

[3]Wiederholt sind sogenannte "exotische Sterne" als Alternativmodelle für Schwarze Löcher vorgeschlagen worden, Objekte, die zum Beispiel als "Quarksterne" rein aus Quarks aufgebaut sind (siehe z.B. Drake et al., 2002).

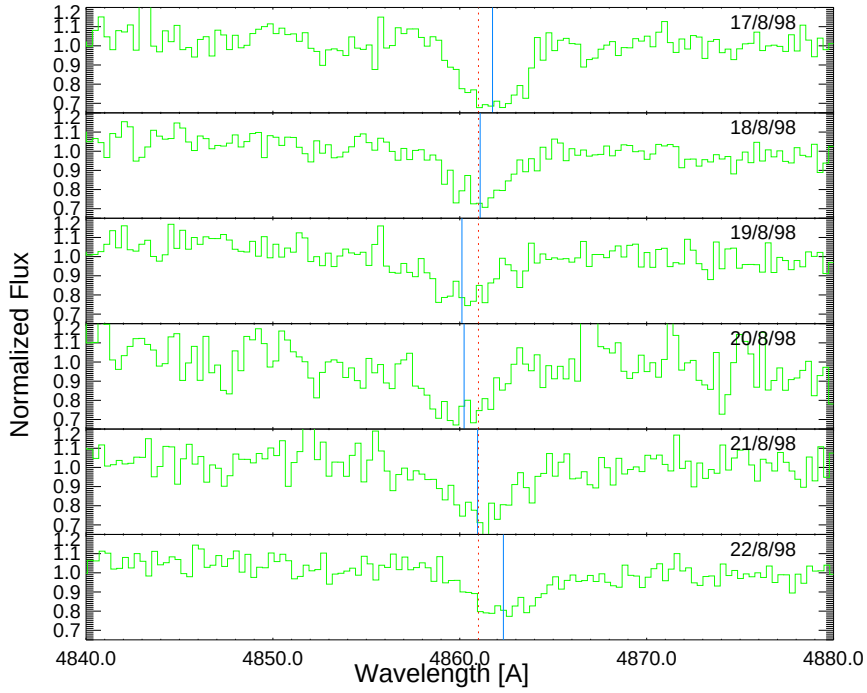

Abbildung 2.3: Hβ Linie von HDE 226868, gemessen im August 1998 am 1.5 m Teleskop des Observatoire d'Haute Provence. Die gestrichelte Linie ist die Laborwellenlänge der Hβ Linie, die durchgezogenen Linien geben die durch Anpassung eines Gaußförmigen Linienprofi ls gemessene Zentralwellenlänge der Hβ Linie während der jeweiligen Nacht an.

Ereignishorizonts

$$R_{\mathrm{s}} = 2\,\frac{GM}{c^2} = 3\,\mathrm{km}\,\frac{M}{\mathrm{M}_\odot} \tag{2.4}$$

charakterisiert werden. Schwarze Löcher haben damit eine Größe, die nur wenig kleiner als die der Neutronensterne ist.

Eine eindeutige Aussage über die Art eines kompakten Objekts kann dann gemacht werden, wenn seine Masse bekannt ist: Hat das Objekt eine Masse oberhalb der Oppenheimer-Volkoff-Grenze, dann handelt es sich mit Sicherheit um ein schwarzes Loch.

2.4 Massenbestimmung

In der Astronomie kann heute eine direkte Massenbestimmung nur auf dynamischem Weg stattfinden, d.h. über den gravitativen Einfluß, den ein astronomisches Objekt auf seine Umgebung ausübt. Im Fall stellarer Objekte ist dies dann möglich, wenn sich das kompakte Objekt in einem Doppelsternsystem befindet. In diesem Fall kreisen das kompakte Objekt und sein Begleiter um ihren gemeinsamen Schwerpunkt. Der Dopplereffekt führt zu einer periodischen Verschiebung der Absorptionslinien im Sternspektrum, aus der auf die Umlaufszeit, P_{orb}, geschlossen werden kann. Ferner kann mit Hilfe des Dopplereffekts auch die Radialgeschwindigkeit des Begleiters, K_{s}, gemessen werden, d.h. die in Beobachterrichtung projizierte Geschwindigkeitskomponente.

Bezeichnet a_{s} die große Halbachse der Bahn des Begleiters, so ist

$$K_{\mathrm{s}} = \frac{2\pi a_{\mathrm{s}}}{P_{\mathrm{orb}}}\,\sin i \tag{2.5}$$

Hier ist i die Bahnneigung des Doppelsternsystems gegenüber der Himmelsfläche, da ja nur die in Beobachterrichtung projizierte Geschwindigkeit gemessen werden kann. Ferner gilt das 3. Keplersche Gesetz

$$\frac{(a_{\rm x}+a_{\rm s})^3}{P_{\rm orb}^2}=\frac{G(M_{\rm x}+M_{\rm s})}{4\pi^2} \tag{2.6}$$

wo $a_{\rm x}$ und $M_{\rm x}$ die große Halbachse und die Masse des kompakten Objekts bezeichnen. Wird noch der Schwerpunktsatz berücksichtigt,

$$M_{\rm x}a_{\rm x}=M_{\rm s}a_{\rm s} \tag{2.7}$$

dann kann einfach die *Massenfunktion*

$$f_{\rm M}=\frac{M_{\rm x}^3\sin^3 i}{(M_{\rm s}+M_{\rm x})^2}=\frac{P_{\rm orb}K_{\rm s}^3}{2\pi G} \tag{2.8}$$

hergeleitet werden. Die Massenfunktion setzt die Beobachtungsgrößen $K_{\rm s}$ und $P_{\rm orb}$ mit den Massen des kompakten Objekts und des Begleiters in Beziehung.

Sind die Inklination i und die Begleitsternmasse $M_{\rm s}$ nicht bekannt, kann aus der Massenfunktion eine untere Grenze für die Masse des kompakten Objekts abgeleitet werden: laut Gl. (2.8) ist $f_{\rm M}\leq M_{\rm x}$.

Sind sowohl i als auch $M_{\rm s}$ bekannt, dann kann $M_{\rm x}$ genauer eingegrenzt werden. Die Bestimmung dieser Größen gestaltet sich allerdings schwierig. Ist der Begleitstern noch auf der Hauptreihe, dann kann $M_{\rm s}$ nach Bestimmung seines Spektraltyps aus der Massenverteilung der Hauptreihensterne mit ausreichender Genauigkeit bestimmt werden. Eingeschränkt ist eine Massenbestimmung auch aus der quantitativen Spektralanalyse des Spektrums möglich (siehe z.B. Herrero et al., 1995, für die Massenbestimmung von HDE 226868, dem Begleiter des Schwarzlochkandidaten Cyg X-1), insbesondere bei Vorhandensein von Sternwinden ist diese Methode aber unsicher.

Noch komplizierter ist die Bestimmung der Inklination. Außer im geometrisch ausgezeichneten Fall von $i\sim 90^\circ$, bei dem das kompakte Objekt bei jedem Umlauf einige Zeit hinter dem Begleitstern verschwindet und eine "Röntgenfinsternis" auslöst, kann i nur sehr ungenau bestimmt werden. Hier kann die optische Lichtkurve des Begleitsterns herangezogen werden: Während eines Umlaufs des kompakten Objekts um den Begleitstern ändert dieser seine Helligkeit, da er aufgrund der Nähe des kompakten Objekts verformt ist und daher die projizierte Sternoberfläche unterschiedlich groß ist (Hutchings, 1978; Balog, Goncharskiĭ & Cherepashchuk, 1981; Vrtilek, Soker & Raymond, 1993). Eine Bestimmung der Inklination ist auch mit Polarisationsmessungen möglich: Das zum Beobachter gelangende Sternlicht ist in Abhängigkeit von der projizierten Oberfläche unterschiedlich polarisiert, woraus auf die Form des Sterns und daraus auf die Inklination geschlossen werden kann (Bochkarëv et al., 1986; Ninkov, Walker & Yang, 1987; Dolan, 1992).

Als Beispiel, wie eine solche Messung praktisch durchgeführt wird, sind in Abb. 2.3 die Spektren von HDE 226868 im Bereich der Hβ Linie für sechs aufeinanderfolgende Nächte dargestellt. Diese Daten wurden von uns im Rahmen einer Beobachtungskampagne am Observatoire d'Haute Provence, Frankreich, aufgenommen (Pottschmidt et al., in Vorb.). Durch Anpassung eines Gaußförmigen Linienprofils, das in erster Näherung ausreichend für die Beschreibung der Linienform ist, kann die Zentralwellenlänge der Hβ Linie in den Spektren bestimmt werden. Abb. 2.3 illustriert die Verschiebung dieser Linien im Vergleich zur Ruhewellenlänge von Hβ, die durch die Dopplerverschiebung verursacht wird. Für eine Kreisbewegung gilt für die Radialgeschwindigkeit zum Zeitpunkt t

$$v_{\rm rad}(t)=\gamma+K_{\rm s}\sin\left(2\pi\frac{t-T_0}{P}\right) \tag{2.9}$$

wo γ die Schwerpunktsgeschwindigkeit des Doppelsternsystems in Bezug auf den Schwerpunkt des Sonnensystems bezeichnet. In Gl. (2.9) bezeichnet T_0 den Zeitnullpunkt der Ephemeride, der definitionsgemäß mit der unteren Konjunktion des Sterns gleichgesetzt wird, das heißt den Zeitpunkt, an dem sich der Stern von der Erde aus betrachtet "vor" dem kompakten Objekt befindet. Durch Kombination vieler Messungen wie der in

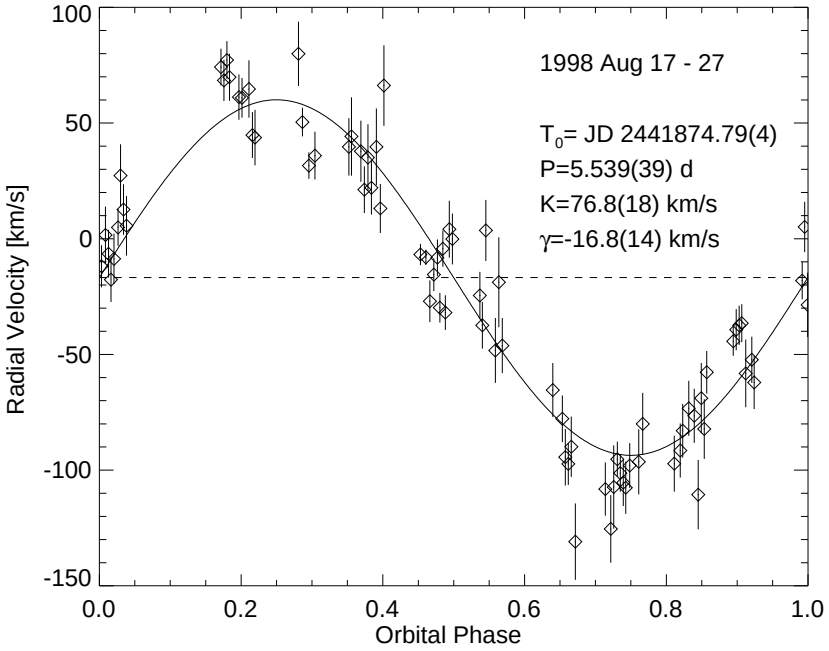

Abbildung 2.4: Gemessene Radialgeschwindigkeiten während der Messungen am Observatoire d'Haute Provence und angepasste Lösung für die Radialgeschwindigkeit unter Annahme einer Kreisbahnbewegung (Gl. 2.9).

Abb. 2.4 dargestellten, kann die Massenfunktion für viele Objekte mit guter Genauigkeit bestimmt werden. Für Cyg X-1 ergibt sich zum Beispiel eine Massenfunktion von $0.25 \pm 0.01\,\mathrm{M}_\odot$ (Gies & Bolton, 1982).

Die meisten Objekte, in denen Schwarze Löcher vermutet werden, haben Massenfunktionen *unterhalb* der Oppenheimer-Volkoff Grenze! Da damit ihre untere Massengrenze $< M_{\mathrm{OV}}$ ist, werden sie daher *Schwarzlochkandidaten* (englisch *black hole candidates*, häufig abgekürzt BHC) genannt. Ausnahmen sind V404 Cyg (=GS 2023+34) mit einer Massenfunktion von $6.08 \pm 0.06\,\mathrm{M}_\odot$ und $M_{\mathrm{BH}} = 7 \ldots 10\,\mathrm{M}_\odot$ (Casares & Charles, 1994), XTE J1118+480 mit $f_{\mathrm{M}} = 6.00 \pm 0.36\,\mathrm{M}_\odot$ und $M_{\mathrm{BH}} = 6 \ldots 10\,\mathrm{M}_\odot$ (McClintock et al., 2001), und GRS 1915+105 mit $f_{\mathrm{M}} = 9.5 \pm 3.0\,\mathrm{M}_\odot$ (Greiner, Cuby & McCaughrean, 2001). Nach Berücksichtigung der Inklination hat damit GRS 1915+105 die höchste zur Zeit bekannte Schwarzlochmasse.

Abbildung 2.5 gibt einen Überblick über die Massen von Neutronensternen und Schwarzlochkandidaten, in die auch Abschätzungen über die Begleitermasse und die Inklination eingegangen sind. Trotz der kleinen Massenfunktion ergibt sich so, daß Cygnus X-1 eine wahrscheinliche Masse von $\sim 10\,\mathrm{M}_\odot$ hat (Herrero et al., 1995). Insgesamt haben die meisten Neutronensterne wohl Massen knapp um die Chandrasekhar-Masse herum (die einzige Ausnahme ist hier Vela X-1 mit einer Neutronensternmasse von $1.86 \pm 0.16\,\mathrm{M}_\odot$ Barziv et al., 2001), während Schwarzlochkandidaten Massen im Bereich von $\sim 10\,\mathrm{M}_\odot$ haben.

Massenschätzungen sind für ca. 50% aller Schwarzlochkandidaten möglich, einen Überblick über die Massenverteilung der BHC und der Neutronensterne gibt Abb. 2.5. Auch wenn viele BHC das strenge Kriterium einer Massenfunktion oberhalb der Oppenheimer-Volkoff Grenze nicht erfüllen oder ihre Masse nicht bestimmt werden kann, so gibt es dennoch gute Gründe, sie zumindest als Schwarzlochkandidaten zu bezeichnen. Eines der großen Ziele der Erforschung der BHC ist deshalb auch, klare Kriterien zu finden, mit denen die Existenz eines schwarzen Lochs aus anderen als dynamischen Beobachtungen gefolgert werden kann. Zur Zeit gibt es für diese Fragestellung noch keine wirklich befriedigende Antwort.

Während es noch vergleichsweise einfach ist, ein kompaktes Objekt als Weißen Zwerg zu klassifizieren, macht die Unterscheidung zwischen einem Neutronenstern und einem Schwarzen Loch große Probleme. Dies liegt daran, daß die Größenskalen dieser Objekte sehr ähnlich sind. Die Beobachtung relativistischer Effekte als Unterscheidungsmerkmal scheidet daher aus, da sie in beiden Objektklassen ähnlich stark sind. Ein wirklich sicheres Kriterium, daß ein astronomisches Objekt *kein* Schwarzes Loch ist, ist daher nur, die Existenz des Ereignishorizonts auszuschließen – Neutronensterne haben eine Oberfläche, Schwarze Löcher haben keine. Ohne Anspruch auf Vollständigkeit werden die folgenden Punkte herangezogen, um ein kompaktes Objekt als Neutronenstern zu klassifizieren:

- die Beobachtung von X-ray Bursts, also von thermonuklearen Explosionen auf der Oberfläche von Neutronensternen (Lewin, van Paradijs & Taam, 1995).

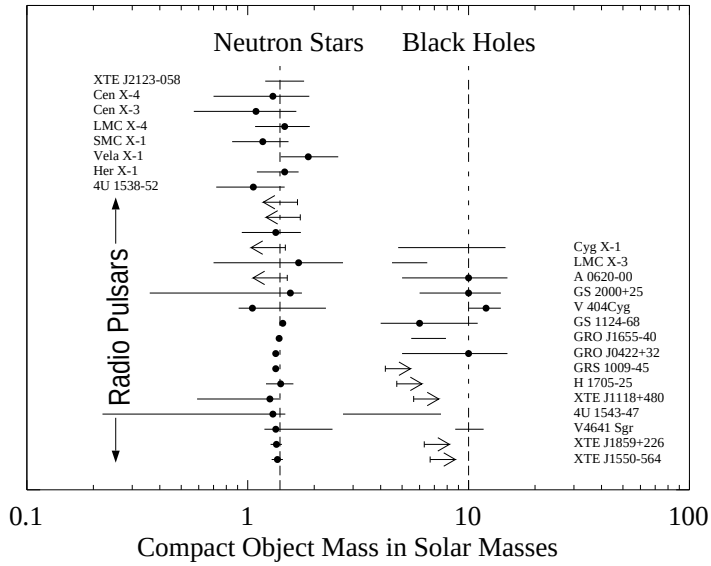

Abbildung 2.5: Ergebnisse der Massenbestimmung von Doppelsternen mit einem Neutronenstern beziehungsweise einem Schwarzlochkandidaten (Kalemci, priv. Mitt.). Die Massenfunktion von GRS 1915+105, mit $9.5 \pm 3.0\,\mathrm{M}_\odot$ zur Zeit Rekordhalter, fehlt, da diese erst nach Erstellung der Abbildung publiziert wurde.

- die Detektion von Röntgenpulsationen, die bei akkretierenden Neutronensternen mit starken ($\gtrsim 10^{12}$ G) Magnetfeldern beobachtet werden. Solche Pulsationen rühren von heißen Flecken an den Magnetpolen eines Neutronensterns her, wo Material mit hoher Geschwindigkeit ($v \sim 0.3c$) auf die Oberfläche des Neutronensterns fällt. Dieses Material strahlt Röntgenstrahlung in einen kleinen Raumwinkel ab. Aufgrund der Rotation des Neutronensterns und dieser engen Strahlungscharakteristik ändert die Röntgenquelle ihre Intensität periodisch. Neuere Beispiele für Messungen solcher Pulsationen, die in unserer Arbeitsgruppe am Institut für Astronomie und Astrophysik durchgeführt wurden, werden von Kreykenbohm et al. (1999, für Vela X-1), Kuster et al. (1999, Her X-1), Heindl et al. (1999, 4U 0115+63) und Kreykenbohm et al. (2002, GX 301−2) gegeben.

Allerdings zeigen nicht alle Neutronensterne X-ray Bursts oder Pulsationen. Daher ist das wichtigste Klassifikationsmerkmal für einen Schwarzlochkandidaten

- seine Ähnlichkeit mit anderen Schwarzlochkandidaten.

Wie oben schon angesprochen wurde, ist diese Situation natürlich unbefriedigend. Dennoch stellen die BHC eine Gruppe astronomischer Objekte dar, die sich durch eine große Anzahl gemeinsamer Eigenschaften auszeichnen, auch wenn es einige Objekte gibt, bei denen die Klassifikation noch nicht auf einer soliden Grundlage steht (beispielsweise 4U 1957+11 = V1408 Aql; Nowak & Wilms, 1999, abgedruckt in Anhang E), und es auch Beispiele für bekannte Neutronensternsysteme gibt, die ansonsten eine sehr große Ähnlichkeit mit Schwarzlochkandidaten haben (Barret, McClintock & Grindlay, 1996; Barret et al., 2000).

KAPITEL 3

Röntgenstrahlung stellarer Schwarzer Löcher

In diesem Kapitel werden meine Arbeiten der letzten Jahre auf dem Gebiet der Theorie der Strahlungserzeugung stellarer Schwarzer Löcher und ihrer Beobachtung zusammengefaßt. In Abschnitt 3.1 werden zunächst die verschiedenen möglichen astronomischen Energieerzeugungsmechanismen verglichen. Es zeigt sich, daß die Energieerzeugung durch Akkretion von Material auf ein kompaktes Objekt effizienter ist als die Energieerzeugung aus anderen Quellen wie zum Beispiel der Kernfusion. Abschnitt 3.2 ist dann einer Beschreibung der Standardtheorie der Akkretion gewidmet. Ein großer Teil der nahe des kompakten Objekts entstandenen Strahlung wird im Röntgenbereich emittiert, die zur Untersuchung benutzten Röntgensatelliten werden in Abschnitt 3.3 vorgestellt. Abschnitt 3.4 bildet den Kern dieses Kapitels. Nach einer Einführung über die verschiedenen beobachteten spektralen Zustände werden in diesem Abschnitt verschiedene Aspekte zu meinen Beobachtungen an galaktischen Schwarzen Löchern dargestellt. Hierbei wird sowohl auf spektrale Untersuchungen und Änderungen der Spektralzustände eingegangen, als auch auf Untersuchungen zum Zeitverhalten dieser Quellen.

3.1 Astronomische Energieerzeugungsmechanismen

Schwarze Löcher zählen mit zu den leuchtkräftigsten bekannten astronomischen Quellen. Ein typischer stellarer Schwarzlochkandidat kann leicht eine Leuchtkraft von $10^4\,\mathrm{L}_\odot$ bis $10^5\,\mathrm{L}_\odot$ besitzen, während aktive Galaxien Leuchtkräfte von $10^{10}\,\mathrm{L}_\odot$ und mehr erreichen können. Die Mechanismen zur Erzeugung dieser Energie und die Erklärung des beobachteten Photonenspektrums sind einer der großen Arbeitsschwerpunkte bei der Erforschung astronomischer Schwarzer Löcher. Um solche Energiemengen unter Verwendung der vorhandenen Materie erzeugen zu können, müssen sehr effektive Mechanismen benutzt werden. Daher kommen eigentlich nur zwei Mechanismen in Frage: Energieerzeugung aus Kernfusion und Energieerzeugung durch Umwandlung von potentieller Energie.

Wie in Kapitel 2 angesprochen wurde, ist Kernfusion über sehr lange Phasen im Leben der Sterne deren Hauptenergiequelle. Beim wichtigsten Kernfusionsprozeß, der Fusion von Wasserstoff zu Helium, werden knapp 1% der verfügbaren Ruhemasse der Protonen in Energie umgewandelt

$$\Delta E_{\mathrm{nuc}} = 0.007 m_{\mathrm{p}} c^2 \tag{3.1}$$

Umgerechnet auf ein Kilogramm Material ergibt sich so bei Kernfusion eine Energieausbeute von $\sim 5 \times 10^{14}\,\mathrm{J\,kg^{-1}}$.

Der Energiegewinn einer Masse m, die aus der Unendlichkeit auf ein Objekt der Masse M und dem Radius R fällt, beträgt dagegen

$$\Delta E_{\mathrm{acc}} = \frac{GMm}{R} \tag{3.2}$$

Für ein Schwarzes Loch mit $M = 10\,\mathrm{M}_\odot$ und $R = 30\,\mathrm{km}$ ergibt sich eine Energieausbeute von $\sim 3 \times 10^{16}\,\mathrm{J\,kg^{-1}}$. Damit ist die Akkretion von Material auf ein kompaktes Objekt, aufgrund des besonders tiefen Potentialtopfes, also fast $100\times$ effizienter als die Kernfusion. Genauere Rechnungen unter Berücksichtigung relativistischer Effekte zeigen, daß durch Akkretion im Idealfall knapp 40% der Ruhemasse in Energie umgesetzt werden können (Akkretion auf ein maximal rotierendes Schwarzes Loch, siehe Frank, King & Raine

1992, S. 191f.). Damit ist die Akkretion von Material der effizienteste Energieerzeugungsprozeß im Universum – man könnte sagen, daß Newtons Apfel doch über $E = mc^2$ siegt ...

Durch Akkretion können auch die beobachteten Leuchtkräfte erzeugt werden. Die maximale Leuchtkraft eines akkretierenden Objektes wird dann erreicht, wenn der Strahlungsdruck der bei der Akkretion entstandenen Photonen größer ist als der Gravitationsdruck der einfallenden Materie. Unter der Annahme, daß die akkretierende Materie aus Wasserstoff besteht und voll ionisiert ist, wird die Strahlung hauptsächlich durch Thomson-Streuung mit den Elektronen in der einfallenden Materie wechselwirken, während die Gravitationskraft hauptsächlich auf die Protonen wirkt. Durch Coulomb-Wechselwirkung sind Elektronen und Protonen aneinander gebunden. Unter der Annahme, daß die Akkretion sphärisch symmetrisch erfolgt, wird ein Gleichgewicht erreicht, wenn (Frank, King & Raine, 1992, sec. 1.2)

$$\frac{GMm_\mathrm{p}}{r^2} = \frac{\sigma_\mathrm{T} S}{c} \qquad \text{wo} \qquad S = \frac{L}{4\pi r^2} \tag{3.3}$$

wo σ_T der Thomson-Wirkungsquerschnitt ist. Dies entspricht einer maximalen Leuchtkraft der Zentralquelle von

$$L_\mathrm{Edd} = \frac{4\pi GMm_\mathrm{p}c}{\sigma_\mathrm{T}} = 3 \times 10^4 \, L_\odot \cdot \left(\frac{M}{M_\odot}\right) \tag{3.4}$$

der sogenannten Eddington-Leuchtkraft. Diese ist die maximale Leuchtkraft, die ein akkretierender Körper haben kann. Sie liegt in der Größenordnung der oben angegebenen Leuchtkräfte der Schwarzen Löcher, das heißt, daß Akkretion für diese Objekte als Energieerzeugungsquelle in Frage kommt.

3.2 Akkretion

Akkretion ist natürlich nur dann möglich, wenn auch genügend Material zur Verfügung steht, das akkretiert werden kann. Prinzipiell ist dies in der ganzen Milchstraße der Fall, nur sind die typischen Dichten im interstellaren Medium mit einigen H-Atomen pro Kubikzentimeter so gering, daß die durch Akkretion erhaltene Leuchtkraft in den meisten Fällen nicht mehr detektierbar ist: Aus Gl. (3.2) ergibt sich für die Leuchtkraft bei Akkretion

$$L_\mathrm{acc} = \frac{GM\dot{M}}{R} \sim 2 \times 10^2 \, \mathrm{L}_\odot \left(\frac{\dot{M}}{10^{-10} \, \mathrm{M}_\odot \, \mathrm{yr}^{-1}}\right) \left(\frac{M}{\mathrm{M}_\odot}\right) \left(\frac{R}{10 \, \mathrm{km}}\right)^{-1} \tag{3.5}$$

wo $\dot{M}$ die Massenakkretionsrate ist. Um die typische Leuchtkraft eines Schwarzlochkandidaten zu erhalten, müssen also $10^{-9} \, \mathrm{M}_\odot \, \mathrm{yr}^{-1}$, oder $\sim 10^{14} \, \mathrm{kg \, s}^{-1}$ Material akkretiert werden, was aus dem interstellaren Medium nicht möglich ist. So gut wie alle gut studierten Schwarzlochkandidaten sind daher Mitglieder von Doppelsternsystemen[1]. Wie schon in Kapitel 2.2 beschrieben wurde, füllt bei diesen Objekten der Begleitstern sein Roche-Lobe aus. Material wird über den inneren Lagrange-Punkt auf das kompakte Objekt akkretiert. Die durch Roche-Lobe Overflow erhaltene Massenakkretionsrate kann ohne Probleme in der oben angegebenen Größenordnung liegen.

Aufgrund der Bahnbewegung des kompakten Objekts und des Sterns um ihren gemeinsamen Schwerpunkt hat das akkretierende Material einen Drehimpuls und kann daher nicht direkt auf das kompakte Objekt fallen. Durch Wechselwirkung mit schon vorher akkretiertem Material wird seine Bahn kreisförmig (Zirkularisation). Daher bildet sich eine Akkretionsscheibe aus, in der das akkretierte Material aufgrund seiner Viskosität Drehimpuls verliert und sich aufheizt. Das Material bewegt sich dann auf quasi-Kreisbahnen langsam nach innen bis es schließlich auf den Neutronenstern fällt oder, im Fall eines Schwarzen Lochs, den letzten stabilen Radius erreicht und dann durch den Ereignishorizont verschwindet. Die dabei erreichten Temperaturen führen

[1] Erst in den letzten Jahren wurde aufgrund der Entwicklung empfi ndlicher Röntgenteleskope wie dem amerikanischen *Chandra*-Satelliten auch die Untersuchung isolierter kompakter Objekte, die direkt aus dem interstellaren Medium akkretieren, möglich. Diese Objekte haben Leuchtkräfte im Bereich von $\lesssim 10^{-2} \, \mathrm{L}_\odot$ (Burwitz et al., 2001; Garcia et al., 2001).

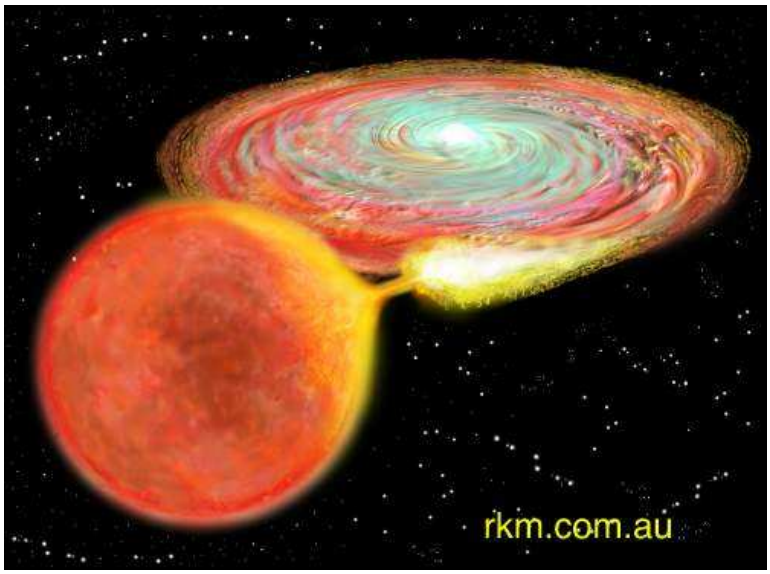

Abbildung 3.1: Künstlerische Darstellung eines Röntgendoppelsterns, in diesem Fall ist der Donor-Stern ein Stern späten Spektraltyps, während das kompakte Objekt ein Weißer Zwerg ist (© Russell Kightley Media, `rkm.com.au`).

im Fall Weißer Zwerge zu Emission von Ultraviolettstrahlung, während aufgrund des tieferen Gravitationspotentials bei Neutronensternen und Schwarzen Löchern Röntgenstrahlung emittiert werden kann. Daher heißen die hier betrachteten Systeme auch Röntgendoppelsterne. Abbildung. 3.1 zeigt die künstlerische Darstellung eines Röntgendoppelsterns.

Die Untersuchung der Akkretionsscheiben ist eines der Hauptgebiete der modernen astrophysikalischen Forschung. Es existiert eine große Zahl an Lehrbüchern und Übersichtsartikeln, in denen die Grundgedanken der Akkretionsscheibentheorie behandelt werden (Frank, King & Raine, 1992; Shore, 1992; King, 1995; Padmanabhan, 2001). Daher sollen hier nur kurz die Grundgedanken der Standardtheorie der Akkretionsscheiben wiedergegeben werden, bevor auf deren Anwendung auf Schwarzlochkandidaten eingegangen wird.

Da der Hauptanteil des Drehimpulses des akkretierenden Materials durch den Bahndrehimpuls verursacht wird, kann angenommen werden, daß sich die Akkretionsscheibe in der Bahnebene des Systems befinden wird. Wird ferner angenommen, daß die Kühlung der Akkretionsscheibe durch Strahlung so hoch ist, daß die Akkretionsscheibe "dünn" ist, daß also die lokale Skalenhöhe der Scheibe

$$H \ll R \tag{3.6}$$

ist, wo R der Abstand vom kompakten Objekt ist, dann spricht man von einer "dünnen Akkretionsscheibe". Diese Annahme einer dünnen Scheibe ist äquivalent zu der Annahme, daß die lokale Keplergeschwindigkeit in der Scheibe größer als die lokale Schallgeschwindigkeit ist (King, 1995).

Wird angenommen, daß die lokal erzeugte Energie in der Akkretionsscheibe sofort abgestrahlt wird, dann ergibt sich das Temperaturprofil der Scheibe zu (Frank, King & Raine, 1992, Gl. 5.39)

$$T(R) \sim \left(\frac{3GM\dot{M}}{8\pi\sigma R^3} \right)^{1/4} \propto R^{-3/4} \tag{3.7}$$

Die Akkretionsscheibe ist also im Inneren heiß und wird nach außen schnell kälter. Für typische Schwarzlochparameter ergibt sich aus Gl. (3.7), daß die Innenregion der Scheibe eine Temperatur von einigen $10^7\,\mathrm{K}$ hat, sie strahlt also im weichen Röntgenbereich.

Ist das Scheibenmaterial optisch dick, was bei den oben erwähnten Massenakkretionsraten meist angenommen werden kann, dann wird die von jedem Flächenelement emittierte Strahlung in erster Näherung ein schwarzer Körper mit der durch Gl. (3.7) gegebenen Temperatur sein. Das Gesamtspektrum einer Akkretionsscheibe ergibt sich in diesem Fall durch Integration über alle Radien

$$F_\nu \propto \int_{R_\mathrm{in}}^{R_\mathrm{out}} B_\nu(T(R)) 2\pi R \,\mathrm{d}R \tag{3.8}$$

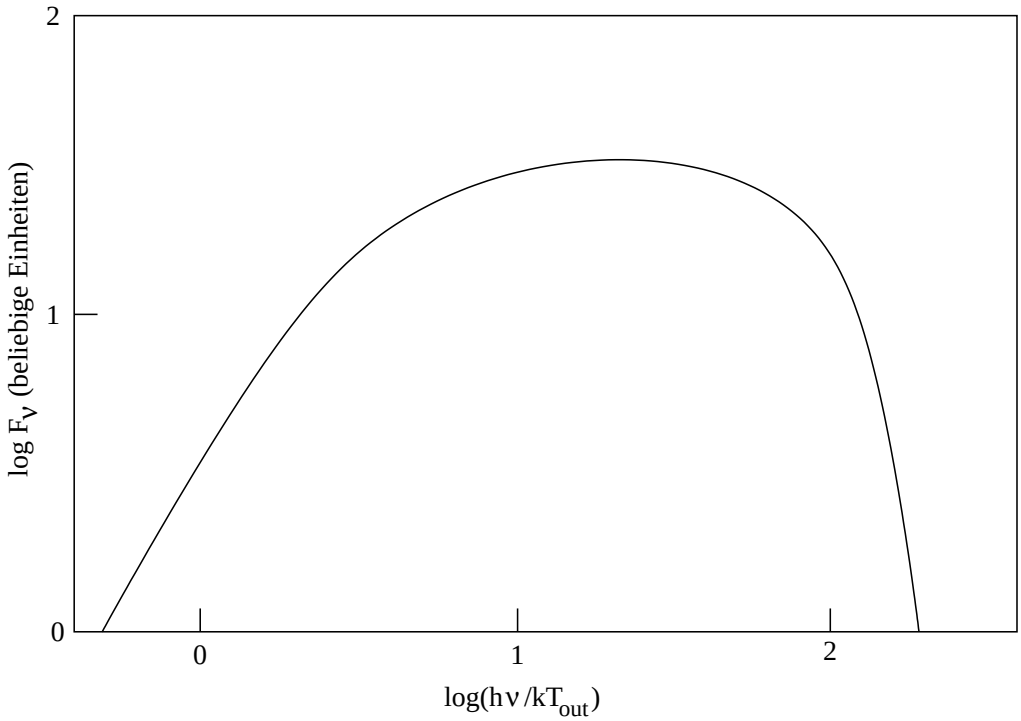

Abbildung 3.2: Emittiertes Spektrum einer dünnen Akkretionsscheibe (nach Frank, King & Raine, 1992, Abb. 20).

wo $B_\nu(T)$ die Strahlungsdichte des schwarzen Körpers bezeichnet und R_{in} und R_{out} den inneren und äußeren Rand der Akkretionsscheibe. Abbildung 3.2 gibt das nach Gl. (3.8) berechnete Akkretionsscheibenspektrum wieder. Das Spektrum ähnelt einem langgezogenen Schwarzkörperspektrum, bei hohen Frequenzen dominiert das Wienspektrum der am inneren Rand emittierten Strahlung. Für die Röntgenstrahlung einer normalen Akkretionsscheibe würde man also erwarten, daß hauptsächlich im weichen Röntgenspektrum Strahlung mit einem thermischen Spektrum detektiert wird.

Auch wenn die lokale Scheibentemperatur, $T(R)$, unabhängig ist von dem genauen Mechanismus, mit dem das akkretierte Material geheizt wird, so geht in die oben skizzierten Rechnungen doch die Annahme ein, daß es einen Viskositätsmechanismus gibt, der Drehimpuls nach außen transportiert und der für den Energieverlust des nach innen fallenden Materials verantwortlich ist. Ein großes Problem ist hier, daß die auf der Erde vorherrschende kinematische Viskosität aufgrund molekularer Wechselwirkungen um Größenordnungen zu klein ist. Die Reynolds-Zahl des akkretierenden Materials kann für typische Akkretionsscheibenparameter zu $\sim 10^9$ abgeschätzt werden (Padmanabhan, 2001, S. 363), das heißt, daß die molekulare Viskosität vernachlässigt werden kann. Bei Reynoldszahlen größer als $\sim 10^3$ werden Flüssigkeiten unter Laborbedingungen stark turbulent. Daher haben Shakura & Sunyaev (1973) vorgeschlagen, daß die für Akkretionsscheiben maßgebliche Viskosität turbulenten Ursprungs ist. Shakura & Sunyaev (1973) parametrisieren die Viskosität durch

$$\nu_{\text{turb}} = \alpha c_{\text{S}} H \tag{3.9}$$

wo α ein unbestimmter Parameter, der α-Parameter ist, c_{S} die Schallgeschwindigkeit, und H die Skalenhöhe der Akkretionsscheibe. Dieser "α-Viskosität" liegt die Annahme zugrunde, daß die typische Größe turbulenter Wirbel maximal gleich der Höhe der Akkretionsscheibe ist und daß die Geschwindigkeit, mit der sich diese Wirbel bewegen, kleiner als die Schallgeschwindigkeit sein sollte. Damit ergibt sich, daß $\alpha \lesssim 1$ gelten sollte.

3.3 Meßmethoden der Röntgenastronomie

Aufgrund der Undurchlässigkeit der Erdatmosphäre ist die Messung von kosmischer Röntgenstrahlung nur mit Hilfe von Instrumenten in der oberen Atmosphäre oder aus dem Erdorbit möglich. Wurden in den 1960er Jahren dafür hauptsächlich Ballons und Forschungsraketen eingesetzt (Giacconi et al., 1962; Bowyer et al.,

1965), die in den 1970er Jahren mit *UHURU* (Start Dezember 1970, Missionsende März 1973, eine Beschreibung des Satelliten findet sich bei Giacconi et al., 1971), HEAO-1 (August 1977–Januar 1979; Peterson, 1975; Rothschild et al., 1979), und dem *Einstein*-Satelliten (HEAO 2, November 1978–April 1981; Giacconi et al., 1979) durch Satelliten ergänzt wurden, werden seit den 1980er Jahren hauptsächlich Satelliten in der röntgenastronomischen Forschung eingesetzt und Ballons nur noch für Entwicklungszwecke oder spezielle Beobachtungsaufgaben genutzt. Der wissenschaftlich interessante Energiebereich ist dabei bei Energien größer als 0.1 keV, da unterhalb dieser Grenze die Absorption der Röntgenstrahlung im interstellaren Medium unserer Milchstraße die Beobachtungen sehr erschwert. Eine genaue Beschreibung der Modifikation der Röntgenstrahlung im ISM ist in Anhang F dieser Arbeit zu finden (Wilms, Allen & McCray, 2000).

Für die Röntgenastronomie im Energiebereich $\gtrsim$10 keV sind hierbei der europäische EXOSAT (Mai 1983–April 1986; Turner, Smith & Zimmermann, 1981), das russisch-deutsche Mir-HEXE Experiment (Start im April 1987, der Hauptteil der Mission endete 1990, die Instrumente waren vor dem Absturz der Mir im Januar 2001 noch einsatzfähig; Reppin et al., 1983; Brinkman et al., 1983) und das amerikanische Compton Gamma-Ray Observatory (CGRO, April 1991–Juni 2000, siehe z.B. Schönfelder, 1995) zu nennen. Unterhalb $\sim$10 keV ist neben *Ginga* (Februar 1987–November 1991; Turner et al., 1989) und *ASCA* (Februar 1993–März 2001; Makishima et al., 1996) insbesondere der deutsche Röntgensatellit *ROSAT* (Juni 1990–Februar 1999; Briel & Pfeffermann, 1995; Zombeck et al., 1995) zu nennen, durch dessen "ROSAT All Sky Survey" die Zahl der bekannten Röntgenquellen von vorher knapp 1000 auf $\sim$150000 erhöht wurde. Ein sehr großer Anteil dieser Quellen sind Aktive Galaxien und enthalten damit Schwarze Löcher.

Im Energiebereich $\gtrsim 15$ keV existieren (noch) keine ausgereiften Techniken, die Röntgenstrahlung zu fokussieren. Daher arbeiten Satelliten in diesem Energiebereich mit Kollimatoren. Jüngstes Beispiel für einen Röntgensatelliten mit einem nicht-abbildenden Detektor ist der von der NASA am 30. Dezember 1995 gestartete Rossi X-ray Timing Explorer (RXTE). Dieser Satellit hat in den letzten Jahren die Erforschung der Röntgendoppelsterne maßgeblich beeinflußt. An Bord von RXTE befinden sich zwei pointierte Instrumente. Bei diesen handelt es sich um ein im Niederenergetischen empfindliches Xenon Proportionalzählerarray (proportional counter array, PCA; Jahoda et al., 1997), mit einem nutzbaren Energiebereich von $\sim$2.5 keV bis $\sim$25 keV und einer Energieauflösung von $\Delta E/E = 18\%$ bei 6 keV, sowie um im Bereich von ~ 15 keV bis $\sim$150 keV empfindliche Phoswich-Detektoren mit einer Energieauflösung von 16% bei 60 keV, das "High Energy X-ray Timing Experiment" (HEXTE; Rothschild et al., 1998). Durch Kollimatoren wird das Gesichtsfeld von HEXTE und PCA auf 1° Halbwertsbreite eingeschränkt. Beide Instrumente haben eine für Röntgeninstrumente vor dem Start von RXTE unerreicht hohe Zeitauflösung im μs Bereich. Ferner hat der PCA mit einer effektiven Sammelfläche von ungefähr $6000\,\mathrm{cm}^2$ die bislang größte Sammelfläche eines Röntgensatelliten. Mit einem systematischen Fehler von $\lesssim 1\%$ (Wilms et al., 1999, siehe auch Anhang A) ist der PCA für ein Instrument dieser Größe ausreichend gut geeicht. In der Kombination von moderater Energieauflösung, sehr guter Zeitauflösung, und hoher Sammelfläche bei niederen Energien ist der RXTE ideal geeignet für die Untersuchung heller Röntgenquellen, die zeitlich stark variabel sind. Wie im weiteren Verlauf dieser Arbeit gezeigt werden wird, fallen die galaktischen schwarzen Löcher in diese Kategorie. Nicht gut geeignet ist RXTE für die Untersuchung schwacher Röntgenquellen. Zwar ist die effektive Sammelfläche unterhalb 20 keV sehr groß, allerdings ist aufgrund der großen Detektorfläche der instrumentelle Hintergrund im PCA sehr hoch. Ferner sind aufgrund des niedrigen Orbits nur Beobachtungen von $\sim$1 h möglich, bevor eine Quelle von der Erde bedeckt wird.

Das dritte wissenschaftliche Instrument auf RXTE ist der "All Sky Monitor" (ASM), der den gesamten vom Satelliten sichtbaren Röntgenhimmel beobachtet. Der ASM (Levine et al., 1996) besteht aus drei jeweils in einer Raumrichtung positionsempfindlichen Proportionalzählern, die gegeneinander verdreht angebracht sind und im Bereich von 2–10 keV empfindlich sind. Jeder der Proportionalzähler ist unter einer Schattenmaske, einer sogenannten kodierten Aperturmaske, angebracht. Diese Maske wird so gestaltet, daß sich aus dem von Röntgenquellen geworfenen Schattenbild die Position und Intensität der Quellen möglichst gut bestimmen läßt (in't Zand, Heise & Jager, 1994; in't Zand, 1992; Caroli et al., 1987; Fenimore, 1987). Der ASM scannt täglich den Röntgenhimmel mehrere Male ab. Die gemessenen Flüsse der $\sim$150 hellsten Röntgenquellen werden im World Wide Web typischerweise einige Tage nach der Messung veröffentlicht.

Bei Energien unterhalb $\sim$10 keV kann Röntgenstrahlung durch streifenden Einfall fokussiert werden. Häu-

fig ist hier die Kombination eines Paraboloiden und eines Hyperboloiden, in Form eines sogenannten "Wolter-Teleskops". Prominentestes Beispiel solcher Teleskope war der oben angesprochene ROSAT. Hier wurde ein positionsempfindlicher Proportionalzähler in der Brennebene des Wolter-Teleskops als Röntgendetektor verwendet wurde, so daß das Instrument auch eine moderate Energieauflösung besaß.

Mit der Entwicklung energiedispersiver "Charge coupled devices" (CCDs) wurde in der neuesten Generation astronomischer Röntgendetektoren eine wesentliche Steigerung der Energieauflösung ermöglicht. Auf dem europäischen XMM-Newton Satelliten, der am 10. Dezember 1999 gestartet wurde, hat die europäische Röntgenastronomie ein neues Großinstrument bekommen, das in den nächsten 10 Jahren noch viele Entdeckungen verspricht. XMM-Newton hat drei parallel ausgerichtete Wolter-Teleskope mit einer räumlichen Auflösung von $6''$ FWHM. In der Fokalebene dieser Teleskope sitzen drei Detektorsysteme, die alle simultan Daten aufnehmen. Hinter zwei der drei Teleskope ist zum einen ein Röntgen-Gitterspektrometer, das "Reflection Grating Spectrometer" (RGS), installiert, das eine hohe Energieauflösung ($E/\Delta E = 200 \ldots 800$) im Bereich von 0.35 bis 2.5 keV besitzt (den Herder et al., 2001), zum anderen befinden sich in der nullten Ordnung des RGS röntgenempfindliche MOS-CCDs (Turner et al., 2001). In der Fokalebene des dritten Wolterteleskops befindet sich als Einzelinstrument die vom Max-Planck-Institut für Extraterrestrische Physik (MPE) in Garching bei München und in Tübingen entwickelte pn-CCD (Strüder et al., 2001). Sowohl die MOS- als auch die pn-Kameras wurden im Rahmen des "European Photon Imaging Camera" (EPIC) Konsortiums entworfen und werden daher als EPIC-MOS und EPIC-pn Kamera bezeichnet. Mit einer Energieauflösung von $E/\Delta E = 20 \ldots 50$ haben die EPIC Kameras eine wesentlich höhere Energieauflösung als Proportionalzähler. Der nutzbare Energiebereich der EPIC-pn geht dabei von $\sim$0.2 keV bis zu $\sim$10 keV, d.h. er überstreicht den Bereich des Röntgenspektrums, in dem Emissionslinien der astrophysikalisch relevanten Elemente beobachtbar sind. Die gesamte Sammelfläche der MOS- und pn-Kamera beträgt $\sim 3000\,\mathrm{cm}^2$, d.h. sie liegt in vergleichbarer Größenordnung mit RXTE. Da es sich bei den EPIC-Kameras um abbildende Instrumente handelt, ist ihr Volumen wesentlich kleiner als der der Proportionalzähler und damit ist auch der instrumentelle Hintergrund fast vernachlässigbar. Damit können mit XMM-Newton auch Quellen niedriger Intensität in vernünftiger Zeit mit einem guten Signal zu Rausch-Verhältnis spektroskopiert werden. Im Rahmen dieser Arbeit sind als schwache Quellen die Aktiven Galaxien zu nennen, die daher auch mit XMM untersucht wurden (Benlloch et al., 2001; Wilms et al., 2001b, siehe auch Kapitel 4). Diese Untersuchungen profitieren auch davon, daß sich XMM-Newton in einem exzentrischen 48 h Orbit befindet und daher lange Beobachtungen ohne störende Bedeckungen der Quellen durch die Erde möglich sind.

Komplementär zu XMM-Newton sind die Instrumente an Bord des amerikanischen *Chandra*-Satelliten, der am 23. Juli 1999 gestartet worden ist (Weisskopf et al., 2002). Hauptmerkmal von *Chandra* ist seine extrem gute Röntgenoptik, die es mit $< 1''$ FWHM Auflösung erlaubt, im Röntgenbereich Bilder mit einer Qualität zu erstellen, die sonst nur im Optischen und Radiobereich möglich war. Dazu stehen als Instrumente wahlweise das ACIS, ein MOS-CCD Detektor, oder die "High Resolution Camera" (HRC), aus Mikrokanalplatten bestehende Detektoren ohne Energieauflösung, zur Verfügung. Mit Hilfe von Röntgen-Gitterspektrometern kann auch mit *Chandra* hochaufgelöste Spektroskopie (maximal $E/\Delta E = 2000$) betrieben werden. Aufgrund von Strahlenschäden an den ACIS-Detektoren ist deren ursprünglich mit den EPIC Detektoren auf XMM-Newton vergleichbare Energieauflösung stark reduziert worden. Die lichtsammelnde Fläche von *Chandra* ist mit 800 cm^2 bei 0.25 keV kleiner als bei XMM. Wie auch XMM befindet sich Chandra in einem Orbit mit langer Umlaufzeit (64 h).

3.4 Physik galaktischer Schwarzer Löcher

3.4.1 Breitbandspektren im Röntgenbereich

Zur Untersuchung der Physik galaktischer Schwarzer Löcher werden sowohl spektrale Informationen als auch Informationen über deren Zeitverhalten auf allen Zeitskalen vom Millisekundenbereich bis hin zur Variabilität über Jahrzehnte hinweg verwendet. Abbildung 3.3 gibt eine Zusammenstellung verschiedener typischer Schwarzlochspektren. Sie zeigt, daß die Breitbandspektren im Röntgenbereich als die Summe zweier spektraler Komponenten dargestellt werden können: Bei niedrigen Energien, unterhalb ungefähr $\sim$2 keV, wird eine

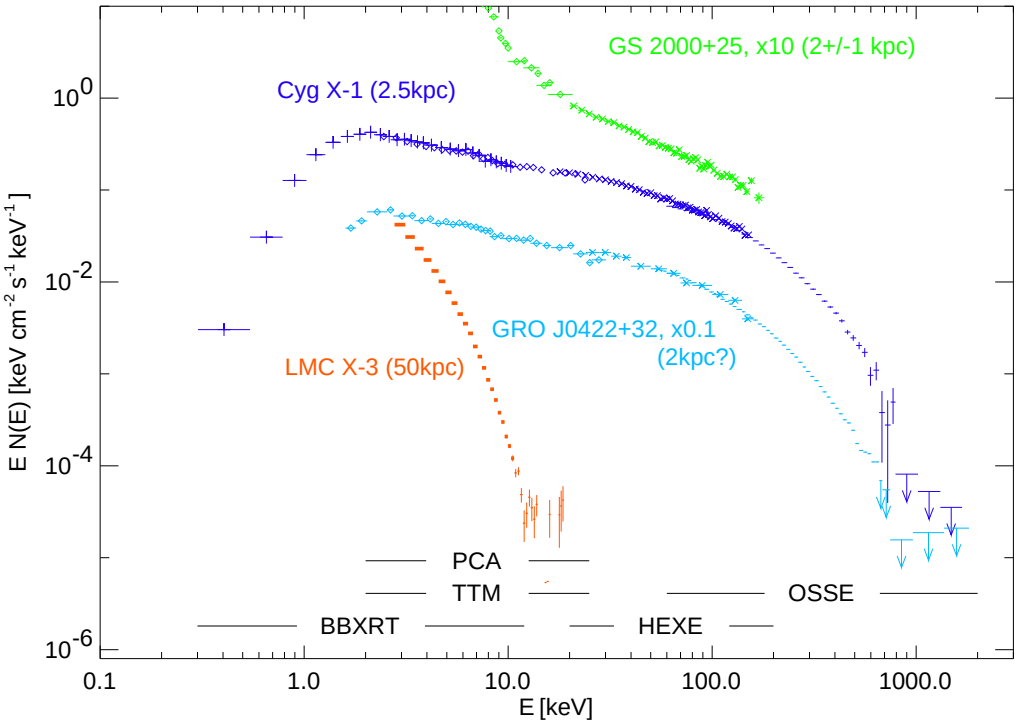

Abbildung 3.3: Zusammenstellung der Breitbandspektren verschiedener galaktischer Schwarzlochkandidaten zur Illustration der möglichen Spektralformen.

thermische Komponente beobachtet, die sich gut durch die in Abschnitt 3.2 beschriebenen Akkretionsscheibenspektren beschreiben läßt. Zusätzlich zu dieser thermischen Komponente wird ein Potenzgesetzspektrum detektiert, das bei Photonenenergien im Bereich von typischerweise $\sim$150 keV in einen exponentiellen Abbruch übergeht. Die relative Stärke dieser zwei Komponenten kann stark variieren. Dominiert die thermische Spektralkomponente, dann spricht man vom “soft/high state”, dominiert das Potenzgesetz, dann ist die Quelle im sogenannten “low/hard state”. In Abbildung 3.3 ist Cygnus X-1 ein Beispiel für eine Quelle im “hard state”, während LMC X-3 eine typische “soft state” Quelle ist.

Die Bezeichnungen “high state” und “low state” wurden in den 1970er Jahren eingeführt, als diese zwei Zustände der Schwarzlochkandidaten das erste Mal mit Instrumenten entdeckt wurden, die im Bereich $\lesssim$ 2 keV empfindlich waren. In diesem Spektralband hat eine Quelle, die vom spektral härteren “hard state” in den spektral weichen “soft state” wechselt, in letzterem eine höhere Zählrate. Spätestens seit genauen Untersuchungen solcher spektralen Änderungen mit RXTE (Cui et al., 1997, 1998) haben sich die physikalisch exakteren Bezeichnungen “hard state” und “soft state” durchgesetzt, die daher hier ausschließlich verwendet werden sollen.

Diese Existenz zweier spektraler Zustände zeigt, daß das in Abschnitt 3.2 dargestellte einfache Bild einer Akkretionsscheibe modifiziert werden muß, da dieses die Erzeugung der harten Potenzgesetzkomponente nicht erklären kann. Die Beschreibung der physikalischen Prozesse, die mit den Zustandsänderungen einhergehen, sowie die Beobachtung von Schwarzlochkandidaten in beiden Zuständen waren ein Schwerpunkt der Arbeiten, die ich in den vergangenen Jahren durchgeführt habe. Sie sollen daher im folgenden genauer beschrieben werden. Für Details sei dabei auf die in den Anhängen abgedruckten Originalpublikationen verwiesen.

3.4.2 Hard State: Einzelbeobachtungen

3.4.2.1 Einführung

Der hard state kann als “klassischer Zustand” der Schwarzen Löcher angesehen werden, da er in der Anfangszeit der Röntgenastronomie lange als der einzige Zustand der Schwarzen Löcher betrachtet wurde. Grund dafür ist, daß der klassische Schwarzlochkandidat Cygnus X-1 für den überwiegenden Teil der Zeit in diesem

Zustand beobachtet wird (Liang & Nolan, 1984; Oda, 1977). Wie oben schon angesprochen wurde, ist das im hard state beobachtete Potenzgesetzspektrum natürlich mit einem thermischen Akkretionsscheibenspektrum nicht erklärbar. Während frühe Arbeiten das beobachtete Röntgenspektrum noch durch thermische Bremsstrahlung zu erklären versuchten, konnten Sunyaev & Trümper (1979) überzeugend zeigen, daß das Spektrum durch thermische Comptonisierug zustande kommt.

Die grundlegende Annahme dieses Modells ist, daß niederenergetische Photonen aus der Akkretionsscheibe beim Durchgang durch ein Elektronenplasma aufgrund von inversen Comptonstößen an hochenergetischen Elektronen von diesen Energie gewinnen. Der mittlere relative Energiegewinn eines Photons der Energie E pro Compton-Stoß an maxwellverteilten Elektronen der Temperatur T_e ist (Rybicki & Lightman, 1979)

$$\frac{\Delta E}{E} = \frac{4kT_\mathrm{e} - E}{m_\mathrm{e}c^2} \tag{3.10}$$

so daß ein Energiegewinn immer dann zu erwarten ist, wenn die Photonenenergie kleiner als die Temperatur des Elektronenplasmas ist. Das Comptonisierungsspektrum ist ein Potenzgesetz mit einem durch die Maxwell-Verteilung bedingten exponentiellen Abbruch. In frühen Modellen (z.B. Haardt & Maraschi, 1993, und die darin angegebene Literatur) wurde allgemein angenommen, daß das heiße Elektronenplasma sich "sandwichförmig" um die Akkretionsscheibe herum befindet. In Analogie an Modelle der Sonnenkorona (z.B. Burm, 1986), bei der ebenfalls ein heißes Gas nahe der kühlen Sonnenoberfläche gefunden wird, wird das Elektronenplasma auch die "Akkretionsscheibenkorona" genannt. Mögliche physikalische Ursachen für die Bildung der Korona sind wahrscheinlich magnetohydrodynamischen Ursprungs, beispielsweise durch die Balbus-Hawley-Chandrasekhar Instabilität, bei der aufgrund der differentiellen Rotation der Akkretionsscheibe der magnetische Druck im Inneren der Akkretionsscheibe so stark ansteigt, daß magnetische Flußschläuche in der Scheibe aufsteigen. Auf der Scheibenoberfläche kann dann durch magnetische Rekonnexion Energie freigesetzt werden, so daß das Material der Oberfläche stark geheizt wird (Hawley & Balbus, 1991; Balbus & Hawley, 1991; Stone et al., 1996; Hawley & Stone, 1998; Miller & Stone, 2000).

Die genaue analytische Berechnung des Comptonisierungsspektrums ist kompliziert, da dieses im allgemeinen von Annahmen über die Quellgeometrie, wie zum Beispiel der relativen Lage der Akkretionsscheibenkorona und der Quelle der weichen Photonen oder der Elektronendichteverteilung innerhalb der Akkretionsscheibenkorona abhängt. Die Rechnung basiert auf der Lösung der Kompaneets-Gleichung, einer quantenmechanisch modifizierten Form der Fokker-Planck-Gleichung für den Photonentransport. Herleitungen der Fokker-Planck-Gleichung finden sich zum Beispiel in meiner Dissertation (Wilms, 1998) oder bei Rybicki & Lightman (1979). Analytische Lösungen der Kompaneets-Gleichung sind unter anderem von Sunyaev & Titarchuk (1980), Sunyaev & Titarchuk (1985), Poutanen (1994), Titarchuk (1994), Titarchuk & Lyubarskij (1995) und Hua & Titarchuk (1995) gegeben worden. Ein Problem all dieser Lösungen ist, daß sie nur für sehr einfache Quellgeometrien anwendbar sind. Der Vergleich dieser analytischen Comptonisierungsspektren mit den Beobachtungen zeigt, daß die Spektren im hard state durch Comptonisierung erklärbar sind. Allerdings sind vielfach die dabei erhaltenen Spektralparameter nicht selbstkonsistent. Für galaktische Schwarze Löcher findet sich beispielsweise häufig, daß die beobachteten Spektren durch heiße ($kT_\mathrm{e} \sim 100\,\mathrm{keV}$) Akkretionsscheibenkoronen hoher optischer Tiefe, $\tau_\mathrm{e} \gg 1$, beschrieben werden. Dies ist aber physikalisch nicht erlaubt: hohe optische Tiefen führen dazu, daß die Comptonkorona sehr effizient von der eingestrahlten niederenergetischen Strahlung gekühlt wird (Haardt & Maraschi, 1993; Haardt, Maraschi & Ghisellini, 1994; Dove, Wilms & Begelman, 1997; Dove et al., 1997).

Weitere Selbstkonsistenzprobleme der einfachen analytischen Comptonisierungsmodelle ergeben sich daraus, daß ein Teil der von der Akkretionsscheibenkorona emittierten Strahlung wieder auf die Akkretionsscheibe eingestrahlt wird. Ein Teil dieser Strahlung wird durch Thomson-Streuung in der Akkretionsscheibe reflektiert und führt zur Emission eines sogenannten "Compton-Reflektionsbuckels" (Lightman & White, 1988). Ein weiterer Teil der eingestrahlten Strahlung wird in der Akkretionsscheibe absorbiert und dann in Form von Fluoreszenzstrahlung re-emittiert. Als stärkste Fluoreszenzlinie wird hier die Fe Kα Linie bei 6.4 keV emittiert, die in den Röntgenspektren auch beobachtet wird (siehe auch Kapitel 4.1). Je nach Geometrie werden schließlich bis zu 30% der eingestrahlten Energie in der Akkretionsscheibe selbst absorbiert, thermalisiert und als weiche Röntgenstrahlung wieder reemittiert. Es existiert daher eine starke Wechselwirkung zwischen der

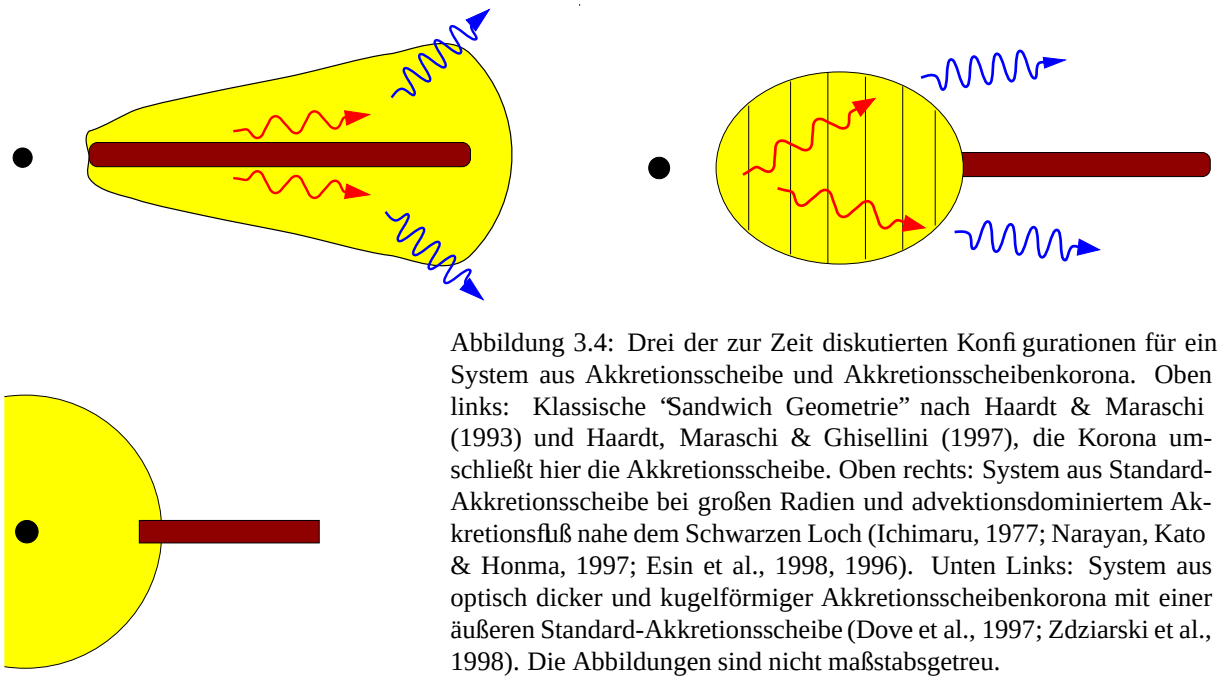

Abbildung 3.4: Drei der zur Zeit diskutierten Konfigurationen für ein System aus Akkretionsscheibe und Akkretionsscheibenkorona. Oben links: Klassische "Sandwich Geometrie" nach Haardt & Maraschi (1993) und Haardt, Maraschi & Ghisellini (1997), die Korona umschließt hier die Akkretionsscheibe. Oben rechts: System aus Standard-Akkretionsscheibe bei großen Radien und advektionsdominiertem Akkretionsfluß nahe dem Schwarzen Loch (Ichimaru, 1977; Narayan, Kato & Honma, 1997; Esin et al., 1998, 1996). Unten Links: System aus optisch dicker und kugelförmiger Akkretionsscheibenkorona mit einer äußeren Standard-Akkretionsscheibe (Dove et al., 1997; Zdziarski et al., 1998). Die Abbildungen sind nicht maßstabsgetreu.

Emission der Akkretionsscheibe und der Akkretionsscheibenkorona, so daß eine strikte Trennung dieser Komponenten, wie dies von den oben angesprochenen analytischen Comptonisierungsmodellen aus prinzipiellen Gründen erfolgen muß, nicht möglich ist.

3.4.2.2 Röntgenspektroskopie und Akkretionsscheibenmodelle

In Zusammenarbeit mit der Gruppe von Prof. Dr. Mitchell C. Begelman am JILA, University of Colorado, Boulder, habe ich seit der Zeit meiner Dissertation an einem Monte Carlo Code gearbeitet, der die oben angesprochenen Selbstkonsistenzprobleme durch Simulation aller wichtigen physikalischen Prozesse in der Akkretionsscheibe und der Korona umgeht (Dove, Wilms & Begelman, 1997; Dove et al., 1997; Wilms, 1998). Basierend auf einer Idee von Stern et al. (1995a) wird dabei das Photonenfeld und die Elektronendistribution parallel berechnet. Damit können die durch Energieverlust der Elektronen bei Comptonstößen in der Korona auftretenden Kühlprozesse direkt implementiert werden. Außer Compton-Streuung werden auch Photon-Photon Paarproduktion, die Annihilation von Elektron-Positron-Paaren und Synchrotronstrahlung berücksichtigt (Bremsstrahlung ist in dem betrachteten Parameterraum nur sekundär von Interesse). Alle Prozesse werden dabei mit korrekter relativistischer Kinematik und unter Verwendung winkelabhängiger quantenelektrodynamischer Wirkungsquerschnitte simuliert. Die Elektronen und Positronen haben eine durch die relativistische Maxwell-Verteilung gegebene Geschwindigkeitsverteilung. Bei der Wechselwirkung der harten Photonen in der Akkretionsscheibe sind Thomson-Streuung, die Photoabsorption und die eventuelle Reemission von Fluoreszenzstrahlung die relevanten physikalischen Prozesse. Ferner können harte Photonen auch in der Akkretionsscheibe thermalisieren. Ihre Energie wird dabei in Form von thermischer Strahlung wieder abgestrahlt.

Die Anwendung dieser Modelle auf RXTE und ASCA Beobachtungen des hard state liefert sehr gute Ergebnisse: Hard State Spektren können mit den selbstkonsistenten Modellen gut beschrieben werden. Als Beispiel für solche Untersuchungen seien unsere Studien des galaktischen Schwarzen Loches GX 339−4 in Anhang A genannt (Wilms et al., 1999). Wie schon bei unseren Untersuchungen an Cygnus X-1 (Dove et al., 1998) finden wir, daß die "Sandwich-Geometrie" (Abb. 3.4, oben rechts) aufgrund der oben angesprochenen starken Kühlung die beobachteten Röntgenspektren nicht beschreiben kann. Wird dagegen eine geometrische Trennung zwischen Korona und Akkretionsscheibe postuliert, dann erreicht das Plasma die notwendige Temperatur. Im konkreten Fall der von uns vorgeschlagenen "sphere+disk" Geometrie (Dove et al., 1997; Wilms et al., 1997, siehe Abb. 3.4, unten links) erreichen wir eine exzellente Anpassung an die Meßdaten. Das dabei

erreichte reduzierte χ^2 ist extrem klein, da die Abweichungen zwischen Daten und Modell in der Größenordnung der Kalibrationsunsicherheiten des RXTE-PCA liegen, die durch die Einführung einer systematischen Unsicherheit der Meßdaten in die χ^2-Summe nur unzureichend beschrieben werden können. Eine zusätzlich zum Monte Carlo Modell noch notwendige Fe Kα Linie bei 6.4 keV kann durch den plausiblen Überlapp zwischen äußerer Akkretionsscheibe und innerer Akkretionsscheibenkorona erklärt werden, der zum Zeitpunkt der in Anhang A beschriebenen Rechnungen noch nicht im Monte Carlo Code enthalten war.

Das Ergebnis, daß eine zu 100% überdeckende Sandwich-Korona keine physikalisch selbstkonsistente Erklärung der Beobachtungen ermöglicht, war zum Zeitpunkt unserer ersten Veröffentlichungen zu diesem Thema noch stark umstritten. Inzwischen hat sich diese Einsicht jedoch durchgesetzt und wurde von mehreren unabhängig arbeitenden Gruppen bestätigt (siehe z.B. Gierliński et al., 1997; Zdziarski et al., 1998; Stern et al., 1995b).

Eine physikalische Motivation für die "sphere+disk" Geometrie boten unter anderem die sogenannten advektions-dominierten Akkretionsflüsse (ADAF; siehe Abb. 3.4, oben rechts), die seit Mitte der 1990er Jahre als Alternativmodelle zur Standardakkretionsscheibe vorgeschlagen wurden (Narayan & Yi, 1995; Esin et al., 1996; Narayan, Kato & Honma, 1997; Esin et al., 1998, und die darin angegebene Literatur)[2]. Akkretionsscheiben sind dann dünn, wenn sie effizient gekühlt werden (Abschnitt 3.2). Während ein Großteil der potentiellen Energie in den Protonen (bzw. allgemeiner in den Ionen) transportiert wird, wird die Akkretionsscheibe hauptsächlich durch durch Elektronen vermittelte Prozesse gekühlt, da diese effizient strahlen können. In der Theorie der Standardakkretionsscheibe wird vorausgesetzt, daß es einen effizienten Mechanismus gibt, durch den die freiwerdende potentielle Energie von den Ionen auf die Elektronen übertragen werden kann. Ob es einen solchen Mechanismus gibt, ist allerdings nicht geklärt (siehe z.B. Quataert, 1998, und die darin angegebene Literatur). Ist die Kopplung zwischen Ionen und Elektronen schwächer, dann können diese unterschiedliche Temperaturen haben. In ADAFs wird vorausgesetzt, daß die Kopplung zwischen Elektronen und Ionen so gering ist, daß die Zeitskalen für die Kühlung der Ionen größer sind als die dynamische Zeitskala zum Erreichen des Schwarzschildradius. Ein großer Teil der potentiellen Energie verschwindet daher im Schwarzen Loch (Advektion), so daß ADAFs äußerst ineffiziente Strahler sind. Da der Akkretionsfluß nicht mehr effizient gekühlt werden kann, haben die Ionen wesentlich höhere Temperaturen. Dadurch ist die Skalenhöhe der Akkretionsscheibe wesentlich größer als bei Standard-Akkretionsscheiben, wie dies auch von den "sphere+disk" Modellen postuliert wird.

Das Spektrum der ADAFs bei niederen Frequenzen wird hauptsächlich von Synchrotronstrahlung und Bremsstrahlung erzeugt, die von den Elektronen comptonisiert werden kann, um die Potenzgesetzkomponente im hard state zu erklären (Esin et al., 1998). Ein Vergleich zwischen den Vorhersagen der ADAF-Modelle und den Beobachtungen erfordert daher simultane Beobachtungen im Radiobereich und mit Röntgensatelliten. Am Beispiel von GX 339−4 (Anhang A) konnten wir zeigen, daß solche simultane Beobachtungen *nicht* mit ADAF-Modellen in Einklang zu bringen sind – der beobachtete Radiofluß ist um ein Vielfaches höher als der von ADAF-Modellen, die die Röntgendaten erklären können. Bei der beobachteten Radiostrahlung scheint es sich daher um einen Synchrotronstrahlung erzeugenden Ausfluß von Materie zu handeln und nicht um einen ADAF. Dieser könnte das Resultat der von Blandford & Begelman (1999) gefundenen Instabilität der ADAFs sein: Gas in ADAFs ist gravitativ nicht gebunden, so daß es zu einem Materieausfluß kommen kann (siehe dazu allerdings auch Ogilvie 1999, Turolla & Dullemond 2000 und die darin angegebene Literatur).

3.4.2.3 Kurzzeitvariabilität: Das Periodogramm

Außer der Spektroskopie können wertvolle Informationen über die Physik der Akkretionsscheibe aus der Zeitreihenanalyse der Röntgendaten gewonnen werden. Da ein großer Teil der Röntgenstrahlung aus der Zone nahe des Schwarzen Lochs kommt, werden charakteristische Zeitskalen bis in den Bereich von Zeitdauern der Größenordnung

$$t_{\rm lc} \approx \frac{r_{\rm st}}{c} = 0.1\,{\rm ms}\,\frac{M}{10\,{\rm M}_\odot} \tag{3.11}$$

[2] ADAFs lassen sich in der Literatur bis in die 1960er Jahre zurückverfolgen, allerdings wurden die Arbeiten auf diesem Gebiet weithin ignoriert (Svensson, 1997, und die darin angegebene Literatur).

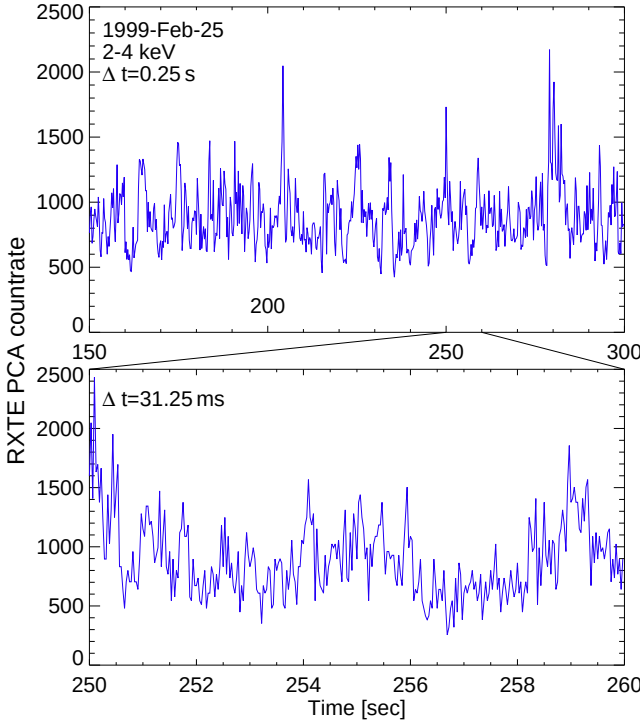

Abbildung 3.5: Beispiel für die stark variablen Lichtkurven von Cyg X-1, dargestellt in zwei verschiedenen Zeitauflösungen. Die durch die Poissonstatistik herrührende Meßungenauigkeit beträgt für die obere Lichtkurve $\sim 60\,\mathrm{counts\,s^{-1}}$, für die untere Lichtkurve $\sim 180\,\mathrm{counts\,s^{-1}}$. Damit sind die die sichtbaren Strukturen in der Lichtkurve durch den Akkretionsprozeß bedingt.

zu erwarten sein. Wie Abbildung 3.5 zeigt, sind Schwarzlochkandidaten im “hard state” stark variabel. Die starken stochastischen Schwankungen sind dabei nicht durch statistische Schwankungen zurückzuführen, die durch den Meßprozeß bedingt sind (Poissonrauschen), sondern in der Tat quellintrinsisch.

Zur Charakterisierung der Variabilität werden in der Astronomie meist aus der Fourieranalytik entlehnte Techniken verwendet (Lewin, van Paradijs & van der Klis, 1988; van der Klis, 1989, 1995, 1997), daneben kommen in zunehmenden Maße auch in der Zeitdomäne arbeitende Verfahren zum Tragen (Scargle, 1981; König, Staubert & Wilms, 1997; Pottschmidt et al., 1998; Timmer et al., 2000). Die zur Beschreibung einer Einzellichtkurve wichtigste Größe ist das Periodogramm (Schuster, 1906), auch “power spectral density” (PSD) oder “power density spectrum” (PDS) genannt. Das PSD ist definiert als das Quadrat der Fouriertransformierten der Lichtkurve,

$$P_j = A|X_j|^2 \quad \text{wo } j \in [0 \ldots N/2] \tag{3.12}$$

wo

$$X_j = \sum_{k=0}^{N-1} x_k \mathrm{e}^{2\pi i j k/N} \quad \text{wo } j \in [-(N/2) \ldots (N/2)-1] \tag{3.13}$$

und wo die zugehörige Frequenz gegeben ist durch

$$\nu_j = \frac{j}{N\Delta t} \tag{3.14}$$

Hier ist Δt die Zeitauflösung und N die Gesamtzahl der Punkte in der Lichtkurve. Die Konstante A in Gl. (3.12) hängt von der gewählten Normierung des Periodogramms ab. In der Röntgenastronomie üblich sind insbesondere die Normierung von Miyamoto et al. (1991) und Belloni & Hasinger (1990a), in der das Integral über X_j die Gesamtvarianz der Lichtkurve ergibt, und die im Fall von PSDs, die für den Einfluß des Poissonrauschens korrigiert wurden, unabhängig von der Quellzählrate ist. Eine weitere Normierung geht auf Leahy et al. (1983) zurück und ist so gewählt, daß für “weißes Rauschen”, d.h. für einen Poisson-Prozeß, der Wert des PSDs gleich 2 ist. Für weitere Erläuterungen zu diesen Normierungen sei auf van der Klis (1989), Wilms (1998) und insbesondere auf die Dissertation von Katja Pottschmidt (Pottschmidt, 2002) verwiesen.

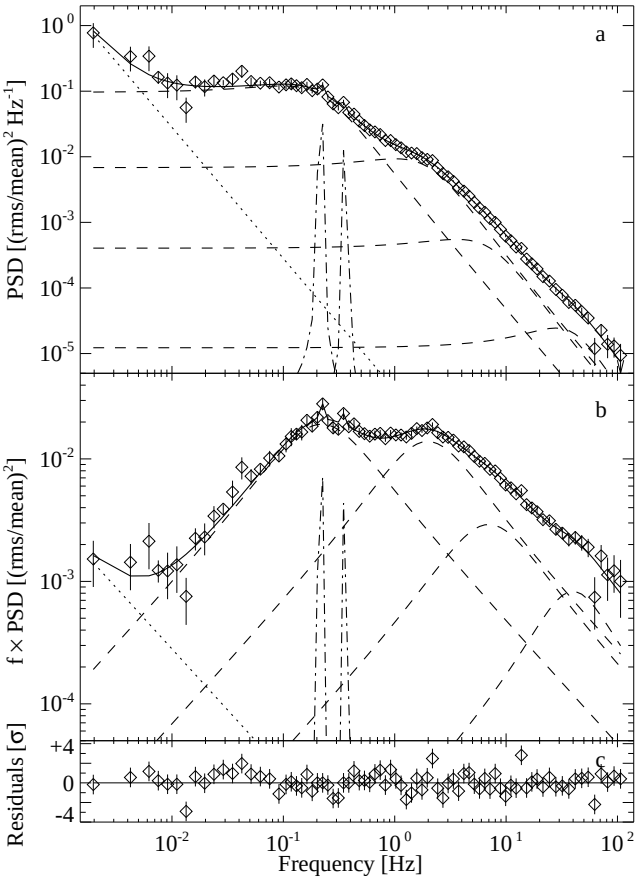

Abbildung 3.6: Beispiel für die Beschreibung des Periodogramms von Cygnus X-1 durch mehrere breite Lorentzfunktionen.

Letztere enthält insbesondere eine gute Zusammenstellung der Formeln, die für die Korrektur instrumenteller Effekte (Totzeit, instrumenteller Hintergrund, ...) benötigt werden.

Das beobachtete PSD der Schwarzlochkandidaten läßt sich bei Frequenzen oberhalb $\sim 10^{-1}$ Hz grob durch ein Potenzgesetz darstellen (siehe z.B. Belloni & Hasinger, 1990b,a), das unterhalb dieser Grenzfrequenz, $f_{\rm cut}$, flach ist (siehe z.B. Abbildung 2 in Anhang B, Nowak et al. 1999a),

$$\mathrm{PSD}(f) \propto \begin{cases} f^{-\beta} & \text{für } f > f_{\rm cut} \\ \text{const.} & \text{for } f \leq f_{\rm cut} \end{cases} \tag{3.15}$$

Der Index dieses Potenzgesetzes ist $\beta \sim 1$. Diesem Kontinuum überlagert sind resonante Strukturen, sogenannte "Quasi-periodische Oszillationen" (QPOs). Häufig treten diese nahe $f_{\rm cut}$ auf, sie werden jedoch über das gesamte Frequenzspektrum beobachtet. Normalerweise werden diese QPOs durch eine Lorentzfunktion gut beschrieben. Es wird daher davon ausgegangen, daß die QPOs durch gedämpfte Schwingungen im emittierenden Medium verursacht werden (Psaltis & Norman, 2001). Welcher physikalische Prozeß diese Schwingungen anregt, ist jedoch unbekannt. Siehe dazu auch die Diskussionen in Anhang B (Nowak et al., 1999a).

In den letzten Jahren hat sich herausgestellt, daß die Beschreibung des PSD durch ein Potenzgesetz nicht ausreichend ist. Schon Abbildung 2 in Anhang B zeigt, daß das PSD viele weitere Strukturen aufweist. Diese beschrieben wir zunächst durch die Summe eines Potenzgesetzes und mehrerer breiter Lorentzfunktionen. Nowak (2000) konnte dann anhand dieser Beobachtungen von GX 339−4 sowie von Daten von Cyg X-1 zeigen, daß die PSDs sehr gut als die Summe *breiter* Lorentzfunktionen dargestellt werden konnten und ein Potenzgesetz nur in seltenen Fällen notwendig ist. Normalerweise werden vier Lorentzfunktionen benötigt, um das ganze PSD, einschließlich des flachen Teils unterhalb $f_{\rm cut}$, gut zu beschreiben. Dieses wichtige Ergebnis wurde durch van Straaten et al. (2001) anhand der Daten vieler Neutronensterne und Schwarzlochkandidaten bestätigt und kann jetzt als gesichert gelten.

Im Rahmen einer von K. Pottschmidt und dem Autor initiierten großangelegten Beobachtungskampagne haben wir in den letzten Jahren das zeitliche und spektrale Verhalten des kanonischen Schwarzlochkandidaten

Cygnus X-1 systematisch untersucht. Dazu wurde das Objekt im Zeitabstand von 2 bis 3 Wochen mit RXTE beobachtet. Typische Beobachtungsdauern waren zwischen 10 und 20 ksec, d.h. ausreichend, um gute spektrale und zeitliche Informationen zu erhalten. Simultan dazu wurde Cygnus X-1 im Radiobereich vom Ryle Teleskop, Cambridge, U.K., beobachtet (Beobachter: G.G. Pooley), ferner liegen quasi-simultane optische photometrische Daten vom Krim-Observatorium vor (Beobachter: V. Lyutyi, A.E. Tarasov). Ziel dieser Kampagne ist es, Änderungen im spektralen und zeitlichen Verhalten der Quelle zu dokumentieren und im Rahmen der in diesem Kapitel beschriebenen physikalischen Modelle zu interpretieren. Alleine im Röntgenbereich haben wir die Gesamtbeobachtungszeit, mit der Cyg X-1 seit seiner Entdeckung beobachtet wurde, vervielfacht. Die Analyse dieser Daten ist noch nicht abgeschlossen, und wird noch mehrere Jahre in Anspruch nehmen.

Eine ausführliche Beschreibung der Ergebnisse der zeitlichen Analyse der Röntgendaten bildet die Grundlage der Dissertation von Katja Pottschmidt (Pottschmidt 2002, siehe auch Pottschmidt et al. 2000a,b, 2002), auf die für die Details verwiesen sei. Im Gegensatz zu den oben angesprochenen wenigen Beobachtungen von GX 339−4 und Cyg X-1 handelt es sich hier um ∼130 Einzelbeobachtungen, die es erlauben, sehr detailliert das Verhalten des PSD zu untersuchen. Wir finden, daß dieses während des "hard state" immer durch vier breite Lorentzfunktionen beschrieben werden kann. Da sich die Breite dieser Lorentzfunktionen kaum ändert, obwohl die Quellleuchtkraft variabel ist, kann davon ausgegangen werden, daß die physikalische Ursache für diese Lorentzfunktionen im hard state immer die selbe ist. Abhängig von der Quellleuchtkraft ist hingegen die charakteristische Frequenz der Lorentzfunktionen, das heißt, die Frequenz, bei der die Lorentzfunktion ein Maximum hat. Diese charakteristische Frequenz liegt bei höherem L_{X} bei höheren Frequenzen. Dieser Effekt, daß charakteristische Frequenzen im PSD mit L_{X} zunehmen, ist schon in früheren Studien angesprochen worden (z.B. Belloni & Hasinger, 1990b,a), aufgrund der neuen Interpretation der Komponenten des PSD ist es jetzt jedoch möglich geworden, dieses Verhalten mit physikalischen Modellen zu überprüfen.

Eine mögliche Erklärung dieses Verhaltens des PSD ist in Änderungen der Massenakkretionsrate des Systems zu suchen. Allen in Abschnitt 3.4.2.2 dargestellten Akkretionsscheibenmodellen ist zu eigen, daß sie sich durch charakteristische Radien auszeichnen. Bei den "sphere+disk" Modellen oder den ADAFs ist ein solcher charakteristischer Radius der Übergang von der äußeren Akkretionsscheibe in die heiße Comptonisierende innere Region. Bei "Sandwich-Modellen" wird der charakteristische Radius beispielsweise durch den Radius definiert, bei dem die Bedingungen für das Einsetzen der Balbus-Hawley Instabilität erfüllt sind. Steigt die Massenakkretionsrate an, dann rückt der charakteristische Radius näher an das Schwarze Loch heran. Modelle für die Variabilität im hard state gehen typischerweise davon aus, daß die f^{-1}-Proportionalität des PSD durch stochastische Prozesse in der Akkretionsscheibe selbst entsteht (siehe z.B. Negoro et al., 1995; Nowak et al., 1999a,b; Psaltis & Norman, 2001). Diese intrinsische Variabilität wird dann durch physikalische Prozesse moduliert. Durch diese intrinsische Variabilität könnte zum Beispiel die Akkretionsscheibe zu resonanten, gedämpften Schwingungen angeregt werden, die den vier Lorentzfunktionen entsprechen. Ändert sich die Massenakkretionsrate adiabatisch, so daß die Scheibengeometrie selbstähnlich bleibt, dann ist es vernünftig anzunehmen, daß der für die Lorentzfunktion verantwortliche Resonator bei höherem $\dot{M}$ bei kleineren Radien liegt. Da unter sehr allgemeinen Annahmen alle charakteristischen Frequenzen in einer Akkretionsscheibe mit der lokalen Keplerfrequenz zusammenhängen (siehe z.B. Psaltis, Belloni & van der Klis, 1999; di Matteo & Psaltis, 1999), heißt dies, daß bei größerem $\dot{M}$ auch die Resonatorfrequenz ansteigen sollte. Genaue (magneto-)hydrodynamische Rechnungen, die diese Effekte bestätigen, stehen jedoch noch aus (siehe allerdings Psaltis & Norman, 2001).

3.4.2.4 Kurzzeitvariabilität: Time Lags und Kohärenzfunktion

Die Untersuchung der Quellvariabilität mithilfe des PSD ermöglicht es nur schwer, die Zusammenhänge der Variabilität in verschiedenen Energiebändern zu erklären. Diese sind wichtig, da die physikalischen Ursachen für die Entstehung des Röntgenspektrums wesentlich besser verstanden sind, als die Ursachen zur Entstehung der Variabilität selbst. Diese physikalischen Modelle sind jedoch nur dann wirklich selbstkonsistent, wenn sie auch das zeitliche Verhalten der Quelle beschreiben können.

Eine Abhängigkeit der Röntgenlichtkurven in zwei Energiebändern kann zum Beispiel durch thermische Comptonisierung erzeugt werden. Aufgrund verschiedener Prozesse in der Akkretionsscheibe werden die Compton-gestreuten weichen Photonen eine charakteristische Variabilität besitzen. Da die weichen Photonen

in der Akkretionsscheibenkorona gestreut werden, sollte diese charakteristische Variabilität auch in der comptonisierten Strahlung beobachtbar sein, d.h. prinzipiell sollten eine bei niederen Photonenenergien und eine bei höheren Photonenenergien beobachtete Lichtkurve einander ähnlich sein. Das Maß dieser Ähnlichkeit wird durch die Eigenschaften der Comptonkorona bestimmt. So ist leicht einsichtig, daß aufgrund des Streuprozesses in der Korona die Weglänge, die Photonen zurücklegen, von der Endenergie der Photonen abhängig sein wird: Im Mittel haben Photonen, die aus der Korona bei höheren Photonenenergien entweichen, mehr Compton-Stöße erfahren und sind daher länger in der Korona geblieben. Daher ist zu erwarten, daß aufgrund der Comptonisierung die beobachtete Lichtkurve in einem härteren Energieband zwar die gleiche charakteristische Variabilität aufweist wie die Lichtkurve in einem niedrigeren Energieband, aber gegenüber letzterer verzögert ist. Ferner ist zu erwarten, daß aufgrund der Photonendiffusion durch die Korona die Variabilität bei hohen Frequenzen "ausgeschmiert" wird.

Mit Hilfe von Monte Carlo Rechnungen, insbesondere mit dem von mir entwickelten linearen Monte Carlo Code, kann dieser Prozeß quantifiziert werden. Dabei wird die Green's Funktion für die Diffusion von Photonen durch die Compton-Korona berechnet, d.h. für ein vorgegebenes Anfangsspektrum, das zur Zeit $t = 0$ emittiert wird, wird berechnet, zu welchem Zeitpunkt Photonen in eine gewissen Energieband aus der Compton-Korona austreten. Unter der Kenntnis der Green's Funktion kann dann die in diesem Energieband erwartete Variabilität berechnet werden, wenn ein bestimmtes Variabilitätsverhalten des Anfangsspektrums vorausgesetzt wird.

Zum Testen solcher Vorhersagen wurden in unserer Gruppe in den letzten Jahren verschiedene Verfahren entwickelt. Hier sind insbesondere die fourierfrequenzabhängigen "Time lags" zu nennen. In Schwarzlochkandidaten wird beobachtet, daß eine in einem härteren Energiebereich beobachtete Lichtkurve der in einem weicheren Energieband beobachteten sehr ähnelt, allerdings um einige 10^{-3} bis 10^{-2} Sekunden verzögert ist. Quantitativ wird dieses Verhalten über die "Time Lags" beschrieben. Zur Berechnung des "Time lags" wird die Phaseninformation der Fouriertransformierten der beiden Lichtkurven benutzt (Nowak & Vaughan, 1996), während die "Ähnlichkeit" der Lichtkurven formaler mit Hilfe der Kohärenzfunktion beschrieben wird (Vaughan & Nowak, 1997).

Mit derartigen Rechnungen konnten wir zeigen, daß Comptonisierung *nicht* die Ursache für die oben beschriebenen "Time Lags" in galaktischen BHC ist (Nowak et al., 1999b). Auch weitere von uns untersuchte Ursachen für die Variabilität scheinen auszuscheiden, so daß die Ursache der Variabilität noch als offen anzusehen ist.

3.4.3 Zustandsänderungen und Soft State

Im "soft state" ist die Akkretionsscheibe die klar dominierende spektrale Komponente. Die Untersuchung des soft state ist gegenüber der des hard state lange vernachlässigt worden. Dies liegt daran, daß die zwei Quellen, die immer im soft state beobachtet worden waren, LMC X-1 und LMC X-3, aufgrund ihrer Lage in der Großen Magellanischen Wolke und der damit verbundenen Entfernung von 50 kpc Quellen wesentlich kleinerer Intensität sind, als die galaktischen hard state Quellen. Die von uns mit RXTE durchgeführten Beobachtungen dieser Quellen waren die ersten Untersuchungen, bei denen diese Objekte systematisch über längere Zeiträume (mehrere Jahre hinweg) beobachtet wurden[3]. Eine ausführliche Darstellung unserer Beobachtungen wird in den Anhängen C und D gegeben (Nowak et al., 2001; Wilms et al., 2001a).

Wie schon bei den Untersuchungen des hard state konnten wir auch hier durch den Vergleich vieler Beobachtungen Fortschritte bei der Erklärung der beobachteten Phänomene gewinnen, die bei Einzelbeobachtungen nur schwer verständlich sind. LMC X-1 und LMC X-3 sind recht ähnliche Objekte. In beiden Systemen sind die Donorsterne frühen Typs und auch die Leuchtkraft und die typischen spektralen Parameter der Röntgenspektren dieser Quellen sind vergleichbar: Das Röntgenspektrum wird durch eine thermische Komponente dominiert, die bei höheren Energien in ein weiches Potenzgesetzspektrum übergeht. Schon Ebisawa, Mitsuda & Hanawa (1991) und Ebisawa et al. (1993) hatten jedoch bemerkt, daß LMC X-1 auf längeren Zeitskalen nur wenig variabel ist, während bei LMC X-3 Intensitätsänderungen über einen Faktor 4 und mehr erkennbar waren. Diese sind auch gut in den RXTE-ASM Lichtkurven dieser Quellen zu erkennen (Abbildung 3

[3] Frühere Studien, wie zum Beispiel die *Ginga* Analysen von Ebisawa, Mitsuda & Hanawa (1991) and Ebisawa et al. (1993), waren auf einige wenige Beobachtungen beschränkt.

in Anhang D). Die optische Variabilität von LMC X-3 ist jedoch gering. Wie wir in der Analyse photometrischer Daten des Begleitsterns von LMC X-3 zeigen konnten, ist diese nur schwach und nicht mit der Langzeitvariabilität im Röntgenbereich korreliert (Brocksopp, Groot & Wilms, 2001).

Wichtigstes Ergebnis unserer Monitoringkampagne war, daß wir diesen Unterschied in der Röntgenvariabilität erklären konnten: Im Gegensatz zu LMC X-1 zeigt LMC X-3 deutliche spektrale Änderungen, die typisch sind für spektrale Zustandsänderungen vom soft state in den hard state. Besonders deutlich wurde dies im Jahr 1998, als zum ersten Mal in dieser Quelle ein reines Potenzgesetzspektrum beobachtet werden konnte (Abbildung 4 in Anhang D). In der Zwischenzeit wurde diese Entdeckung durch weitere Beobachtungen bestätigt (Boyd & Smale, 2000; Boyd et al., 2000; Wu et al., 2001; Soria et al., 2001). Damit ist LMC X-1 der einzige Schwarzlochkandidat, der bisher keine Zustandsänderungen aufweist. Ähnliche Analysen von spektralen Änderungen und der damit verbundenen physikalischen Parameter bei Zustandsänderungen habe ich auch bei GX 339−4 (Anhänge A und B) durchgeführt.

Als Ursache für Zustandsänderungen werden Änderungen in der Massenakkretionsrate angenommen. Dies ist wahrscheinlich, da klare Änderungen von $\dot{M}$ mit Zustandsänderungen in den nicht-persistenten Schwarzlochkandidaten einhergehen (Tanaka & Shibazaki, 1996; Wheeler, 1996). Physikalisch begründet werden kann diese Annahme damit, daß alle vorgeschlagenen Mechanismen für die Entstehung von Akkretionsscheibenkoronen nur unterhalb einer kritischen Massenakkretionsrate funktionieren. Die Modulation von $\dot{M}$ kann im Fall von LMC X-3 im Akkretionsmechanismus selbst gesucht werden. Eine Zeitreihenanalyse von LMC X-1 und LMC X-3 zeigt, daß LMC X-3 eher als Objekt, das über Roche-Lobe Overflow akkretiert, zu sehen ist, während bei LMC X-1 Windakkretion als wahrscheinlich erscheint (Nowak et al., 2001, abgedruckt in Anhang C). Damit ist die Akkretionsscheibe in LMC X-3 größer als die in LMC X-1, insbesondere kann der äußere Rand der Akkretionsscheibe durch die Röntgenstrahlung des zentralen Objekts aufgeheizt werden. Es kann gezeigt werden, daß diese Heizung ausreicht, $\dot{M}$ signifikant zu ändern. Bei LMC X-1 ist die Akkretionsscheibe kleiner, so daß dieser Mechanismus hier nicht funktioniert. Ein solches Modell kann auch die Langzeitvariation von LMC X-3 prinzipiell erklären (Anhang D), während wir bei V1408 Aql eher von einer präzedierenden Akkretionsscheibe als Ursache für die Langzeitvariation ausgehen (Nowak & Wilms, 1999, abgedruckt in Anhang E). Siehe auch Pottschmidt et al. (2002) für Untersuchungen der Langzeitvariabilität von Cygnus X-1.

KAPITEL 4

Röntgenstrahlung supermassiver Schwarzer Löcher

Die zweite heute studierte Art Schwarzer Löcher sind die supermassiven Schwarzen Löcher in den Zentren Aktiver Galaxien (englisch *active galactic nuclei*, AGN). Obwohl diese mit Massen von 10^6 bis $10^8\,\mathrm{M}_\odot$ wesentlich höhere Massen haben, als die im letzten Kapitel behandelten Schwarzlochkandidaten, sind AGN in vielen Eigenschaften den galaktischen Schwarzlochkandidaten doch ähnlich – beispielsweise werden ihre Röntgenspektren ebenfalls durch Comptonisierung erzeugt.

In diesem Kapitel werden verschiedene Aspekte meiner Untersuchungen zu Aktiven Galaxien zusammengefaßt. Abschnitt 4.1 führt in die benutzten Bezeichnungen, insbesondere die Klassifikation der AGN, ein. Abschnitt 4.3 ist dann der Darstellung meiner Untersuchungen gewidmet, unter besonderer Berücksichtigung der Analyse der in diesen Objekten beobachteten Kα-Linie des Eisens.

4.1 Aktive Galaxien

Aktive Galaxien wurden in den frühen 1960er Jahren zunächst im Radiobereich als Objektklasse erkannt. Bei Durchmusterungen des Himmels im Radiobereich wurden Radioquellen entdeckt, deren Winkelausdehnung mit den damals vorhandenen Radioteleskopen nicht meßbar war. Dies wurde als atypisch angesehen, da die meisten in dieser Zeit bekannten Radioquellen ausgedehnte Objekte waren; diese punktförmigen Radioquellen bekamen den Namen "Radiosterne". Das optische Spektrum dieser Objekte war durch Emissionslinien gekennzeichnet, was atypisch für Sterne ist, bei denen Spektrallinien typischerweise in Absorption beobachtet werden. Ferner konnten diese Emissionslinien zunächst nicht identifiziert werden, da sie bei Wellenlängen gefunden wurden, bei denen keine bekannten Spektrallinien existieren. Schmidt (1963) erkannte, daß die Emissionslinien sehr wohl bekannten Elementen zugeordnet werden konnten, wenn man annahm, daß sie rotverschoben waren. Für den "Radiostern" 3C 273 wurde eine Rotverschiebung von $z = 0.158$ ermittelt, wenig später fanden Greenstein & Matthews (1963) für 3C 48 die Rotverschiebung $z = 0.368$. Gemeinhin wurde und wird angenommen, daß diese Rotverschiebung der Spektrallinien kosmologischen Ursprungs ist, das heißt, diese großen Rotverschiebungen werden durch die Expansion des Universums verursacht und nicht durch eine Eigenbewegung des Strahlung emittierenden Objekts. "Radiosterne" sind daher keine stellaren Objekte, sondern stellen Quellen dar, die kosmologische Entfernungen von vielen Mpc und dementsprechend hohe Leuchtkräfte haben. Sie sind daher nur quasi-stellare Objekte, sogenannte *Quasare*. In der Folgezeit nach der Entdeckung der Quasare wurden Objekte mit ähnlichen Charakteristika auch bei niedriger Rotverschiebung entdeckt, bei denen außer dem Quasar auch noch eine Galaxie beobachtbar ist. Die Leuchtkraft der Galaxie ist allerdings auch hier kleiner als die der Punktquelle, die sich im Zentrum der Galaxie befindet. Alle Objekte dieser Art werden als "Aktive Galaxien" bezeichnet. Einen ausführlichen Überblick über die Geschichte der Aktiven Galaxien geben Kembhavi & Narlikar (1999).

Die wesentlichen Beobachtungseigenschaften von AGN sind ein sehr kleiner Winkeldurchmesser, Leuchtkräfte im Bereich von Galaxienleuchtkräften, starke zeitliche Variabilität, häufig ein flaches (nichtthermisches) Breitbandspektrum vom radio oder Infrarotbereich bis in den MeV- oder sogar GeV-Bereich und starke und sehr breite Emissionslinien im Optischen und Ultraviolet (Krolik, 1999). Ihrer Entdeckungsgeschichte zum Trotz ist nur ein kleiner Teil von AGN radiolaut, für die überwiegende Zahl der AGN trägt die Radioleuchtkraft nur einen kleinen Teil zur bolometrischen Leuchtkraft bei ("radioleise AGN"). Im Folgenden soll hauptsächlich letzterer Typ der AGN angesprochen werden, da diese für meine Röntgenbeobachtungen von größerem

Interesse waren.

Wie es oben schon angesprochen wurde, werden die optischen Spektren Aktiver Galaxien durch Emissionslinien dominiert. Die Spektren sind dabei den planetarischen Nebeln in unserer Milchstraße ähnlich, insbesondere wird auch eine große Zahl an Linien aus verbotenen Übergängen beobachtet, wie zum Beispiel die [O III]λ5007Å und λ4959Å Linien, oder Linien von N II oder S II. Solche Linien sind typisch für Gase mit Teilchendichten von einigen $1000\,\mathrm{cm}^{-3}$ und Temperaturen im Bereich von $\sim 10^4\,\mathrm{K}$. Die typischen Linienbreiten entsprechen Dopplerbreiten von einigen $100\,\mathrm{km\,s}^{-1}$. Im Gegensatz zu planetarischen Nebeln werden in Aktiven Galaxien jedoch auch Linien von vergleichsweise hochionisierten Spezies beobachtet. Das Linienspektrum ist charakteristisch für das eines Gases, das von einem nichtthermischen Spektrum photoionisiert wird. Außer den verbotenen Linien werden in den AGN Spektren auch erlaubte Linien, wie z.B. die Hα λ6563Å Linie oder weitere Linien von He I, He II, usw. beobachtet. Je nach beobachtetem AGN sind diese Linien entweder von ähnlicher Breite wie die verbotenen Linien, oder aber sie werden mit Breiten von 1000 bis $5000\,\mathrm{km\,s}^{-1}$ beobachtet. Das Gas, das diese breiten Linien emittiert, hat Dichten im Bereich von einigen 10^8 bis $10^{10}\,\mathrm{cm}^{-3}$. Aufgrund thermischer Bewegung werden Geschwindigkeiten in der Größenordnung von

$$v = \sqrt{\frac{kT}{m_\mathrm{p}}} \sim 10\,\mathrm{km\,s}^{-1} \left(\frac{T}{10^4\,\mathrm{K}}\right)^{1/2} \tag{4.1}$$

erwartet, also Geschwindigkeiten, die wesentlich geringer sind, als die aus der beobachteten Linienverbreiterung ermittelten. Daher ist davon auszugehen, daß das Gas, das die verbotenen bzw. erlaubten Linien aussendet, relativ zur Galaxie in Bewegung ist. Aus der symmetrischen Linienform ist ferner davon auszugehen, daß das emittierende Gas in der Form von Wolken auftritt, deren Geschwindigkeitsvektoren in erster Näherung isotrop verteilt sind. Für AGN, in denen sowohl breite erlaubte als auch dünne verbotene Linien auftreten, bedeutet dies, daß zwei kinematisch unterschiedliche Regionen existieren sollten, in denen die jeweiligen Linien entstehen.

Radioleise Aktive Galaxien, in denen breite erlaubte Linien und dünne verbotene Linien beobachtet werden, werden als Seyfert 1 Galaxien bezeichnet (nach Carl Seyfert, der diese Objekte als erster beschrieben hat). Sind sowohl die erlaubten als auch die verbotenen Linien nur einige $100\,\mathrm{km\,s}^{-1}$ breit, dann handelt es sich um eine Seyfert 2 Galaxie. Die Kontinuumsspektren von Seyfert 1 Galaxien sind zudem wesentlich stärker, als die von Seyfert 2 Galaxien. Weitere Unterschiede und Gemeinsamkeiten der Seyfert Galaxien und anderer Aktiver Galaxien, sowie der Klassifikation dieser Objekte werden von Lawrence (1987) und Urry & Padovani (1995) diskutiert.

Entscheidend für das heutige Bild Aktiver Galaxien waren Messungen von Antonucci & Miller (1985), die das Spektrum der Seyfert 2 Galaxie NGC 1068 polarimetrisch untersuchten und feststellten, daß es sehr dem Spektrum einer Seyfert 1 Galaxie ähnelt. Solche und weitere Untersuchungen führten zu der Hypothese, daß es sich bei *allen* Aktiven Galaxien prinzipiell um die gleiche Art von astronomischen Objekt handelt und daß die Unterschiede zwischen den verschiedenen Aktiven Galaxien nur von unserem Blickwinkel auf das Objekt herrühren. Auch wenn dieses "Vereinigungsmodell" (*unified model*) der Aktiven Galaxien noch keineswegs als gesichert gelten kann, so bietet es doch ein Paradigma, innerhalb dessen Beobachtungen von AGN interpretiert werden können. Im folgenden sollen die Haupteigenschaften die Vereinigungsmodells kurz dargestellt werden, für die Details sei auf Urry & Padovani (1995), Krolik (1999), Antonucci (1993) und die darin angegebene Literatur verwiesen.

Dem "Vereinigungsmodell" zufolge befindet sich im Zentrum eines AGN ein supermassives Schwarzes Loch mit einer Masse von $10^6\,\mathrm{M}_\odot$ bis $10^8\,\mathrm{M}_\odot$, auf das $\sim 3\,\mathrm{M}_\odot\,\mathrm{yr}^{-1}$ über eine Akkretionsscheibe akkretiert werden. Um das Schwarze Loch und die Akkretionsscheibe herum befinden sich in einer Zone mit einem Durchmesser von $\lesssim 1\,\mathrm{pc}$ dichte Gaswolken, die durch die Strahlung des Schwarzen Lochs photoionisiert werden. Diese dichten Wolken haben Geschwindigkeiten von einigen $1000\,\mathrm{km\,s}^{-1}$ und sind verantwortlich für die beobachteten breiten Spektrallinien. Daher wird die Zone dieser Wolken als "Broad Line Region" (BLR) bezeichnet. Ob die Wolken der BLR sich um das Schwarze Loch bewegen, oder ob es zusätzlich zur oben angesprochenen statistischen Geschwindigkeitsverteilung auch noch einen Einfall der Wolken auf oder eine Entfernung vom Schwarzen Loch gibt, ist noch nicht endgültig geklärt. Bei größeren Entfernungen vom Schwarzen Loch, das heißt bei Abständen von einigen 10 pc, existiert im "Vereinigungsmodell" eine zweite

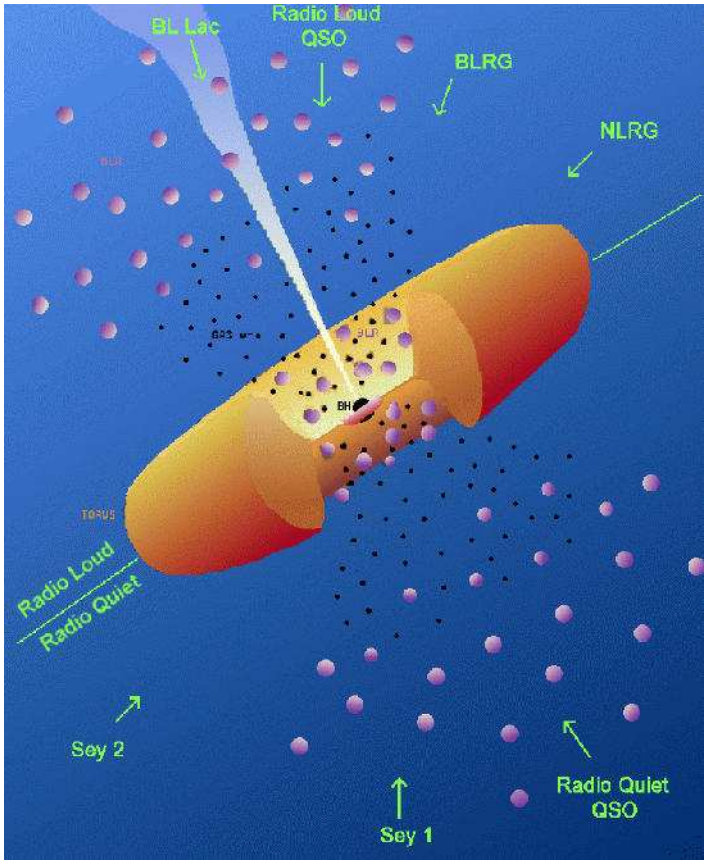

Abbildung 4.1: Das Vereinigungsmodell der Aktiven Galaxien (Urry & Padovani, 1995). Die obere Hälfte der Abbildung erklärt die verschiedenen Typen radiolauter AGN, die untere Hälfte die verschiedenen Typen radioleiser AGN. Die Abbildung ist *nicht* maßstabsgerecht.

Klasse von Wolken, die ebenfalls von der Zentralquelle photoionisiert werden. Diese Wolken haben geringere Dichten, so daß auch Emission verbotener Linien zu erwarten ist. Aufgrund des großen Abstands ist die Geschwindigkeit dieser Wolken geringer, was zu einer geringeren Linienverbreitung führt. Diese zweite Zone ist die “Narrow Line Region”. Abbildung 4.1 skizziert den Aufbau Aktiver Galaxien nach dem “Vereinigungsmodell”.

Der Unterschied zwischen Typ 1 und Typ 2 AGN wird dadurch erklärt, daß bei einer Entfernung von $\sim 1\,\mathrm{pc}$ vom Schwarzen Loch in der Ebene der Akkretionsscheibe, optisch dickes und daher wahrscheinlich kühles Material vorhanden ist, der sogenannte Molekültorus (Abbildung 4.1). Bei AGN vom Typ 2, also zum Beispiel bei Seyfert 2 Galaxien, ist für Beobachter auf der Erde die Sicht auf das Schwarze Loch versperrt. Die Strahlung des Schwarzen Lochs wird nur im Streulicht gesehen, so daß diese Objekte ein schwächeres Kontinuumsspektrum haben, als AGN vom Typ 1, bei denen die Sichtlinie nicht versperrt ist. Da die BLR-Wolken sich nahe am Schwarzen Loch befinden, wird ihre Strahlung ebenfalls vom Torus blockiert, so daß das optische Spektrum von AGN vom Typ 2 durch die Linien der NLR dominiert wird. Nur ein geringer Anteil von Strahlung der BLR wird in unsere Sichtlinie gestreut. Da diese Strahlung durch die Streuung polarisiert wird, kann diese spektrale Komponente in spektropolarimetrische Beobachtungen, wie den schon angesprochenen Beobachtungen von Antonucci & Miller (1985), nachgewiesen werden.

Der Unterschied zwischen radioleisen und radiolauten AGN besteht in der Stärke der Radioemission von Elektronen in einem sogenannten Jet (Abbildung 4.1). Diese Elektronen werden durch einen bislang noch nicht verstandenen physikalischen Prozeß nahe des Schwarzen Lochs auf Geschwindigkeiten von $v \approx c$ beschleunigt und emittieren im schwachen Magnetfeld des Jets Synchrotronstrahlung. Jets werden in $\sim 1\%$ aller AGN beobachtet (Krolik, 1999) und können über Distanzen von mehreren 100 kpc hinweg kollimiert bleiben. Siehe Begelman, Blandford & Rees (1984) für eine ausführliche Darstellung der relevanten Theorie.

4.2 Die Existenz Schwarzer Löcher in Aktiven Galaxien

Außer der Existenz des Molekültorus ist *die* wesentliche Annahme des Vereinigungsmodells die Existenz Schwarzer Löcher in den Zentren Aktiver Galaxien. Diese wurde primär aus der geringen Ausdehnung, hohen Leuchtkraft und starken Zeitvariabilität gefolgert (Rees, 1984, und die darin angegebene Literatur), solche Folgerungen sind jedoch noch kein *Beweis* für die Existenz der Schwarzen Löcher (Kormendy & Richstone, 1995).

Zentrales Gebiet der Erforschung der Aktiven Galaxien in den letzten Jahren war daher insbesondere die Frage, inwiefern die Existenz des zentralen Schwarzen Lochs auch durch direktere Messungen nachgewiesen werden kann. Als direkte Methoden kommen hier insbesondere kinematische Verfahren in Frage, bei denen aus der Bewegung von Material nahe des Schwarzen Lochs Hinweise auf die vom Material eingeschlossene Masse gezogen werden können (Ford et al., 1997, und die darin angegebene Literatur). Hierfür sind räumlich aufgelöste spektroskopische Untersuchungen erforderlich, mit denen das Geschwindigkeitsfeld nahe des Schwarzen Lochs gemessen wird. Diese Daten liefern immer nur Informationen über die mittlere Bewegung der beobachteten Sterne, da schon die nächsten Aktiven Galaxien nicht mehr in Einzelsterne auflösbar sind. Die durch eine Punktmasse M verursachte Geschwindigkeitsdispersion σ ist näherungsweise gegeben durch

$$\sigma^2 = \frac{GM}{R} \tag{4.2}$$

wo R der Abstand von der Punktmasse ist. Der Einflußbereich der Punktmasse ist bei einer intrinsischen Geschwindigkeitsdispersion der Sterne, σ_0, definiert durch den Bereich, in dem $\sigma > \sigma_0$ gilt, das heißt, das Schwarze Loch hat einen Einfluß auf die Sternbewegungen bis zu einem Radius

$$R \sim \frac{GM}{\sigma_0^2} \sim 40\,\mathrm{pc} \left(\frac{M}{10^8\,\mathrm{M}_\odot}\right) \left(\frac{\sigma_0^2}{100\,\mathrm{km\,s^{-1}}}\right) \tag{4.3}$$

(siehe zum Beispiel de Zeeuw, 2001). Im Virgohaufen (Entfernung: 20 Mpc) entspricht diese Entfernung einem Winkelabstand von $0.2''$, das heißt, daß solche Messungen mit weltraumbasierten Teleskopen wie dem Hubble Space Telescope durchgeführt werden müssen. Die dabei erhaltenen Massenkonzentrationen von $M \sim 10^8\,\mathrm{M}_\odot$ sind verträglich mit den aus der AGN-Leuchtkraft abgeschätzten (Gebhardt et al., 2000), allerdings ist diese Masse die Masse in einem Radius von $R \lesssim 40\,\mathrm{pc}$, das heißt, daß sie noch keinen tatsächlichen Beweis für ein Schwarzes Loch liefern, da prinzipiell im beobachteten Volumen auch ein Sternhaufen hoher Sterndichte verborgen sein könnte.

Aufgrund der höheren Auflösung interferometrisch arbeitender Radioteleskope kann im Radiobereich ein kleineres Volumen abgebildet werden. Die Entdeckung sehr dünner Emissionslinien eines Wasser-Masers in NGC 4258 ($d = 6.5\,\mathrm{Mpc}$) durch Miyoshi et al. (1995) und Greenhill et al. (1995), die im Abstand von ~ 0.05 Millibogensekunden vom Zentrum dieser Seyfert-Galaxie gefunden wurden, ermöglichte die Messung des Geschwindigkeitsfelds dieser Galaxie bei Abständen von $\lesssim 0.25\,\mathrm{pc}$ vom Zentralobjekt. Die VLBI-Beobachtungen von Greenhill et al. (1996), mit denen die Position der Wassermaser gemessen werden konnte, lassen sich gut durch Emission aus einer leicht verdrehten Akkretionsscheibe erklären. Die aus dem Geschwindigkeitsfeld gefolgerte Masse von $\sim 4 \times 10^7\,\mathrm{M}_\odot$ innerhalb eines Volumen mit $R \lesssim 0.25\,\mathrm{pc}$ (Neufeld & Maloney, 1995) weist stark auf die Existenz eines Schwarzen Lochs hin. Allerdings besteht bei NGC 4258 immer noch Uneinigkeit über den Modus der Akkretion, so könnte die Akkretion in NGC 4258 auch advektionsdominiert sein (Lasota et al., 1996; Lasota, 1999).

Die prinzipiell wohl direkteste Methode, die Existenz des zentralen Schwarzen Lochs nachzuweisen, rührt jedoch von der Beobachtung der Röntgenstrahlung Aktiver Galaxien her, da diese im Abstand von nur einigen Schwarzschildradien sehr nah am Schwarzen Loch entsteht.

4.3 Röntgenbeobachtungen Aktiver Galaxien

Die Röntgenspektren der Seyfert-Galaxien sind den in Kapitel 3 beschriebenen Röntgenspektren galaktischer Schwarzlochkandidaten sehr ähnlich. Auch die Röntgenspektren von Seyfert-Galaxien können in erster Näherung durch Potenzgesetze mit einem Photonenindex von $\Gamma \sim 1.7$ und einem exponentiellen Abfall des

Spektrums bei einer charakteristischen Energie von $\sim 150\,\mathrm{keV}$ beschrieben werden. Daher ist es auch hier sehr wahrscheinlich, daß das Röntgenspektrum durch Comptonisierung erzeugt wird.

Im Gegensatz zu galaktischen Schwarzlochkandidaten ist das Röntgenspektrum der Aktiven Galaxien jedoch stärker von weiteren spektralen Features gekennzeichnet. Viele Aktive Galaxien zeigen im Niederenergiespektrum bei $\sim 0.7\,\mathrm{keV}$ Strukturen, die als Absorptionskanten von O VII oder O VIII gedeutet wurden (Nandra et al., 1993; Turner et al., 1993; Reynolds & Fabian, 1995). Diese Absorptionsstrukturen rühren wahrscheinlich von einem heißen Gas her, dem "Warmen Absorber", das sich ähnlich der Broad Line Region in der näheren Umgebung des Schwarzen Lochs befindet (Porquet & Dubau, 2000; Lee et al., 2001; Komossa & Fink, 1997; Reynolds & Fabian, 1995, und die darin angegebene Literatur). Mit dem Aufkommen hochaufgelöster Instrumente ist diese Interpretation in jüngster Zeit kritisiert worden (Branduardi-Raymont et al., 2001; Sako et al., 2002). Ich werde auf diese Kritik später noch einmal zurückkommen.

Bei höheren Energien, im Band zwischen 6 keV und 7 keV, wird ferner eine starke Kα Linie von Eisen beobachtet, die Äquivalentbreiten von 150 eV und mehr erreichen kann. Wie auch bei galaktischen Schwarzlochkandidaten weicht das Röntgenspektrum oberhalb $\sim$10 keV von der Potenzgesetzform ab und zeigt deutliche Anzeichen für einen Compton-Reflektionsbuckel (George & Fabian, 1991; Magdziarz & Zdziarski, 1995). Auch hier ist bei AGN wiederum die Stärke dieses Reflektionsbuckels stärker als bei galaktischen Schwarzlochkandidaten.

Aufgrund der größeren Stärke der Eisenlinien und des Reflektionsbuckels wird bei Aktiven Galaxien davon ausgegangen, daß die in Kapitel 3 für den Fall der galaktischen Schwarzlochkandidaten bereits diskutierte "Sandwich-Geometrie" die für AGN gültige Akkretionsgeometrie ist. Offen ist lediglich, inwiefern die comptonisierende Korona die Akkretionsscheibe vollständig oder teilweise bedeckt (siehe zum Beispiel Zdziarski, Lubiński & Smith, 1999; Stern et al., 1995b). Aufgrund der geometrischen Nähe von comptonisierendem Medium und Akkretionsscheibe wird bis zu 50% der in der Korona erzeugten harten Strahlung auf die Akkretionsscheibe zurückgestrahlt und kann dort durch Fluoreszenz die Eisenlinie und durch Compton- beziehungsweise Thomsonstreuung an den Elektronen in der Akkretionsscheibe den Reflektionsbuckel erzeugen.

Da die beobachtete Strahlung nahe des Schwarzen Lochs entsteht, wird sie durch die physikalischen Effekte in der Nähe des Schwarzen Lochs beeinflußt. Typische Keplergeschwindigkeiten nahe des inneren Rands der Akkretionsscheibe können bis zu 30% der Lichtgeschwindigkeit erreichen, so daß die von der Scheibe emittierte Emissionslinie stark dopplerverbreitert sein kann, ferner wird eine geringe Rotverschiebung der Linienenergie aufgrund von Gravitationsrotverschiebung zu erwarten sein. Wichtig ist ferner das relativistische Boosting, das zu stark asymetrischen Linienprofilen führt. Eine genauere Beschreibung dieser Effekte findet sich in Anhang G (Wilms, Speith & Reynolds, 1998), einen ausführlicheren Überblick bieten Fabian et al. (2000) und Fabian (1997). Solche relativistisch verbreiterten Linien werden tatsächlich beobachtet. Nach der ersten Entdeckung einer solchen Linie in MCG$-$6-30-15 mit ASCA (Tanaka et al., 1995) wurde in vielen weiteren Objekten stark verbreiterte Fe Kα-Linien beobachtet (Fabian et al., 1995; Nandra et al., 1997; Reynolds, 1997). Diese Linien erwiesen sich alle als stark zeitlich variabel. Insbesondere wurde die Eisenlinie in MCG$-$6-30-15 während einer Phase besonders niedriger Leuchtkraft als so breit beobachtet, daß ihre Verbreiterung nicht mehr durch Linienprofile, wie sie von einem nichtrotierenden Schwarzen Loch erwartet wurden, erklärt werden konnte. Linien aus der Akkretionsscheibe eines maximal rotierenden Schwarzen Lochs konnten das beobachtete Linienprofil jedoch erklären (Iwasawa et al., 1996). Bei rotierenden Schwarzen Löchern (Kerr-Schwarzlöcher) ist der innerste Orbit, auf dem Teilchen sich noch auf Kreisbahnen um das Schwarze Loch bewegen können, näher am Ereignishorizont, als im Schwarzschild Fall. Gas am inneren Rand einer Akkretionsscheibe um ein Kerr-Schwarzloch hat daher eine höhere Geschwindigkeit, so daß die beobachteten Linien breiter sind. Alternativmodelle zu einer relativistischen Interpretation der Eisenlinie sind schwierig. Beispielsweise konnten wir zeigen, daß eine Linienverbreiterung aufgrund von Compton-Streuung, wie sie von Misra & Sutaria (1999) vorgeschlagen worden war, aus grundlegenden physikalischen Gründen nicht möglich ist.

Aufgrund der im Vergleich zu ASCA wesentlich höheren effektiven Fläche eignet sich XMM-Newton gut, diese früheren ASCA-Beobachtungen zu Überprüfen. Im Rahmen des "guaranteed time program" von XMM-Newton hatten wir die Gelegenheit zu einer 100 ksec langen Beobachtung von MCG$-$6-30-15. Erste Ergebnisse dieser Untersuchungen sind in Anhang H dargestellt (Wilms et al., 2001b). Während unserer XMM-

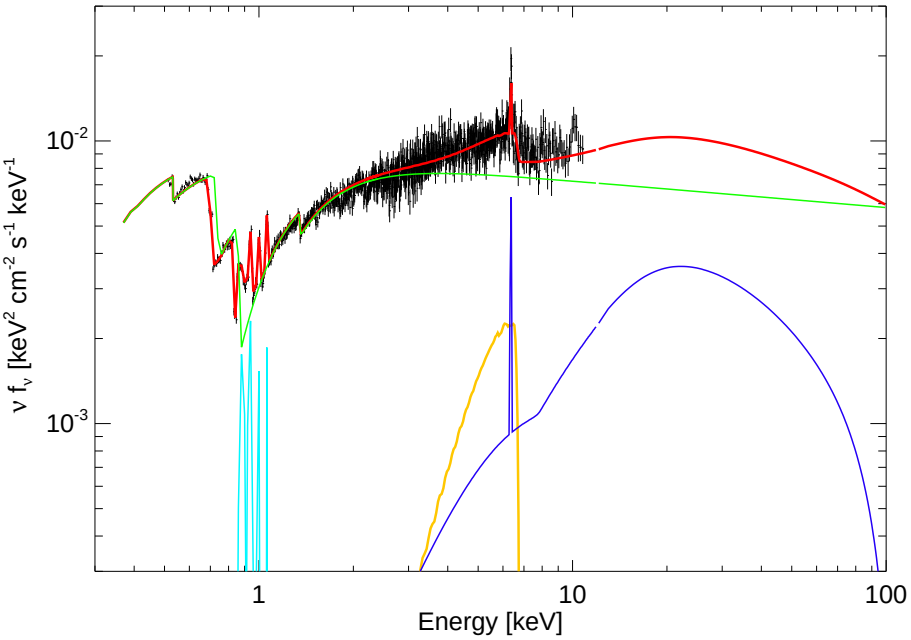

Abbildung 4.2: Ungefaltenes Spektrum von MCG−6-30-15, sowie die verschiedenen spektralen Komponenten, die zur Erklärung der Meßdaten benötigt werden, das heißt bei Energien $\lesssim 1$ keV den "warmen Absorber" mit Absorptionskanten und Emissionslinien, die dünne und die breite Fe α Emissionslinie bei $\sim$6.4 keV und das Reflektionskontinuum.

Newton Beobachtung von MCG−6-30-15 befand sich die Galaxie in einem Zustand geringer Leuchtkraft, der vergleichbar ist mit dem von Iwasawa et al. (1996) beschriebenen, und die Eisenlinie ist tatsächlich ebenfalls sehr breit. Das von uns beobachtete Spektrum und die zur Beschreibung der beobachteten Daten benutzten Modellkomponenten sind in Abbildung 4.2 dargestellt.

Bei niedrigen Energien wird der Einfluß des sehr dominanten warmen Absorbers in dieser Quelle (Lee et al., 2001; Reynolds et al., 1995) deutlich. Dies erschwert die Datenanalyse, da aufgrund der Breite der Eisenlinie ihre Stärke sehr vom angenommenen Kontinuumspektrum abhängt. Die in Anhang H dargestellten Untersuchungen gehen von einem reinen Potenzgesetzspektrum aus, das bei niedrigen Energien durch den Warmen Absorber modifiziert wird. Zur Beschreibung dieser Modifikationen wird ein empirisches Modell benutzt, das die simultan gemessenen RGS-Daten gut beschreibt. Dabei verwenden wir zum einen die oben dargestellte klassische Interpretation des weichen Röntgenspektrums, zum anderen die von Branduardi-Raymont et al. (2001) und Sako et al. (2002) vorgeschlagene Uminterpretation. Anders als frühere Autoren gehen diese davon aus, daß die spektralen Features bei niederen Energien nicht durch Absorption, sondern durch Emissionslinien verursacht werden. Diese Emissionslinien entstehen analog zur Fe Kα-Linie in der Akkretionsscheibe und sind stark relativistisch verbreitert. In diesem Modell werden nur wenige Absorptionslinien im RGS-Spektrum durch einen warmen Absorber erhalten. Welche Interpretation des niederenergetischen Spektrums tatsächlich korrekt ist, ist zur Zeit Gegenstand heftiger wissenschaftlicher Diskussionen.

Unsere Datenanalyse zeigt, daß die Parameter der Eisenlinie von dem benutzten Spektralmodell für die weiche Röntgenstrahlung nicht abhängen. In beiden Fällen läßt sich eine gute Beschreibung für das Röntgenspektrum dann erhalten, wenn die Eisenlinie durch eine stark verbreiterte Linie und eine weitere sehr dünne Linie beschrieben wird. Die dünne Linie wird im Ruhesystem von MCG−6-30-15 bei 6.4 keV gefunden und rührt wahrscheinlich von Fluoreszenz am Molekültorus her. Die breite Linie ist in Abbildung 4.2 deutlich zu sehen. Ihr Aussehen ist deutlich anders, als die doppelhöckerige Linienform, die in früheren Beobachtungen von MCG−6-30-15 gesehen wurde (siehe zum Beispiel die Abbildung in Anhang G), was seine Ursache im besonderen Spektralzustand von MCG−6-30-15 zur Zeit der Beobachtung hat. Das Emissivitätsprofil der Linie wird in unserer Beobachtung durch ein Potenzgesetz $I \propto r^{-\beta}$ beschrieben. Wir finden $\beta = 4 \ldots 5$, das heißt, daß ein großer Teil der beobachteten Linienemission nahe des Schwarzen Lochs emittiert wird.

Aufgrund der oben skizzierten Theorie der Entstehung der Fe Kα-Linie ist ihre Emissivität proportional zur Intensität der Strahlung, mit der die Akkretionsscheibe bestrahlt wird. In Comptonisierungsmodellen ist diese

Intensität jedoch wiederum proportional zur lokalen Emissivität der Akkretionsscheibe, das heißt, zur Energie, die in der Akkretionsscheibe freigesetzt wird. Damit scheinen unsere Beobachtungen zu implizieren, daß die lokale Energiefreisetzungsrate $\propto r^{-4...-5}$ ist. Dies ist im Rahmen der Theorie der Akkretionsscheiben nur schwer erklärbar, so daß weitere Energiequellen postuliert werden müssen. Wie in Anhang H ausgeführt wird, ist eine mögliche Energiequelle die Extraktion von Energie aus dem rotierenden Schwarzen Loch (Blandford & Znajek, 1977; Li, 2000; Agol & Krolik, 2000).

Bevor eine solche Interpretation der breiten Eisenlinie in MCG−6-30-15 als gesichert gelten kann, sind jedoch noch weitere Beobachtungen notwendig. In einer 300 ksec langen *XMM-Newton*-Beobachtung von MCG−6-30-15, während derer die Quelle eine wesentlich höhere Röntgenleuchtkraft hatte als in der unseren, finden Fabian et al. (priv. Mitteilung) ebenfalls eine sehr breite Eisenlinie. Das aus dieser Beobachtung geschlossene Emissionsprofil ist ebenfalls $\propto r^{-4.5}$ am inneren Rand der Scheibe und geht dann in ein weniger steiles r^{-3}-Gesetz über (Vaughan, 2002, priv. Mitteilung). Allerdings benutzen diese Autoren andere Annahmen über das Kontinuumsspektrum, so daß diese Werte nicht einfach mit den unseren verglichen werden können, auch wenn dieses Profil tendenziell unsere Schlußfolgerungen bestätigt.

Dennoch ist eine genauere Analyse unserer Daten sicherlich notwendig. In einer gerade in Vorbereitung befindlichen Arbeit versuchen wir, durch verschiedene Kontinuumsmodelle zu überprüfen, inwiefern unsere Annahme eines reinen Potenzgesetzkontinuums bestätigt werden kann. Durch die Analyse simultaner RXTE-Daten erweitern wir den zur Beschreibung des Spektrums benutzten Spektralbereich, um die Stärke des Reflektionskontinuums besser abschätzen zu können. Ferner wird mit Hilfe alternativer Modelle für die Linienemission (Reynolds & Begelman, 1997; Young, Ross & Fabian, 1998; Martocchia, Matt & Karas, 2002) überprüft, inwiefern das von uns gefundene Linienprofil tatsächlich eindeutig ist. Schließlich ist aufgrund der Variabilität der Quelle und der Eisenlinie (Iwasawa et al., 1996) eine zeitlich aufgelöste Untersuchung des Quellspektrums erforderlich.

KAPITEL 5

Zusammenfassung und Ausblick

In den letzten dreißig Jahren hat sich die Röntgenastronomie von einem von nur wenigen Personen betriebenen exotischen Forschungsgebiet zu einem der Hauptzweige der modernen Astrophysik entwickelt. Hauptgrund für diese Entwicklung war, daß es dieses Forschungsgebiet erlaubt, Materie unter extremsten Bedingungen zu untersuchen, die auf der Erde niemals erreichbar wären. Dazu gehören Magnetfelder mit Stärken von 10^7 T genauso wie die hier behandelten Schwarzen Löcher.

Im Rahmen meiner Forschungen der letzten Jahre habe ich versucht, theoretische Verfahren und Beobachtungsmethoden zu entwickeln, mit denen die Strahlungsprozesse in der Umgebung Schwarzer Löcher untersucht werden können. Ergebnisse dieser Untersuchungen waren unter anderem, daß mit Hilfe systematischer, langjährig angelegter Untersuchungen ein tieferes Verständnis des Verhaltens galaktischer Schwarzer Löcher erreicht wurde, das sowohl deren spektrale Entwicklung als auch die Entwicklung ihres zeitlichen Verhaltens einschließt. Dieses Verhalten konnte mit Hilfe von Akkretionsmodellen interpretiert werden. Im Bereich der supermassiven Schwarzen Löcher konnte mit Hilfe neuer Instrumente wie XMM-Newton aufgezeigt werden, daß Vorhersagen der Elektrodynamik Schwarzer Löcher möglicherweise beobachtbar sind.

In den nächsten Jahren sind von *Chandra* und XMM-Newton weitere überraschende Entdeckungen zu erwarten, mit denen der in dieser Arbeit dargestellte Stand der Forschung weiterentwickelt werden wird. Aktuelle Forschungsgebiete sind hier zum Beispiel die Evolution der supermassiven Schwarzen Löcher, wie sie aufgrund der großen Sammelfläche von XMM-Newton jetzt mit einem vernünftigen zeitlichen Aufwand durchführbar sind oder die in Kapitel 4 angedeuteten Untersuchungen des heißen Gases in Aktiven Galaxien mit Hilfe hochaufgelöster Röntgenspektroskopie.

Die Untersuchungen an Röntgendoppelsternen werden von den zur Zeit geplanten Instrumenten, wie den von NASA und ESA geplanten “All Sky Monitor”-Instrumenten auf der Internationalen Raumstation und insbesondere den für die nächsten zehn Jahre geplanten Detektoren mit sehr großer Sammelfläche, sehr profitieren. Instrumente wie das europäische XEUS-Projekt oder die Constellation-X Mission der NASA werden es ermöglichen, mit bislang unerreichtem Signal zu Rausch Verhältnis die Strahlung von Neutronensternen und Schwarzen Löchern zu untersuchen. Eines der wichtigen Ziele ist hier zum Beispiel der Test der Zustandsgleichung nuklearer Materie mit Hilfe zeitlich höchstaufgelöster Untersuchungen der Strahlung von akkretierenden Neutronensterne oder die Untersuchung der Eisenlinien in Aktiven Galaxien im frühen Universum. Es ist daher zu erwarten, daß die Hochenergieastrophysik auch noch in den nächsten dreißig Jahren ein interessantes und zukunftsweisendes Forschungsgebiet bleiben wird.

Literaturverzeichnis

Agol, E. & Krolik, J. H. 2000, Astrophys. J., 528, 161

Antonucci, R. 1993, Ann. Rev. Astron. Astrophys., 31, 473

Antonucci, R. R. J. & Miller, J. S. 1985, Astrophys. J., 297, 621

Arnett, D. 1996, Supernovae and Nucleosynthesis (Princeton: Princeton Univ. Press)

Balbus, S. A. & Hawley, J. F. 1991, Astrophys. J., 376, 214

Balog, N. I., Goncharskiĭ, A. V., & Cherepashchuk, A. M. 1981, Sov. Astron. Lett., 7, 336

Barret, D., McClintock, J. E., & Grindlay, J. E. 1996, Astrophys. J., 473, 963

Barret, D., Olive, J. F., Boirin, L., et al. 2000, Astrophys. J., 533, 329

Barziv, O., Kaper, L., van Kerkwijk, M. H., Telting, J. H., & van Paradijs, J. 2001, Astron. Astrophys., 377, 925

Begelman, M. C., Blandford, R. D., & Rees, M. J. 1984, Rev. Mod. Phys., 56, 255

Belloni, T. & Hasinger, G. 1990a, Astron. Astrophys., 230, 103

—. 1990b, Astron. Astrophys., 227, L33

Benlloch, S., Wilms, J., Edelson, R. A., & Yaqoob, T. 2001, Astrophys. J., 562, L121

Blandford, R. D. & Begelman, M. C. 1999, Mon. Not. R. Astron. Soc., 303, L1

Blandford, R. D. & Znajek, R. L. 1977, Mon. Not. R. Astron. Soc., 179, 433

Bochkarëv, N. G., Karitskaya, E. A., Luskutov, V. M., & Sokolov, V. V. 1986, Sov. Astron., 30, 43

Bowyer, S., Byram, E. T., Chubb, T. A., & Friedman, H. 1965, Science, 147, 394

Boyd, P. & Smale, A. 2000, IAU Circ. 7424

Boyd, P. T., Smale, A. P., Homan, J., et al. 2000, Astrophys. J., 542, L127

Branduardi-Raymont, G., Sako, M., Kahn, S. M., et al. 2001, Astron. Astrophys., 365, L140

Briel, U. G. & Pfeffermann, E. 1995, in EUV, X-Ray, and Gamma-Ray Instrumentation for Astronomy VI, ed. O. H. Siegmund & J. V. Vallerga, Proc. SPIE No. 2518 (Bellingham, WA: SPIE), 120–131

Brinkman, A. C., Dam, J., Mels, W. A., Skinner, G. K., & Willmore, W. P. 1983, in Non-Thermal and Very High Temperature Phenomena in X-Ray Astronomy, ed. G. C. Perola & M. Salvati (Roma: Istituto Astronomico, Università "La Sapienza"), 263

Brocksopp, C., Groot, P. J., & Wilms, J. 2001, Mon. Not. R. Astron. Soc., in press

Brown, G. E., Lee, C.-H., Wijers, R. A. M. J., & Bethe, H. A. 1999, Phys. Rep., 333-334, 471

Bruenn, S. W., De Nisco, K. R., & Mezzacappa, A. 2001, Astrophys. J., 560, 326

Burm, H. 1986, Astron. Astrophys., 165, 120

Burwitz, V., Zavlin, V. E., Neuhäuser, R., et al. 2001, Astron. Astrophys., 379, L35

Caroli, E., Stephen, J. B., di Cocco, G., Natalucci, L., & Spizzichino, A. 1987, Space Sci. Rev., 45, 349

Casares, J. & Charles, P. A. 1994, Mon. Not. R. Astron. Soc., 271, L5

Chandrasekhar, S. 1931, Astrophys. J., 74, 81

Cui, W., Ebisawa, K., Dotani, T., & Kubota, A. 1998, Astrophys. J., 493, L75

Cui, W., Heindl, W. A., Rothschild, R. E., et al. 1997, Astrophys. J., 474, L57

de Zeeuw, T. 2001, in ESO workshop on Black Holes in Binaries and Galactic Nuclei, ed. L. Kaper, E. P. J. van den Heuvel, & P. A. Woudt (Heidelberg: Springer), 78–87

den Herder, J. W., Brinkman, A. C., Kahn, S. M., et al. 2001, Astron. Astrophys., 365, L7

di Matteo, T. & Psaltis, D. 1999, Astrophys. J., 526, L101

Dolan, J. F. 1992, Astrophys. J., 384, 249

Dominguez, I., Chieffi , A., Limongi, M., & Straniero, O. 1999, Astron. Astrophys., 524, 226

Dove, J. B., Wilms, J., & Begelman, M. C. 1997, Astrophys. J., 487, 747

Dove, J. B., Wilms, J., Maisack, M. G., & Begelman, M. C. 1997, Astrophys. J., 487, 759

Dove, J. B., Wilms, J., Nowak, M. A., Vaughan, B., & Begelman, M. C. 1998, Mon. Not. R. Astron. Soc., 289, 729

Drake, J. J., Marshall, H. L., Dreizler, S., et al. 2002, Astrophys. J., in press (astro-ph/0204159)

Ebisawa, K., Makino, F., Mitsuda, K., et al. 1993, Astrophys. J., 403, 684

Ebisawa, K., Mitsuda, K., & Hanawa, T. 1991, Astrophys. J., 367, 213

Ergma, E. & van den Heuvel, E. P. J. 1998, Astron. Astrophys., 331, L29

Esin, A. A., Narayan, R., Cui, W., Grove, J. E., & Zhang, S.-N. 1998, Astrophys. J., 505, 854

Esin, A. A., Narayan, R., Ostriker, E. C., & Yi, I. 1996, Astrophys. J., 465, 327

Fabian, A. 1997, Astron. Geophys., 38, 10

Fabian, A. C., Iwasawa, K., Reynolds, C. S., & Young, A. J. 2000, Publ. Astron. Soc. Pac., 112, 1145

Fabian, A. C., Nandra, K., Reynolds, C. S., et al. 1995, Mon. Not. R. Astron. Soc., 277, L11

Fenimore, E. E. 1987, Appl. Opt., 26, 2760

Filippenko, A. V. 1997, Ann. Rev. Astron. Astrophys., 35, 309

Ford, H. C., Zsvetanov, Z. I., Ferrarese, L., & Jaffe, W. 1997, in The Central Regions of the Galaxy and Galaxies, IAU Symp. No. 184 (Dordrecht: Kluwer), in press

Frank, J., King, A., & Raine, D. 1992, Accretion Power in Astrophysics, 2nd edn. (Cambridge: Cambridge Univ. Press)

Garcia, M. R., McClintock, J. E., Narayan, R., et al. 2001, Astrophys. J., 553, L47

Gebhardt, K., Bender, R., Bower, G., et al. 2000, Astrophys. J., 539, L13, erratum: ApJ 555, L75

George, I. M. & Fabian, A. C. 1991, Mon. Not. R. Astron. Soc., 249

Giacconi, R., Branduari, G., Briel, U., et al. 1979, Astro-

phys. J., 230, 540
Giacconi, R., Gursky, H., Paolini, F. R., & Rossi, B. B. 1962, Phys. Rev. Lett., 9, 439
Giacconi, R., Kellogg, E., Gorenstein, P., Gursky, H., & Tananbaum, H. 1971, Astrophys. J., 165, L27
Gierliński, M., Zdziarski, A. A., Done, C., et al. 1997, Mon. Not. R. Astron. Soc., 288, 958
Gies, D. R. & Bolton, C. T. 1982, Astrophys. J., 260, 240
Greenhill, L. J., Gwinn, C. R., Antonucci, R., & Barvainis, R. 1996, Astrophys. J., 472, L21
Greenhill, L. J., Jiang, D. R., Moran, J. M., et al. 1995, Astrophys. J., 40, 619
Greenstein, J. L. & Matthews, T. A. 1963, Astron. J., 68, 279
Greiner, J., Cuby, J. G., & McCaughrean, M. J. 2001, Nature, 414, 522
Haardt, F. & Maraschi, L. 1993, Astrophys. J., 413, 507
Haardt, F., Maraschi, L., & Ghisellini, G. 1994, Astrophys. J., 432, L95
—. 1997, Astrophys. J., 476, 620
Hansen, C. J. & Kawaler, S. D. 1994, Stellar Interiors: Physical Principles, Structure, and Evolution (New York, Berlin, Heidelberg: Springer)
Hawley, J. F. & Balbus, S. A. 1991, Astrophys. J., 376, 223
Hawley, J. F. & Stone, J. M. 1998, Astrophys. J., 501, 758
Heindl, W. A., Coburn, W., Gruber, D. E., et al. 1999, Astrophys. J., 521, L49
Herrero, A., Kudritzki, R. P., Gabler, R., Vilchez, J. M., & Gabler, A. 1995, Astron. Astrophys., 297, 556
Hua, X.-M. & Titarchuk, L. 1995, Astrophys. J., 449, 188
Hutchings, J. B. 1978, Astrophys. J., 226, 264
Iben, I. J. 1991, Astrophys. J., Suppl. Ser., 76, 55
Ichimaru, S. 1977, Astrophys. J., 214, 840
in't Zand, J. J. M. 1992, PhD thesis, SRON
in't Zand, J. J. M., Heise, J., & Jager, R. 1994, Astron. Astrophys., 288, 665
Iwasawa, K., Fabian, A. C., Reynolds, C. S., et al. 1996, Mon. Not. R. Astron. Soc., 282, 1038
Jahoda, K., Swank, J. H., Giles, A. B., et al. 1997, in EUV, X-Ray, and Gamma-Ray Instrumentation for Astronomy VII, ed. O. H. Siegmund, Proc. SPIE No. 2808 (Bellingham, WA: SPIE), 59–70
Kalogera, V. & Baym, G. 1996, Astrophys. J., 470, L61
Kaper, L., van den Heuvel, E. P. J., & Woudt, P. A., eds. 2001, ESO workshop on Black Holes in Binaries and Galactic Nuclei (Heidelberg: Springer)
Kembhavi, A. K. & Narlikar, J. V. 1999, Quasars and Active Galactic Nuclei (Cambridge: Cambridge Univ. Press)
King, A. 1995, in X-Ray Binaries, ed. W. H. G. Lewin, J. van Paradijs, & E. P. J. van den Heuvel, Cambridge Astrophysics Series No. 26 (Cambridge: Cambridge Univ. Press), 419–456
Kippenhahn, R. & Weigert, A. 1990, Stellar Structure and Evolution, 1st edn. (Berlin, Heidelberg: Springer)
Komossa, S. & Fink, H. 1997, Astron. Astrophys., submitted
König, M., Staubert, R., & Wilms, J. 1997, Astron. Astrophys., 326, L25
Kormendy, J. & Richstone, D. 1995, Ann. Rev. Astron. Astrophys., 33, 581
Kreykenbohm, I., Coburn, W., Wilms, J., et al. 2002, in New Visions of the X-Ray Universe in the XMM-Newton and Chandra Era, ed. F. Jansen et al., ESA SP-488, ESA Publications, Noordwijk, in press
Kreykenbohm, I., Kretschmar, P., Wilms, J., et al. 1999, Astron. Astrophys., 341, 141
Krolik, J. H. 1999, Active Galactic Nuclei, Princeton Series in Astrophysics (Princeton, N.J.: Princeton Univ. Press)
Kuster, M., Wilms, J., Blum, S., et al. 1999, Astrophys. Lett. Commun., 38, 161
Laplace, P. S. 1796, Le Système du Monde, Vol. II. Des Mouvements Réels des Corps Célestes (Paris: Duprat)
Lasota, J.-P. 1999, Phys. Rep., in press
Lasota, J.-P., Abramowicz, M. A., Chen, X., et al. 1996, Astrophys. J., 462, 142
Lawrence, A. 1987, Publ. Astron. Soc. Pac., 99, 309
Leahy, D. A., Darbro, W., Elsner, R. F., et al. 1983, Astrophys. J., 266, 160
Lee, J. C., Ogle, P. M., Canizares, C. R., et al. 2001, Astrophys. J., 554, L13
Levine, A. M., Bradt, H., Cui, W., et al. 1996, Astrophys. J., 469, L33
Lewin, W. H. G., van Paradijs, J., & Taam, R. E. 1995, in X-Ray Binaries, ed. W. H. G. Lewin, J. van Paradijs, & E. P. J. van den Heuvel, Cambridge Astrophysics Series No. 26 (Cambridge: Cambridge Univ. Press), 175–232
Lewin, W. H. G., van Paradijs, J., & van den Heuvel, E. P. J., eds. 1995, X-Ray Binaries, Cambridge Astrophysics Series No. 26 (Cambridge: Cambridge Univ. Press)
Lewin, W. H. G., van Paradijs, J., & van der Klis, M. 1988, Space Sci. Rev., 46, 273
Li, L.-X. 2000, Astrophys. J., submitted (astro-ph/0012469)
Liang, E. P. & Nolan, P. L. 1984, Space Sci. Rev., 38, 353
Lightman, A. P. & White, T. R. 1988, Astrophys. J., 335, 57
Magdziarz, P. & Zdziarski, A. A. 1995, Mon. Not. R. Astron. Soc., 273, 837
Makishima, K., Tashiro, M., Ebisawa, K., et al. 1996, Publ. Astron. Soc. Jpn., 48, 171
Martocchia, A., Matt, G., & Karas, V. 2002, Astron. Astrophys., 383, L23
McClintock, J. E., Garcia, M. R., Caldwell, N., et al. 2001, Astrophys. J., 551, L147
Michell, J. 1784, Philosophical Transactions of the Royal Society of London, 74, 35, presented 1783 November 27
Miller, K. A. & Stone, J. M. 2000, Astrophys. J., 534, 398
Misra, R. & Sutaria, F. K. 1999, Astrophys. J., 517, 661
Miyamoto, S., Kimura, K., Kitamoto, S., Dotani, T., & Ebisawa, K. 1991, Astrophys. J., 383, 784
Miyoshi, M., Moran, J., Herrnstein, J., et al. 1995, Nature, 373, 127
Nandra, K., Fabian, A. C., George, I. M., et al. 1993, Mon. Not. R. Astron. Soc., 260, 504

Nandra, K., George, I. M., Mushotzky, R. F., Turner, T. J., & Yaqoob, T. 1997, Astrophys. J., 477, 602
Narayan, R., Kato, S., & Honma, F. 1997, Astrophys. J., 476, 49
Narayan, R. & Yi, I. 1995, Astrophys. J., 452, 710
Negoro, H., Kitamoto, S., Takeuchi, M., & Mineshige, S. 1995, Astrophys. J., 452, L49
Neufeld, D. A. & Maloney, P. R. 1995, Astrophys. J., 447, L17
Ninkov, Z., Walker, G. A. H., & Yang, S. 1987, Astrophys. J., 321, 425
Nowak, M. A. 2000, Mon. Not. R. Astron. Soc., in press (astro
Nowak, M. A. & Vaughan, B. A. 1996, Mon. Not. R. Astron. Soc., 280, 227
Nowak, M. A., Vaughan, B. A., Wilms, J., Dove, J. B., & Begelman, M. C. 1999a, Astrophys. J., 510, 874
Nowak, M. A. & Wilms, J. 1999, Astrophys. J., 522, 476
Nowak, M. A., Wilms, J., Heindl, W. A., et al. 2001, Mon. Not. R. Astron. Soc., 320, 316
Nowak, M. A., Wilms, J., Vaughan, B. A., Dove, J. B., & Begelman, M. C. 1999b, Astrophys. J., 515, 726
Oda, M. 1977, Space Sci. Rev., 20, 757
Ogilvie, G. I. 1999, Mon. Not. R. Astron. Soc., 306, L9
Olson, T. S. 2001, Phys. Rev. C, 63, 015802
Oppenheimer, J. R. & Volkoff, G. M. 1939, Phys. Rep., 55, 374
Padmanabhan, T. 2001, Theoretical Astrophysics. II. Stars and Stellar Systems (Cambridge: Cambridge Univ. Press)
Perola, G. C. & Salvati, M., eds. 1983, Non-Thermal and Very High Temperature Phenomena in X-Ray Astronomy (Roma: Istituto Astronomico, Università "La Sapienza")
Perryman, M. A. C., Lindegren, L., Kovalevsky, J., et al. 1995, Astron. Astrophys., 304, 69
Peterson, L. E. 1975, Ann. Rev. Astron. Astrophys., 13, 423
Porquet, D. & Dubau, J. 2000, Rev. Mex. Astron. Astrophys. (Serie de Conferencias), 9, 316
Pottschmidt, K. 2002, PhD thesis, Universität Tübingen
Pottschmidt, K., König, M., Wilms, J., & Staubert, R. 1998, Astron. Astrophys., 334, 201
Pottschmidt, K., Wilms, J., Nowak, M. A., et al. 2000a, Astron. Astrophys., 357, L17
—. 2002, Astron. Astrophys., submitted (astro-ph/0202258)
Pottschmidt, K., Wilms, J., Staubert, R., et al. 2000b, Adv. Space Res., submitted (astro-ph/0008059)
Poutanen, J. 1994, Academic dissertation, University of Helsinki, Helsinki
Psaltis, D., Belloni, T., & van der Klis, M. 1999, Astrophys. J., 520, 262
Psaltis, D. & Norman, C. 2001, Astrophys. J., submitted (astro-ph/0001391)
Quataert, E. 1998, Astrophys. J., 500, 978
Rees, M. J. 1984, Ann. Rev. Astron. Astrophys., 22, 471
Reppin, C., Pietsch, W., Trümper, J., Kendziorra, E., & Staubert, R. 1983, in Non-Thermal and Very High Temperature Phenomena in X-Ray Astronomy, ed. G. C. Perola & M. Salvati (Roma: Istituto Astronomico, Università "La Sapienza"), 279–282
Reynolds, C. S. 1997, Mon. Not. R. Astron. Soc., 286, 513
Reynolds, C. S. & Begelman, M. C. 1997, Astrophys. J., 487, 109
Reynolds, C. S. & Fabian, A. C. 1995, Mon. Not. R. Astron. Soc., 274, 1167
Reynolds, C. S., Fabian, A. C., Nandra, K., et al. 1995, Mon. Not. R. Astron. Soc., 277, 901
Rhoades, C. E. & Ruffini, R. 1974, Phys. Rev. Lett., 32, 324
Rolfs, C. E. & Rodney, W. S. 1988, Cauldrons in the Cosmos: Nuclear Astrophysics (Chicago, London: Univ. Chicago Press)
Rothschild, R., Boldt, E., Holt, S., et al. 1979, Space Sci. Inst., 4, 269
Rothschild, R. E., Blanco, P. R., Gruber, D. E., et al. 1998, Astrophys. J., 496, 538
Rybicki, G. B. & Lightman, A. P. 1979, Radiative Processes in Astrophysics (New York: Wiley)
Sako, M., Kahn, S. M., Branduardi-Raymont, G., et al. 2002, Astrophys. J., eingereicht (astro-ph/0112436)
Scargle, J. D. 1981, Astrophys. J., Suppl. Ser., 45, 1
Schmidt, M. 1963, Nature, 197, 1040
Schönfelder, V. 1995, Adv. Space Res., 15, 1
Schröder, K., Pols, O. R., & Eggleton, P. P. 1997, Mon. Not. R. Astron. Soc., 285, 696
Schuster, A. 1906, Astrophys. J., 23, 101
Schwarzschild, K. 1916, Sitzber. Dtsch. Akad. Wiss. Berlin, Kl. Math. Phys. Tech., 189
Shakura, N. I. & Sunyaev, R. 1973, Astron. Astrophys., 24, 337
Shapiro, S. L. & Teukolsky, S. A. 1983, Black Holes, White Dwarfs, and Neutron Stars (New York: Wiley)
Shore, S. N. 1992, An Introduction to Astrophysical Hydrodynamics (San Diego: Academic Press)
Siegmund, O. H. & Vallerga, J. V., eds. 1995, EUV, X-Ray, and Gamma-Ray Instrumentation for Astronomy VI, Proc. SPIE No. 2518 (Bellingham, WA: SPIE)
Soria, R., Wu, K., Page, M. J., & Sakelliou, I. 2001, Astron. Astrophys., 365, L273
Stern, B. E., Begelman, M. C., Sikora, M., & Svensson, R. 1995a, Mon. Not. R. Astron. Soc., 272, 291
Stern, B. E., Poutanen, J., Svensson, R., Sikora, M., & Begelman, M. C. 1995b, Astrophys. J., L13
Stone, J. M., Hawley, J. F., Gammie, C. F., & Balbus, S. A. 1996, Astrophys. J., 463, 656
Strüder, L., Briel, U., Dennerl, K., et al. 2001, Astron. Astrophys., 365, L18
Sunyaev, R. A. & Titarchuk, L. G. 1980, Astron. Astrophys., 86, 121
—. 1985, Astron. Astrophys., 143, 374
Sunyaev, R. A. & Trümper, J. 1979, Nature, 279, 506
Svensson, R. 1997, iceland Conference on Accretion Disks, Reykjavik
Tanaka, Y., Nandra, K., Fabian, A. C., et al. 1995, Nature,

375, 659
Tanaka, Y. & Shibazaki, N. 1996, Ann. Rev. Astron. Astrophys., 34, 607
Tassoul, J.-L. 1978, Theory of Rotating Stars (Princeton: Princeton Univ. Press)
Timmer, J., Schwarz, U., Voss, H. U., et al. 2000, Phys. Rev. E, in press
Titarchuk, L. 1994, Astrophys. J., 434, 570
Titarchuk, L. & Lyubarskij, Y. 1995, Astrophys. J., 450, 876
Turner, M. J. L., Abbey, A., Arnaud, M., et al. 2001, Astron. Astrophys., 365, L27
Turner, M. J. L., Smith, A., & Zimmermann, H. U. 1981, Space Sci. Rev., 30, 513
Turner, M. J. L., Thomas, H. D., Patchett, B. E., et al. 1989, Publ. Astron. Soc. Jpn., 41, 345
Turner, T. J., Nandra, K., George, I. M., Fabian, A. C., & Pounds, K. A. 1993, Astrophys. J., 419, 127
Turolla, R. & Dullemond, C. P. 2000, Astrophys. J., 531, L49
Urry, C. M. & Padovani, P. 1995, Publ. Astron. Soc. Pac., 107, 803
van der Klis, M. 1989, in Timing Neutron Stars, ed. H. Ögelman & E. P. J. van den Heuvel, NATO ASI No. C262 (Dordrecht: Kluwer), 27–69
van der Klis, M. 1995, in X-Ray Binaries, ed. W. H. G. Lewin, J. van Paradijs, & E. P. J. van den Heuvel, Cambridge Astrophysics Series No. 26 (Cambridge: Cambridge Univ. Press), 252–307
van der Klis, M. 1997, in Statistical Challenges in Modern Astronomy, II, ed. G. J. Babu & E. D. Feigelson (New York, Heidelberg: Springer), 321–331
van Straaten, S., van der Klis, M., di Salvo, T., Belloni, T., & Psaltis, D. 2001, Astrophys. J., in press (astro-ph/0107562)
Vanbeveren, D., de Loore, C., & Van Rensbergen, W. 1998, Astron. Astrophys. Rev., 9, 63
Vaughan, B. A. & Nowak, M. A. 1997, Astrophys. J., 474, L43
Verbunt, F. 2001, in ESO workshop on Black Holes in Binaries and Galactic Nuclei, ed. L. Kaper, E. P. J. van den Heuvel, & P. A. Woudt (Heidelberg: Springer), 279
Verbunt, F. & van den Heuvel, E. P. J. 1995, in X-Ray Binaries, ed. W. H. G. Lewin, J. van Paradijs, & E. P. J. van den Heuvel, Cambridge Astrophysics Series No. 26 (Cambridge: Cambridge Univ. Press), 457–494
Vrtilek, S. D., Soker, N., & Raymond, J. C. 1993, Astrophys. J., 404, 696
Wallerstein, G., Iben, Jr., I., Parker, P., et al. 1997, Rev. Mod. Phys., 69, 995
Weisskopf, M. C., Brinkman, B., Canizares, C., et al. 2002, Publ. Astron. Soc. Pac., 114, 1
Wellstein, S. & Langer, N. 1999, Astron. Astrophys., 350, 148
Wheeler, J. C. 1996, in Relativistic Astrophysics (Festschrift I. Novikov), ed. B. J. T. Jones & D. Marković (Cambridge: Cambridge Univ. Press)
Wilms, J. 1998, PhD thesis, Universität Tübingen, Tübingen
Wilms, J., Allen, A., & McCray, R. 2000, Astrophys. J., 542, 914
Wilms, J., Dove, J., Staubert, R., & Begelman, M. C. 1997, in The Transparent Universe, ed. C. Winkler, T. J.-L. Courvoisier, & P. Durouchoux, ESA SP No. 382 (Noordwijk: ESA Publications Division), 233–236
Wilms, J., Nowak, M. A., Dove, J. B., Fender, R. P., & di Matteo, T. 1999, Astrophys. J., 522, 460
Wilms, J., Nowak, M. A., Pottschmidt, K., et al. 2001a, Mon. Not. R. Astron. Soc., 320, 327
Wilms, J., Reynolds, C. S., Begelman, M. C., et al. 2001b, Mon. Not. R. Astron. Soc., in press
Wilms, J., Speith, R., & Reynolds, C. S. 1998, in Black Holes: Theory and Observation, ed. F. W. Hehl, C. Kiefer, & R. Metzler, Lecture Notes in Physics No. 514 (Berlin, Heidelberg: Springer), 69–79
Woosley, S. E., Langer, N., & Weaver, T. A. 1993, Astrophys. J., 411, 823
Wu, K., Soria, R., Page, M. J., et al. 2001, Astron. Astrophys., 365, L267
Young, A. J., Ross, R. R., & Fabian, A. C. 1998, Mon. Not. R. Astron. Soc., 300, L11
Young, P. A., Mamajek, E. E., Arnett, D., & Liebert, J. 2001, Astrophys. J., 556, 230
Zdziarski, A. A., Lubiński, P., & Smith, D. A. 1999, Mon. Not. R. Astron. Soc., 303, L11
Zdziarski, A. A., Poutanen, J., Mikołajewska, J., et al. 1998, Mon. Not. R. Astron. Soc., 301, 435
Zombeck, M. V., David, L. P., Harnden, F. R., & Kearns, K. 1995, in EUV, X-Ray, and Gamma-Ray Instrumentation for Astronomy VI, ed. O. H. Siegmund & J. V. Vallerga, Proc. SPIE No. 2518 (Bellingham, WA: SPIE), 304–321

ANHANG A

Low-Luminosity States of the Black Hole Candidate GX 339−4
I. ASCA and Simultaneous RXTE/Radio Observations

J. Wilms, M.A. Nowak, J.B. Dove, R.P. Fender, T. di Matteo

1999

Nachdruck aus

The Astrophysical Journal
Vol. 522, S. 460–475

THE ASTROPHYSICAL JOURNAL, 522:460–475, 1999 September 1

LOW-LUMINOSITY STATES OF THE BLACK HOLE CANDIDATE GX 339−4. I. *ASCA* AND SIMULTANEOUS RADIO/*RXTE* OBSERVATIONS

JÖRN WILMS,[1] MICHAEL A. NOWAK,[2] JAMES B. DOVE,[2,3] ROBERT P. FENDER,[4] AND TIZIANA DI MATTEO[5,6]
Received 1998 October 12; accepted 1999 April 14

ABSTRACT

We discuss a series of observations of the black hole candidate GX 339−4 in low-luminosity, spectrally hard states. We present spectral analysis of three separate archival *Advanced Satellite for Cosmology and Astrophysics* (*ASCA*) data sets and eight separate *Rossi X-Ray Timing Explorer* (*RXTE*) data sets. Three of the *RXTE* observations were strictly simultaneous with 843 MHz and 8.3–9.1 GHz radio observations. All of these observations have (3–9 keV) flux $\lesssim 10^{-9}$ ergs s^{-1} cm^{-2}. The *ASCA* data show evidence for an $\approx$6.4 keV Fe line with equivalent width $\approx$40 eV, as well as evidence for a soft excess that is well modeled by a power law plus a multicolor blackbody spectrum with peak temperature $\approx$150–200 eV. The *RXTE* data sets also show evidence of an Fe line with equivalent widths $\approx$20–140 eV. Reflection models show a hardening of the *RXTE* spectra with decreasing X-ray flux; however, these models do not exhibit evidence of a correlation between the photon index of the incident power law flux and the solid angle subtended by the reflector. "Sphere+disk" Comptonization models and advection-dominated accretion flow (ADAF) models also provide reasonable descriptions of the *RXTE* data. The former models yield coronal temperatures in the range 20–50 keV and optical depths of $\tau \approx 3$. The model fits to the X-ray data, however, do not simultaneously explain the observed radio properties. The most likely source of the radio flux is synchrotron emission from an extended outflow of size greater than $\mathcal{O}(10^7 GM/c^2)$.

Subject headings: binaries: close — black hole physics — radiation mechanisms: nonthermal — stars: individual (GX 339−4) — X-rays: stars

1. INTRODUCTION

The Galactic black hole candidate (BHC) GX 339−4 is unique among persistent sources in that it shows a wide variety of spectral states and transitions among these states. In presumed order of increasing bolometric luminosity, GX 339−4 exhibits a state with hard, power-law spectra ("off state:" Ilovaisky et al. 1986; "low state:" Grebenev et al. 1991); a soft state with no evidence of a power-law tail ("high state;" Grebenev et al. 1991); and a very bright, soft state with an extended power-law tail ("very high state;" Miyamoto et al. 1991). There also are apparently times when the flux is high but the spectrum is not as soft as in the high or very high state. Méndez & van der Klis (1997) refer to this as the "intermediate state." We also note that there is some evidence of overlap between the states. The broadband (*Granat* SIGMA) hard-state data presented by Grebenev et al. (1991) apparently represents a more luminous state than does the broadband soft-state data taken with the same instrument. (Miyamoto et al. 1995 has suggested the possibility of hysteresis in Galactic BHC state transitions.) Similarly diverse sets of states have been observed in X-ray transients such as Nova Muscae (Kitamoto et al. 1992; Miyamoto et al. 1994); however, GX 339−4 is closer to being a persistent source.

Although there have been a number of observations of GX 339−4 in the near-infrared and optical (Doxsey et al. 1979; Motch et al. 1983, 1985; Steiman-Cameron et al. 1990; Imamura et al. 1990; Cowley et al. 1991), including detection of a 14.8 hr periodicity in the optical (Callanan et al. 1991), there is no convincing mass function for the system. In the optical, the system is faint, variable ($M_V \approx$ 16–20), and reddened ($A_V = 3.5$). The physical source of the optical emission is unknown. It has been hypothesized that it is entirely dominated by the accretion disk, as the optical flux is apparently anticorrelated with the soft X-ray emission (Steiman-Cameron et al. 1990; Imamura et al. 1990). These properties of the emission have made it difficult to obtain a good distance measurement, with estimates ranging from 1.3 kpc (Predehl et al. 1991) to 8 kpc (Grindlay 1979), with many authors choosing 4 kpc (Doxsey et al. 1979; Cowley, Crampton, & Hutchings 1987). A careful study of these distance estimates is presented by Zdziarski et al. (1998), who argue for a distance of $\approx$4 kpc.

GX 339−4 also has been detected in the radio (Sood & Campell-Wilson 1994) and possibly even has exhibited extended emission (Fender et al. 1997). Within the hard state, the radio spectrum is flat/inverted with a spectral index of $\alpha = 0.1$–0.2 (Fender et al. 1997; Corbel et al. 1997), where the radio flux density $S_\nu \propto \nu^\alpha$. Furthermore, in this state the radio flux is correlated with the X-ray and gamma-ray fluxes (Hannikainnen et al. 1999), but the radio flux disappears as GX 339−4 transits to a higher X-ray flux/softer state (Fender et al. 1999), which is comparable to the behavior of Cyg X-1 (Pooley, Fender, & Brocksopp 1999).

During the *Rossi X-Ray Timing Explorer* (*RXTE*) Cycle 2 observing phase (1996 December–1998 February), we performed a series of eight *RXTE* observations of GX 339−4.

[1] Institut für Astronomie und Astrophysik, Abt. Astronomie, Waldhäuser Strasse 64, D-72076 Tübingen, Germany; wilms@astro.uni-tuebingen.de.
[2] JILA, University of Colorado, Campus Box 440, Boulder, CO 80309-0440; mnowak@rocinante.colorado.edu.
[3] Present address, CASA, University of Colorado, Campus 389, Boulder, CO 80309-0389; dove@casa.colorado.edu.
[4] Astronomical Institute Anton Pannekoek, University of Amsterdam, and Center for High-Energy Astrophysics, Kruislaan 403, 1098 SJ, Amsterdam, Netherlands; rpf@astro.uva.nl.
[5] Institute of Astronomy, Madingley Road, Cambridge CB3 OHA, UK; tiziana@ast.cam.ac.uk.
[6] *AXAF* Fellow; present address: Harvard -Smithsonian Center for Astrophysics, Cambridge, MA 01238; tdimatteo@cfa.harvard.edu.

TABLE 1

LOG OF THE *ASCA* OBSERVATIONS

Observation	Date	Integration Time (ks)	SIS0 (counts s^{-1})	3–9 keV Flux (10^{-9} ergs cm^{-2} s^{-1})
1	1994 Aug 24	15	3.6	0.11
2	1994 Sep 12	17	6.4	0.19
3	1995 Sep 8	30	17.5	0.63

NOTE.—All observations were taken in Bright 1-CCD mode. SIS0: filtered SIS0 count rate.

The first three observations were spaced a week apart from one another from 1997 February 4 to 1997 February 18. These three observations were scheduled to be simultaneous with 8.3–9.1 GHz radio observations that were conducted at the Australian Telescope Compact Array (ATCA). The results of the radio observations have been reported by Corbel et al. (1997). Additionally, three 843 MHz observations performed at the Molongolo Observatory Synthesis Telescope (MOST) and reported by Hannikainnen et al. (1999) are also simultaneous with these *RXTE* observations. This paper is structured as follows. We discuss the spectral analysis of archival *Advanced Satellite for Cosmology and Astrophysics* (*ASCA*) data in § 2. We look for evidence of Fe lines in the data and we characterize the soft ($\lesssim 1$ keV) X-ray data. In § 3 we present the *RXTE* data. We first discuss the All Sky Monitor (ASM) data, and then we discuss the pointed observations. We perform spectral analysis much akin to that which we considered for Cyg X-1 (Dove et al. 1998). Here, however, we consider advection-dominated accretion flow (ADAF) models as well by using the models described by Di Matteo et al. (1999). We discuss the implications of the simultaneous radio data in § 4. In § 5 we discuss the implications of the X-ray observations for theoretical models. We summarize our results in § 6. We present timing analysis of the *RXTE* data in a companion paper (Nowak, Wilms, & Dove 1999, hereafter Paper II).

2. ARCHIVAL *ASCA* OBSERVATIONS

The *ASCA* archives contain four observations of the GX 339−4 region. A log of the observations is given in Table 1. In Appendix A, we describe the methods that we used to extract, filter, and analyze these *ASCA* observations. To the best of our knowledge, an analysis of these observations has not been published previously, except for a power spectrum for one of the observations (date not given; Dobrinskaya et al. 1997). The first of the observations (1993 September 16) did not detect the source, with the upper limit to the 3–9 keV flux being $\approx 10^{-12}$ ergs s^{-1} cm^2. As we will discuss below, the inferred 3–9 keV fluxes for the remaining three observations (Table 1) are lower by factors of 2–10 than the fluxes of the *RXTE* observations discussed in § 3.

We chose to fit the *ASCA* data with a phenomenological model consisting of a multicolor blackbody spectrum plus a broken power law, considered with and without a narrow Gaussian line at ≈ 6.4 keV. These fits are similar to those performed for *ASCA* observations of the hard state of Cyg X-1 (Ebisawa et al. 1996), which shows evidence for a weak and narrow Fe line with equivalent width ≈ 40 eV, as well as for a soft excess well modeled as a multicolor blackbody with peak temperature ≈ 150 eV.

The fits with the phenomenological models yield $\chi^2_{\rm red}$ ranging from 0.98 to 1.4. The brightest data set showed the greatest evidence for structure beyond this simple model. A sample fit is shown in Figure 1. Note that the neutral hydrogen column was fixed to 6×10^{21} cm^{-2}. Allowed to freely vary, the neutral hydrogen column tended to float between 4 and 8×10^{21} cm^{-2}, depending upon what combination of phenomenological models was chosen, with minimal changes in the χ^2 of the fits. Associated with these changes in the best-fit neutral hydrogen column were $\gtrsim \pm 30\%$ changes of the best-fit peak temperature of the multicolor blackbody and even larger changes (factors of ≈ 3) in the best-fit normalization of the multicolor blackbody component. We should thus associate systematic error bars with these two parameters that are somewhat larger than the statistical error bars presented in Table 2.

All fits improved with the addition of a narrow Gaussian line. In all fits we fixed the line width to 0.1 keV (see Ebisawa et al. 1996; who always found $\sigma < 0.1$ keV in fits to *ASCA* data of Cyg X-1), and for the lowest flux data set we also fix the line energy to 6.4 keV. For the lowest flux data set, $\Delta\chi^2 = 5.5$ for one additional parameter. By the *F*-test (Bevington & Robinson 1992), this is an improvement to the fit for one additional parameter at the 98% confidence level. The other two data sets show even more significant

TABLE 2

PARAMETERS FOR A MULTICOLOR BLACKBODY PLUS BROKEN POWER-LAW PLUS GAUSSIAN LINE FITS TO *ASCA* DATA

Date	$T_{\rm in}$ (keV)	$A_{\rm dbb}$ ($\times 10^4$)	Γ_1	$E_{\rm b}$ (keV)	Γ_2	$A_{\rm bpl}$ ($\times 10^{-2}$)	$E_{\rm l}$ (keV)	$A_{\rm l}$ ($\times 10^{-4}$)	EW (eV)	χ^2/dof	$\chi^2_{\rm red}$
1994 Aug 24.....	$0.14^{+0.01}_{-0.02}$	$2.2^{+0.9}_{-1.6}$	$1.78^{+0.03}_{-0.03}$	$3.4^{+0.4}_{-0.5}$	$1.62^{+0.04}_{-0.03}$	$4.2^{+0.1}_{-0.1}$	...	...	...	1500/1439	1.04
1994 Aug 24.....	$0.14^{+0.01}_{-0.02}$	$2.2^{+0.7}_{-1.6}$	$1.78^{+0.03}_{-0.03}$	$3.3^{+0.5}_{-0.6}$	$1.64^{+0.03}_{-0.03}$	$4.2^{+0.1}_{-0.1}$	*6.4*	$0.6^{+0.4}_{-0.3}$	34^{+25}_{-19}	1494/1438	1.04
1994 Sep 12	$0.15^{+0.01}_{-0.01}$	$2.5^{+0.6}_{-1.0}$	$1.81^{+0.02}_{-0.01}$	$3.8^{+0.2}_{-0.2}$	$1.56^{+0.03}_{-0.03}$	$7.2^{+0.1}_{-0.1}$	...	...	...	1603/1621	0.99
1994 Sep 12	$0.15^{+0.00}_{-0.00}$	$2.5^{+0.1}_{-0.4}$	$1.81^{+0.01}_{-0.01}$	$3.8^{+0.1}_{-0.1}$	$1.59^{+0.01}_{-0.02}$	$7.2^{+0.0}_{-0.1}$	$6.36^{+0.08}_{-0.09}$	$1.6^{+0.7}_{-0.2}$	56^{+26}_{-7}	1580/1619	0.98
1995 Sep 08	$0.19^{+0.00}_{-0.01}$	$2.4^{+0.1}_{-0.3}$	$1.93^{+0.02}_{-0.01}$	$3.7^{+0.1}_{-0.1}$	$1.60^{+0.01}_{-0.02}$	$25.6^{+0.3}_{-0.3}$	...	...	...	2597/1838	1.41
1995 Sep 08	$0.19^{+0.00}_{-0.00}$	$2.4^{+0.0}_{-0.1}$	$1.93^{+0.01}_{-0.00}$	$3.7^{+0.1}_{-0.0}$	$1.63^{+0.01}_{-0.01}$	$25.6^{+0.0}_{-0.1}$	$6.51^{+0.07}_{-0.06}$	$3.3^{+0.6}_{-0.5}$	40^{+7}_{-6}	2523/1836	1.37

NOTES.—$T_{\rm in}$: Peak multicolor blackbody temperature. $A_{\rm dbb}$: Multicolor blackbody normalization. Γ_1, Γ_2: Broken power-law photon indexes. $E_{\rm b}$: Break energy. $A_{\rm bpl}$: Power-law normalization (photons keV^{-1} cm^{-2} s^{-1} at 1 keV). $E_{\rm l}$: Line energy. $A_{\rm l}$: Line normalization (photons cm^{-2} s^{-1} in the line). EW: Line equivalent width. Uncertainties are at the 90% confidence level for one interesting parameter ($\Delta\chi^2 = 2.71$). Parameters set in italic type have been held constant for that particular fit.

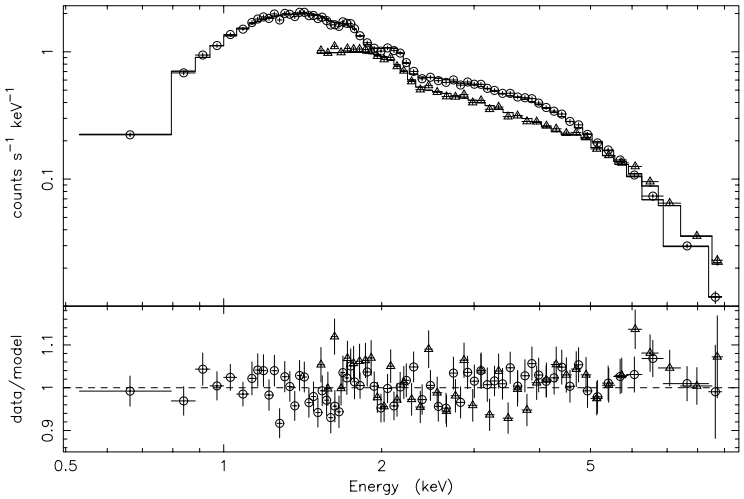

FIG. 1.—GX 339−4 *ASCA* observation of 1994 August 24, with energy bins rebinned by a factor of 25 for clarity. Model and associated residuals (data/model) are for the best-fit multicolor blackbody plus broken power law without a Gaussian line component. For clarity, only the SIS0 (*circles*) and GIS2 (*triangles*) data are shown.

improvements to χ^2. The best-fit line equivalent widths ranged from ≈ 30 to 60 eV. There is no compelling evidence for a strong flux dependence to the equivalent width of the line.

The transition to the bright, soft state typically occurs at 3–9 keV luminosities $\gtrsim 10^{-9}$ ergs cm^{-2} s^{-1}; i.e., factors of 2–10 brighter than these *ASCA* observations. Thus these observations offer useful tests of ADAF models, which are hypothesized to be most relevant to low-luminosity, hard-state systems (Narayan 1996; Esin, McClintock, & Narayan 1997). ADAF models predict a detectable correlation between the temperature of the soft excess, the strength of the Fe line, and the source luminosity. They hypothesize that the luminosity decay of BH transients is due, in part, to an increase of the radius at which the accretion flow transits from cold, geometrically thin, and radiatively efficient to hot, geometrically thick, and advective (Esin et al. 1997). In some models, the transition radius can grow to as large as $\mathcal{O}(10^4 R_G)$, where $R_G \equiv GM/c^2$. (Such large transition radii are not a strict requirement of ADAF models; in § 3.2.4 we show that somewhat smaller transition radii, ≈ 200–$400 R_G$, are preferred for ADAF models of the *RXTE* data.) As discussed by Esin et al. (1997), one then expects the peak temperature of the soft excess to decrease below 150 eV and the equivalent width of any Fe line to decrease to values less than ≈ 30 eV.

The best-fit equivalent widths found for GX 339−4 are greater than can be accommodated in ADAF models with a large transition radius, and they are also slightly larger than predicted by the "sphere + disk" corona models described in § 3.2.3 (see also Dove et al. 1997b, 1998). These latter models have a similar geometry to the ADAF models, and they often posit a coronal radius $\lesssim 100 R_G$. Likewise, we do not detect any large decreases in the best-fit disk temperatures with decreasing luminosity. Although it is dangerous to make a one-to-one correspondence between a phenomenological fit component and a physical component, these best-fit values are suggestive of, but not definitive proof of, temperatures hotter than can be accommodated in models in which cold, soft X-ray–emitting material exists at very large radii.

3. *RXTE* OBSERVATIONS

3.1. *The Monitoring Campaign*

To study the long-term behavior of GX 339−4, and to place our pointed observations within the context of the overall behavior of the source, we used data from the All Sky Monitor (ASM) on *RXTE*. The ASM provides light curves in three energy bands, 1.3–3.0 keV, 3.0–5.0 keV, and 5.0–12.2 keV, typically consisting of several 90 s measurements per day (see Levine et al. 1996; Remillard & Levine 1997; Lochner & Remillard 1997). In Figure 2 we present the ASM data of GX 339−4 until Truncated Julian Date (TJD) ≈ 1000 (1998 July 6). We also indicate the dates of our *RXTE* observations, as well as the dates of ATCA and MOST radio observations (Fender et al. 1997; Corbel et al. 1997; Hannikainnen et al. 1999). We discuss the long-timescale variability of this light curve in Paper II.

Based on model fits to the observations of Grebenev et al. (1991) (low and high state) and Miyamoto et al. (1991) (very high state), we expect the different states of GX 339−4 to have ASM count rates as indicated in Table 3. The *ASCA* and *RXTE* observations discussed here are most characteristic of weak to average luminosity hard states. Confirmation that the eight *RXTE* observations taken between TJD 481 and 749 do indeed represent a typical low/hard state comes from the broadband spectral analysis presented in § 3, as well as from the timing analysis presented in Paper II. The X-ray variability of these observations show root mean square variability of $\mathcal{O}(30\%)$ and show a power spectrum (PSD) that, roughly, is flat below 0.1 Hz, $\propto f^{-1}$ between

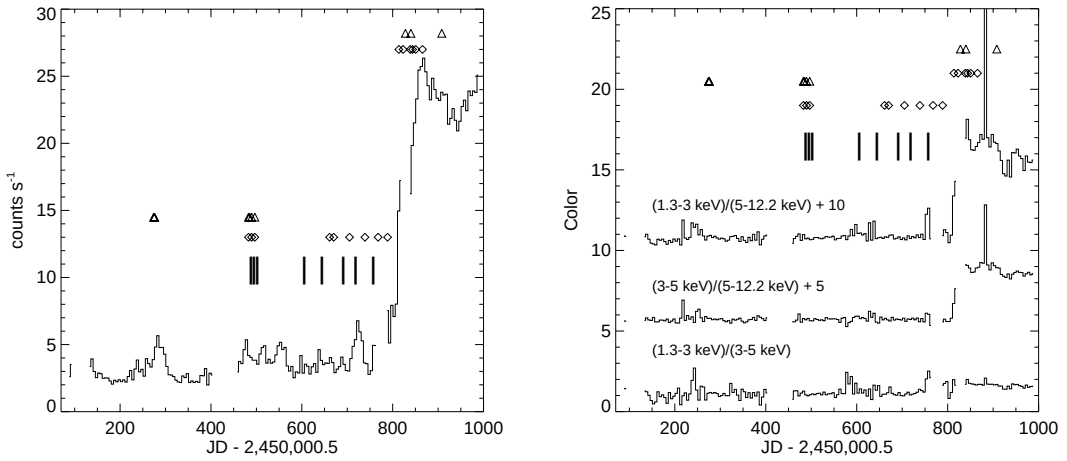

FIG. 2.—*Left panel: RXTE* All Sky Monitor data for GX 339−4 (5 day averages in the 1.3–12.2 keV band) vs. Truncated Julian Date (TJD) ≡ Julian Date (JD) −2450000.5. Vertical bars indicate dates of our *RXTE* pointed observations, diamonds indicate dates of MOST radio observations (Hannikainnen et al. 1999), and triangles indicate dates of ATCA radio observations (Fender et al. 1997; Corbel et al. 1997). *Right panel:* ASM colors for GX 339−4 vs. TJD. Colors shown are (1.3–3 keV)/(3–5 keV), (3–5 keV)/(5–12 keV) + 5, and (1.3–3 keV)/(5–12.2 keV) + 10 (the latter two colors have been offset for clarity).

0.1–3 Hz, and $\propto f^{-2}$ above 3 Hz. Time lags and coherence functions were also comparable to previously observed hard states of Cygnus X-1 (see Paper II, and references therein). Further discussion and analyses of the timing data can be found in Paper II.

The transition to a higher flux level that occurs at TJD ≈ 800 appears to have a characteristic flux of a high state but is not as soft in the 2–10 keV bands as expected from the above cited high and very high states. This might be an example of what Méndez & van der Klis (1997) refer to as an "intermediate state" between hard and soft. No pointed *RXTE* observations were taken during the transition, and four pointed observations, which were not part of our monitoring campaign, occurred shortly after the transition. Detailed confirmation of the spectral state suggested by the ASM data awaits analysis of these pointed observations. Note that the radio flux became quenched over the course of this transition to a higher ASM flux level (Fender et al. 1999).

The variations observed in both the ASM light curve (prior to TJD ≈ 800) and the pointed *RXTE* observations discussed below represent more than a factor 5 variation in observed flux. Comparable variations have been observed in the radio, and furthermore the radio light curves show evidence of a correlation with both the ASM and Burst and Transient Survey Explorer (BATSE) light curves (Hannikainnen et al. 1999).

TABLE 3

APPROXIMATE EXPECTED ASM COLORS FOR THE DIFFERENT STATES OF GX 339−4

	Count Rate (counts s^{-1})	1.3–3 keV / 3–5 keV	1.3–3 keV / 5–12.2 keV
Low	7	2	2
High	15	4	30
Very high	60	4	15

3.2. *PCA and HEXTE Observations*

In this section we present the results from our analysis of the data from the two pointed instruments on *RXTE*: the Proportional Counter Array (PCA), and the High-Energy X-Ray Timing Experiment (HEXTE). See Appendix B for a description of the instruments and of the details of the data extraction and processing. A log of the *RXTE* pointed observations and the simultaneous radio observations is given in Table 4.

As we show in Appendix B, there is a difference in the power-law slopes obtained from an analysis of spectra of the Crab with both instruments on *RXTE*. In order to minimize the impact of this difference in the instrumental calibration onto the data analysis, we primarily analyze the data from both instruments individually and use the difference in model parameters between instruments as a gauge of the systematic uncertainties. We do perform some joint analysis of PCA and HEXTE data using various reflection models. In the following sections we discuss in detail the implications of the calibration uncertainty for our analysis.

For our analysis of the *RXTE* broadband spectrum, we used several different spectral models consistent with the range of parameterizations currently used in the literature to describe the spectra of BHCs. As in the *ASCA* analysis (§ 2), we fixed $N_{\rm H} = 6 \times 10^{21}$ cm^2. We first used the purely phenomenological exponentially cut-off power-law and broken power-law models as a broad characterization of the data. The results of this modeling are given in § 3.2.1 and in Tables 5 and 6. We then applied the three more physically motivated models that are currently discussed in the literature: reflection of a power law off an (ionized) accretion disk (§ 3.2.2 and Table 7), "sphere and disk" corona Comptonization models (§ 3.2.3 and Table 8), and ADAF

TABLE 4

LOG OF *RXTE* AND RADIO OBSERVATIONS

OBSERVATION	DATE	TJD	T (ks)	RATE (counts s^{-1})	FLUX (10^{-9} ergs cm^{-2} s^{-1}) 3–9 keV	9–30 keV	30–100 keV	ATCA (mJy)	MOST (mJy)	α
01	1997 Feb 02	481	11	830	1.07	1.68	2.65	9.1 ± 0.2	7.0 ± 0.7	0.11
02	1997 Feb 10	489	10	730	0.94	1.50	2.41	8.2 ± 0.2	6.3 ± 0.7	0.11
03	1997 Feb 17	496	8	700	0.90	1.43	2.35	8.7 ± 0.2	6.1 ± 0.7	0.15
04	1997 Apr 29	567	10	470	0.60	0.97	1.55			
05	1997 Jul 07	636	10	200	0.25	0.43	0.75			
06	1997 Aug 23	683	11	650	0.74	1.18	1.98			
07	1997 Sep 19	710	10	730	0.96	1.48	2.36			
08	1997 Oct 28	749	10	480	0.63	1.01	1.68			

NOTES.—We list T, the duration of the *RXTE* observations; the average PCA count rate; the average (3–9 keV), (9–30 keV), and (30–100 keV) energy fluxes (all normalized to the PCA calibration); the flux density of the 8.3–9.1 GHz ATCA observations; the flux density of the 843 MHz MOST observations; and $\alpha = \Delta \log \nu / \Delta \log S_\nu$, the spectral index of the radio observations (Fender et al. 1997; Corbel et al. 1997; Hannikainnen et al. 1999).

models (§ 3.2.4). The ADAF models are applied to only the unfolded data. Residuals for each of the best fits to the data from observations 5 and 7 are shown in Figures 3, 4, and 5 (except for the ADAF models, for which we present observations 1 and 5). We chose to present these former two observations not only because are they at extremes in terms of observed luminosity (observation 5 is the faintest, and observation 7 is the second brightest; Table 4), but also because they show detectable differences in their timing properties (Paper II).

3.2.1. *Phenomenological Models*

Results from the purely phenomenological fits to the data, i.e., the broken power law and exponentially cut-off power law, are presented in Tables 5 and 6. We see that a broken power law plus a Gaussian line models the PCA data very well. The low $\chi^2_{\rm red}$ (0.15–0.32) indicates that to some extent we may be fitting systematic features in the PCA response. The same may be true for the best-fit parameters of the Fe line. The line widths ($\sigma \approx 0.6$ keV) and equivalent widths ($\approx$130 eV) are larger than for the *ASCA* observations, with the exception of observation 5, which has line parameters comparable to the *ASCA* observations. As observation 5 has the lowest count rate, it is more dominated by statistical errors and less dominated by systematic errors than the other observations. Even ignoring the possible systematic effects, however, we see that any observed line is narrower and weaker than is commonly observed in active galactic nuclei.

The $\approx$3–10 keV spectral power-law slope is close to the canonical value of $\Gamma = 1.7$; however, the PCA shows evidence for a hardening of this spectral slope above $\approx$10 keV.

TABLE 5

PARAMETERS FOR GAUSSIAN LINE PLUS BROKEN POWER-LAW MODELS AND GAUSSIAN LINE PLUS CUT-OFF BROKEN POWER-LAW MODELS

Observation	$E_{\rm line}$ (keV)	σ (keV)	$A_{\rm line}$ ($\times 10^{-3}$)	EW (eV)	Γ_1	$E_{\rm break}$ (keV)	Γ_2	$A_{\rm bkn}$	χ^2/dof	$\chi^2_{\rm red}$
01	$6.48^{+0.14}_{-0.15}$	$0.6^{+0.2}_{-0.2}$	$1.97^{+0.42}_{-0.36}$	130^{+24}_{-22}	$1.80^{+0.01}_{-0.01}$	$11.2^{+0.3}_{-0.4}$	$1.53^{+0.02}_{-0.02}$	$0.44^{+0.01}_{-0.01}$	13.6/ 52	0.26
02	$6.47^{+0.15}_{-0.16}$	$0.6^{+0.2}_{-0.2}$	$1.73^{+0.40}_{-0.35}$	129^{+26}_{-24}	$1.80^{+0.01}_{-0.01}$	$10.9^{+0.4}_{-0.4}$	$1.53^{+0.02}_{-0.02}$	$0.38^{+0.01}_{-0.01}$	16.6/52	0.32
03	$6.47^{+0.14}_{-0.15}$	$0.5^{+0.2}_{-0.2}$	$1.55^{+0.29}_{-0.31}$	121^{+24}_{-23}	$1.79^{+0.01}_{-0.01}$	$10.9^{+0.4}_{-0.4}$	$1.53^{+0.02}_{-0.03}$	$0.37^{+0.01}_{-0.01}$	13.5/ 52	0.26
04	$6.45^{+0.08}_{-0.15}$	$0.5^{+0.2}_{-0.2}$	$1.05^{+0.25}_{-0.22}$	121^{+28}_{-23}	$1.78^{+0.01}_{-0.01}$	$10.8^{+0.4}_{-0.5}$	$1.54^{+0.03}_{-0.03}$	$0.24^{+0.00}_{-0.00}$	20.7/ 52	0.38
05	$6.43^{+0.15}_{-0.17}$	$0.2^{+0.3}_{-0.2}$	$0.31^{+0.09}_{-0.08}$	84^{+25}_{-21}	$1.72^{+0.01}_{-0.01}$	$10.8^{+0.8}_{-0.8}$	$1.49^{+0.04}_{-0.05}$	$0.09^{+0.00}_{-0.00}$	22.9/ 52	0.44
06	$6.40^{+0.14}_{-0.15}$	$0.5^{+0.2}_{-0.2}$	$1.32^{+0.28}_{-0.27}$	123^{+23}_{-23}	$1.80^{+0.01}_{-0.01}$	$10.9^{+0.4}_{-0.4}$	$1.51^{+0.03}_{-0.03}$	$0.30^{+0.01}_{-0.01}$	25.2/ 52	0.48
07	$6.45^{+0.13}_{-0.13}$	$0.6^{+0.2}_{-0.2}$	$1.92^{+0.38}_{-0.34}$	140^{+23}_{-23}	$1.83^{+0.01}_{-0.01}$	$10.9^{+0.3}_{-0.4}$	$1.55^{+0.02}_{-0.02}$	$0.42^{+0.01}_{-0.01}$	27.3/ 52	0.53
08	$6.40^{+0.14}_{-0.15}$	$0.5^{+0.2}_{-0.2}$	$1.20^{+0.27}_{-0.23}$	130^{+26}_{-23}	$1.79^{+0.01}_{-0.01}$	$10.8^{+0.5}_{-0.5}$	$1.54^{+0.03}_{-0.03}$	$0.26^{+0.01}_{-0.01}$	28.3/ 52	0.54

NOTES.—Gaussian line plus broken power-law models: PCA only, 52 dof. Parameters are described in the text.

TABLE 6

PARAMETERS FOR EXPONENTIALLY CUT-OFF POWER-LAW MODELS

Observation	Constant	Γ	$E_{\rm cut}$ (keV)	$A_{\rm PL}$	Constant	χ^2/dof	$\chi^2_{\rm red}$
01	*1.00*	$1.25^{+0.06}_{-0.06}$	101^{+18}_{-14}	$0.082^{+0.014}_{-0.012}$	$0.99^{+0.01}_{-0.01}$	69.2/ 80	0.87
02	*1.00*	$1.12^{+0.08}_{-0.08}$	79^{+13}_{-10}	$0.052^{+0.011}_{-0.009}$	$0.92^{+0.02}_{-0.02}$	69.0/ 80	0.86
03	*1.00*	$1.16^{+0.17}_{-0.18}$	94^{+63}_{-28}	$0.052^{+0.029}_{-0.019}$	$1.08^{+0.04}_{-0.04}$	71.8/ 80	0.90
04	*1.00*	$1.15^{+0.11}_{-0.11}$	85^{+25}_{-16}	$0.035^{+0.011}_{-0.009}$	$0.98^{+0.02}_{-0.02}$	76.2/ 80	0.95
05	*1.00*	$1.18^{+0.19}_{-0.23}$	115^{+85}_{-46}	$0.016^{+0.011}_{-0.007}$	$0.99^{+0.05}_{-0.05}$	71.3/ 80	0.89
06	*1.00*	$1.19^{+0.09}_{-0.09}$	103^{+29}_{-19}	$0.049^{+0.012}_{-0.010}$	$0.93^{+0.02}_{-0.02}$	87.9/ 80	1.10
07	*1.00*	$1.21^{+0.07}_{-0.08}$	95^{+20}_{-14}	$0.066^{+0.014}_{-0.012}$	$0.96^{+0.02}_{-0.02}$	101.5/ 80	1.27
08	*1.00*	$1.08^{+0.10}_{-0.10}$	81^{+19}_{-13}	$0.031^{+0.009}_{-0.007}$	$0.98^{+0.02}_{-0.02}$	106.6/ 80	1.33

NOTES.—HEXTE only, 80 dof. Parameters are described in the text. Parameters set in italic type have been held constant for that particular fit.

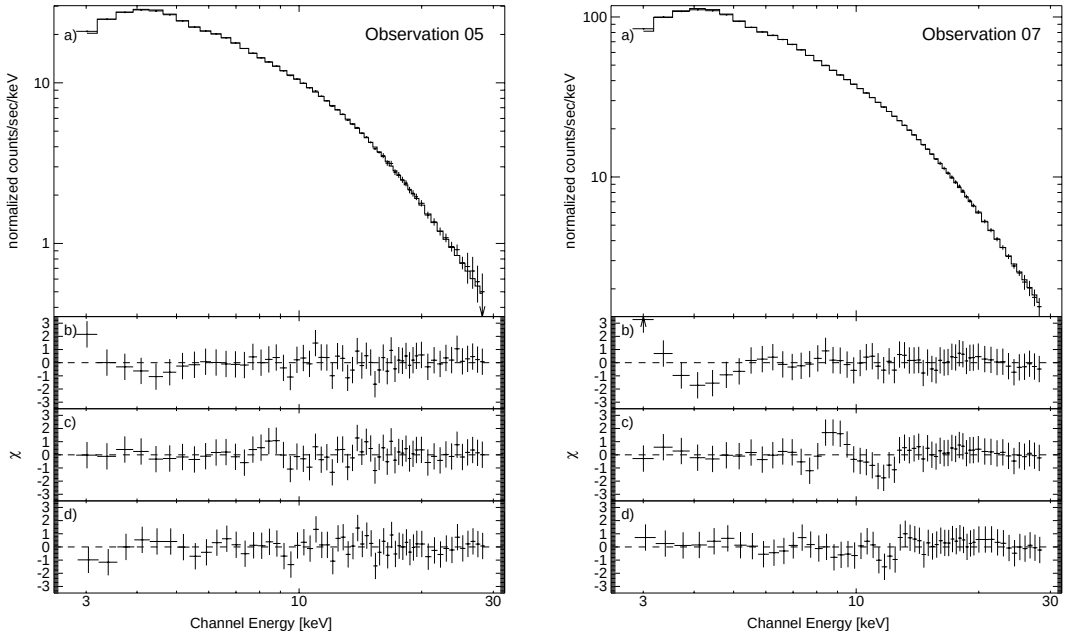

FIG. 3.—Spectral modeling of the PCA data from (*left panel*) observation 5 and (*right panel*) observation 7. Residues are shown as the contribution to χ. *In each panel:* (*a*) Count rate spectrum and the best-fit broken power law with a Gaussian line, (*b*) contribution to χ from the broken power law with a Gaussian line, (*c*) contribution to χ from the ionized reflection model (PEXRIV) with Gaussian line, and (*d*) contribution to χ from the sphere+disk model with an additional Gaussian line.

HEXTE data alone also show the high-energy spectrum to be harder than the 3–10 keV spectrum (Fig. 4 and Table 6). Note that the difference between the PCA and HEXTE photon indices is greater than the discrepancy between the PCA and HEXTE best-fit Crab photon indices (Appendix B), and therefore it is unlikely to be a systematic effect.

Such a hard HEXTE spectrum is consistent with previous observations by the Oriented Scintillation Spectrometer Experiment (OSSE) on board the *Compton Gamma-Ray Observatory* (*CGRO*) (Grabelski et al. 1995; see also Zdziarski et al. 1998). Grabelsky et al. (1995) found a slightly harder photon index of $\Gamma = 0.88$ and an exponential cutoff of $E_{\rm cut} = 68$ keV, somewhat lower than observed here. Note, however, that the OSSE observations extended to ≈ 500 keV as opposed to the ~ 110 keV of our HEXTE observation. Therefore, the HEXTE data for GX 339−4 do not strongly constrain the exponential rollover, and slightly harder power laws with lower exponential cutoffs are permitted.

3.2.2. *Reflection Models*

A spectral hardening above ≈ 7 keV is the expected signature of reflection of a hard continuum off of cold material (Magdziarz & Zdziarski 1995). Ueda, Ebisawa, & Done (1994) applied reflection models to *Ginga* data of GX 339−4 and found strong evidence of reflection, whereas Grabelsky et al. (1995) found no evidence of reflection in OSSE data. Zdziarski et al. (1998) jointly fit these simultaneously observed data sets and find that reflection models, albeit with a large Fe abundance, provide a very good description of the data. We have applied the models of Magdziarz & Zdziarski (1995), as implemented in XSPEC (PEXRAV, PEXRIV), to the GX 339−4 data. These models consider an exponentially cut-off power law reflected off of neutral (PEXRAV) or partially ionized (PEXRIV) cold material.

In Table 7 we show the fit results for reflection off of partially ionized material similar to the models presented by Zdziarski et al. (1998). Just as in Zdziarski et al. (1998), we include a disk component where we fix the inner disk temperature to 250 eV. As PCA does not usefully constrain models below 3 keV, the disk component is not strongly constrained; typically the χ^2 values were higher by 5–20 without this component. We also fix the reflector inclination angle at 45°, fix the disk temperature at $T_{\rm disk} = 10^6$ K, and freeze the abundances at solar, but we let the Fe abundance be a free parameter. In all our fits we found that the Gaussian line width, σ, would tend to drift toward 0, so we fixed $\sigma = 0.1$ keV. For the combined PCA and HEXTE data, we also fixed the Gaussian line energy to 6.4 keV. For fits to PCA data alone and joint PCA/HEXTE data, the exponential cut-off energy, $E_{\rm fold}$, would drift toward very large energy ($\gg 1000$ keV). We therefore considered only pure power laws without cutoffs. Zdziarski et al. (1998) have argued that the high-energy cutoff is sharper than exponential, which one would not expect to be strongly constrained by the combined PCA/HEXTE data.

As for the *Ginga* data of GX 339−4 (Ueda et al. 1994), the PCA data alone were extremely well described by reflection models. Again, however, the extremely low $\chi^2_{\rm red}$ (as low as

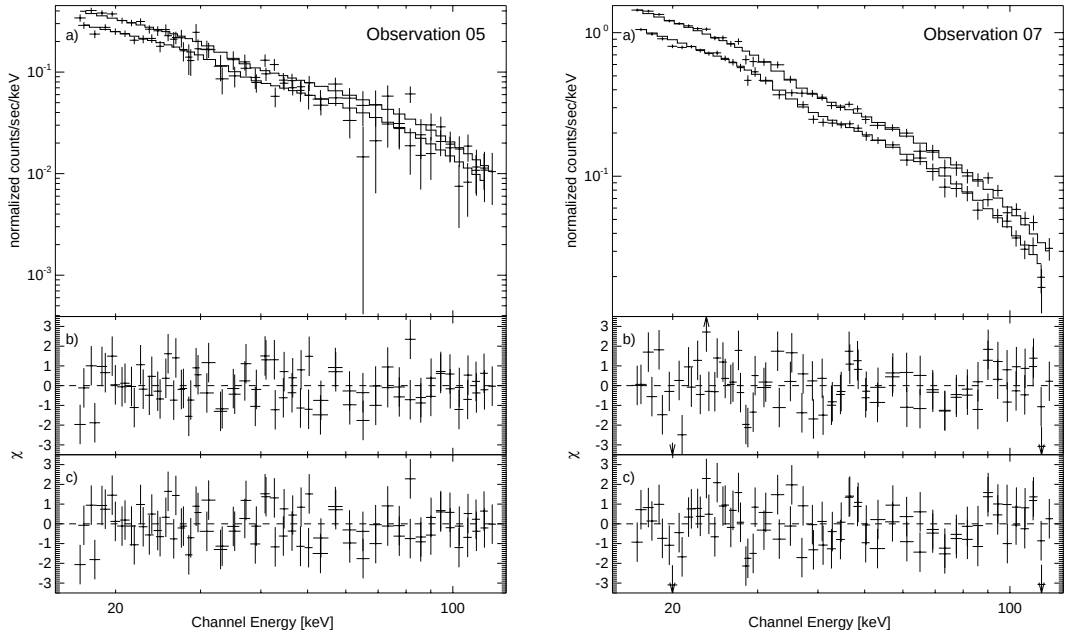

FIG. 4.—Spectral modeling of the HEXTE data from (*left panel*) observation 5 and (*right panel*) observation 7. Residues are shown as the contribution to χ. *In each panel:* (*a*) count rate spectrum and the best-fit power law with exponential cutoff, (*b*) contribution to χ from the power law with exponential cutoff, and (*c*) contribution to χ from the sphere + disk model.

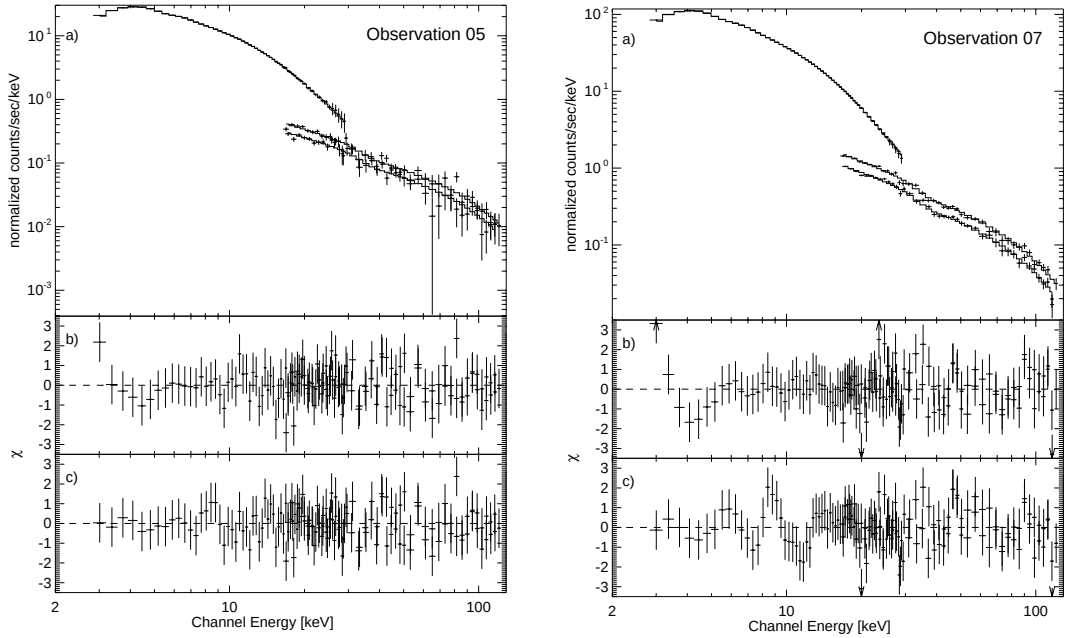

FIG. 5.—Spectral modeling of the joint PCA and HEXTE data for observation 5 and 7. Residues are shown as the contribution to χ. *In each panel:* (*a*) Count rate spectrum and the best-fit broken power law with a Gaussian line, (*b*) contribution to χ from the best-fit broken power law with a Gaussian line (parameters not given in text), and (*c*) contribution to χ from the best-fit ionized reflector model with a Gaussian line.

TABLE 7

PARAMETERS FOR GAUSSIAN LINE PLUS MULTICOLOR DISK PLUS IONIZED REFLECTION MODELS

Observation	$A_{\rm dbb}$	Γ ($\times 10^5$)	$\Gamma_{\rm HEXTE}$	f	$A_{\rm Fe}$ ($A_{\rm Fe_\odot}$)	ξ (ergs cm s^{-1})	$A_{\rm pex}$	$E_{\rm line}$ (keV)	$A_{\rm line}$ ($\times 10^{-4}$)	EW (eV)	Constant	Constant	χ^2/dof	$\chi^2_{\rm red}$
01	$1.64^{0.82}_{-0.83}$	$1.81^{+0.02}_{-0.02}$	...	$0.41^{+0.06}_{-0.05}$	$1.54^{+0.67}_{-0.40}$	$78.2^{+28.7}_{-23.7}$	$0.43^{+0.01}_{-0.01}$	$6.22^{+0.22}_{-0.23}$	$7.00^{+2.95}_{-3.10}$	41^{+18}_{-18}	...	...	25./51	0.49
01	$1.54^{+0.81}_{-0.82}$	$1.81^{+0.02}_{-0.02}$	$1.76^{+0.04}_{-0.03}$	$0.47^{+0.07}_{-0.06}$	$2.26^{+1.01}_{-0.65}$	$60.5^{+20.8}_{-21.8}$	$5.85^{+2.75}_{-2.98}$	*6.4*	$5.85^{+2.75}_{-2.98}$	35^{+18}_{-17}	$0.57^{+0.09}_{-0.07}$	$0.57^{+0.09}_{-0.07}$	113./132	0.86
02	$1.68^{+0.73}_{-0.73}$	$1.81^{+0.02}_{-0.02}$	...	$0.41^{+0.06}_{-0.05}$	$1.36^{+0.58}_{-0.36}$	$82.2^{+31.6}_{-23.9}$	$0.37^{+0.01}_{-0.01}$	$6.16^{+0.23}_{-0.25}$	$5.96^{+2.60}_{-2.82}$	40^{+17}_{-19}	...	...	21./51	0.41
02	$1.49^{+0.73}_{-0.73}$	$1.80^{+0.02}_{-0.02}$	$1.75^{+0.05}_{-0.04}$	$0.52^{+0.09}_{-0.07}$	$2.46^{+1.50}_{-0.80}$	$54.0^{+21.3}_{-22.5}$	$4.08^{+2.45}_{-2.68}$	*6.4*	$4.08^{+2.45}_{-2.68}$	18^{+28}_{-10}	$0.57^{+0.12}_{-0.08}$	$0.52^{+0.11}_{-0.07}$	124./132	0.94
03	$1.34^{+0.70}_{-0.69}$	$1.81^{+0.02}_{-0.02}$	...	$0.42^{+0.06}_{-0.05}$	$1.49^{+0.62}_{-0.42}$	$59.8^{+24.1}_{-24.8}$	$0.36^{+0.01}_{-0.01}$	$6.22^{+0.24}_{-0.27}$	$5.56^{+2.53}_{-2.66}$	39^{+16}_{-18}	...	...	14./51	0.28
03	$1.23^{+0.70}_{-0.70}$	$1.81^{+0.02}_{-0.02}$	$1.68^{+0.05}_{-0.05}$	$0.44^{+0.07}_{-0.06}$	$1.61^{+0.76}_{-0.46}$	$50.9^{+22.6}_{-22.9}$	$4.96^{+2.46}_{-2.56}$	*6.4*	$4.96^{+2.46}_{-2.56}$	36^{+19}_{-18}	$0.42^{+0.09}_{-0.07}$	$0.45^{+0.09}_{-0.07}$	89./132	0.68
04	$1.13^{+0.47}_{-0.48}$	$1.79^{+0.02}_{-0.02}$	...	$0.37^{+0.07}_{-0.06}$	$1.33^{+0.77}_{-0.43}$	$70.2^{+31.3}_{-27.3}$	$0.23^{+0.00}_{-0.01}$	$6.17^{+0.23}_{-0.23}$	$4.56^{+1.80}_{-1.90}$	47^{+18}_{-19}	...	...	15./51	0.30
04	$1.03^{+0.47}_{-0.47}$	$1.79^{+0.02}_{-0.02}$	$1.73^{+0.07}_{-0.05}$	$0.46^{+0.12}_{-0.08}$	$2.26^{+1.78}_{-0.86}$	$44.2^{+24.1}_{-23.7}$	$3.61^{+1.60}_{-1.88}$	*6.4*	$3.61^{+1.60}_{-1.88}$	39^{+18}_{-20}	$0.54^{+0.14}_{-0.09}$	$0.52^{+0.14}_{-0.08}$	100./132	0.76
05	$0.39^{+0.23}_{-0.24}$	$1.73^{+0.03}_{-0.02}$	...	$0.43^{+0.49}_{-0.13}$	$2.43^{+11.04}_{-1.35}$	$10.1^{+35.8}_{-10.1}$	$0.09^{+0.00}_{-0.00}$	$6.32^{+0.27}_{-0.27}$	$1.84^{+1.06}_{-0.94}$	48^{+29}_{-25}	...	...	18./51	0.34
05	$0.36^{+0.22}_{-0.23}$	$1.73^{+0.03}_{-0.02}$	$1.65^{+0.12}_{-0.08}$	$0.44^{+0.24}_{-0.12}$	$2.41^{+3.49}_{-1.22}$	$6.1^{+25.2}_{-6.1}$	$1.87^{+1.09}_{-0.96}$	*6.4*	$1.87^{+1.09}_{-0.96}$	50^{+30}_{-48}	$0.49^{+0.24}_{-0.12}$	$0.49^{+0.23}_{-0.12}$	88./132	0.67
06	$1.61^{+0.57}_{-0.57}$	$1.80^{+0.02}_{-0.02}$	...	$0.47^{+0.10}_{-0.07}$	$1.87^{+1.05}_{-0.56}$	$55.0^{+24.0}_{-24.2}$	$0.29^{+0.00}_{-0.01}$	$6.08^{+0.22}_{-0.23}$	$5.45^{+2.16}_{-2.30}$	45^{+18}_{-19}	...	...	17./51	0.33
06	$1.46^{+0.55}_{-0.55}$	$1.81^{+0.02}_{-0.02}$	$1.71^{+0.05}_{-0.04}$	$0.52^{+0.10}_{-0.07}$	$2.38^{+1.26}_{-0.74}$	$36.7^{+22.0}_{-19.2}$	$4.06^{+2.08}_{-2.05}$	*6.4*	$4.06^{+2.08}_{-2.05}$	26^{+30}_{-8}	$0.50^{+0.10}_{-0.07}$	$0.47^{+0.09}_{-0.07}$	113./132	0.86
07	$2.29^{+0.73}_{-0.73}$	$1.83^{+0.02}_{-0.02}$	...	$0.42^{+0.06}_{-0.05}$	$1.37^{+0.58}_{-0.37}$	$84.8^{+32.5}_{-23.9}$	$0.40^{+0.01}_{-0.01}$	$6.16^{+0.18}_{-0.19}$	$8.36^{+2.67}_{-2.96}$	54^{+18}_{-19}	...	...	25./51	0.48
07	$2.10^{+0.72}_{-0.72}$	$1.83^{+0.02}_{-0.02}$	$1.74^{+0.04}_{-0.03}$	$0.48^{+0.07}_{-0.06}$	$1.97^{+0.93}_{-0.57}$	$61.5^{+21.9}_{-22.7}$	$6.23^{+2.76}_{-2.48}$	*6.4*	$6.23^{+2.76}_{-2.48}$	43^{+20}_{-17}	$0.50^{+0.08}_{-0.06}$	$0.48^{+0.08}_{-0.06}$	144./132	1.09
08	$1.25^{+0.47}_{-0.47}$	$1.80^{+0.02}_{-0.02}$	...	$0.38^{+0.06}_{-0.05}$	$1.36^{+0.67}_{-0.42}$	$72.6^{+30.7}_{-26.6}$	$0.25^{+0.01}_{-0.01}$	$6.15^{+0.19}_{-0.20}$	$5.55^{+1.95}_{-1.87}$	55^{+19}_{-18}	...	...	18./51	0.35
08	$1.14^{+0.47}_{-0.47}$	$1.80^{+0.02}_{-0.02}$	$1.71^{+0.07}_{-0.05}$	$0.50^{+0.15}_{-0.09}$	$2.81^{+2.23}_{-1.11}$	$39.0^{+24.8}_{-21.7}$	$4.14^{+1.89}_{-1.72}$	*6.4*	$4.14^{+1.89}_{-1.72}$	44^{+20}_{-19}	$0.51^{+0.14}_{-0.09}$	$0.50^{+0.14}_{-0.09}$	141./132	1.07

NOTES.—After Magdziarz & Zdziarski 1995. Models have been fit to PCA data only (51 dof), and PCA and HEXTE data where the photon index of the reflected power law has been allowed to differ between the PCA and the HEXTE data (132 dof). Fit parameters are the normalization of the multicolor disk blackbody, $A_{\rm dbb}$ (the disk temperature has been fixed to 250 eV); the power-law slope, Γ; the cut-off energy, $E_{\rm fold}$; the relative reflection fraction, $f \equiv \Delta\Omega/2\pi$; the Fe abundance relative to solar, $A_{\rm Fe}$; the disk ionization parameter, $\xi \equiv$ luminosity/(density $\times$ radius^2); and a normalization, $A_{\rm pex}$. The ionized reflection models also have parameters for the temperature of the disk, $T_{\rm disk}$ (fixed at 10^6 K); abundances of elements heavier than He relative to solar, A_X (fixed at unity); and disk inclination angle, i (fixed at 45°). Parameters set in italic type have been held constant for that particular fit. The iron line width was fixed at 0.1 keV.

0.28) makes us caution that these models might partly be fitting systematics in the PCA response. PCA and *Ginga* are also very similar instruments in terms of design, and so to some extent they should exhibit similar systematic effects (as discussed in Appendix B, the internal consistency of the PCA calibration is now as good as or better than that of the *Ginga* calibration.). Note that the best-fit Fe line equivalent widths here are significantly smaller than those found with the purely phenomenological models discussed in § 3.2.1.

The fits for the HEXTE data alone (not shown) were similar to the OSSE results of Grabelsky et al. (1995). Namely, if one allows for an exponential cutoff (typically $\approx$100 keV) to the power law, the best-fit reflection fraction becomes $f \lesssim 0.01$. Such a small reflection fraction is not surprising considering how well a pure exponentially cut-off power law fits the HEXTE data (Table 6). If one does not allow an exponential cutoff, the reflection fraction becomes $f \gtrsim 3$. Such a fit is trying to mimic a hard power law with a high-energy cutoff.

A joint analysis of the PCA and the HEXTE data should be similar to a joint analysis of the Ginga and OSSE data. Indeed, such an analysis yields results comparable to those presented by Zdziarski et al. (1998) if we constrain the photon index of the incident power law to be the same for both the PCA and HEXTE data. Notable for the results of such fits (not presented) is the fairly large overabundance of Fe ($A_{\rm Fe} = 3.2$–5.2). Similarly, Zdziarski et al. (1998) find a large $A_{\rm Fe} = 2.5$–3.0 except for a short data set, more likely dominated by statistical errors rather than systematic errors, for which they find $A_{\rm Fe} = 1.6$–2.0. For our joint PCA/HEXTE data, the best-fit reflection fractions were approximately 20% larger than the best-fit reflection fraction for PCA data alone. Such an increase in reflection fraction in general will reproduce the spectral hardening seen in the HEXTE energy bands. Increasing the average best-fit Fe abundance from $\langle A_{\rm Fe}\rangle = 1.6$ (PCA data alone) to $\langle A_{\rm Fe}\rangle = 4.0$ (joint PCA/HEXTE data) also leads to an increased spectral hardening above $\approx$7 keV while leaving the spectrum below $\approx$7 keV relatively unchanged. That is, such a fit helps to reproduce the spectral break at $\approx$10 keV.

For the joint PCA/HEXTE analysis, there is clearly a worry that these results are influenced by the systematic differences between the PCA and the HEXTE responses. We therefore performed reflection model fits where we constrained all fit parameters to be the same for the PCA and the HEXTE data except for the incident power-law photon index, which we allowed to vary between the two instruments.[7] Such models provided reasonably good fits to the data, with $\chi^2_{\rm red}$ ranging from 0.67 to 1.09. The differences between the PCA and the HEXTE best-fit photon indices ranged from 0.05 to 0.13, with an average value of 0.08. This is consistent with the systematic difference between the best-fit photon indexes for the Crab spectrum. For these models we find $\langle A_{\rm Fe}\rangle = 2.3$, which is more consistent with the results for fits to the PCA data only and is slightly smaller than the results found by Zdziarski et al. (1998). Note that we also find smaller values of the ionization parameter, ξ, than were found by Zdziarski et al. (1998).

[7] The photon index was constrained to be the same for HEXTE Cluster A and B. The necessary different normalizations between the PCA and the HEXTE models were subsumed into the constants multiplying the HEXTE models. As HEXTE requires a harder power law, these constants were now 0.42–0.57, as opposed to $\approx$0.7. Furthermore, the constants showed larger uncertainties, as the uncertainty of the HEXTE photon index now couples strongly to the value of the constants.

3.2.3. *Corona Models*

We considered sphere + disk Comptonization models (Dove et al. 1997b) of the GX 339−4 observations. We have previously applied these models to an *RXTE* observation of Cygnus X-1 (Dove et al. 1998). The models each consist of a central, spherical corona surrounded by a geometrically thin, flat disk. Seed photons for Comptonization come from the disk, which has a radial temperature distribution $kT_{\rm disk}(R) \propto R^{-3/4}$ and a temperature of 150 eV at the inner edge of the disk. Hard flux from the corona further leads to reflection features from the disk or to soft photons due to thermalization of the hard radiation. The (nonuniform) temperature and pair balance within the corona are self-consistently calculated from the radiation field (Dove, Wilms, & Begelman 1997a; Dove et al. 1997b).

As described by Dove et al. (1997a, 1997b), we parameterize our models by the coronal compactness

$$\ell_c \equiv \frac{\sigma_{\rm T}}{m_e c^3}\frac{L_C}{R_C}, \tag{1}$$

where $\sigma_{\rm T}$ is the Thomson cross section, m_e is the electron mass, L_C is the luminosity of the corona, and R_C is the radius of the corona. Likewise, we define a disk compactness, $\ell_d \equiv (1 - f_c)(\sigma_{\rm T}/m_e c^3)P_G/R_C$, where P_G is the total rate of gravitational energy dissipated in the system, and f_c is the fraction dissipated in the corona. In calculating the numerical models, we set $\ell_d = 1$. Models with other values of ℓ_d yield the same ranges of self-consistent coronal temperatures and opacities. In general $f_c = \ell_c/(\ell_d + \ell_c)$ (Dove et al. 1997a). Based upon the sphere + disk geometry, a fraction $f \approx 0.32$ of the coronal flux is absorbed by the disk (Dove et al. 1997b). The models are further parameterized by an initial electron coronal optical depth, τ_c (approximately equal to the total optical depth, as pair production is negligible for the parameters of interest to us), and a normalization constant $A_{\rm kot}$. From the best-fit compactness and optical depth, the average coronal temperature can be calculated a posteriori.

Attempts to fit these models to the joint PCA/HEXTE data failed. Typical $\chi^2_{\rm red}$ values, even allowing for the inclusion of an extra Gaussian line component, were $\gtrsim$1.3. These fits showed a clear tendency for a hardening in the HEXTE band, and therefore we considered them to be influenced by the cross-calibration uncertainties between the PCA and the HEXTE instruments (Note that our previous fits of Cyg X-1 used an earlier version of the PCA response in which we applied 1.5% systematic uncertainties across the entire PCA band; these fits yielded $\chi^2_{\rm red} \approx 1.6$, without considering an additional Gaussian component). We therefore considered sphere + disk models fit to the PCA and the HEXTE data separately. In Table 8, we present the best-fit parameters for these models applied to our GX 339−4 data.

Although our numerical sphere + disk models do include reflection and a fluorescent Fe line (typical equivalent width $\approx$25 eV) from the disk, the PCA data showed residuals in the 5–7 keV band, as in our fits to *RXTE* data of Cyg X-1 (Dove et al. 1998). We included an additional Gaussian component to our fits. The equivalent widths of the additional lines were $\approx$150 eV, and they appeared to be broad ($\sigma \approx 0.8$ keV). This additional line may be attributable partly to uncertainties in the PCA response. For these fits,

TABLE 8

MODELS OF "SPHERE + DISK" COMPTONIZATION PLUS GAUSSIAN LINE FITS TO PCA DATA ONLY AND TO HEXTE DATA ONLY

Observation	$E_{\rm Line}$ (keV)	σ (keV)	$A_{\rm Line}$ ($\times 10^{-3}$)	EW (eV)	l_c	τ_c	$A_{\rm kot}$	Constant	kT_c (keV)	χ^2/dof	$\chi^2_{\rm red}$
01	$6.39^{0.18}_{-0.17}$	$0.8^{+0.2}_{-0.1}$	$3.09^{+0.60}_{-0.53}$	197^{+30}_{-30}	$0.62^{+0.05}_{-0.04}$	$3.2^{+0.1}_{-0.1}$	$2.38^{+0.06}_{-0.08}$	...	$28.6^{+0.4}_{-0.4}$	19.2/53	0.36
01	...	...	...	...	$1.83^{+0.17}_{-0.13}$	$2.9^{+0.5}_{-0.3}$	$0.91^{+0.09}_{-0.09}$	$0.99^{+0.01}_{-0.01}$	43.9^{+8}_{-8}	71.2/80	0.89
02	$6.36^{+0.19}_{-0.19}$	$0.8^{+0.2}_{-0.1}$	$2.69^{+0.57}_{-0.50}$	194^{+41}_{-36}	$0.63^{+0.06}_{-0.05}$	$3.3^{+0.1}_{-0.1}$	$2.07^{+0.06}_{-0.07}$	...	$27.9^{+0.4}_{-0.4}$	15.7/53	0.30
02	...	...	...	...	$1.96^{+0.12}_{-0.12}$	$3.6^{+0.3}_{-0.3}$	$0.73^{+0.04}_{-0.03}$	$0.92^{+0.02}_{-0.02}$	34.0^{+3}_{-2}	67.6/80	0.84
03	$6.36^{+0.21}_{-0.16}$	$0.8^{+0.2}_{-0.2}$	$2.42^{+0.44}_{-0.49}$	182^{+33}_{-37}	$0.66^{+0.06}_{-0.06}$	$3.4^{+0.1}_{-0.1}$	$1.95^{+0.06}_{-0.06}$	...	$27.9^{+0.4}_{-0.4}$	16.7/53	0.31
03	...	...	...	...	$2.21^{+0.48}_{-0.34}$	$3.4^{+0.7}_{-1.1}$	$0.61^{+0.17}_{-0.08}$	$1.08^{+0.04}_{-0.04}$	37.4^{+26}_{-7}	72.4/80	0.90
04	$6.40^{+0.22}_{-0.17}$	$0.8^{+0.2}_{-0.2}$	$1.53^{+0.32}_{-0.34}$	174^{+36}_{-39}	$0.70^{+0.08}_{-0.07}$	$3.6^{+0.1}_{-0.1}$	$1.27^{+0.05}_{-0.05}$	...	$26.6^{+0.4}_{-0.4}$	13.5/53	0.25
04	...	...	...	...	$2.09^{+0.19}_{-0.22}$	$3.4^{+0.6}_{-0.5}$	$0.46^{+0.04}_{-0.04}$	$0.98^{+0.02}_{-0.02}$	36.9^{+9}_{-6}	78.1/80	0.98
05	$6.28^{+0.31}_{-0.97}$	$0.9^{+0.3}_{-0.3}$	$0.52^{+0.73}_{-0.17}$	138^{+100}_{-100}	$0.68^{+0.15}_{-0.08}$	$4.4^{+0.3}_{-0.1}$	$0.53^{+0.02}_{-0.02}$	...	$20.6^{+0.4}_{-0.4}$	20.5/53	0.39
05	...	...	...	...	$2.89^{+0.78}_{-0.65}$	$3.1^{+1.1}_{-2.0}$	$0.16^{+0.03}_{-0.03}$	$0.99^{+0.05}_{-0.05}$	44.9^{+103}_{-13}	71.8/80	0.90
06	$6.26^{+0.24}_{-0.22}$	$0.9^{+0.2}_{-0.2}$	$2.06^{+0.50}_{-0.46}$	186^{+45}_{-42}	$0.66^{+0.07}_{-0.05}$	$3.6^{+0.1}_{-0.1}$	$1.57^{+0.04}_{-0.06}$	...	$26.2^{+0.4}_{-0.4}$	16.5/53	0.31
06	...	...	...	...	$2.33^{+0.21}_{-0.18}$	$3.1^{+0.6}_{-0.4}$	$0.54^{+0.08}_{-0.04}$	$0.93^{+0.02}_{-0.02}$	42.3^{+11}_{-8}	88.7/80	1.11
07	$6.40^{+0.19}_{-0.18}$	$0.8^{+0.2}_{-0.2}$	$2.67^{+0.56}_{-0.49}$	192^{+41}_{-35}	$0.65^{+0.06}_{-0.05}$	$3.3^{+0.1}_{-0.1}$	$2.06^{+0.05}_{-0.07}$	...	$28.4^{+0.4}_{-0.4}$	15.6/53	0.30
07	...	...	...	...	$1.99^{+0.13}_{-0.16}$	$3.1^{+0.4}_{-0.4}$	$0.75^{+0.09}_{-0.04}$	$0.96^{+0.02}_{-0.02}$	40.7^{+10}_{-6}	102.9/80	1.29
08	$6.34^{+0.23}_{-0.21}$	$0.9^{+0.2}_{-0.2}$	$1.74^{+0.40}_{-0.40}$	189^{+43}_{-43}	$0.71^{+0.08}_{-0.07}$	$3.7^{+0.1}_{-0.1}$	$1.30^{+0.05}_{-0.05}$	...	$25.9^{+0.4}_{-0.4}$	15.5/53	0.29
08	...	...	...	...	$2.37^{+0.29}_{-0.23}$	$3.7^{+0.4}_{-0.5}$	$0.43^{+0.03}_{-0.03}$	$0.98^{+0.02}_{-0.02}$	34.6^{+7}_{-5}	109.0/80	1.36

NOTES.—The three fit parameters of the Comptonization model are the compactness of the corona, ℓ_c, the coronal optical depth, τ_c, and a normalization constant, $A_{\rm kot}$. The Gaussian line is parameterized as in the previous tables. From the best-fit parameters, the equivalent width of the line, EW, and the density averaged coronal temperature, kT_c, are derived.

as well as for the reflection model fits, lines with energies significantly less than 6.4 keV can be fit, and this is likely a systematic effect. Part of the discrepancy between the data and the model, however, is significant. As we have discussed for our fits to the *RXTE* Cyg X-1 data, there are several possible physical interpretations for the additional required equivalent width: there may be an overlap between the disk and the sphere (our models invoke a sharp transition), the disk may be flared (we model a flat disk), the disk may have nonsolar abundances, or, alternatively, one might invoke a "patchy disk" embedded in the corona (Zdziarski et al. 1998). The best-fit reflection fractions of $f \approx 0.4$–0.5 found above are further indication that our models may require an additional source of reflected flux.

Allowing an additional Gaussian line component, the fits to the PCA data yield extremely low $\chi^2_{\rm red}$, which could be indicating that we are partly fitting systematic features in the PCA response. Note also that the PCA data fits yielded consistently larger optical depths and consistently lower compactness parameters than the HEXTE data fits. The latter was more significant and is again indicative of the HEXTE response being harder than the PCA response. Both instruments yielded optical depths $\tau_c \approx 3$–4; however, because of the discrepancy in the best-fit spectral slopes between the PCA and the HEXTE bands, the best-fit average coronal temperatures range from 21–30 keV (PCA) to 34–45 keV (HEXTE).

3.2.4. *ADAF Models*

The basic picture of mass accretion via an ADAF in the context of Galactic BHCs was introduced by Ichimaru (1977) and has been elaborated upon in a series of papers by Narayan and collaborators (Narayan, Kato, & Honma 1997; Esin et al. 1997). The accretion flow is divided into two distinct zones: the inner part is modeled as a hot, optically thin ADAF similar in some respects to the spherical corona discussed above, while the outer part consists of a standard optically thick, geometrically thin disk. The transition radius between the two zones, $r_{\rm tr} = R_{\rm tr}/R_G$, is one of the model parameters. We compute the ADAF spectrum according to the procedure described by Di Matteo et al. (1999). The electrons in an ADAF cool via three processes: bremsstrahlung, synchrotron radiation, and inverse Compton scattering. In addition we add the emission from a thin disk—calculated as a standard multicolor blackbody—and include the Compton reflection component due to the scattering of high-energy photons incident on the disk.

In the ADAF models discussed here, we fix the black hole mass to be $m \equiv M/M_\odot = 6$, assume the magnetic field to be in equipartition with thermal pressure ($\beta = 0.5$), and set the standard Shakura-Sunyaev viscosity parameter (Shakura & Sunyaev 1973) to be $\alpha_{\rm SS} = 0.3$. We normalize the accretion rate to $\dot{m} \equiv \dot{M}c^2/L_{\rm Edd}$, where $L_{\rm Edd}$ is the Eddington luminosity of the source. The hard state corresponds to mass accretion rates $\dot{m} \leq \dot{m}_{\rm crit} = 10^{-2}$, where $\dot{m}_{\rm crit}$ is the critical value above which an ADAF no longer exists. As $\dot{m}$ increases toward $\dot{m}_{\rm crit}$, the scattering optical depth of the ADAF goes up which causes the spectrum to become harder and smoother. Most of the flux from the ADAF plus disk configuration is emitted around 100 keV, and the spectrum falls off at higher energies.

The model spectrum changes mainly as a function of $r_{\rm tr}$ and $\dot{m}$. The various spectral states correspond to different values of these parameters. For example, Esin et al. (1997) attempt to explain the initial transition from soft to hard seen in the decay of Nova Muscae by a large change in $r_{\rm tr}$ (from $r_{\rm tr} \approx 10$ to $r_{\rm tr} \approx 10^4$), followed by an exponential decay in $\dot{m}$ for the subsequent evolution of this transient system. The *ASCA* data of GX 339−4 discussed in § 2 imply that comparably large changes in $r_{\rm tr}$ are not relevant to those observations. Here, however, unfolded *RXTE* data from observations 1 and 5, the brightest and faintest observations, respectively, can be described by ADAF models with $r_{\rm tr} = 200$, $\dot{m} = 0.08$ and $r_{\rm tr} = 400$, $\dot{m} = 0.05$, respectively. These model spectra and *RXTE* spectra for observations 1 and 5 unfolded with a cut-off broken power law plus a Gaussian line are shown in Figure 6. In these ADAF models, the observed spectral and luminosity changes of GX 339−4 are predominantly driven by changes in the

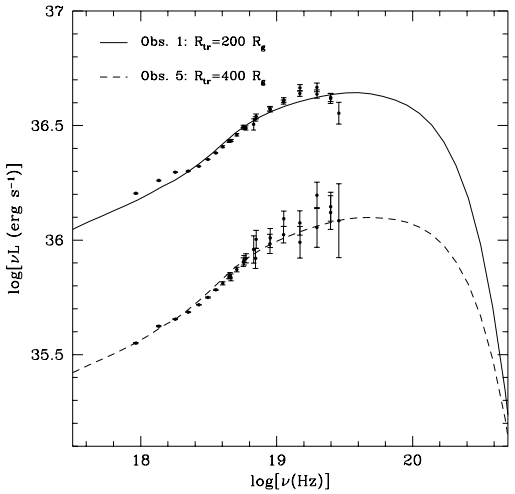

FIG. 6.—Advection-dominated accretion flow models for the unfolded *RXTE* data from observation 1 (*solid line*) and observation 5 (*dot-dashed line*). Parameters consistent with the unfolded data are described in the text. A source distance of 4 kpc was assumed.

transition radius; the implied accretion rate change is substantially smaller than the factor of 5 for the observed luminosity change.

For $r_{\rm tr} \sim 200$, which provides a rough description of observation 1, the disk blackbody emission peaks in the far UV/soft X-rays and dominates over the synchrotron emission, which peaks in the optical/UV (see also Zdziarski et al. 1998). The peak synchrotron emission frequency scales as $\propto m^{-1/2}\dot{m}^{1/2}r_{\rm tr}^{5/4}$ and peaks in the range $\nu = 10^{11}$–10^{12} Hz for supermassive black holes and $\nu = 10^{15}$–10^{16} Hz for Galactic black holes. The spectrum below the peak is approximately $S_\nu \propto \nu^2$. The synchrotron emission can contribute significantly to the radio emission of supermassive black holes (although see Di Matteo et al. 1999); however, the predicted radio flux of GX 339−4 is ten orders of magnitude below the observed 7 mJy flux at 843 MHz. Thus, there must be an extended source of radio emission, which we further discuss in the next section.

4. SIMULTANEOUS RADIO OBSERVATIONS

The first three of our *RXTE* observations were simultaneous with 843 MHz observations taken with the Molongolo Observatory Synthesis Telescope (MOST) and with 8.3–9.1 GHz observations taken at the Australian Telescope Compact Array (ATCA). Extensive discussion of the MOST and ATCA observations can be found in Hannikainnen et al. (1999) and Corbel et al. (1997), respectively (see also Table 4).

An estimate of the minimum size of the radio emitting region can be obtained by noting that,observationally, the brightness temperatures of radio sources usually are not larger than 10^{12} K; otherwise, the electrons will suffer catastrophic inverse Compton losses. The brightness temperature of a uniformly bright spherical source is given by $(cD/d\nu)^2 S_\nu/2\pi k$, where d is the diameter of the source, D is its distance, ν is the observed radio frequency, S_ν is the observed radio flux density, c is the speed of light, and k is the Boltzmann constant. Taking the 7 mJy observed at 843 MHz by MOST and the fact that GX 339−4 is unresolved, we derive

$$d \gtrsim 4 \times 10^{12}\ {\rm cm}\left(\frac{D}{4\ {\rm kpc}}\right) \approx 3 \times 10^6 R_G \left(\frac{D}{4\ {\rm kpc}}\right)\left(\frac{M}{10\ M_\odot}\right)^{-1}, \quad (2)$$

which is orders of magnitude larger than the inferred size of the X-ray–emitting region, even for models that posit extremely extended coronae (e.g., Esin et al. 1997; Kazanas, Hua, & Titarchuk 1997).

This size scale is $\propto \nu^{-1}$, so emission at 8.6 GHz could arise in a region an order of magnitude smaller than that responsible for the emission at 843 MHz. Indeed, the flat spectrum emission is likely to arise in a conical jet with a radially decreasing optical depth (e.g., Hjellming & Johnston 1988). Thus the outflow likely has an extent of $\mathcal{O}(10^7 GM/c^2)$ or greater. Similar estimates for source size have been made for the other persistent black hole candidate and Z-source neutron star X-ray binaries by Fender & Hendry (1999).

Assuming a radio spectral index of $\alpha = 0.1$ and a sharp cutoff at 10 μm (a reasonable upper limit for where the synchrotron flux becomes optically thin, and typical of where ADAF models become optically thin to synchrotron), the synchrotron flux is approximately 0.1% of the 3–100 keV X-ray flux. The correlation between the X-ray and radio fluxes found by Hannikainnen et al. (1999), comparable to the X-ray/radio correlation observed in Cyg X-1 (Pooley, Fender & Brocksopp 1999), suggests that there is a coupling between the inner accretion disk and the extended outflow on timescales of 7 days or less. Matter leaving the corona at the escape velocity ($0.25c$ at $30R_G$) and thereafter decelerating under the influence of gravity would take roughly 7 days to travel a distance of $10^7 R_G$. As 7 days is the upper bound to the correlation timescale, the radio-emitting outflow must leave at slightly greater than escape velocity, or there must be at least some amount of acceleration of the outflow.

Although the radio observations are strictly simultaneous with our first three *RXTE* observations, GX 339−4 exhibits less than 1% rms variability over the shortest timescales for which a reasonable radio flux estimate can be made ($\gtrsim$10 minutes). Thus there are no strong features to correlate between the radio and X-ray bands.

5. DISCUSSION

5.1. *Coronal Size and Luminosity Variation*

The relationship between the inferred size of the corona and the magnitude of the observed flux depends upon which spectral model we are considering. As discussed in § 3.2.4, for ADAF models one can associate lower fluxes with increased coronal radii. A larger coronal radius implies a lower efficiency and hence a decreased observed flux, even for constant accretion rates. Paper II shows that the characteristic power spectral density (PSD) timescale for GX 339−4 decreases for the lowest observed flux (observation 5). If one associates the PSD timescale with characteristic disk timescales, this could be in agreement with an increased coronal radius. However, in Paper II we also

show that the time lag between hard and soft X-ray variability decreases with decreasing flux, which seems counter to a positive correlation between flux and coronal size.

The sphere+disk coronal models make no assumptions about the radiative efficiency of the accretion. The flux can be either positively or negatively correlated with coronal radius, depending upon the variations of the coronal compactness, ℓ_c, and the temperature, T_d, at the inner edge of the accretion disk that surrounds the corona (Dove et al. 1997b). Note that the sphere+disk models used in this work, unlike those in many ADAF models, do not consider synchrotron photons as a source of seed photons for Comptonization.

Using the definitions of ℓ_c, ℓ_d, and f given in § 3.2.3, energy balance in the sphere+disk system determines the coronal radius, to within factors of order unity, to be given by

$$R_C \approx 160\left(\frac{\ell_d + f\ell_c}{\ell_d + \ell_c}\right)^{1/2}\left(\frac{kT_d}{150\ \mathrm{eV}}\right)^{-2}\left(\frac{6\ M_\odot}{M}\right) \times \left(\frac{D}{4\ \mathrm{kpc}}\right)\left(\frac{F_{\mathrm{tot}}}{10^{-8}\ \mathrm{ergs\ cm^{-2}\ s^{-1}}}\right)^{1/2} R_G\ , \quad (3)$$

where M is the mass of the compact object, D is the distance to the source, and F_{tot} is the bolometric flux of the source. If T_d, f, ℓ_d, and ℓ_c were held fixed, then the coronal radius would be positively correlated with flux. Whereas this might pose some problems for understanding the flux dependence of the characteristic timescales observed in the PSD, this would agree with the flux dependence of the X-ray variability time lags (Paper II). However, as the *RXTE* bandpass does not usefully extend below ≈ 3 keV, we do not have a good understanding of the flux dependence of T_d. If $T_d \propto F_{\mathrm{tot}}^{\beta}$ with $\beta > 1/4$, then increasing flux could imply decreasing coronal radius.

5.2. *Correlation among Spectral Parameters*

Ueda et al. (1994) claimed that reflection models of GX 339−4 exhibited a correlation between photon index, Γ, and reflection fraction, f, with softer spectra implying greater reflection. Zdziarski (1999) has claimed that this correlation extends to reflection models of Seyfert 1 galaxies as well. To expect such a correlation is not unreasonable. For example, if we allow the corona and disk to overlap to some extent in the sphere+disk model (Poutanen, Krolik, & Ryde 1997), then we expect the increase in the flux of seed photons to cool the corona and lead to a softer spectral index. Likewise, the covering fraction of the disk would be increased, in agreement with the suggested correlation. In Figure 7 we plot f versus Γ for our reflection model fits to GX 339−4. Contrary to the claims of Ueda et al. (1994) and Zdziarski (1999), however, there is no strong evidence for a correlation. Fitting the reflection fraction with a function linear in Γ, as opposed to fitting with the mean value of f, improves the χ^2 of the fits by 0.2, which is not significant. Fitting with the mean gives $\chi^2_{\mathrm{red}} = 0.2$.

We do note two possible trends from the reflection model fits. First, as has been noted for other hard-state Galactic black hole candidates (Tanaka & Lewin 1995; and references therein), there may be a correlation between flux and photon index, with lower flux implying a harder source. (The significance of the correlation is driven by observation 5, the faintest and hardest of the observations. However, a

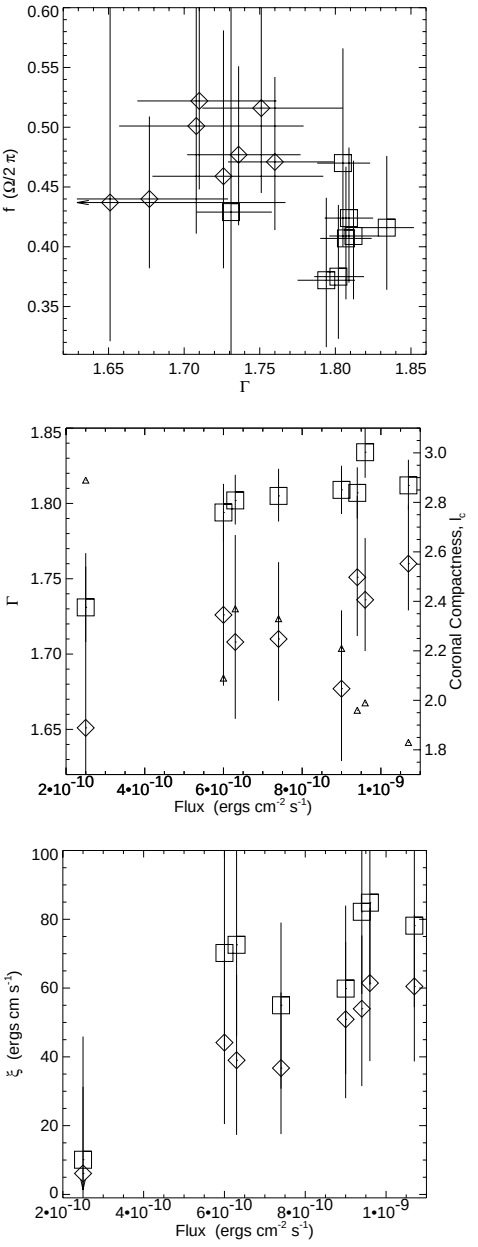

FIG. 7.—*Left panel:* Reflection fraction vs. photon index, Γ, for models fit to PCA data only (*squares*), and models fit to PCA plus HEXTE data that allowed the PCA and HEXTE photon indexes and normalizations to be different (*diamonds*; HEXTE photon index shown). *Middle panel:* Photon index, Γ, vs. observed 3–9 keV flux for the same reflection models as on the left. Also shown, without error bars, is the best-fit compactness, ℓ_c, for sphere+disk coronal models fit to HEXTE data (*small triangles*). *Right panel:* Disk ionization parameter, ξ, in units of ergs cm s^{-1} for the same reflection models as in the left panel.

similar correlation is also present in color-intensity diagrams.) Such a correlation is consistent with the expectations of ADAF models, in which the radius increases with decreasing flux (Fig. 6). Again, the sphere + disk corona models do not predict a clear trend without knowledge of the flux dependences of other parameters such as T_d.

Second, the ionization parameter, ξ, is positively correlated with flux. Such a correlation was noted by Życki, Done, & Smith (1998) for Ginga observations of Nova Muscae. It is not unreasonable to expect the disk to become increasingly ionized with increasing flux. We again caution that it is dangerous to make one-to-one correlations between a model fit parameter and a true physical parameter. Furthermore, the significance of the correlation is again almost entirely determined by observation 5, the faintest observation, which has $\xi \approx 0$. However, if we take the flux dependence of ξ as being real and interpret it physically, it provides some constraints on the flux dependence of the coronal radius. The ionization parameter is $\propto F_{\rm tot}/(\rho R^2)$, where ρ is the density of the disk. For a gas pressure–dominated Shakura-Sunyaev α disk, $\rho \propto R^{-1.65}$ (Shakura & Sunyaev 1973). In order for ξ to be roughly linear in flux (the actual dependence is not strongly constrained by the data), we require $F_{\rm tot} \propto R^{1.35}$. (For the sphere + disk models this would further require that approximately $T_d \propto R^{-1/3}$, depending upon the flux dependences of ℓ_d, ℓ_c, g, etc.) Taken physically and in the context of a gas pressure–dominated Shakura-Sunyaev α model, the flux dependence of ξ implies that the coronal radius increases with increasing flux.

6. SUMMARY

We have presented a series of observations of the black hole candidate GX 339−4 in low-luminosity, spectrally hard states. These observations consisted of three separate archival *ASCA* and eight separate *RXTE* data sets. All of these observations exhibited (3–9 keV) flux $\lesssim 10^{-9}$ ergs s^{-1} cm^{-2}, and the observed fluxes spanned roughly a factor of 5 in range for both the *ASCA* and *RXTE* data sets. Subject to uncertainties in the cross calibration between *ASCA* and *RXTE*, the faintest *ASCA* observation was approximately a factor of 2 fainter than the faintest *RXTE* observation.

All of these observations showed evidence for an $\approx$6.4 keV Fe line with equivalent widths in the range of $\approx$20–140 eV. The *ASCA* observations further showed evidence for a soft excess that was well modeled by a power law plus a multicolor blackbody spectrum with peak temperatures in the range $\approx$150–200 eV. Both of these factors considered together argue against sphere + disk or ADAF type–geometry coronae with extremely large coronal radii of $\mathcal{O}(10^4 R_G)$ (e.g., Esin et al. 1997).

The *RXTE* data sets were well fit by sphere + disk Comptonization models with coronal temperatures in the range 20–50 keV and optical depths near $\tau \approx 3$. These fits were similar to our previous fits to *RXTE* data of Cyg X-1. Advection-dominated accretion flow models, which posit a similar geometry, also provided reasonable descriptions of the unfolded *RXTE* data. The sphere + disk and ADAF models were not able, however, to also model the observed radio fluxes. Thus, a static corona seems to be ruled out by the observations. The ADAF models can imply that the coronal radius increases with decreasing flux. The sphere + disk corona models do not make a specific prediction for the dependence of the coronal radius on the flux; however, they can be consistent with a positive correlation between coronal radius and flux. As described in Paper II, a positive correlation between flux and coronal radius is consistent with the observed flux dependence of the time lags between hard and soft X-ray variability.

We also considered "reflection models" of the *RXTE* data. These models showed evidence of a hardening of the *RXTE* spectra with decreasing X-ray flux. They further showed evidence of a positive correlation between the best-fit ionization parameter, ξ, and the observed flux. Especially the latter of these correlations, however, was dominated by the model fits of the faintest observation. The reflection models did not exhibit any evidence of a correlation between the photon index of the incident power-law flux and the solid angle subtended by the reflector.

Three of the *RXTE* observations were strictly simultaneous with 843 MHz and 8.3–9.1 GHz radio observations. The most likely source of the radio flux is synchrotron emission from an extended outflow with a size of $\mathcal{O}(10^7 GM/c^2)$. The correlation between radio and X-ray emission on timescales of 7 days or less (Hannikainnen et al. 1999) implies a strong coupling of the inner disk accretion flow with this spatially extended outflow as is expected by recent theoretical arguments (Blandford & Begelman 1999). Further simultaneous radio/X-ray observations, preferably with the addition of IR/optical monitoring to constrain the location of the synchrotron break and with the addition of soft X-ray monitoring to constrain the accretion disk parameters, are required to test such models in detail.

We would like to thank Christopher Reynolds for keeping a stiff upper lip while explaining *ASCA* data analysis to us. We would also like to thank K. Mukai of the *ASCA* GOF for useful advice. W. A. Heindl and D. Gruber kindly provided assistance with the HEXTE data extraction, and S. Corbel provided assistance with the radio data. We are grateful to B. Stern for writing the original version of KOTELP, and, more importantly, for finally telling us what the name means ("cauldron"). We would also like to acknowledge useful conversations with B. Begelman, J. Chiang, B. A. Harmon, K. Pottschmidt, R. Staubert, C. Thompson, and A. Zdziarski. This work has been financed by NASA Grants NAG 5-4731 and NAG 5-3225 (M. A. N., J. B. D.). M. N. was supported in part by the National Science Foundation under Grant Phy94-07194. J. W. was supported by a travel grant from the Deutscher Akademischer Austauschdienst, R. P. F. was supported by an EC Marie Curie Fellowship (ERBFMBICT 972436), and T. D. M. thanks Trinity College and PPARC for financial support. This research has made use of data obtained through the High Energy Astrophysics Science Archive Research Center Online Service, provided by the NASA/Goddard Space Flight Center.

APPENDIX A

ASCA DATA EXTRACTION

We extracted data from the two solid state detectors (SIS0, SIS1) and the two gas detectors (GIS2, GIS3) on board *ASCA* by using the standard FTOOLS as described in the *ASCA* Data Reduction Guide (Day et al. 1998). The data extraction radius was limited by the fact that all the observations were in one-CCD mode and that the source was typically placed close to the chip edge. We chose circular extraction regions with radii of $\approx 4'$ for SIS0, $\approx 3'$ for SIS1 (the maximum possible extraction radii for these detectors), and $\approx 6'$ for GIS2 and GIS3. For observation 3 we excluded the central 40″ to avoid the possibility of photon pileup. We used the SISCLEAN and GISCLEAN tools (with default values) to remove hot and flickering pixels. We filtered the data with the strict cleaning criteria outlined in the *ASCA* Data Analysis Handbook; however, we took the larger value of 7 GeV/c for the rigidity. We rebinned the spectral files so that each energy bin contained a minimum of 20 photons. We retained SIS data in the 0.5–9 keV range and GIS data in the 1.5–9 keV range.

We accounted for the cross-calibration uncertainties of the three instruments by introducing a multiplicative constant for each detector in all of our fits. Relative to SIS0, the SIS1 detector normalization was always found to be within 2%, the GIS2 normalization was found to be within 9%, and the GIS3 normalization was found to be within 15%. For any given observation, the normalization constants varied by $\lesssim \pm 1\%$ for different spectral fits. The background was measured from rectangular regions on the two edges of the chip farthest from the source (SIS data), or from annuli with inner radii $> 6'$ (GIS data). These data were cleaned and filtered in the same manner as the source files.

The resulting data files showed reasonable agreement between all four detectors. The most discrepant detector was SIS1, which also was the detector limited to the smallest extraction radius. This detector tended to show deviations from the other detectors for energies $\gtrsim 9$ keV, and from the SIS0 detector for energies ≈ 0.5–1 keV. The detectors were mostly in mutual agreement for the lowest flux observations. It is likely that the agreement could be further improved for observations located closer to the center of the chips (thereby allowing larger extraction radii) and if low–Galactic latitude dark sky observations in one-CCD mode were available to use as background.

APPENDIX B

RXTE DATA EXTRACTION

In § 3 we present data from both pointed instruments on *RXTE*, the Proportional Counter Array (PCA) and the High-Energy X-Ray Timing Experiment (HEXTE). As we showed in § 3, the large effective area of these instruments results in a data analysis approach that is dominated by the calibration uncertainty of these detectors (especially the PCA). In this appendix we summarize the major properties of both instruments and study their (inter-) calibration. All *RXTE* results obtained in this paper were obtained using the standard *RXTE* data analysis software, FTOOLS version 4.1 (including the *RXTE* patch 4.1.1 and the correct accounting of the time dependence of the PCA response; K. Jahoda 1998, private communication). Spectral modeling was done using XSPEC, version 10.00s (Arnaud 1996).

The PCA consists of five nearly identical coaligned Xenon proportional counter units (PCUs) with a total effective area of about 6500 cm^2. The instrument is sensitive in the energy range from 2 to ~ 60 keV (Jahoda et al. 1996). We used only data for which all five PCUs were turned on. Background subtraction was done in the same manner as for our *RXTE* Cyg X-1 observations (Dove et al. 1998). Specifically, a model using the rate of Very Large Events in the detector was used to estimate the background flux. The major uncertainty of this estimated background is due to activation of radioactivity in the detectors during South Atlantic Anomaly passages. Since this background component is present for about 30 minutes after the passage, we ignored data measured during these intervals. Furthermore, data were not accumulated at times of high electron contamination. The electron contamination is measured by a certain ratio of veto rates in the detectors, the so-called electron ratio (Jahoda et al. 1999). As recommended by the *RXTE* Guest Observer's Facility (GOF), we excluded times during which the "electron ratio" was larger than 0.1 in at least one of the detectors. Note that the observed count rates from GX 339−4 are too high to allow the use of the newer background model made available by the *RXTE* GOF in 1998 June.

For spectral fitting, we limited the energy range of the PCA data from 3 to 30 keV and used version 2.2.1 of the PCA response matrices. These matrices are newer than those used by us previously (Dove et al. 1998), and they are primarily characterized by assuming a higher instrumental resolution (Jahoda et al. 1999). Because of the large PCA count rate of GX 339−4 (~ 800 counts s^{-1}) our observations are dominated by the remaining uncertainties in the detector calibration and not by Poisson errors. Therefore, a good understanding of these uncertainties is necessary.

Since the Crab spectrum is commonly assumed to be a featureless power law (Toor & Seward 1974), at least over narrow energy ranges, the ratio between the fit to the Crab and the data can be used to deduce the systematic uncertainty associated with the detector calibration. We therefore extracted a public domain spectrum of the Crab nebula and pulsar measured with the PCA on 1997 April 1. The Crab data were screened using the same criteria as those applied to our GX 339−4 data, except for that the "electron ratio" check was not applied since the background contributes only 0.6% to the total number of photons detected for the Crab. Modeling the 3 to 30 keV Crab data with an absorbed power law resulted in a best-fit photon spectrum of the form

$$N_{\rm ph} = 13.3E^{-2.187} \exp\left[-2.54 \times 10^{21}\ {\rm cm}^{-2}\sigma_{\rm bf}(E)\right]\ {\rm cm}^{-2}\ {\rm s}^{-1}\ {\rm keV}^{-1}\ , \quad \text{(B1)}$$

where $\sigma_{\rm bf}(E)$ is the energy dependent bound-free absorption cross section for material of cosmic abundances as given by Morrison & McCammon (1983), and where E is the photon energy measured in keV. For this fit to the Crab data,

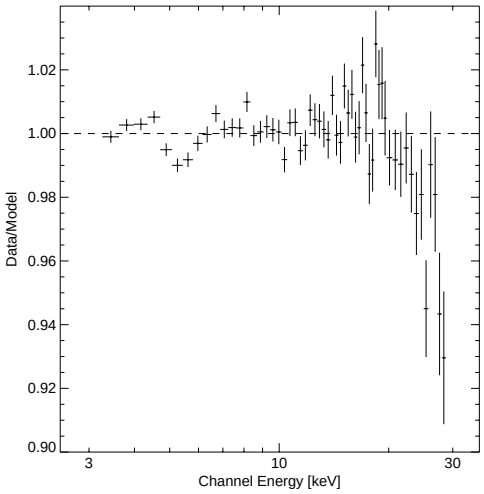

FIG. 8.—Ratio between the power-law fit of eq. (B1) and the PCA Crab nebula data. The major deviations between the data and the model are due to the Xe $L_{1,2,3}$ edges at ~ 5.1 keV and to the Xe K edge at 34.6 keV.

χ^2/dof = 168/56. In Figure 8 we display the ratio between the best fit to the Crab and the data. Using this ratio plot, we deduced the systematic uncertainties of the detector (Table 9). Adding them in quadrature to the Poisson errors of our data, the χ^2 of the above Crab fit was reduced to $\chi^2_{\rm red} = 0.56$. Note that the internal consistency of the detector calibration of the PCA appears to be on the 1% level, i.e., comparable to that obtained for previously flown instruments like the *Ginga* LAC (Turner et al. 1989) or the *ASCA* GIS (Makishima et al. 1996), even though the much larger effective area of the PCA makes it necessary to include many "dirt effects" into the detector model.

We caution that the statistical uncertainties of the fit parameters presented in this work were derived using the above systematic uncertainties. It is questionable, therefore, whether the approach of Lampton, Margon, & Bowyer (1976) to determine the uncertainties from the χ^2 contours can really be used since this approach makes use of the assumption of Poisson-type errors. The uncertainties given in this work should be taken with these caveats in mind, especially for those fits for which the $\chi^2_{\rm red}$ values are very small (i.e., $\lesssim 0.5$), and thus they should not be construed literally as "90% uncertainties."

The HEXTE consists of two clusters of four Na I/Cs I–phoswich scintillation counters, sensitive from 15 to 250 keV. A full description of the instrument is given by Rothschild et al. (1998). Source-background rocking of the two clusters provides a direct measurement of the HEXTE background with measured long-term systematic uncertainties of $< 1\%$ (Rothschild et al. 1998). Although no other strong sources in the field around GX 339−4 are known (Covault, Grindlay, & Manandhar 1992; Bouchet et al. 1993; Trudolyubov et al. 1998), we extracted individual background spectra for both HEXTE cluster background positions to check for contamination of the spectrum from weak background sources. In all cases the background spectra differed by $\lesssim 1$ count s^{-1}. Thus, we used the added background spectra from both cluster positions in our data analysis. We used the standard response matrices dated 1997 March 20 and used data measured between 17 and 110 keV. An analysis of the detector calibration similar to that performed for the PCA reveals that the HEXTE calibration is good on a level comparable to the PCA. Because of the much smaller effective area of the detector and because of the smaller flux from the source at higher energies, however, the HEXTE spectrum is completely dominated by the Poisson error of the data. Therefore we did not attempt to take the systematic calibration uncertainty into account. To improve the statistics of individual energy bins, we rebinned the raw (≈ 1 keV wide) energy channels by a factor of 2 for the energy range from 30 to 51 keV, and by a factor of 3 above that.

TABLE 9

SYSTEMATIC UNCERTAINTIES OF VERSION 2.2.1 OF THE PCA RESPONSE MATRIX AS OBTAINED FROM A POWER-LAW FIT TO THE CRAB SPECTRUM (FIG. 8)

	CHANNEL[a]			
PARAMETER	0–15	16–39	40–57	58–128
Channel energy (keV).....	0–7	7–16	16–25	>25
Uncertainty (%)	1	0.5	2	5

[a] PCA channels assuming the standard2 channel binning.

When modeling the spectrum of GX 339−4 from 3 to 110 keV as measured by the PCA and the HEXTE, the intercalibration between the instruments is of some concern. Our experience with previous data and the response matrix described by Dove et al. (1998) indicated that the flux calibration of the HEXTE with respect to the PCA was off by about 25%; i.e., the derived HEXTE fluxes were ∼75% of those found with the PCA. This deviation is mainly due to a slight misalignment of the HEXTE collimators, which has not yet been taken into account in the HEXTE response matrix (B. Heindl 1998, private communication). Using the new PCA response, the flux ratio now appears to be larger and was found to be 62%–69% in our data. Extracting spectra with internal software used by the HEXTE hardware team produced spectra identical to those found using our extraction procedure. Therefore we do not believe this change in the flux calibration to be due to errors in the dead-time correction. To take this offset in the effective areas into account, we modeled the spectra using a multiplicative constant that was set to unity for the PCA, and that was a fit parameter for both HEXTE clusters. Thus, all fluxes given below were measured with respect to the PCA. The maximum deviation of the HEXTE clusters relative to each other was found to be less than 8%.

Apart from the flux calibration, however, even more crucial for our analysis is the question of how well the inferred spectral shapes agree for the two instruments. Our Crab fits show that the PCA results in a photon index of $\Gamma = 2.187$ (eq. [B1]), while our HEXTE fits gave $\Gamma = 2.053$. The generally accepted value for the Crab photon index in the 1–100 keV range is $\Gamma = 2.10 \pm 0.03$. This value was adopted by Toor & Seward (1994) in their analysis of 28 different rocket flight measurements. There are indications that the spectrum softens to $\Gamma \sim 2.5$ above 150 keV (Jung 1989). Although the absolute uncertainty of the Crab flux in the 2–100 keV range has been estimated as large as 2%, and even larger below 2 keV (Nørgaard-Nielsen et al. 1994), the $\Delta\Gamma = 0.134$ deviation between the PCA and the HEXTE best-fit Crab photon index is still very worrisome, and it is currently being studied by both the PCA and HEXTE instrument teams (K. Jahoda 1998, private communication).

REFERENCES

Arnaud, K. A. 1996, in ASP Conf. Ser. 101, Astronomical Data Analysis Software and Systems V, ed. J. H. Jacoby & J. Barnes (San Francisco: ASP), 17
Bevington, P. R., & Robinson, D. K. 1992, Data Reduction and Error Analysis for the Physical Sciences (2d ed.; New York: McGraw-Hill)
Blandford, R. D., & Begelman, M. C. 1999, MNRAS, 303, 1
Bouchet, L., et al. 1993, ApJ, 407, 739
Callanan, P. J., Charles, P. A., Honey, W. B., & Thorstensen, J. R. 1991, MNRAS, 259, 395
Corbel, S., Fender, R. P., Durouchoux, P., Sood, R. K., Tzioumis, A. K., Spencer, R. E., & Campbell-Wilson, D. 1997, in Proc. 4th Compton Symposium, ed. C. D. Dermer, M. S. Strickman, & J. D. Kurfess, (Woodbury, NY: AIP), 937
Covault, C. E., Grindlay, J. E., & Manandhar, R. P. 1992, ApJ, 388, L65
Cowley, A. P., Crampton, D., & Hutchings, J. B. 1987, AJ, 93, 195
Cowley, A. P., Schmidtke, P. C., Crampton, D., Hutchings, J. B., & Bolte, M. 1991, ApJ, 373, 228
Day, C., Arnaud, K., Ebisawa, K., Gotthelf, E., Ingham, J., Mukai, K., & White, N. 1998, The *ASCA* Data Reduction Guide, technical report, version 2.0 (Greenbelt, Md.: NASA GSFC)
Di Matteo, T., Fabian, A. C., Rees, M. J., Carilli, C. L., & Ivison, R. J. 1999, MNRAS, submitted
Dobrinskaya, J., Liang, E., Luo, C., Sheth, S., & Smith, I. 1997, in X-Ray Imaging and Spectroscopy of Cosmic Hot Plasmas, ed. F. Makino & K. Mitsuda (Tokyo: Universial Academy), 481
Dove, J. B., Wilms, J., & Begelman, M. C. 1997a, ApJ, 487, 747
Dove, J. B., Wilms, J., Maisack, M. G., & Begelman, M. C. 1997b, ApJ, 487, 759
Dove, J. B., Wilms, J., Nowak, M. A., Vaughan, B. A., & Begelman, M. C. 1998, MNRAS, 298, 729
Doxsey, R., Grindlay, J., Griffiths, R., Bradt, H., Johnston, M., Leach, R., Schwartz, D., & Scwartz, J. 1979, ApJ, 228, L67
Ebisawa, K., Ueda, Y., Inoue, H., Tanaka, Y., & White, N. E. 1996, ApJ, 467, 419
Esin, A. A., McClintock, J. E., & Narayan, R. 1997, ApJ, 489, 865
Fender, R. P., & Hendry, M. A. 1999, MNRAS, in press
Fender, R. P., Spencer, R. E., Newell, S. J., & Tzioumis, A. K. 1997, MNRAS, 286, L29
Fender, R. P., et al. 1999, ApJ, 519, L165
Grabelsky, D. A., et al. 1995, ApJ, 441, 800
Grebenev, S. A., Syunyaev, R., Pavlinsky, M. N., & Dekhanov, I. A. 1991, Soviet Astron. Lett., 17, 413
Grindlay, J. E. 1979, ApJ, 232, L33
Hannikainnen, D. C., Hunstead, R. W., Campbell-Wilson, D., & Sood, R. K. 1999, A&A, in press
Hjellming, R. M., & Johnston, K. J. 1988, ApJ, 328, 600
Ichimaru, S. 1977, ApJ, 214, 840
Ilovaisky, S. A., Chevalier, C., Motch, C., & Chiappetti, L. 1986, A&A, 164, 671
Imamura, J. N., Kristian, J., Middleditch, J., & Steiman-Cameron, T. Y. 1990, ApJ, 365, 312
Jahoda, K., Swank, J. H., Giles, A. B., Stark, M. J., Strohmayer, T., Zhang, W., & Morgan, E. H. 1996, in EUV, X-Ray, and Gamma-Ray Instrumentation for Astronomy VII, ed. O. H. Siegmund (Bellingham, WA: SPIE), 59
Jahoda, K., et al. 1999, in preparation
Jung, G. V. 1989, ApJ, 338, 972
Kazanas, D., Hua, X.-M., & Titarchuk, L. 1997, ApJ, 480, 280
Kitamoto, S., Tsunemi, H., Miyamoto, S., & Hayashida, K. 1992, ApJ, 394, 609
Lampton, M., Margon, B., & Bowyer, S. 1976, ApJ, 208, 177
Levine, A. M., Bradt, H., Cui, W., Jernigan, J. G., Morgan, E. H., Remillard, R., Shirey, R. E., & Smith, D. A. 1996, ApJ, 469, L33
Lochner, J., & Remillard, R. 1997, ASM Data Products Guide, version dated 1997 August 27[8]
Magdziarz, P., & Zdziarski, A. A. 1995, MNRAS, 273, 837
Makishima, K., et al. 1996, PASJ, 48, 171
Méndez, M., & van der Klis, M. 1997, ApJ, 479, 926
Miyamoto, S., Kimura, K., Kitamoto, S., Dotani, T., & Ebisawa, K. 1991, ApJ, 383, 784
Miyamoto, S., Kitamoto, S., Iga, S., Hayashida, K., & Egoshi, W. 1995, ApJ, 442, L13
Miyamoto, S., Kitamoto, S., Iga, S., Hayashida, K., & Terada, K. 1994, ApJ, 435, 398
Morrison, R., & McCammon, D. 1983, ApJ, 270, 119
Motch, C., Ilovaisky, S. A., Chevalier, C., & Angebault, P. 1985, Space Sci. Rev., 40, 219
Motch, C., Ricketts, M. J., Page, C. G., Ilovaisky, S. A., & Chevalier, C. 1983, A&A, 119, 171
Narayan, R. 1996, ApJ, 462, 136
Narayan, R., Kato, S., & Honma, F. 1997, ApJ, 476, 49
Nørgaard-Nielsen, H. U., Budtz-Jørgensen, C., Westergaard, N. J., & Schnopper, H. W. 1994, A&A, 284, 705
Nowak, M. A., Wilms, J., & Dove, J. B. 1999, ApJ, 517, in press (Paper II)
Pooley, G. G., Fender, R. P., & Brocksopp, C. 1999, MNRAS, 302, L1
Poutanen, J., Krolik, J. H., & Ryde, F. 1997, MNRAS, 221, 21p
Predehl, P., Bräuninger, H., Burkert, W., & Schmitt, J. H. M. M. 1991, A&A, 246, L40
Remillard, R. A., & Levine, A. M. 1997, in All-Sky X-Ray Observations in the Next Decade, ed. N. Matsuoka & N. Kawai (Tokyo: Riken), 29
Rothschild, R. E., et al. 1998, ApJ, 496, 538
Shakura, N. I., & Sunyaev, R. 1973, A&A, 24, 337
Sood, R., & Campell-Wilson, D. 1994, IAU Circ. 6006
Steiman-Cameron, T. Y., Imamura, J. N., Middleditch, J., & Kristian, J. 1990, ApJ, 359, 197
Tanaka, Y., & Lewin, W. H. G. 1995, in X-Ray Binaries, ed. W. H. G. Lewin, J. van Paradijs, & E. P. J. van den Heuvel (Cambridge: Cambridge Univ. Press), 126
Toor, A., & Seward, F. D. 1974, AJ, 79, 995
Trudolyubov, S., et al. 1998, A&A, 334, 895
Turner, M. J. L., et al. 1989, PASJ, 41, 345
Ueda, Y., Ebisawa, K., & Done, C. 1994, PASJ, 46, 107
Zdziarski, A. 1999, in ASP Conf. Proc. 161, High-Energy Processes in Accreting Black Holes: Observational and Theoretical Advances Due to Ongoing Space Missions, ed. J. Poutanen & R. Svensson (San Francisco: ASP), in press
Zdziarski, A. A., Poutanen, J., Mikołajewska, J., Gierliński, M., Ebisawa, K., & Johnson, W. N. 1998, MNRAS, 301, 435
Życki, P. T., Done, C., & Smith, D. A. 1998, ApJ, 496, L25

[8] The ASM Data Products Guide is available on the World Wide Web at http://heasarc.gsfc.nasa.gov/docs/xte/asm_products_guide.html.

ANHANG B

Low Luminosity States of the Black Hole Candidate GX 339−4
II. Timing Analysis

1999

M.A. Nowak, J. Wilms, J.B. Dove

Nachdruck aus

The Astrophysical Journal
Vol. 517, S. 355–366

THE ASTROPHYSICAL JOURNAL, 517:355–366, 1999 May 20

LOW-LUMINOSITY STATES OF THE BLACK HOLE CANDIDATE GX 339−4. II. TIMING ANALYSIS

MICHAEL A. NOWAK,[1] JÖRN WILMS,[2] AND JAMES B. DOVE[1,3]
Received 1998 September 10; accepted 1998 November 4

ABSTRACT

Here we present timing analysis of a set of eight *Rossi X-Ray Timing Explorer* (*RXTE*) observations of the black hole candidate GX 339−4 that were taken during its hard/low state. On long timescales, the *RXTE* All Sky Monitor data reveal evidence of a 240 day periodicity, comparable to timescales expected from warped, precessing accretion disks. On short timescales all observations save one show evidence of a persistent $f_{\rm QPO} \approx 0.3$ Hz quasi-periodic oscillation. The broadband (10^{-3} to 10^{2} Hz) power appears to be dominated by two independent processes that can be modeled as very broad Lorentzian fits with $Q \lesssim 1$. The coherence function between soft and hard photon variability shows that if these are truly independent processes, then they are individually coherent, but they are incoherent with one another. This is evidenced by the fact that the coherence function between the hard and soft variability is near unity between 5×10^{-3} to 10 Hz but shows evidence of a dip at $f \approx 1$ Hz. This is the region of overlap between the broad Lorentzian fits to the power spectral density. As in Cyg X-1, the coherence also drops dramatically at frequencies $\gtrsim 10$ Hz. Also as in Cyg X-1, the hard photon variability is seen to lag the soft photon variability with the lag time increasing with decreasing Fourier frequency. The magnitude of this time lag appears to be positively correlated with the flux of GX 339−4. We discuss all of these observations in light of current theoretical models of both black hole spectra and temporal variability.

Subject headings: accretion, accretion disks — black hole physics — binaries: general — X-rays: stars

1. INTRODUCTION

In a companion paper to this work (Wilms et al. 1999a, hereafter Paper I) we have presented spectral analysis of a series of *Advanced Satellite for Cosmology and Astrophysics* (*ASCA*) and simultaneous radio/*Rossi X-Ray Timing Explorer* (*RXTE*) observations of the black hole candidate (BHC) GX 339−4. This source has exhibited both spectrally soft states (see Grebenev et al. 1991; Miyamoto et al. 1991) and spectrally hard states (see Grebenev et al. 1991; Miyamoto et al. 1992; Zdziarski et al. 1998). Both the *ASCA* and *RXTE* observations presented in Paper I showed GX 339−4 to be in spectrally hard and low-luminosity (3–9 keV flux $\lesssim 10^{-9}$ ergs cm^{-2} s^{-1}) states. The eight *RXTE* observations spanned roughly a factor of 5 in terms of observed 3–9 keV flux.

In this work we shall consider the timing analysis of the eight *RXTE* observations. Timing analysis for GX 339−4 previously has been presented for the soft, bright "very high state" (Miyamoto et al. 1991), the soft, fainter "high state" (Grebenev et al. 1991), and the hard "low state" (Grebenev et al. 1991; Miyamoto et al. 1992). In addition, timing analysis has been presented for so-called "intermediate states," which are bright but spectrally harder than the typical very high or high states (Méndez & van der Klis 1997). In general, the harder states exhibit more temporal variability than the softer states (see van der Klis 1989). Timing analyses of the GX 339−4 hard state have shown similar results to analyses of other hard-state BHCs (Miyamoto et al. 1992). Specifically, the GX 339−4 temporal variability has been observed to be similar to that of Cygnus X-1 (Belloni & Hasinger 1990a, 1990b; Miyamoto et al. 1992; Nowak et al. 1999a, and references therein).

A discussion of Fourier techniques in specific, and timing analysis in general, has been presented by van der Klis 1989. Here we apply these Fourier analysis techniques in the same manner as for our *RXTE* observations of Cyg X-1 (Nowak et al. 1999a). Specifically, we used the same techniques for estimating: deadtime corrections (Zhang et al. 1995; Zhang & Jahoda 1996); the error bars and Poisson noise levels of the power spectral density (PSD) (Leahy et al. 1983; van der Klis 1989); the error bars and noise levels for the coherence function (Bendat & Piersol 1986; Vaughan & Nowak 1997); and the error bars and noise levels for the Fourier frequency–dependent time lag between hard and soft photon variability (Bendat & Piersol 1986; Nowak et al. 1999a). A self-contained discussion of these techniques as regards *RXTE* timing analysis is given by Nowak et al. (1999a).

This paper is organized as follows. First we consider evidence for long-term periodicities in the *RXTE* All Sky Monitor (ASM) data in § 2. In § 3 we consider the power spectral density (PSD). In § 4 we consider both the coherence function (see Vaughan & Nowak 1997) and the Fourier frequency–dependent time lags between hard and soft photon variability. We discuss the theoretical implications of these observations in § 5. We then summarize our results in § 6.

2. ALL SKY MONITOR OBSERVATIONS OF LONG "CHARACTERISTIC TIMESCALES" IN GX 339−4

We used data from the All Sky Monitor (ASM) on *RXTE* to study the long-term behavior of GX 339−4. The ASM is an array of three shadow cameras combined with position-sensitive proportional counters that provides for a quasi-continuous coverage of the sky visible from *RXTE*.

[1] JILA, University of Colorado, Campus Box 440, Boulder, CO 80309-0440; mnowak@rocinante.colorado.edu, dove@rocinante.colorado.edu.
[2] Institut für Astronomie und Astrophysik, Abt. Astronomie, Waldhäuser Strasse 64, D-72076 Tübingen, Germany; wilms@astro.uni-tuebingen.de.
[3] Also CASA, University of Colorado, Campus Box 389, Boulder, CO 80309-0389.

In practice, light curves in three energy bands—1.3–3.0 keV, 3.0–5.0 keV, and 5.0–12.2 keV—as well as over the whole ASM band are publicly available from the ASM data archives (Lochner & Remillard 1997). Typically there are several 90 s measurements available for each day. Further descriptions of the instrument and first year results are presented by Levine et al. (1996) and Remillard & Levine (1997).

In Figure 1 we present the ASM data of GX 339−4 up until Truncated Julian Date (TJD) ≈800 (1998 November 15). See Paper I for a presentation of the complete to date ASM data of GX 339−4. We also indicate in this figure the dates of our *RXTE* observations, as well as the dates of Australian Telescope Compact Array (ATCA) and Molongolo Observing Synthesis Telescope (MOST) radio observations of GX339−4 (Fender et al. 1997; Corbel et al. 1998; Hannikainnen et al. 1999; Paper I). The average 1 σ error bar for a point presented in Figure 1 is ≈0.4 counts s^{-1}. Note the three peaks (at TJD ≈ 280, 480–580, 780) in the ASM data that occur at intervals separated by ≈250 days.

We determined the significance of any possible long-term periodicities in the ASM light curves by computing the Lomb-Scargle Periodogram (Lomb 1976; Scargle 1982) for the 1.3–12.2 keV band for 5 day average data. Here we average data only where the best fit to the source position and flux in an ASM observation has $\chi^2_{\rm red} \leq 1.5$ (see Lochner & Remillard 1997) in each of the three ASM energy channels. We considered only ASM data taken before TJD 800, as GX 339−4 underwent a state change shortly thereafter (see Paper I). The periodogram shown in Figure 1 reveals evidence of a 240 day period at greater than the 99.9% significance level. (The significance levels were estimated following the methods of Horne & Baliunas 1986.) Epoch folding (see Leahy et al. 1983; Schwarzenberg-Czerny 1989; Davies 1990) of the ASM light curves also shows evidence of this 240 day periodicity.

Long timescale periodicities and quasi periodicities are relatively common in ASM observations of binary sources (R. A. Remillard 1997, private communication). Evidence for a 294 day periodicity in Cygnus X-1 has been previously reported (Kemp et al. 1983; Priedhorsky, Terrell, & Holt 1983) and is readily apparent in the ASM data during the hard state. A 198 day periodicity also has been observed in LMC X-3 (Cowley et al. 1991; Wilms et al. 1999b). We note that the observed timescales of these periodicities are comparable to the timescales expected from the radiation pressure–driven warping instability discovered by Pringle (1996; see also Maloney, Begelman & Pringle 1996; Maloney & Begelman 1997; Maloney, Begelman & Nowak 1998). This is a fairly generic instability that causes a radiatively efficient (i.e., non–advection dominated) accretion disk to warp and precess on $\mathcal{O}$(100 day) timescales. Such a timescale is consistent with the periodicities seen in many binaries and with the 240 day periodicity that we see in GX 339−4.

As discussed in Paper I, however, both the Compton corona models and the advection-dominated accretion flow (ADAF) models of the spectral data suggest that the observed flux variations are in large part attributable to variations of the coronal radius. A pure warped, precessing disk model would invoke only inclination angle effects. This is unlikely to be the case for GX 339−4. As discussed by Maloney et al. (1996), however, the precession timescale and warp shape are more sensitive to the outer boundary conditions than the inner boundary conditions. Perhaps then it is possible that what we observe is a combination of a quasi-steadily precessing disk on large radii combined with coronal structure changes on small radii. Although 240 days is a characteristic timescale in both the Lomb-Scargle periodogram and in the epoch folding analysis, it is obvious from Figure 1 that we are not observing a strictly periodic phenomenon.

3. POWER SPECTRAL DENSITIES

We studied the variability of GX 339−4 using data from the Proportional Counter Array (PCA) on-board *RXTE*. The PCA consists of five nearly identical coaligned Xenon proportional counter units (PCUs) with a total effective area of about 6500 cm^2, and it is sensitive in the energy

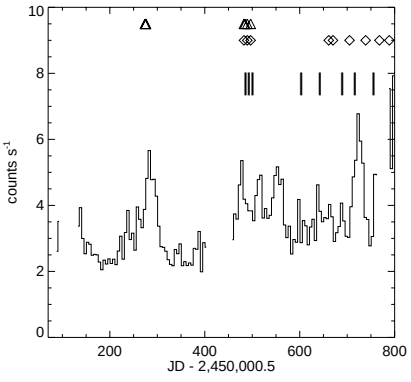

FIG. 1*a*

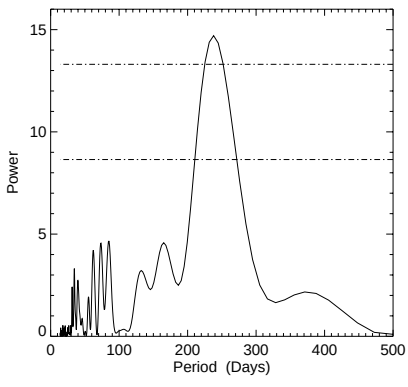

FIG. 1*b*

FIG. 1.—(*a*) *RXTE* All Sky Monitor data for GX 339−4 (5 day averages in the 1.3–12.2 keV band) vs. Truncated Julian Date (TJD) ≡ Julian Date (JD) −2,450,000.5. Dashes indicate dates of our *RXTE* pointed observations, diamonds indicate dates of MOST observations (Hannikainnen et al. 1999), and triangles indicate dates of ATCA radio observations (Corbel et al. 1998). (*b*) A Lomb-Scargle Periodogram (see Lomb 1976; Scargle 1982) of the ASM data for TJD < 800. We have used 600 periods ranging from 2 weeks to 500 days. Lines are estimates of the 99.9% and 90% significance levels.

range from 2 keV to ~60 keV (Jahoda et al. 1996). We used only data from when all five PCUs were turned on, and when the elevation angle between the spacecraft pointing direction and the limb of the earth was greater than 10°. PCA count rates for the GX 339−4 observations ranged from 200 to 800 counts s^{-1} and were of $\mathcal{O}$(10 ks) duration.

To study the short-timescale variability, we created 2^{-8} s resolution light curves in four different energy bands: 0–3.9 keV, 3.9–7.5 keV, 7.5–10.8 keV, 10.8–21.9 keV, hereafter bands A, B, C, and D, respectively.[4] Note that this is one fewer energy band and one-half the time resolution than for our Cyg X-1 observations (Nowak et al. 1999a). This was required to obtain good statistics because the GX 339−4 observations discussed here ranged from 200–800 counts s^{-1}, as opposed to the 4500 counts s^{-1} observed for Cyg X-1. Energy bands A–D each had roughly the same count rate for a given observation. As for the spectral analysis (Paper I), we found that all the observations were similar in their properties, with the exception of observation 5. Observation 5 was approximately a factor of 5 fainter than the brightest observation (observation 1).

As for our *RXTE* observations of Cyg X-1 (Nowak et al. 1999a), we combined low-frequency ($\approx 8 \times 10^{-4}$ to 7×10^{-3} Hz) fast Fourier transforms (FFTs) made from a few (6–16) data segments of length 512–1024 s with higher frequency (7×10^{-3} to 128 Hz) FFTs made from somewhat more ($\gtrsim 70$) data segments of length 128 s. From these data segments we created PSDs for all of our observations. We present two examples of the resulting PSDs in Figure 2. With the exception of observation 5, all PSDs were qualitatively and quantitatively similar to that presented in Figure 2 for observation 7. The PSDs for observations 1–4 and 6–7 have shapes roughly similar to what we observed for Cyg X-1: flat from $\approx 10^{-3}$ to 0.03 Hz, approximately $\propto f^{-1}$ between 0.03 and 3 Hz, and steeper above ≈ 3 Hz (Nowak et al. 1999a). The PSDs for observation 5 have qualitatively similar shapes; however, the break frequencies are approximately a factor of 3 lower.

Doubly broken power laws provided adequate descriptions of the PSDs for our *RXTE* observations of Cyg X-1 (Nowak et al. 1999a). Here, however, we clearly see that the GX 339−4 PSDs contain more structure. A ≈ 0.3 Hz quasi-periodic oscillation (QPO) is evident in observation 7. In fact, this QPO appears at some level in all of our observations except observation 5. Even ignoring the QPO features, the PSD is only marginally approximated by a doubly broken power law.

We have tried to fit the shape of the PSDs with a number of different functional forms. For example, a singly broken power law with a Lorentzian absorption feature at ≈ 0.3–1 Hz provides good fits to all of the PSDs. Here we show the results of fitting a weak power law plus two broad Lorentzian features. As we further elaborate in §§ 4 and 5, such a fit may have some physical relevance. The Lorentzian and power-law components may represent separate, broadband processes that are individually coherent (between their soft and hard variability) but that are incoherent with one another.

Sample fits to the broadband power are presented in Figure 3, and results for all of our data are presented in

[4] We also created 2^{-13} s resolution light curves to search for signatures of high-frequency features. No evidence for such features was found. Note also that the effective lower limit for energy band A is more ≈ 2 keV.

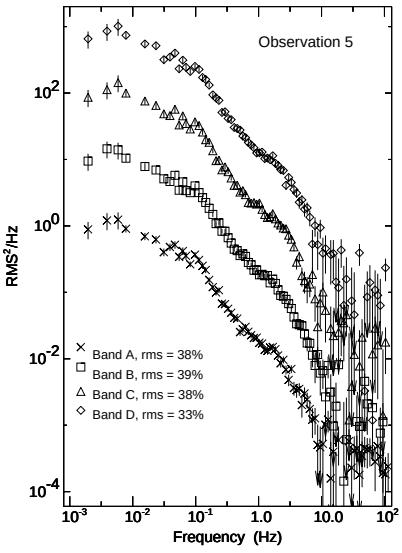

FIG. 2*a*

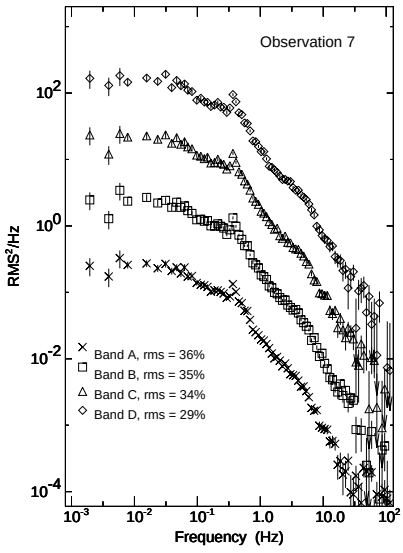

FIG. 2*b*

FIG. 2.—PSDs with associated uncertainties for (*a*) observation 5 and (*b*) observation 7. All PSD are for the one-sided normalization of Belloni & Hasinger (1990b), where integrating over positive frequencies yields the total mean square variability. Crosses correspond to energy band A, squares to energy band B shifted upward by a factor of 10, triangles to energy band C shifted upward by a factor of 100, and diamonds to energy band D shifted upward by a factor of 1000. (See text for the energy range of the bands.) Root mean square (rms) variability values were calculated between $f = 7 \times 10^{-3}$ and 40 Hz.

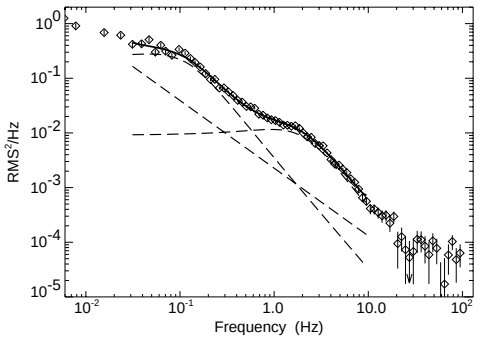

FIG. 3*a*

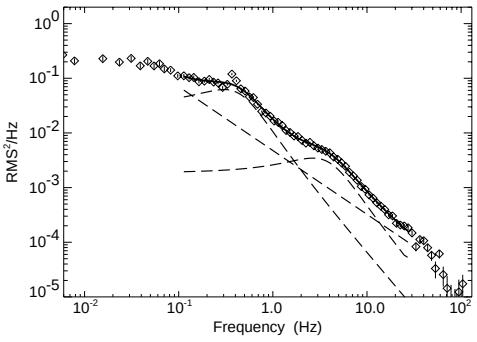

FIG. 3*b*

FIG. 3.—(*a*) Diamonds are the PSD for observation 5 (energy bands A–D summed), normalized as in Belloni & Hasinger (1990b). (*b*) Diamonds are the PSD for observation 7 (energy bands A–D summed). For both figures, the solid line is the best-fit power law plus two broad Lorentzian components. (Fit range is 0.03–10 Hz for observation 5, and 0.1–30 Hz for observaion 7.) Dashed lines show the individual components of the fits.

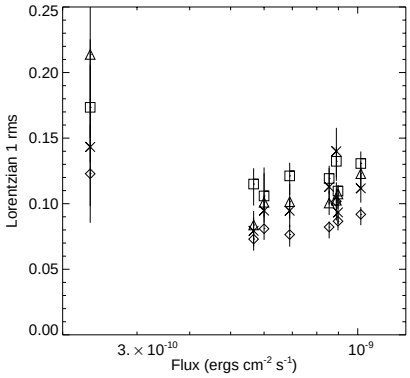

FIG. 4*a*

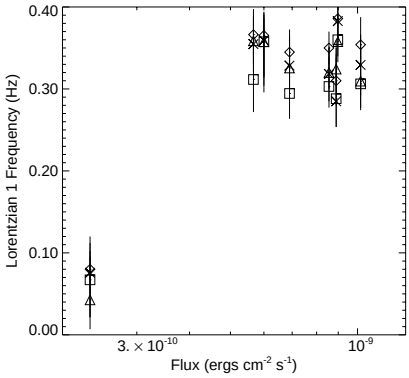

FIG. 4*b*

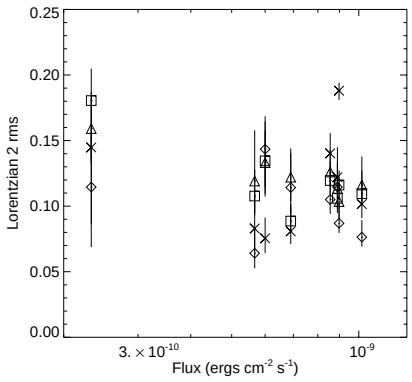

FIG. 4*c*

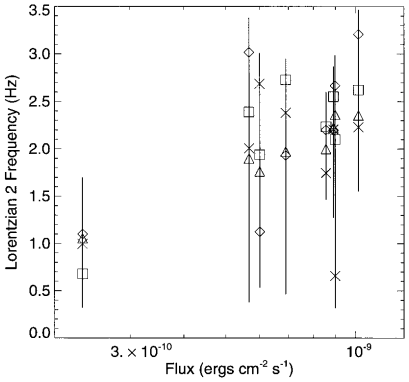

FIG. 4*d*

FIG. 4.—(*a*) rms variability of the low-frequency broad Lorentzian fit component vs. the 3–9 keV flux of the observation. (*b*) Peak frequency of the low-frequency broad Lorentzian fit component vs. the 3–9 keV flux of the observation. (*c*) rms variability of the high-frequency broad Lorentzian fit component vs. the 3–9 keV flux of the observation. (*d*) Peak frequency of the high-frequency broad Lorentzian fit component vs. the 3–9 keV flux of the observation. Symbols are the same as for Fig. 2.

TABLE 1

FITS TO THE PSD

Observation	Band	R_1 ($\times 10^{-2}$)	f_1 (Hz)	Q_1	A ($\times 10^{-3}$)	Γ	R_2 ($\times 10^{-2}$)	f_2 (Hz)	Q_2	χ^2
1	A	$24.^{+2.}_{-2.}$	$0.33^{+0.04}_{-0.04}$	$1.2^{+0.3}_{-0.2}$	$7.5^{+1.4}_{-1.7}$	$-1.23^{+0.06}_{-0.11}$	$19.^{+3.}_{-2.}$	$2.2^{+0.3}_{-0.6}$	$0.9^{+0.2}_{-0.3}$	102.
1	B	$26.^{+2.}_{-2.}$	$0.31^{+0.04}_{-0.02}$	$1.0^{+0.3}_{-0.2}$	$5.4^{+1.4}_{-1.8}$	$-1.28^{+0.07}_{-0.18}$	$21.^{+3.}_{-2.}$	$2.6^{+0.3}_{-0.6}$	$0.8^{+0.2}_{-0.3}$	116.
1	C	$25.^{+2.}_{-2.}$	$0.31^{+0.04}_{-0.03}$	$1.0^{+0.3}_{-0.2}$	$4.7^{+1.6}_{-2.5}$	$-1.26^{+0.08}_{-0.32}$	$21.^{+4.}_{-2.}$	$2.4^{+0.4}_{-0.8}$	$0.7^{+0.2}_{-0.3}$	84.
1	D	$20.^{+1.}_{-2.}$	$0.35^{+0.03}_{-0.02}$	$1.3^{+0.3}_{-0.2}$	$5.6^{+1.0}_{-1.1}$	$-1.17^{+0.04}_{-0.09}$	$16.^{+3.}_{-2.}$	$3.2^{+0.3}_{-0.6}$	$1.1^{+0.2}_{-0.4}$	112.
1	T	$25.^{+2.}_{-2.}$	$0.30^{+0.04}_{-0.03}$	$0.9^{+0.3}_{-0.1}$	$5.7^{+0.9}_{-0.9}$	$-1.19^{+0.04}_{-0.06}$	$18.^{+1.}_{-1.}$	$2.9^{+0.1}_{-0.3}$	$1.1^{+0.1}_{-0.2}$	129.
2	A	$27.^{+3.}_{-4.}$	$0.28^{+0.06}_{-0.03}$	$0.9^{+0.4}_{-0.1}$	$4.6^{+2.7}_{-3.4}$	$-1.46^{+0.13}_{-0.51}$	$23.^{+4.}_{-3.}$	$2.2^{+0.4}_{-0.7}$	$0.8^{+0.3}_{-0.2}$	103.
2	B	$26.^{+2.}_{-3.}$	$0.29^{+0.05}_{-0.03}$	$0.9^{+0.3}_{-0.1}$	$6.3^{+1.8}_{-1.7}$	$-1.30^{+0.08}_{-0.15}$	$20.^{+3.}_{-2.}$	$2.6^{+0.3}_{-0.5}$	$0.9^{+0.2}_{-0.3}$	73.
2	C	$22.^{+2.}_{-3.}$	$0.32^{+0.04}_{-0.03}$	$1.3^{+0.4}_{-0.2}$	$6.7^{+1.8}_{-2.9}$	$-1.27^{+0.08}_{-0.23}$	$21.^{+4.}_{-3.}$	$2.2^{+0.5}_{-1.0}$	$0.7^{+0.3}_{-0.4}$	74.
2	D	$21.^{+3.}_{-3.}$	$0.31^{+0.04}_{-0.03}$	$1.1^{+0.4}_{-0.2}$	$3.7^{+2.0}_{-3.4}$	$-1.35^{+0.13}_{-0.62}$	$20.^{+3.}_{-3.}$	$2.2^{+0.4}_{-0.7}$	$0.6^{+0.3}_{-0.3}$	94.
2	T	$25.^{+2.}_{-3.}$	$0.28^{+0.05}_{-0.03}$	$0.9^{+0.3}_{-0.1}$	$6.1^{+1.1}_{-0.9}$	$-1.24^{+0.04}_{-0.06}$	$18.^{+1.}_{-1.}$	$2.8^{+0.1}_{-0.3}$	$1.0^{+0.1}_{-0.2}$	102.
3	A	$24.^{+3.}_{-3.}$	$0.32^{+0.03}_{-0.03}$	$1.3^{+0.4}_{-0.2}$	$4.6^{+2.8}_{-2.9}$	$-1.46^{+0.16}_{-0.51}$	$24.^{+3.}_{-4.}$	$1.8^{+0.5}_{-0.3}$	$0.6^{+0.3}_{-0.1}$	77.
3	B	$25.^{+2.}_{-2.}$	$0.30^{+0.04}_{-0.03}$	$1.1^{+0.3}_{-0.2}$	$5.3^{+1.8}_{-1.6}$	$-1.32^{+0.09}_{-0.16}$	$22.^{+3.}_{-2.}$	$2.2^{+0.3}_{-0.4}$	$0.8^{+0.2}_{-0.2}$	86.
3	C	$22.^{+2.}_{-2.}$	$0.32^{+0.03}_{-0.02}$	$1.3^{+0.4}_{-0.2}$	$5.9^{+1.7}_{-3.4}$	$-1.27^{+0.06}_{-0.38}$	$22.^{+3.}_{-2.}$	$2.0^{+0.4}_{-0.4}$	$0.6^{+0.3}_{-0.3}$	73.
3	D	$19.^{+1.}_{-2.}$	$0.35^{+0.02}_{-0.02}$	$1.5^{+0.3}_{-0.2}$	$5.0^{+1.3}_{-2.7}$	$-1.25^{+0.08}_{-0.33}$	$19.^{+3.}_{-2.}$	$2.2^{+0.4}_{-0.4}$	$0.7^{+0.3}_{-0.3}$	92.
3	T	$24.^{+1.}_{-1.}$	$0.30^{+0.04}_{-0.02}$	$1.1^{+0.3}_{-0.1}$	$5.4^{+1.0}_{-0.8}$	$-1.26^{+0.03}_{-0.08}$	$20.^{+2.}_{-1.}$	$2.5^{+0.1}_{-0.4}$	$0.9^{+0.1}_{-0.2}$	119.
4	A	$19.^{+2.}_{-3.}$	$0.35^{+0.03}_{-0.03}$	$1.6^{+0.7}_{-0.4}$	$11.5^{+1.8}_{-2.1}$	$-1.17^{+0.05}_{-0.09}$	$16.^{+5.}_{-3.}$	$2.0^{+0.5}_{-0.7}$	$0.9^{+0.5}_{-0.3}$	48.
4	B	$24.^{+2.}_{-3.}$	$0.31^{+0.05}_{-0.04}$	$1.1^{+0.5}_{-0.2}$	$6.3^{+2.1}_{-4.5}$	$-1.30^{+0.09}_{-0.53}$	$20.^{+4.}_{-3.}$	$2.4^{+0.4}_{-1.1}$	$0.8^{+0.3}_{-0.4}$	82.
4	C	$19.^{+2.}_{-2.}$	$0.36^{+0.03}_{-0.03}$	$1.5^{+0.5}_{-0.3}$	$7.5^{+2.1}_{-5.0}$	$-1.24^{+0.07}_{-0.47}$	$21.^{+7.}_{-4.}$	$1.9^{+0.8}_{-1.5}$	$0.6^{+0.4}_{-0.5}$	62.
4	D	$17.^{+2.}_{-2.}$	$0.37^{+0.03}_{-0.03}$	$1.5^{+0.5}_{-0.3}$	$6.8^{+1.3}_{-1.4}$	$-1.16^{+0.05}_{-0.10}$	$14.^{+4.}_{-2.}$	$3.0^{+0.4}_{-0.8}$	$1.2^{+0.5}_{-0.5}$	66.
4	T	$22.^{+2.}_{-3.}$	$0.31^{+0.05}_{-0.03}$	$1.0^{+0.4}_{-0.2}$	$6.5^{+1.1}_{-0.9}$	$-1.23^{+0.04}_{-0.07}$	$18.^{+2.}_{-1.}$	$2.7^{+0.2}_{-0.5}$	$1.0^{+0.1}_{-0.2}$	86.
5	A	$27.^{+12.}_{-8.}$	$0.08^{+0.04}_{-0.05}$	$0.8^{+1.0}_{-0.6}$	$5.1^{+6.5}_{-4.8}$	$-1.11^{+1.06}_{-0.85}$	$25.^{+7.}_{-10.}$	$1.0^{+0.7}_{-0.7}$	$0.6^{+1.1}_{-0.4}$	59.
5	B	$31.^{+9.}_{-7.}$	$0.07^{+0.04}_{-0.05}$	$0.6^{+0.6}_{-0.5}$	$3.5^{+5.0}_{-3.2}$	$-1.23^{+0.92}_{-0.73}$	$29.^{+4.}_{-7.}$	$0.7^{+0.5}_{-0.4}$	$0.4^{+0.5}_{-0.2}$	46.
5	C	$35.^{+8.}_{-10.}$	$0.04^{+0.05}_{-0.04}$	$0.4^{+0.7}_{-0.3}$	$1.6^{+5.1}_{-1.4}$	$-1.30^{+1.10}_{-0.67}$	$28.^{+4.}_{-5.}$	$1.0^{+0.4}_{-0.6}$	$0.6^{+0.3}_{-0.3}$	69.
5	D	$23.^{+7.}_{-7.}$	$0.08^{+0.04}_{-0.03}$	$0.8^{+0.8}_{-0.3}$	$5.0^{+4.0}_{-3.8}$	$-1.07^{+0.19}_{-0.41}$	$20.^{+7.}_{-8.}$	$1.1^{+0.6}_{-0.6}$	$0.6^{+0.9}_{-0.4}$	49.
5	T	$35.^{+5.}_{-8.}$	$0.03^{+0.04}_{-0.03}$	$0.3^{+0.4}_{-0.2}$	$1.0^{+3.2}_{-0.4}$	$-1.25^{+0.60}_{-0.45}$	$27.^{+2.}_{-4.}$	$0.9^{+0.3}_{-0.3}$	$0.5^{+0.2}_{-0.2}$	85.
6	A	$21.^{+2.}_{-3.}$	$0.33^{+0.04}_{-0.03}$	$1.4^{+0.6}_{-0.2}$	$9.6^{+1.7}_{-1.5}$	$-1.17^{+0.04}_{-0.09}$	$17.^{+4.}_{-2.}$	$2.4^{+0.3}_{-0.6}$	$1.2^{+0.4}_{-0.5}$	83.
6	B	$25.^{+2.}_{-3.}$	$0.29^{+0.05}_{-0.03}$	$1.1^{+0.4}_{-0.2}$	$6.6^{+1.7}_{-1.4}$	$-1.18^{+0.06}_{-0.10}$	$18.^{+3.}_{-2.}$	$2.7^{+0.2}_{-0.4}$	$1.1^{+0.2}_{-0.3}$	89.
6	C	$22.^{+3.}_{-3.}$	$0.33^{+0.04}_{-0.02}$	$1.3^{+0.5}_{-0.2}$	$5.3^{+2.1}_{-4.1}$	$-1.31^{+0.10}_{-0.65}$	$22.^{+4.}_{-3.}$	$2.0^{+0.5}_{-1.1}$	$0.7^{+0.3}_{-0.4}$	72.
6	D	$18.^{+2.}_{-2.}$	$0.34^{+0.03}_{-0.02}$	$1.5^{+0.5}_{-0.2}$	$4.7^{+1.7}_{-3.1}$	$-1.26^{+0.09}_{-0.51}$	$20.^{+5.}_{-3.}$	$1.9^{+0.6}_{-1.5}$	$0.6^{+0.3}_{-0.4}$	75.
6	T	$23.^{+1.}_{-3.}$	$0.30^{+0.05}_{-0.02}$	$1.1^{+0.4}_{-0.1}$	$5.8^{+1.1}_{-0.8}$	$-1.21^{+0.04}_{-0.07}$	$19.^{+2.}_{-1.}$	$2.6^{+0.1}_{-0.3}$	$1.0^{+0.1}_{-0.2}$	101.
7	A	$22.^{+2.}_{-2.}$	$0.38^{+0.03}_{-0.02}$	$1.7^{+0.4}_{-0.3}$	$4.6^{+2.5}_{-2.8}$	$-1.45^{+0.18}_{-0.37}$	$28.^{+2.}_{-4.}$	$0.8^{+0.7}_{-0.3}$	$0.3^{+0.3}_{-0.1}$	115.
7	B	$24.^{+1.}_{-2.}$	$0.36^{+0.03}_{-0.02}$	$1.3^{+0.4}_{-0.3}$	$6.2^{+1.4}_{-1.8}$	$-1.22^{+0.06}_{-0.16}$	$21.^{+2.}_{-2.}$	$2.1^{+0.6}_{-0.5}$	$0.7^{+0.4}_{-0.3}$	115.
7	C	$23.^{+1.}_{-2.}$	$0.36^{+0.04}_{-0.03}$	$1.3^{+0.4}_{-0.2}$	$6.1^{+1.3}_{-2.1}$	$-1.15^{+0.06}_{-0.20}$	$19.^{+3.}_{-2.}$	$2.4^{+0.5}_{-1.6}$	$0.7^{+0.3}_{-0.5}$	112.
7	D	$20.^{+1.}_{-2.}$	$0.39^{+0.03}_{-0.03}$	$1.4^{+0.4}_{-0.2}$	$4.8^{+0.7}_{-2.2}$	$-1.14^{+0.04}_{-0.24}$	$16.^{+3.}_{-1.}$	$2.7^{+0.3}_{-1.5}$	$0.8^{+0.2}_{-0.5}$	124.
7	T	$25.^{+1.}_{-2.}$	$0.33^{+0.04}_{-0.03}$	$1.0^{+0.2}_{-0.1}$	$4.9^{+0.7}_{-0.8}$	$-1.18^{+0.05}_{-0.06}$	$19.^{+1.}_{-1.}$	$2.7^{+0.2}_{-0.3}$	$0.9^{+0.1}_{-0.1}$	165.
8	A	$21.^{+2.}_{-2.}$	$0.36^{+0.04}_{-0.05}$	$1.3^{+0.3}_{-0.3}$	$9.7^{+1.5}_{-1.8}$	$-1.20^{+0.05}_{-0.08}$	$16.^{+2.}_{-3.}$	$2.7^{+0.3}_{-0.5}$	$1.2^{+0.5}_{-0.4}$	61.
8	B	$23.^{+5.}_{-2.}$	$0.36^{+0.03}_{-0.05}$	$1.2^{+0.3}_{-0.3}$	$5.1^{+2.2}_{-3.9}$	$-1.45^{+0.15}_{-0.69}$	$23.^{+4.}_{-4.}$	$1.9^{+0.6}_{-0.7}$	$0.6^{+0.3}_{-0.2}$	78.
8	C	$21.^{+5.}_{-2.}$	$0.36^{+0.03}_{-0.06}$	$1.2^{+0.3}_{-0.3}$	$5.0^{+2.4}_{-3.7}$	$-1.42^{+0.15}_{-0.71}$	$23.^{+5.}_{-4.}$	$1.8^{+0.8}_{-1.1}$	$0.5^{+0.4}_{-0.3}$	78.
8	D	$18.^{+4.}_{-2.}$	$0.37^{+0.03}_{-0.05}$	$1.3^{+0.3}_{-0.4}$	$3.9^{+2.0}_{-2.8}$	$-1.37^{+0.17}_{-0.60}$	$22.^{+4.}_{-5.}$	$1.1^{+1.2}_{-0.6}$	$0.3^{+0.4}_{-0.2}$	67.
8	T	$21.^{+2.}_{-1.}$	$0.35^{+0.03}_{-0.03}$	$1.1^{+0.2}_{-0.2}$	$5.7^{+0.8}_{-1.0}$	$-1.33\ ^{+0.05}_{-0.07}$	$20.^{+2.}_{-1.}$	$2.3^{+0.3}_{-0.3}$	0.70.10.1	74.

NOTES.—Fits to the PSD are of the form $Af^{\Gamma} + \pi^{-1}\{R_1^2 Q_1\ f_1/[f_1^2 + Q_1^2(f-f_1)^2] + R_2^2 Q_2\ f_2/[f_2^2 + Q_2^2(f-f_2)^2]\}$. Energy ranges of bands A–D are described in the text. "T" represents energy bands A–D summed together. All fits were in the range $f = 0.1$–30 Hz (47 degrees of freedom), except for observation 5, which was fit in the range $f = 0.03$–10 Hz (45 degrees of freedom). Errors are the nominal 90% confidence level for one interesting parameter ($\Delta\chi^2 = 2.71$).

Table 1. The functional form of the Lorentzian components that we fit is given by

$$P(f) = \pi^{-1}\,\frac{R^2 Q f_0}{f_0^2 + Q^2(f-f_0)^2}\,. \tag{1}$$

Here f_0 is the resonant frequency of the Lorentzian component, Q is the quality factor ($\approx f_0/\Delta f$, where Δf is the full-width at half-maximum of the Lorentzian component), and R is the fit amplitude (root mean square variability, $\mathrm{rms} = R[\frac{1}{2} - \tan^{-1}(-Q)/\pi]^{1/2}$, i.e., $\mathrm{rms} = R$ as $Q \to \infty$). For all the fits presented in Table 1, $Q \lesssim 1$. We thus cannot consider the broad peaks in the observed PSDs to be "quasi-periodic oscillations." The fits are more rightly considered to be indicative of broadband power with characteristic timescales $\sim f_0^{-1}$. Note also that, for all of the fits, $\chi^2_{\mathrm{red}} \lesssim 2$–3. Although this formally represents an unacceptable fit, this is partly attributable to the excellent statistics achievable with *RXTE*. Even small fractional deviations from the fit are highly statistically significant. In practice we have found that $\chi^2_{\mathrm{red}} \lesssim 2$ is nearly impossible to achieve with any simple functional fits. Futhermore, the fits with the largest χ^2_{red} showed the most pronounced 0.3 Hz QPO, as in observation 7.

For observations 1–4 and 6–7, the low-frequency broadband power was peaked near ≈ 0.3 Hz, while the high-frequency broadband power was peaked near ≈ 2.5 Hz. The rms variability amplitudes were all comparable for these observations. Observation 5 had a somewhat larger rms variability amplitude. The trend for all observations was for the rms variability amplitude, measured from 7×10^{-3} to 40 Hz, to decrease with increasing energy band, although this is only marginally evident in the individual fit components (see Fig. 4). In Figure 4 we plot the best fit rms

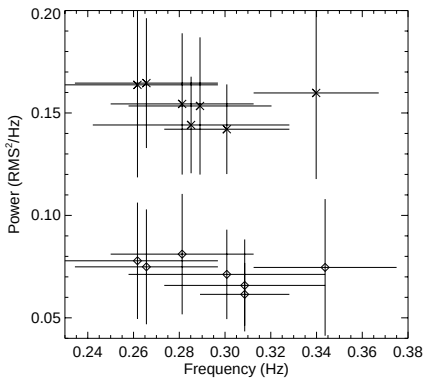

FIG. 5.—QPO PSD amplitude vs. frequency. The bars extend from the values for the dip to the values of the peak (see text), and the points are placed at the midpoint. Crosses are for energy band A and diamonds are for energy band D, with PSD amplitude lowered by 0.1.

variabilities and peak frequencies for the two Lorentzian fit components versus the observed 3–9 keV flux.

Observations 1–4 and 6–7 span a factor of 2 in observed 3–9 keV flux. The PSD parameters, however, show no obvious trends with flux, except for exhibiting weak evidence for the rms variability of the low-frequency Lorentzian fit component to increase with 3–9 keV luminosity. Perhaps the most remarkable aspect of this subset of the observations is how similar all the PSDs appear to one another despite the factor of 2 spread in the observed 3–9 keV flux.

The $\approx$0.3 Hz QPO is most prominent in observation 7. Its strength and width are somewhat difficult to characterize, however, as it is difficult to determine the "continuum" level of the PSD to which it should be compared. The rise of the QPO appears sharper than its decline, and typically there is a PSD "dip" at $\approx$0.05 Hz before the peak of the QPO. We have tried a variety of narrow Lorentzian plus broadband power fits to the features; however, the best-fit parameters are highly dependent on the assumed form of the underlying broadband PSD. Furthermore, narrow Lorentzian fits do not capture the asymmetric shape of the QPO.

Being unable to find a satisfactory functional fit to the QPO, we have chosen to characterize it in the following manner. We have measured the location of the PSD dip that occurs before the QPO peak, as well as the location of the QPO peak. (Factoring in noise fluctuations, the QPO is sharp enough from dip to peak that the location of each is likely accurate to better than two unaveraged frequency bins, i.e., 0.015 Hz.) We have also measured the dip and peak PSD amplitudes. As for the fits to the broadband PSD discussed above, there are no obvious trends between QPO parameters and the observed 3–9 keV flux. Furthermore, there is no obvious trend between QPO peak power and frequency, as shown in Figure 5. Although the QPO frequency is characteristically near 0.3 Hz, it is not at a steady frequency and it varies over a range of 0.08 Hz. Peak QPO amplitudes and widths, however, are somewhat less variable. Note that the total rms variability in the region of the QPO typically is $\approx$5%; therefore the QPO amplitude is at most a few percent.

4. COHERENCE AND TIME LAGS

As discussed by Vaughan & Nowak (1997), the coherence function is a measure of the degree of linear correlation between two time series. Specifically, it gives the fraction of the mean-squared variability at a given Fourier frequency in one time series that can be attributed to, or equivalently predicted from, the other. The fact that coherence is often near unity over a wide range of frequencies (see Vaughan & Nowak 1997; Nowak et al. 1999a) is what then makes it meaningful to talk about characteristic Fourier frequency–dependent time delays between two time series (see Miyamoto & Kitamoto 1989; Miyamoto et al. 1992; van der Klis 1989; Nowak et al. 1999a).

The techniques that we used to calculate the coherence and time delays for the GX 339−4 light curves are discussed in Vaughan & Nowak (1997) and Nowak et al. (1999a). For all observations, we have calculated the coherence function,

$$\gamma^2(f) = \frac{|\langle S^*(f)H(f)\rangle|^2}{\langle |S(f)|^2\rangle\langle |H(f)|^2\rangle}, \quad (2)$$

between the FFTs for energy band A [$S(f)$] and the FFTs for the other three energy bands [$H(f)$, angle brackets indicating averages over Fourier frequencies and individual data segments; see Vaughan & Nowak 1997; Nowak et al. 1999a]. For all observations except for observation 5, we have calculated the time delay between energy band A and the other three energy bands. For observation 5, noise limitations allow us only to calculate the time delay between the light curves for energy band D and energy band A. We have averaged over logarithmically spaced frequency bins, ranging over frequencies $f \rightarrow 1.4f$ for all observations.

As shown in Figure 6, the coherence function is near unity from 10^{-3} to $\approx$3 Hz (observation 5) or $\approx$10 Hz (all other observations). Above $\approx$3–10 Hz, there is a noticeable drop in coherence, similar to what we saw with our *RXTE* observations of Cyg X-1 (Nowak et al. 1999a). The Cyg X-1 observations also showed a loss of coherence below $\approx$0.02 Hz; however, the coherence in GX 339−4 remains near unity down to Fourier frequencies as low as $\approx 10^{-3}$ Hz.

We note that the coherence between energy bands A and D shows evidence of an $\approx$0.1 dip near 0.5 Hz (observation 5) and near 2 Hz (all other observations). The evidence for this dip is weak in observation 5 (comparing band A to D, the 0.45 Hz point is 2 σ below unity, and the adjacent 0.64 Hz point is only 1 σ below unity) but is somewhat stronger for observation 7 and the other observations (comparing band A to band D for observation 7, the 1.8 Hz point is >3 σ below unity, and the adjacent 2.5 Hz point is $\approx$2.7 σ below unity). These dip frequencies, however, are approximately the frequencies at which the two broad Lorentzian and power-law fit components (see Fig. 3 and Table 1) overlap. Thus we hypothesize that there are indeed multiple broadband processes occurring in GX 339−4 that are individually coherent but that are incoherent with one another. As with Cygnus X-1, we further hypothesize that the loss of coherence at high frequency is indicative of multiple incoherent processes, possibly "flares" feeding the corona on dynamical timescales (Nowak et al. 1999a, 1999b).

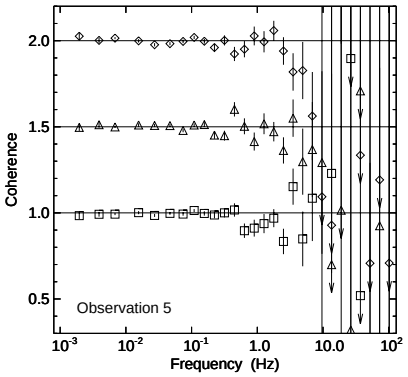

FIG. 6*a*

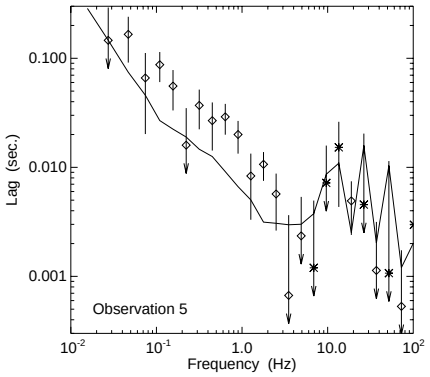

FIG. 6*b*

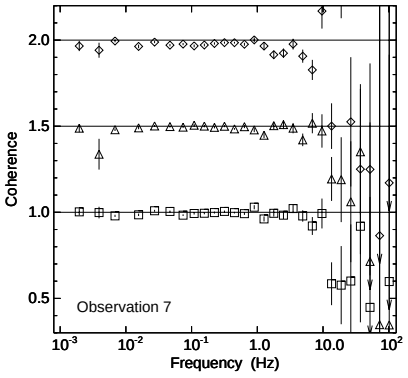

FIG. 6*c*

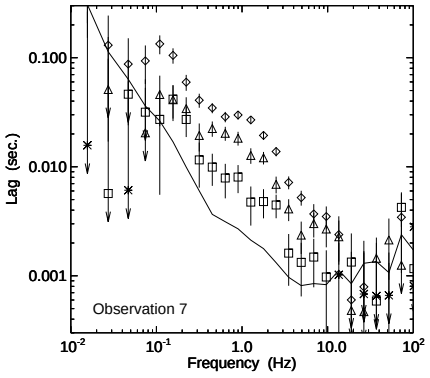

FIG. 6*d*

FIG. 6.—Coherence function and time lags of various energy channels (channel B [*squares*], channel C [*triangles*; coherence offset by 0.5], and channel D [*diamonds*; coherence offset by 1.0]) as compared to energy channel A. (*a*) Coherence for observation 5. Solid lines correspond to unity coherence. (*b*) Time lags for observation 5. Crosses are where the soft variability lags the hard variability. Solid line is the Poisson noise level for channel D time lags. (*c*) Coherence for observation 7. Solid lines correspond to unity coherence. (*d*) Time lags for observation 7. Crosses are where the soft variability lags the hard variability. Solid line is the Poisson noise level for channel D time lags.

In Figure 6 we also show the energy-dependent and Fourier frequency–dependent time delays. The overall structure is very similar to that observed in the hard state of Cyg X-1 (Miyamoto & Kitamoto 1989; Miyamoto et al. 1992; Crary et al. 1999; Nowak et al. 1999a). In the regions not dominated by noise statistics, the hard photon variability always lags the soft photon variability, and the delays decrease with increasing Fourier frequency. The detailed frequency-dependent structure of the delays, however, is more complicated than a simple power law. For example, the time lags between bands A and D for observation 7 show a flattened region near 1 Hz. As for Cyg X-1, there is a large dynamic range in the time delays, with the longest time delays ($\approx$0.1 s) being much longer than typical characteristic timescales of a small corona (see Nowak et al. 1999b). Also as has been observed for Cyg X-1 (Miyamoto & Kitamoto 1989; Miyamoto et al. 1992; Crary et al. 1999; Nowak et al. 1999a), the time delay observed in GX 339−4 is consistent with scaling as the logarithm of the ratio of the two energies being compared. This latter fact has prompted Kazanas, Hua & Titarchuk (1997, hereafter KHT) to suggest that the time delays are related to photon propagation timescales in a very large ($R \approx 10^5 GM/c^2$) corona.

In Figure 7 we show the measured time delay for three Fourier frequencies (0.1, 0.9, and 2.5 Hz) as a function of the measured 3–9 keV flux. The lowest flux observation consistently shows the shortest time delays at nearly all Fourier frequencies. The highest flux observation shows the longest time delays at many Fourier frequencies and shows at least the second longest time delays at nearly all Fourier frequencies. Observations at intermediate fluxes are scattered both positively and negatively about an extrapolation between the low- and high-flux point. It has been previously shown that the time delay decreases in Cyg X-1 as it transits from the hard to soft state (see Cui et al. 1997). Here we present a possible correlation between the magnitude of the time delay and the energy flux for the hard state within a single source. The strong decrease of the time delay for the lowest flux observation is counter to the simplest expectations if the coronal size increases with decreasing flux (see,

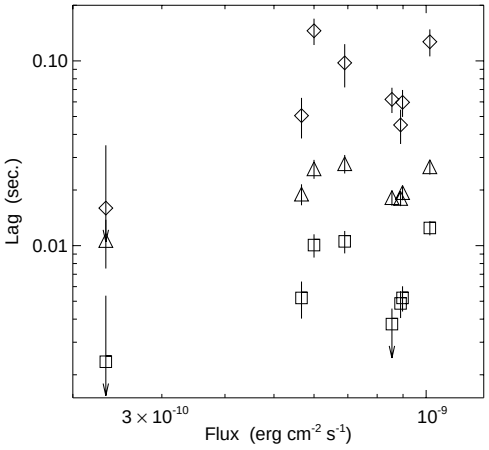

FIG. 7.—Time lags at Fourier frequencies 0.1 Hz (*diamonds*), 0.9 Hz (*triangles*), and 2.5 Hz (*squares*) as a function of measured 3–9 keV flux.

e.g., Esin, McClintock & Narayan 1997), or if characteristic "propagation speeds" in the corona decrease with decreasing luminosity (Nowak et al. 1999b). However, if the coronal size is decreasing with decreasing luminosity, then this observed decrease is understandable in terms of propagation models, whether it be propagation of photons (KHT) or propagation of some sort of other disturbance (Nowak et al. 1999b).

We have found one potential correlation between the measured time lags and the coherence function, related to the vector analogy for the phase lags and coherence function discussed by Nowak et al. (1999a). If we take the Fourier transform of a soft X-ray light curve, $A_s(f)$, and a Fourier transform for the hard X-ray light curve, $A_h(f)$, the cross spectrum is given by $A_s^*(f)A_h(f)$, which can be considered as a vector in the complex plane (see Fig. 8). As discussed by Vaughan & Nowak (1997), the magnitude and angle (corresponding to the phase delay between hard and soft variability) of this vector is well defined if the coherence function is unity.

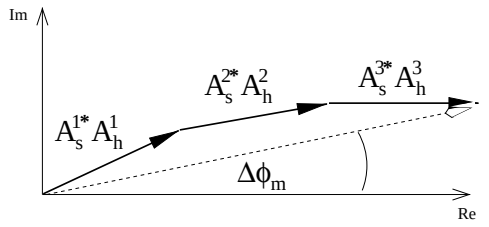

FIG. 8.—Vector analogy for phase lags and coherence. Cross power spectra ($A_s^{1*}A_h^1$, $A_s^{2*}A_h^2$, $A_s^{3*}A_h^3$) can be considered as vectors in the complex plane. The observed phase lag, $\Delta\phi_m$, is the angle of the vector sum of the individual components of the cross power spectrum. The coherence function is the square of the ratio of the magnitude of this sum compared to the magnitude of the sum if all the vectors had the same direction.

If the net observed cross spectrum, however, is made up of the sum of individually coherent processes, it is possible that the net observed coherence will be less than unity. As was noted by Vaughan & Nowak (1997), specifically their equation (10), a sum of individually coherent processes is itself coherent if and only if each process has the same identical transfer function from soft to hard photon variability. In terms of the vector analogy, this is a statement that the vectors representing each process within the sum all lie in the same direction. The coherence function in such a case is the square of the ratio of the magnitude of this sum compared to the magnitude of the sum if all the vectors had the same angle.

Let us consider the following special case of equation (10) from Vaughan & Nowak (1997). Assume that there are multiple input (soft) processes, indexed by i, with Fourier amplitudes $A_s^i(f)$. Let us assume that each of these input processes leads to an output process with Fourier amplitude $A_h^i(f)$ that has a coherent phase delay of $\Delta\phi_i(f)$. (Here we take the Fourier amplitudes to be real quantities.) Finally, assume that the input processes are incoherent with one another, and likewise that the output processes are incoherent with one another. Generalizing equation (10) of Vaughan & Nowak (1997), we find the resulting measured coherence function to be

$$\gamma_m^2(f) \approx \left\{ \sum_i A_s^{i2} A_h^{i2} + \sum_{i \neq j} A_s^i A_h^i A_s^j A_h^j \left[1 - \frac{(\Delta\phi_j - \Delta\phi_i)^2}{2} \right] \right\} ; \times \left(\sum_i A_s^{i2} \sum_j A_h^{i2} \right)^{-1} , \quad (3)$$

where we have adopted a small angle approximation. Under the same assumptions, the net measured phase lag will be given by

$$\Delta\phi_m(f) \approx \frac{\sum_i A_s^i A_h^i \Delta\phi_i}{\sum_i A_s^i A_h^i} . \quad (4)$$

That is, the measured phase lag is simply the weighted mean of the individual phase lags. We illustrate this situation in Figure 8. For such a model as this, the net observed phase delay is related to the net observed coherence function, and both in turn are related to the observed soft and hard PSDs. Fit parameters are the amplitudes (A_s^i, A_h^i) of the individual components of the soft and hard PSDs, and the phase lags ($\Delta\phi_i$) between the soft and hard variability for each of these components.

We have searched for such a connection between the Fourier phase lag and the coherence function by applying equations (3) and (4) to the data. We have assumed that there are three components to the PSD: low- and high-frequency Lorentzian components and a power law, as for the fits presented in Table 1. In the fitting procedure we assumed that all three $\Delta\phi_i(f)$ were independent of Fourier frequency. We refit the PSD data simultaneously while fitting the phase lag and coherence data. We searched for the minimum of the sum of the χ^2 from the four data sets being fit: soft X-ray PSD, hard X-ray PSD, phase lags, and coherence. We fit the PSDs over the same frequency range and with the same frequency binning as in Table 1; however, we fit only the coherence and phase lags over the range $f = 0.2$–4 Hz. This was the frequency range over which the phase lags were least affected by Poisson noise, and it avoided the strong loss of coherence at high fre-

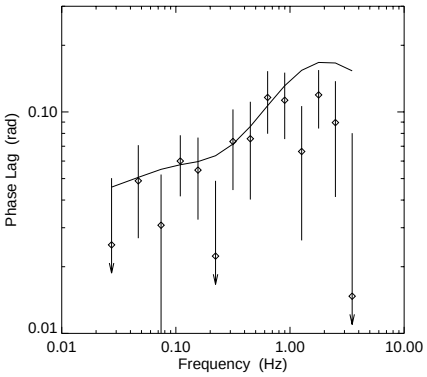

FIG. 9*a*

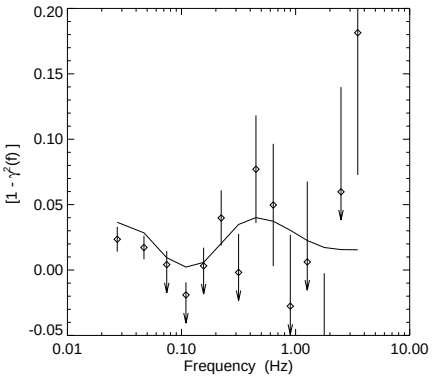

FIG. 9*b*

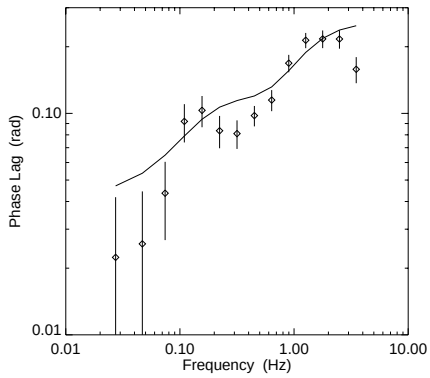

FIG. 9*c*

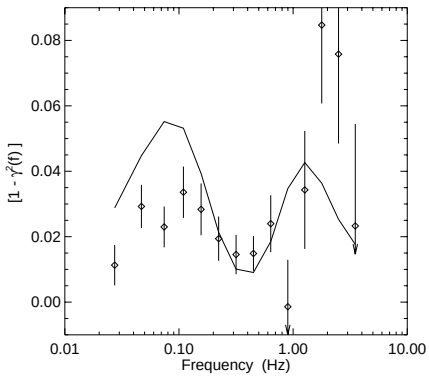

FIG. 9*d*

FIG. 9.—Phase lags between energy bands A and D as a function of Fourier frequency for (*a*) observation 5 and (*c*) observation 7. (All points are hard variability lagging soft variability.) $[1 - \gamma_m^2(f)]$, where $\gamma_m^2(f)$ is the measured, noise-subtracted coherence function between energy bands A and D, for (*b*) observation 5 and (*d*) observation 7. All data has been logarithmically binned over frequencies $f \rightarrow 1.4f$. Solid lines are the best-fit results for fitting equations of the form of eqs. (2) and (3) (see text and Table 2 for further explanation).

quency. These strong high-frequency coherence losses, as we discuss further below, may be due to nonlinear processes rather than to the sum of linear processes (see Vaughan & Nowak 1997). The results for these fits are presented in Figure 9 and in Table 2.

Assuming that the PSD, phase lags, and coherence are the result of summing three independent processes (a power law plus two Lorentzian processes), we see that equations (3) and (4) seem to provide a rough description of the time lag and coherence data. The fits make plausible that there is indeed a deeper underlying connection between the time lag and coherence data. One feature of these fits is notable. Namely, in order to produce coherence drops as large as are seen, one needs to add linear processes with greatly varying intrinsic time lags. In fact, one process, the power law, has nearly no time delay between soft and hard variability, whereas the high-frequency Lorentzian process is seen to require even intrinsically longer time lags than the already very long time lags that are measured.

5. DISCUSSION

Let us consider these results in light of two models: the Comptonization model of KHT and "shot noise" models (see Terrell 1972; Sutherland, Weisskopf & Kahn 1978; Priedhorsky et al. 1979; Miyamoto & Kitamoto 1989; Lochner, Swank & Szymkowiak 1991; Nowak 1994, hereafter N94; Belloni et al. 1997; Poutanen & Fabian 1999, hereafter PF, and references therein). In the former model, a source of white noise is assumed to be present at the center of the system, which is then "filtered" by passage through a Compton corona. The PSD is attenuated on those timescales that are shorter than the characteristic diffusion timescales through the corona. Therefore, the PSD is more attenuated at higher frequencies than at lower frequencies, which leads to the characteristic power-law PSDs that are observed in hard-state BHCs. Time delays are created by the difference in diffusion times through the corona for hard and soft photons. Photons that scatter over large radii will have their intrinsic high-frequency variability wiped out; therefore, any observed high-frequency variability must be due to photons that scattered over short path lengths. High-frequency variability thus exhibits short time delays between hard and soft photon variability. Low-frequency variability potentially can be observed from photons that have scattered over large path lengths, and thus it can exhibit longer time delays between hard and soft variability.

TABLE 2

BEST-FIT FOURIER PHASE LAGS BETWEEN ENERGY CHANNELS A AND D

Observation	$\Delta\phi_{l1}$ (rad)	$\Delta\phi_{pl}$ (rad)	$\Delta\phi_{l2}$ (rad)	χ^2/DoF	χ^2_{red}
1	0.13	0.06	0.49	301.5/119	2.53
2	0.18	0.05	0.26	283.4/119	2.38
3	0.13	0.04	0.28	269.9/119	2.27
4	0.15	0.06	0.66	195.8/119	1.65
5	0.06	0.04	0.25	132.4/113	1.17
6	0.16	0.05	0.38	217.4/119	1.82
7	0.11	0.04	0.27	309.9/119	2.60
8	0.16	0.05	0.41	198.2/119	1.67

NOTES.—Best fit Fourier phase lags between energy channels A and D, where we have used equations of the form of eqs. (2) and (3) and where we have assumed three separate components to the soft and hard X-ray PSD. PSD components are as in Table 1: a low-frequency Lorentzian component ("*l*1"), a power law ("pl"), and a high-frequency Lorentzian component ("*l*2"). PSD data, logarithmically binned over frequencies $f \rightarrow 1.1f$, were included in the fitting process with the resulting fit parameters always being within the error bars shown in Table 1. Phases—$\Delta\phi_{l1}$, $\Delta\phi_{pl}$, $\Delta\phi_{l2}$—are the Fourier phase lags between hard and soft variability for each PSD fit component individually, and positive phase corresponds to hard variability lagging behind soft variability. The phase lags were assumed to be constant as a function of Fourier frequency.

Extremely large coronal sizes of $\mathcal{O}(10^5 GM/c^2)$ are required to produce the longest observed time lags.

In shot noise models the light curve is assumed to be composed of statistically distributed shots of (possibly) varying profiles (see Lochner et al. 1991 for detailed references and applications to Cyg X-1). Shot and distribution parameters are fit to various moments and statistics of the observed light curves. Time delays between hard and soft variability are assumed to be due to differing shot profiles and/or shot distributions in different energy bands (see Miyamoto & Kitamoto 1989; N94; PF). Recently, PF have associated the energy dependent shots with the "energization" of a corona, which was parameterized by a series of equilibrium models where the energy input to the corona was a function of time.

Does the data prefer one model over the other? The detailed structure of the PSD is likely to be more difficult to produce in the KHT model. Although the observed PSD can be modeled as a singly broken power law with an "absorption" feature, it is difficult to imagine a Compton corona configuration that would act as such a "notch filter. It is somewhat easier to imagine, however, two or more preferred shot durations in the distribution of shot timescales. A suitable distribution of shot timescales could easily reproduce the type of PSD fits presented in § 3.

Can the flux dependence of the PSD be reproduced? This depends on whether the coronal radius decreases or increases as the observed flux decreases. The former possibility can be consistent with our "sphere+disk" corona fits to the spectral data (Paper I). The latter is more consistent with the ADAF models to the spectral data (Paper I), as lower luminosity often implies a larger "transition radius" to advective flow. The transition radius in the ADAF models is the radius at which the flow transits from being geometrically thin, optically thick, and radiatively efficient to being geometrically thick, optically thin, and radiatively inefficient. The larger this transition radius, the smaller the overall accretion efficiency (see Narayan 1996; Esin et al. 1997). Lower luminosities can be associated with lower overall efficiencies. The dependence of the coronal radius on observed X-ray luminosity is less constrained for our sphere+disk coronal models (Dove et al. 1997; Paper I). Larger coronae, however, can produce larger observed X-ray fluxes in these models.

In the KHT model, the larger the corona the more attenuated the high-frequency PSD will be. This will cause the PSD to apparently "shift" toward lower frequency. Similarly, shot noise models usually associate the shot timescales with characteristic accretion-flow timescales. What sets these timescales are usually not explicit in shot noise models; however, one expects the timescales to increase for larger coronae, consistent with the expectations of the ADAF models. That is, we expect to see the lower characteristic frequencies associated with the outer accretion flow. Associating a smaller corona with lower luminosity, as can be fitted within the context of sphere+disk corona models, would lead to trends opposite of the observations.

What is the expected relation between the PSD and the observed time lags for these models? If the coronal size decreases with decreasing luminosity, then the KHT model agrees with the observations. The shorter scattering path lengths of a small corona will produce characteristically shorter lags between the hard and soft photon variability. The KHT model also correctly reproduces the observed logarithmic energy dependence of the time lags. However, it is difficult for the KHT model to reconcile the lower frequency PSDs simultaneously with shorter time lags. Predictions for shot noise models are more dependent upon the specifics of each model.

Energy-dependent shots were first suggested by Miyamoto & Kitamoto (1989) as the cause of the hard X-ray variability lags observed in Cyg X-1. This model contained eight input shot profiles (four shot durations in two energy bands) and did not relate the timescales to specific disk physics. The magnitude and frequency dependence of the hard X-ray lags are adjustable by changing the duration of the hard shots relative to the soft shots. In describing observations of the very high state timing properties of GX 339−4, N94 related the shot durations to viscous and thermal instability timescales in an accretion disk. The shots considered in this work were also temperature dependent and became hotter as the shots progressed. This model reproduced the observed energy dependence of the lags, with the exception that it did not reproduce the 1.2–2.3 keV photon variability lagging behind the 2.3–4.6 keV photon variability. As discussed in N94 and Nowak et al. (1997), any shot model in which the characteristic temperature or hardness of the shot smoothly increases as the shot rises will reproduce time lags qualitatively similar to those observed in Cyg X-1 and GX 339−4. In the model of PF, the shot timescales are not related to any specific accretion timescales; however, the time-dependent shot hardness is related to a series of equilibrium Compton coronae models. There is a one-to-one correspondence between the shot amplitude and its hardness in this model. The PF model correctly reproduces the magnitude and energy dependence of the observed time lags.

We expect the following qualitative behavior for the models of both N94 and PF. If we scale the shot duration to

longer timescales, thereby shifting the PSD to lower frequencies, we also expect the time lags to increase, which is contrary to the observations. The only way to have a shot produce a lower frequency PSD and lead to shorter time lags is to alter the spectrum of the shot as well as lengthen its duration. Whereas we do see changes in flux from GX 339−4, we do not see large changes in the best-fit spectral parameters such as optical depth or coronal temperature. The observed energy spectra do not leave much room for varying the spectra of the presumed shots in order to fit both the high-frequency PSD/long time lag data and the low-frequency PSD/short time lag data that are observed. (It is possible, however, for the relative contributions to the spectra from a "steady component" and a "shot component" to vary in such a way that the average spectrum remains relatively unchanged. The rms amplitude of the PSD significantly increases for the faintest observation, and therefore its average spectrum does have a greater contribution from the shots.)

What is the expected coherence function for these various models? Both the KHT model and the PF model produce unity coherence, whereas the model of N94 produces coherence substantially less than unity (Nowak et al. 1997). The KHT model considers only static coronae, whereas the PF model uses the same exact linear Comptonization spectrum for each individual shot. We expect both of these situations to produce unity coherence. The N94 model assumes both a sum of different shot spectra and that each shot represents a nonlinear transfer function from soft to hard variability (Nowak et al. 1997; Vaughan & Nowak 1997).

As in Cyg X-1, GX 339−4 was seen to have near unity coherence over a broad range of frequencies, with a roll-off at $\approx$3–10 Hz. Unlike Cyg X-1 (Nowak et al. 1999a), however, there was no evidence for a loss of coherence below $\approx$0.02 Hz, but there was evidence for a coherence dip near 2 Hz (0.5 Hz for observation 5). At first glance this seems consistent with both the KHT and PF models. We note, however, that the coherence function dips to as low as 0.9. Although still a large coherence value, a dip this low is very difficult to produce by summing different linear transfer functions with different phase delays, if all the hard-to-soft variability phase differences for the individual transfer functions are approximately the same magnitude as the observed phase lags. On the other hand, the nonlinear transfer functions of the N94 model are seen to lead to far stronger losses of coherence, with typical coherence values being $\approx$0.1–0.3 (Nowak et al. 1997). Such coherence values are characteristic of the coherence function observed at high frequency. (We previously have suggested that the observed loss of coherence above $\approx$3–10 Hz may be related to nonlinear effects due to flaring activity feeding a corona on dynamical timescales; Nowak et al. 1999a.)

The question put forth in Vaughan & Nowak (1997) was why observed coherences are so close to unity. With the observations presented here, and in light of the discussion of § 4 and equations (3) and (4), we might wish to modify this question to, "when the coherence function is so close to unity, why is it as low as observed?" We argued in § 4 that if there truly is a relationship between the time lags and the coherence, then there must be a mix of processes with a broad range of time lags. The fits to the phase lag and coherence data suggested one component with near zero lag between hard and soft variability. The fits further suggested that the higher frequency Lorentzian component exhibited characteristically longer time lags (at a fixed Fourier frequency) than the lower frequency Lorentzian component. This possibility was not considered in the models of N94, KHT, or PF. However, as the KHT model postulates only one "transfer function" from soft variability to hard variability (i.e., diffusion through the corona), it is more difficult to reconcile this model with the conjecture that phase lags and coherence are created by a sum of independent processes. Shot noise models, however, can introduce multiple, albeit currently unknown, independent processes in the manner suggested by the fits to the data.

6. SUMMARY

We have presented timing analysis of a series of eight *RXTE* observations of the black hole candidate GX 339−4. On long timescales, there is evidence of a 240 day periodicity in the ASM light curve. This is not a strictly periodic feature but is probably more like a characteristic timescale. Such a timescale is consistent with warping and precession timescales (Pringle 1996; Maloney et al. 1996); however, as we discuss in Paper I, the evidence points more toward coronal size variations than to inclination effects.

In terms of characterizing the short timescale variability, we see that the observations break up into two sets. The seven brightest observations span a range of two in observed 3–9 keV flux and all have comparable timing properties. These observations all show evidence of an $\approx$0.3 Hz QPO. The properties of this QPO are not strictly steady; however, there are no obvious correlations with the flux of the source.

The faintest observation, which is 5 times fainter than the brightest observation, had larger amplitude variability, characteristic PSD frequencies that were a factor of 3 lower than observed for the other PSDs, and shorter time lags between hard and soft variability. This latter feature, albeit with a great deal of scatter about the trend, was also mirrored in the flux dependence of the time lags observed for the brightest observations.

All PSDs were reasonably well fitted by the sum of three fit components: a power law and low- and high-frequency Lorentzian components. We further suggested that the observed Fourier frequency–dependent phase lags and coherence could be explained by summing these three components with differing intrinsic time delays between hard and soft photon variability.

We discussed all these possibilities in light of various theoretical models. The short time delays for the lowest flux observation appear to be more in agreement with "propagation models" (KHT; Nowak et al. 1999b) *if the coronal size decreases with decreasing flux*. If, however, as suggested by ADAF models the coronal (i.e., advection-dominated) region grows with decreasing flux, the trends observed in the time delays are counter to the theory. Conversely, the low-flux/low-frequency PSD observations are more in agreement with the models in which the coronal region grows with decreasing luminosity. Shot noise models are more likely able to be adapted to explain simultaneously the phase lags and coherence as a sum of independent linear components.

None of the models currently address the complicated nonlinear processes that may be occurring on dynamical timescales. Such processes, which could be the "flares" that energize the corona and/or the observed radio-emitting outflow (Fender et al. 1997; Corbel et al. 1998; Hannikain-

nen et al. 1999; Paper I), could be the cause of the strong loss of coherence seen at high frequency in both GX 339−4 and Cyg X-1 (Nowak et al. 1999a), as well as the cause of the "flattening" with increasing photon energy observed at the high-frequency end of the Cyg X-1 PSD (Nowak et al. 1999a).

We would like to acknowledge useful conversations with T. Aldcroft, M. Begelman, R. Fender, P. Maloney, T. DiMatteo, K. Pottschmidt, R. Staubert, and B. Vaughan. This work has been financed by NASA Grants NAG 5-3225, NAG 5-4731, and by a travel grant to J. W. from the DAAD.

REFERENCES

Belloni, T., & Hasinger, G. 1990a, A&A, 227, L33
———. 1990b, A&A, 230, 230
Belloni, T., van der Klis, M., Lewin, W. H. G., van Paradijs, J., Dotani, T., Mitsuda, K., & Miyamoto, S. 1997, A&A, 322, 857
Bendat, J., & Piersol, A. 1986, Random Data: Analysis and Measurement Procedures (New York: Wiley)
Corbel, S., Fender, R. P., Durouchoux, P., Sood, R. K., Tzioumis, A. K., Spencer, R. S., & Campbell-Wilson, D. 1998, in AIP Conf. Proc. 410, Fourth Compton Symposium, ed. C. D. Dermer, M. S. Strickman, & J. D. Kurfess (Woodbury, NY: AIP), 937
Cowley, A. P., et al. 1991, ApJ, 381, 526
Crary, D. J., Finger, M. H., van der Hooft, C. K. F., van Paradijs, J., van der Klis, M., & Lewin, W. H. G. 1999, ApJ, submitted
Cui, W., Zhang, S. N., Focke, W., & Swank, J. H. 1997, ApJ, 484, 383
Davies, S. R. 1990, MNRAS, 244, 93
Dove, J. B., Wilms, J., Maisack, M. G., & Begelman, M. C. 1997, ApJ, 487, 759
Esin, A. A., McClintock, J. E., & Narayan, R. 1997, ApJ, 489, 865
Fender, R. P., Spencer, R. E., Newell, S. J., & Tzioumis, A. K. 1997, MNRAS, 286, L29
Grebenev, S. A., Syunyaev, R., Pavlinsky, M. N., & Dekhanov, I. A. 1991, Soviet Astron. Lett., 17, 413
Hannikainnen, D. C., Hunstead, R. W., Campbell-Wilson, D., & Sood, R. K. 1999, A&A, in press
Horne, J. H., & Baliunas, S. L. 1986, ApJ, 302, 757
Jahoda, K., Swank, J. H., Giles, A. B., Stark, M. J., Strohmayer, T., Zhang, W., & Morgan, E. H. 1996, in EUV, X-Ray, and Gamma-Ray Instrumentation for Astronomy VII, ed. O. H. Siegmund (Bellingham, WA: SPIE), 59
Kazanas, D., Hua, X.-M., & Titarchuk, L. 1997, ApJ, 480, 280 (KHT)
Kemp, J. C., et al. 1983, ApJ, 271, L65
Leahy, D. A., Darbro, W., Elsner, R. F., Weisskopf, M. C., Sutherland, P. G., Kahn, S., & Grindlay, J. 1983, ApJ, 266, 160
Levine, A. M., Bradt, H., Cui, W., Jernigan, J. G., Morgan, E. H., Remillard, R., Shirey, R. E., & Smith, D. A. 1996, ApJ, 469, L33
Lochner, J., & Remillard, R. 1997, ASM Data Products Guide, Version Dated August 27, 1997 (Greenbelt: NASA GSFC)[5]
Lochner, J. C., Swank, J. H., & Szymkowiak, A. E. 1991, ApJ, 376, 295
Lomb, N. R. 1976, Ap&SS, 39, 447
Maloney, P. R., & Begelman, M. C. 1997, ApJ, 491, L43
Maloney, P. R., Begelman, M., & Nowak, M. A. 1998, ApJ, 504, 77
Maloney, P. R., Begelman, M. C., & Pringle, J. E. 1996, ApJ, 472, 582
Méndez, M., & van der Klis, M. 1997, ApJ, 479, 926
Miyamoto, S., Kimura, K., Kitamoto, S., Dotani, T., & Ebisawa, K. 1991, ApJ, 383, 784
Miyamoto, S., & Kitamoto, S. 1989, Nature, 342, 773
Miyamoto, S., Kitamoto, S., Iga, S., Negoro, H., & Terada, K. 1992, ApJ, 391, L21
Narayan, R. 1996, ApJ, 462, 136
Nowak, M. A. 1994, ApJ, 422, 688 (N94)
Nowak, M. A., Vaughan, B. A., Dove, J., & Wilms, J. 1997, in ASP Conf. Proc. 121, Accretion Phenomena and Related Outflows, IAU Colloq. 163, ed. D. Wickramasinghe, L. Ferrario, & G. V. Bicknell (San Francisco: ASP), 366
Nowak, M. A., Vaughan, B. A., Wilms, J., Dove, J., & Begelman, M. C. 1999a, ApJ, 510, 874
Nowak, M. A., Wilms, J., Vaughan, B. A., Dove, J., & Begelman, M. C. 1999b, ApJ, in press
Poutanen, J., & Fabian, A. C. 1999, MNRAS, submitted (PF)
Priedhorsky, W. C., Garmire, G. P., Rothschild, R., Boldt, E., Serlemitsos, P., & Holt, S. 1979, ApJ, 233, 350
Priedhorsky, W. C., Terrell, J., & Holt, S. S. 1983, ApJ, 270, 233
Pringle, J. E. 1996, MNRAS, 281, 357
Remillard, R. A., & Levine, A. M. 1997, in All-Sky X-Ray Observations in the Next Decade, ed. N. Matsuoka, N. Kawai (Tokyo: Riken), 29
Scargle, J. D. 1982, ApJ, 263, 835
Schwarzenberg-Czerny, A. 1989, MNRAS, 241, 153
Sutherland, P. G., Weisskopf, M. C., & Kahn, S. M. 1978, ApJ, 219, 1029
Terrell, N. J. 1972, ApJ, 174, L35
van der Klis, M. 1989, in Timing Neutron Stars, ed. H. Ögelman & E. P. J. van den Heuvel (Dordrecht: Kluwer), 27
Vaughan, B. A., & Nowak, M. A. 1997, ApJ, 474, L43
Wilms, J., Nowak, M. A., Dove, J. B., Fender, R. P., & Di Matteo, T. 1999a, ApJ, submitted (Paper I)
Wilms, J., Nowak, M. A., Dove, J. B., & Heindl, B. 1999b, ApJ, in preparation
Zdziarski, A. A., Poutanen, J., Mikołajewska, J., Gierliński, M., Ebisawa, K., & Johnson, W. N. 1998, MNRAS, 301, 435
Zhang, W., & Jahoda, K. 1996, Deadtime Effects in the PCA, Technical Report, Version Dated 1996 September 26 (Greenbelt: NASA GSFC)
Zhang, W., Jahoda, K., Swank, J. H., Morgan, E. H., & Giles, A. B. 1995, ApJ, 449, 930

[5] The ASM Data Products Guide is available at http://heasarc.gsfc.nasa.gov/docs/xte/asm_products_guide.html.

ANHANG C

A Good Long Look at the Black Hole Candidates LMC X-1 and LMC X-3

M.A. Nowak, J. Wilms, W.A. Heindl, K. Pottschmidt, J.B. Dove, M.C. Begelman

2001

Nachdruck aus

Monthly Notices of the Royal Astronomical Society
Vol. 320, S. 316–326

Mon. Not. R. Astron. Soc. **320**, 316–326 (2001)

A good long look at the black hole candidates LMC X-1 and LMC X-3

M. A. Nowak,[1★] J. Wilms,[2★] W. A. Heindl,[3★] K. Pottschmidt,[2★] J. B. Dove[4,5★] and M. C. Begelman[1,6★]

[1]*JILA, University of Colorado, Campus Box 440, Boulder, CO 80309-0440, USA*
[2]*Institut für Astronomie und Astrophysik, Abt. Astronomie, Waldhäuser Str. 64, D-72076 Tübingen, Germany*
[3]*Center for Astronomy and Space Sciences, University of California at San Diego, La Jolla, CA 92093, USA*
[4]*Center for Astronomy and Space Astrophysics, University of Colorado, Boulder, CO 80309-389, USA*
[5]*Department of Physics, Metropolitan State College of Denver, C. B. 69, PO Box 173362, Denver, CO 80217-3362, USA*
[6]*Department of Astrophysics and Planetary Sciences, University of Colorado, Boulder 80309, USA*

Accepted 2000 August 10. Received 2000 August 10; in original form 2000 January 17

ABSTRACT

LMC X-1 and LMC X-3 are the only known persistent stellar-mass black-hole candidates that have almost always shown spectra that are dominated by a soft, thermal component. We present here results from 170-ks-long *Rossi X-ray Timing Explorer* (*RXTE*) observations of these objects, taken in 1996 December, where their spectra can be described by a disc blackbody plus an additional soft ($\Gamma \sim 2.8$) high-energy power law (detected up to energies of 50 keV in LMC X-3). These observations, as well as archival *Advanced Satellite for Cosmology and Astrophysics* (*ASCA*) observations, constrain any narrow Fe line present in the spectra to have an equivalent width $\lesssim$90 eV. Stronger, broad lines ($\approx$150 eV EW, $\sigma \approx$ 1 keV) are permitted. We also study the variability of LMC X-1. Its X-ray power spectral density (PSD) is approximately proportional to f^{-1} between 10^{-3} and 0.3 Hz with a root-mean-square (rms) variability of $\approx$7 per cent. At energies $>$5 keV, the PSD shows evidence of a break at $f > 0.2$ Hz, possibly indicating an outer disc radius of $\lesssim 1000\,GM/c^2$ in this likely wind-fed system. Furthermore, the coherence function $\gamma^2(f)$, a measure of the degree of linear correlation between variability in the $>$5 keV band and variability in the lower energy bands, is extremely low ($\lesssim$50 per cent). We discuss the implications of these observations for the mechanisms that might be producing the soft and hard X-rays in these systems.

Key words: accretion, accretion discs – black hole physics – binaries: spectroscopic – stars: individual: LMC X-1 – stars: individual: LMC X-3 – X-rays: stars.

1 INTRODUCTION

Since the discovery of Cygnus X-1 in 1964 (Bowyer et al. 1965), the study of galactic black-hole candidates (BHCs) has shown that these objects display a large variety of states which are characterized by their distinct spectral shapes and temporal behaviours. The most important states which have been identified are the 'low/hard state', which is characterized by a hard X-ray spectrum with a photon index $\Gamma = 1.7$ and large root-mean-square (rms) variability $\gtrsim$30 per cent (Tanaka & Lewin 1995; Nowak 1995; and references therein), and the 'high/soft state', which is spectrally softer ($\Gamma \sim 2.5$) and exhibits less variability. The fractional Eddington luminosity of sources in the soft state tends to be higher than that of sources in the hard state (Nowak 1995, and references therein).

The soft state has been observed in steady sources such as LMC X-1 and LMC X-3 (Treviss et al. 1988; Ebisawa, Mitsuda & Inoue 1989; Traviss et al. 1990; Ebisawa, Makino & Mitsuda 1993; Schmidtke, Ponder & Cowley 1999), in recurring transients such as GX 339–4 (Grebenev et al. 1993), and in a number of transients such as Nova Muscae (Miyamoto et al. 1994). The persistent BHC Cygnus X-1 has been observed to switch between the hard and the soft state (albeit with $kT \sim 0.3$ keV for the soft state), with the total X-ray luminosity staying roughly constant (Cui et al. 1997; Zhang et al. 1997).

A great deal of observational attention has been focused on the more commonly observed hard state, since most of the brighter galactic BHCs only occasionally transit to the soft state. Only two of the persistent nearby BHCs, LMC X-1 and LMC X-3, until recently have always been observed in the soft state. Wilms et al. (2001), hereinafter Paper II, present evidence that LMC X-3

★ E-mail: mnowak@rocinante.colorado.edu (MAN); wilms@astro.uni-tuebingen.de (JW); wheindl@mamacass.ucsd.edu (WAH); katja@astro.uni-tuebingen.de (KP); dove@casa.colorado.edu (JBD); mitch@jila.colorado.edu (MCB)

periodically transits into the low/hard state. In this work we present 170-ks long *Rossi X-ray Timing Explorer* (*RXTE*) observations of both LMC X-1 and LMC X-3 during high/soft X-ray states.

LMC X-3 is a highly variable BHC with a probable 9-$M_\odot$ compact object mass (Cowley et al. 1983). Its luminosity has been observed to be as high as 4×10^{38} erg s^{-1}, which is $\approx$30 per cent of its Eddington luminosity, and its soft X-ray flux ($\sim$1–9 keV) is variable by a factor of more than four on long time-scales (see Paper II). LMC X-3 also has exhibited a strong 99- or 198-d periodicity in its soft X-ray flux (Cowley et al. 1991; Cowley et al. 1994), which is also apparent in the ASM monitoring, albeit with a period that varies over time (Paper II). Previously we had suggested that this periodicity might be associated with a warped, precessing accretion disc (Wilms et al. 1999b); however, with the recently observed 'state changes' to a low/hard flux it now seems likely that a systematic variation of the accretion rate is an important part of this long-term variability.

LMC X-1 is also a good candidate for a black hole. Using a large number of *ROSAT* HRI observations, Cowley et al. (1995) were able to identify the counterpart with 'star number 32' of Cowley, Crampton & Hutchings (1978). This object has a mass function of only $f = 0.144\,M_\odot$, but including other evidence the mass of the compact object appears to be $M > 4\,M_\odot$ (Hutchings et al. 1987), and probably $\gtrsim 6\,M_\odot$ (Cowley et al. 1995). The luminosity of the object is typically about 2×10^{38} erg s^{-1} (Long, Helfand & Grabelsky 1981). Although small differences between LMC X-1 and LMC X-3 are apparent, their spectra and short-time temporal behaviours have historically been quite similar. LMC X-1, however, does not exhibit any obvious periodic behaviour in its long-term X-ray light curve.

We have monitored LMC X-1 and LMC X-3 with *RXTE* in three to four weekly intervals since the end of 1996 in order to enable a systematic study of the soft state. The campaign started with 170-ks long observations of both sources, and in this paper we present results from the spectral and temporal analysis of these long observations. In addition, we consider spectral results of archival *Advanced Satellite for Cosmology and Astrophysics* (*ASCA*) observations. Preliminary results of our analyses have already appeared elsewhere (Wilms et al. 1999b; Wilms et al. 1999c). Results from the monitoring observations are presented in Paper II.

The remainder of this paper is structured as follows. We start with a description of our *RXTE* data analysis methodology (Section 2). We then present the results from the spectral analysis from *RXTE* (Section 3) and *ASCA* (Section 4). The *RXTE* timing analysis is discussed in Section 5. We discuss our results in the context of current physical models for the soft state (Section 6) and then summarize the paper (Section 7).

2 *RXTE* DATA ANALYSIS METHODS

Onboard *RXTE* are two pointed instruments, the Proportional Counter Array (PCA) and the High-Energy X-ray Timing Experiment (HEXTE), as well as the all-sky monitor (ASM). We used the standard *RXTE* data analysis software, FTOOLS 4.2. Spectral modelling was performed mostly with XSPEC, version 10.00z (Arnaud 1996). We used essentially the same data extraction and analysis strategy as in our analyses of *RXTE* data from GX 339–4 and V1408 Aql (4U1957+11); therefore, we only present a brief summary of this strategy. For detailed information we refer the reader to Wilms et al. (1999a) and Nowak & Wilms (1999).

Table 1. Observing log for the long RXTE observation of LMC X-3.

Obs.	Date (JD−2 450 000)	Date (y.m.d, time)	Exposure (s)	Count rate (counts s^{-1})
a	417.905	1996.11.30, 09:43	13800	399.3 ± 0.2
b	418.238	1996.11.30, 17:42	10200	412.9 ± 0.2
c	419.843	1996.12.02, 08:14	14000	422.3 ± 0.2
d	420.168	1996.12.02, 16:02	12700	411.3 ± 0.2
e	421.818	1996.12.04, 07:38	12400	369.9 ± 0.2
f	422.100	1996.12.04, 14:25	11300	388.8 ± 0.2
g	422.374	1996.12.04, 20:58	5500	384.2 ± 0.3
h	422.660	1996.12.05, 03:50	16900	374.2 ± 0.2
i	422.960	1996.12.05, 11:02	11300	334.9 ± 0.2
j	423.238	1996.12.05, 17:42	16400	395.0 ± 0.2
k	423.502	1996.12.06, 00:02	15200	392.2 ± 0.2

Exposure times shown are rounded to the closest 100 s. The count rate is the total PCA background-subtracted count rate.

The PCA consists of five co-aligned xenon (with an upper propane layer) proportional counter units (PCUs) with a total effective area of about 6500 cm^2. The instrument is sensitive in the energy range from 2 to $\sim$100 keV (Jahoda et al. 1996), although the response matrix is best calibrated in the energy range $\approx$2.5–30 keV. We chose to increase the signal-to-noise ratio of our data by analysing top xenon layer data only. Background subtraction of the PCA data was performed analogously to our previous study of Cyg X-1 (Dove, Wilms & Nowak 1998). To reduce the uncertainty of the PCA background model, we ignored data measured in the 30 min after South Atlantic Anomaly (SAA) passages. The XSPEC 'corrfile' facility was used to renormalize the background file for all observations, typically by 1–2 per cent.

For short ($\lesssim$10-ks) segments of observations, we assumed the uncertainty of the data to be purely from a Poisson distribution. For analysis of the full ($>$100-ks) observations, we accounted for the remaining detector calibration uncertainty by using the energy dependent systematic errors described by Wilms et al. (1999a).

HEXTE consists of two clusters of four NaI/CsI-phoswich scintillation counters that are sensitive from 15 to 250 keV. A full description of the instrument is given by Rothschild et al. (1998). Background subtraction is done by source–background switching. We used the standard HEXTE response matrices of 1999 August, and considered data measured above 20 keV.

3 RXTE SPECTRAL ANALYSIS

3.1 LMC X-3

RXTE observed LMC X-3 during three observing blocks on 1996 November 30, 1996 December 2 and 1996 December 4 and 5. A log of the observations can be found in Table 1. During part of the observations, some detectors were turned off; however, we added all good data together and combined all background models. The total response matrix was the average of the respective estimates for each individual detector combination, weighted by the fraction of photons measured during the time that such a combination was active.

The light curve of LMC X-3 during the long observation is displayed in Fig. 1. During the first part of the observation the source is characterized by a slight increase of the PCA count rate from $\sim$80 to $\sim$85 cps per PCU. The source was at a relatively

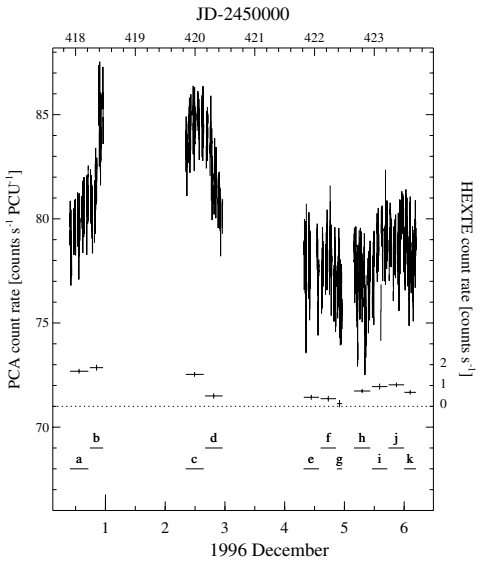

Figure 1. Background-subtracted *RXTE* PCA light curve of LMC X-3, rebinned to a resolution of 64 s (left *y*-axis), and total background-subtracted HEXTE count rate (sum of HEXTE clusters A and B; right *y*-axis). The dashes indicate the individual observations of Table 1.

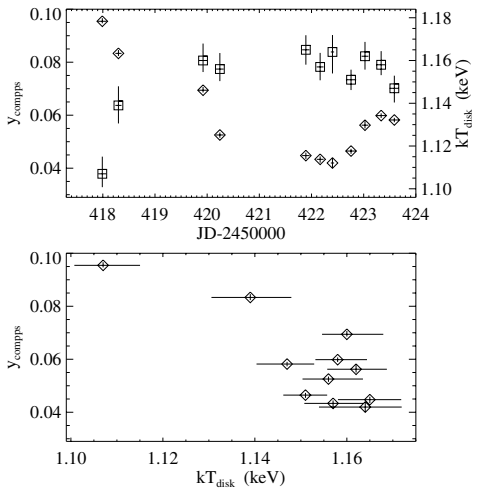

Figure 2. *Top:* Observed spectrum and disc blackbody plus power-law plus broad Fe-line model fit to the long observation of LMC X-3. Dashed lines show the individual model components folded through the detector response. *Middle:* Residuals in units of σ between the data and the model, with a narrow Fe line. *Bottom:* Residuals for the best-fit model, including a very broad Fe line. (Residuals for the COMPPS model are virtually identical.)

steady level of $\sim$77 count s^{-1} per PCU during the last part of the observations. This variation was also observed in the HEXTE (Fig. 1). To see whether this variation was also detectable spectroscopically, we first analysed separately the observations indicated in Table 1. For this analysis, we ignored data below PCA channel 7 and above PCA channel 50, which corresponds to an energy bandpass of 3.6–20 keV. (Here and throughout our spectral discussions, PCA channel number refers to the 'standard_2f' channels, 1–129, as read by XSPEC.)

We first modelled the spectrum via the standard multi-temperature disc blackbody (Mitsuda et al. 1984) plus a power-law component. We modelled absorption in the intervening interstellar medium by fixing the equivalent hydrogen column to the value found from radio observations $N_{\rm H} = 3.2 \times 10^{20}\,{\rm cm}^{-2}$ (Staveley-Smith, private communication), and by using the cross sections of Bałucińska-Church & McCammon (1992). Our preliminary fits to this model had strong residuals in the region around $\sim$6.5 keV (Fig. 2, middle). We therefore included a narrow emission line at 6.4 keV. We will return to the issue of the reality of this line feature below. Table 2 lists the parameters of the best-fit models.

The characteristic temperature of the phenomenological accretion disc component, $kT_{\rm in}$, can be determined to high accuracy (see also Paper II). The formal uncertainty of the values for $kT_{\rm in}$ presented in Table 2 are typically smaller than 0.005 keV. This rather small formal uncertainty value might indicate that the systematic uncertainty of the response matrix needs to be taken into account even for these short observations. These systematic uncertainties, however, are of roughly the same magnitude as the Poisson errors used in our analysis. This fact makes a formal error analysis rather difficult, and it is not clear whether the parameter error analysis methods of Lampton, Margon & Bowyer (1976) yield meaningful results in such a case.

During the week over which the observations were performed, $kT_{\rm in}$ remained more stable than the other fit parameters, although these other parameters had relatively weak variations. It has been observed that on much longer time-scales (months to years) variations of LMC X-3 are correlated predominantly with strong variations of $kT_{\rm in}$, while the phenomenological disc normalization, $A_{\rm disc}$, remains relatively constant (Paper II; Ebisawa et al. 1993). In the literal interpretation of the multi-temperature disc blackbody, $A_{\rm disc} \propto r_{\rm in}^2 \cos i$, where $r_{\rm in}$ is the inner radius of the accretion disc and i is its inclination. The stability of $A_{\rm disc}$ thus has been interpreted as evidence that the inner radius of the accretion disc stays remarkably constant on long-time-scales (Ebisawa et al. 1993). As discussed by Merloni, Fabian & Ross (1999), however, this is not necessarily true for a more physical disc model that accounts for radiative transfer effects, Doppler blurring and gravitational redshifting. For example, a model wherein only the accretion rate and not the inner disc radius varies formally can be fitted with a disc blackbody with varying $A_{\rm disc}$ (Merloni et al. 1999).

As a more physically motivated description, we have also fitted the Compton scattering model of Poutanen & Svensson (1996) (COMPPS). Specifically, we simulate a disc blackbody Compton upscattered via a slab geometry corona with fixed unity covering fraction over the disc. A purely thermal coronal electron distribution was assumed, and the width of the Fe line was fixed to be $\sigma \sim 1.4$ keV (see below). We then fitted the peak temperature of the disc blackbody, as well as the electron temperature and Compton y-parameter of the corona. Results are presented in Table 1 and in Fig. 3. Here the peak temperature of the disc is seen to vary more strongly over the course of the observation than for the multi-temperature blackbody plus power-law models. The variations in the light curve are consistent with being predominantly

Table 2. Results of spectral fitting to the LMC X-3 data.

Obs.	$kT_{\rm in}$ (keV)	$A_{\rm disc}$	$A_{\rm compps}$ $\times10^{-2}$	Γ	$A_{\rm PL}$ $\times10^{-1}$	$kT_{\rm e}$ (keV)	$y_{\rm compps}$ $\times10^{-2}$	$A_{\rm Line}$ $\times10^{-4}$	EW (eV)	χ^2/dof
total	$1.24^{+0.00}_{-0.01}$	$33.6^{+0.9}_{-0.9}$	…	$2.0^{+0.1}_{-0.2}$	$2.4^{+1.1}_{-0.8}$	…	…	$0.6^{+0.5}_{-0.6}$	10	50.4/47
total[a]	$1.20^{+0.01}_{-0.02}$	$37.3^{+1.8}_{-1.4}$	…	$2.6^{+0.2}_{-0.3}$	$1.2^{+0.7}_{-0.6}$	…	…	$8.1^{+3.5}_{-3.8}$	134	37.8/46
a	$1.23^{+0.00}_{-0.00}$	$25.6^{+0.6}_{-0.6}$	…	$2.9^{+0.0}_{-0.0}$	$4.8^{+0.4}_{-0.3}$	…	…	$14.1^{+2.9}_{-3.7}$	22	68.1/39
b	$1.24^{+0.00}_{-0.00}$	$28.2^{+0.6}_{-0.7}$	…	$2.9^{+0.0}_{-0.0}$	$3.7^{+0.4}_{-0.4}$	…	…	$1.6^{+0.4}_{-0.4}$	24	66.6/39
c	$1.25^{+0.00}_{-0.00}$	$29.9^{+0.6}_{-0.6}$	…	$3.0^{+0.0}_{-0.0}$	$3.8^{+0.4}_{-0.4}$	…	…	$2.0^{+0.3}_{-0.3}$	30	99.6/39
d	$1.25^{+0.00}_{-0.00}$	$29.7^{+0.6}_{-0.5}$	…	$3.3^{+0.1}_{-0.1}$	$5.0^{+0.6}_{-0.6}$	…	…	$1.8^{+0.4}_{-0.3}$	28	61.8/39
e	$1.24^{+0.00}_{-0.00}$	$30.5^{+0.6}_{-0.5}$	…	$3.4^{+0.1}_{-0.1}$	$4.6^{+0.7}_{-0.6}$	…	…	$1.9^{+0.3}_{-0.4}$	32	68.6/39
f	$1.24^{+0.00}_{-0.00}$	$30.9^{+0.6}_{-0.6}$	…	$3.4^{+0.1}_{-0.1}$	$4.4^{+0.7}_{-0.6}$	…	…	$1.5^{+0.3}_{-0.4}$	25	59.3/39
g	$1.24^{+0.01}_{-0.01}$	$30.5^{+0.8}_{-0.5}$	…	$3.4^{+0.1}_{-0.1}$	$4.4^{+1.1}_{-0.9}$	…	…	$1.6^{+0.5}_{-0.5}$	28	43.5/39
h	$1.23^{+0.00}_{-0.00}$	$30.8^{+0.5}_{-0.6}$	…	$3.3^{+0.1}_{-0.1}$	$4.0^{+0.5}_{-0.5}$	…	…	$1.4^{+0.3}_{-0.3}$	23	128/39
i	$1.23^{+0.00}_{-0.00}$	$30.8^{+0.7}_{-0.7}$	…	$3.1^{+0.1}_{-0.1}$	$3.3^{+0.6}_{-0.5}$	…	…	$1.9^{+0.3}_{-0.4}$	30	54.5/39
j	$1.24^{+0.00}_{-0.00}$	$29.7^{+0.5}_{-0.5}$	…	$3.1^{+0.0}_{-0.1}$	$4.1^{+0.4}_{-0.4}$	…	…	$1.9^{+0.3}_{-0.3}$	31	63.7/39
k	$1.24^{+0.00}_{-0.00}$	$28.8^{+0.5}_{-0.6}$	…	$3.2^{+0.0}_{-0.1}$	$4.8^{+0.5}_{-0.5}$	…	…	$1.4^{+0.3}_{-0.3}$	23	123/39
total[b]	$1.16^{+0.04}_{-0.02}$	…	$2.5^{+0.2}_{-1.1}$	…	…	62^{+34}_{-12}	$6.1^{+0.1}_{-0.2}$	$10.1^{+3.6}_{-4.6}$	170	39.5/46
a	$1.11^{+0.01}_{-0.01}$	…	$5.6^{+0.4}_{-0.1}$	…	…	46^{+5}_{-3}	$9.5^{+0.1}_{-0.0}$	$13.8^{+1.4}_{-1.4}$	230	57.2/39
b	$1.14^{+0.01}_{-0.01}$	…	$4.6^{+0.6}_{-0.7}$	…	…	48^{+8}_{-5}	$8.3^{+0.2}_{-0.1}$	$13.5^{+1.7}_{-1.7}$	213	46.4/39
c	$1.16^{+0.01}_{-0.01}$	…	$2.8^{+0.4}_{-0.2}$	…	…	64^{+14}_{-6}	$6.9^{+0.2}_{-0.1}$	$14.6^{+1.5}_{-1.5}$	228	88.7/39
d	$1.16^{+0.00}_{-0.00}$	…	$3.3^{+0.1}_{-0.4}$	…	…	43^{+14}_{-5}	$5.3^{+0.1}_{-0.2}$	$13.7^{+1.6}_{-1.5}$	223	71.7/39
e	$1.17^{+0.00}_{-0.01}$	…	$1.3^{+0.3}_{-0.5}$	…	…	84^{+35}_{-15}	$4.5^{+0.1}_{-0.2}$	$13.1^{+1.5}_{-1.6}$	228	80.8/39
f	$1.16^{+0.00}_{-0.00}$	…	$2.9^{+0.1}_{-0.5}$	…	…	40^{+11}_{-5}	$4.3^{+0.1}_{-0.1}$	$11.0^{+1.6}_{-2.2}$	190	67.9/39
g	$1.16^{+0.01}_{-0.01}$	…	$2.1^{+0.3}_{-1.0}$	…	…	50^{+20}_{-10}	$4.2^{+0.2}_{-0.2}$	$10.8^{+3.0}_{-2.2}$	190	57.3/39
h	$1.15^{+0.01}_{-0.00}$	…	$2.8^{+0.0}_{-0.4}$	…	…	44^{+11}_{-4}	$4.6^{+0.1}_{-0.1}$	$11.4^{+1.3}_{-1.3}$	202	113/39
i	$1.16^{+0.01}_{-0.01}$	…	$1.5^{+0.0}_{-0.1}$	…	…	89^{+30}_{-12}	$5.6^{+0.2}_{-0.1}$	$12.2^{+1.7}_{-1.7}$	213	68.8/39
j	$1.16^{+0.00}_{-0.01}$	…	$2.4^{+0.2}_{-0.1}$	…	…	6.4^{+15}_{-6}	$6.0^{+0.1}_{-0.1}$	$12.4^{+1.3}_{-1.4}$	209	80.1/39
k	$1.15^{+0.01}_{-0.00}$	…	$3.1^{+0.2}_{-0.1}$	…	…	50^{+8}_{-6}	$5.8^{+0.1}_{-0.1}$	$12.2^{+1.3}_{-1.2}$	210	130/39

$T_{\rm in}$, $A_{\rm disc}$: Peak multi-temperature disc temperature and normalization. Γ: Photon index of the power law. $A_{\rm PL}$: Power-law normalization (photons $\rm keV^{-1}\,cm^{-2}\,s^{-1}$ at 1 keV). $A_{\rm compps}$: Normalization of COMPPS model. $kT_{\rm e}$: Coronal electron temperature for the COMPPS model. $y_{\rm compps}$: Compton y-parameter for the COMPPS model. $A_{\rm Line}$: Line normalization (photons $\rm cm^{-2}\,s^{-1}$ in the line).
The Gaussian line was fixed at 6.4 keV with a width of $\sigma = 0.1$ keV for the multi-temperature disc plus blackbody models, or $\sigma = 1.4$ keV for the COMPPS models. EW: Line equivalent width. Uncertainties are at the 90 per cent confidence level for one interesting parameter ($\Delta\chi^2 = 2.71$). The interstellar equivalent column was fixed at $N_{\rm H} = 3.2 \times 10^{20}\ \rm cm^{-2}$.
[a] Parameters for a broad Fe line with $\sigma = 1.4^{+0.2}_{-0.2}$ keV.
[b] Parameters for a broad line with $\sigma = 1.4^{+0.2}_{-0.1}$.

driven by variations of the Compton y-parameter, with the large count rate change from observations a to e corresponding to a drop in y. The slight increase in count rate seen in observations h–k corresponds to a slight increase in y. There is a tendency for the peak disc temperature and Compton y-parameter to be anti-correlated; however, this anti-correlation is dominated by observations a and b.

Note that the light curves cover approximately three, 1.7 d orbital periods of LMC X-3. Recent work with these (now archived) *RXTE* observations, along with more recent long-term pointings, reveal evidence for a weak (few per cent) orbital modulation of the X-ray source if one folds the light curves on the known orbital period (Boyd & Smale, in preparation). Such variations would not be unexpected as previous observations have suggested a near edge-on system to account for the ellipticity of the optical light curve (van der Klis et al. 1983). The nature of these variations, possibly due to weak scattering, will be discussed further by Boyd & Smale (in preparation).

We now consider fits to the summed spectrum from the long observation. Taking PCA channels 7 to 58 (≈3.6–26 keV), we again fitted two models: a disc blackbody plus power-law plus Gaussian line, and a COMPPS model plus Gaussian line. The best-fitting disc blackbody plus power-law models are shown in Fig. 2. For both classes of models, we formally required a broad Fe line component with equivalent width ≳150 eV with widths of $\sigma \approx$ 1.4 keV (Table 2). This is approximately twice the PCA spectral resolution. Despite the low reduced χ^2, we do not consider such a strong line to have been detected definitively in LMC X-3 as there is some concern about systematic errors in both the PCA response and the spectral model.

Excluding the line, residuals in the line region are ∼1 per cent, similar to the systematic uncertainties in the PCA response. In addition, for the models that we have fitted, energy channels ≲6 keV are dominated by the disc component, whereas energies ≳10 keV are dominated by the power-law/Comptonized component. The crossover region corresponds to the Fe line region (see Fig. 2). Thus the line strength is especially sensitive to any errors in modelling the continuum spectral shape, such as, e.g., the approximation made by the disc blackbody plus power-law model, where the Comptonized spectrum is represented by a pure power law even at energies where the Comptonized photons have energies comparable with the seed photon energy. This is in contrast to AGN, for example, where the continuum through the line/edge region is thought to be reasonably well-approximated by a featureless power law, and therefore is not subject to systematic uncertainties in the continuum model.

For the case of AGN, the reality of the line can also be verified (independently of response matrix uncertainties) by taking the ratio of the (nearly power-law) observed spectrum to that of the power-law spectrum of the Crab nebula. In principle, a similar procedure could also be used in the case of LMC X-3. Simulating a COMPPS spectrum both with and without a line, utilizing the fitted parameters for LMC X-3 discussed above, shows that a division of these two spectra would reveal the presence of a line. There exists no template spectrum, however, with which to do this comparison. We caution, therefore, that the LMC X-3 line in reality may be weaker and/or narrower than that obtained here.

The Comptonization model implies a coronal temperature of $\approx$60 keV, and a Compton y-parameter of $y \equiv 4kT_{\rm es}/mc^2\ \tau_{\rm es} \approx 0.06$, which implies an optical depth of $\tau_{\rm es} \approx 0.1$. Owing to the limited energy range of our observations, however, these fits are not unique. We assumed a purely thermal electron distribution, but we note that a purely non-thermal Comptonizing electron distribution fits the data equally well. Data at energies significantly higher than 50 keV are required to break this degeneracy.

As regards the power-law component, when considering the HEXTE data as well, we detect the source out to $\approx$50 keV, the highest energy at which this source has ever been detected. The HEXTE data, however, do not place much stronger constraints than were obtained with the PCA data alone. Including the HEXTE data, the observed power law is $\Gamma = 2.8^{+0.1}_{-0.2}$. We do not detect any noticeable curvature in the spectrum, but our limits on the presence of such curvature are weak.

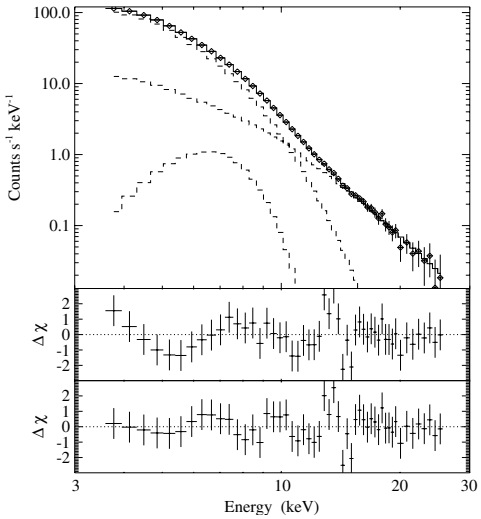

Figure 3. *Top:* Peak disc temperature and Compton y-parameter as a function time for the observations of LMC X-3 presented in Table 1. *Bottom:* Peak disc temperature versus Compton y-parameter.

3.2 LMC X-1

Historically, LMC X-1 has shown relatively little long-time-scale variability (Syunyaev et al. 1990; see also Paper II). Consistent with this, LMC X-1 showed no obvious variations on day-long time-scales during the long *RXTE* observation of 1996 December 6 to 8. The combined spectrum is a typical example of the spectrum of LMC X-1 (see Paper II). Taking our screening criteria into account, we obtained 80 ks of data with 5 PCU on, and another 30 ks of data wherein there were 3 or 4 PCU on. Again, these data have been added together as for LMC X-3. This resulted in a detection of LMC X-1 out to 20 keV in the PCA. In HEXTE, LMC X-1 is detectable out to the same energy, but, owing to its low count rate (the total HEXTE count rate is $\lesssim$1 count s^{-1}), no spectral information can be obtained.

We modelled the data (PCA channels 7 to 52, $\approx$3.6–22 keV) with the same spectral models as for LMC X-3, using an equivalent hydrogen column of $N_{\rm H} = 7.2 \times 10^{21}$ cm^{-2} (Staveley-Smith, private communication), taken from 21-cm measurements. Again, the data required the presence of an iron line at 6.4 keV. The resulting best-fit parameters, with a narrow and with a broad iron line, are shown in Table 3. In Fig. 4, we display the residuals of the disc blackbody fits, showing the improvement of assuming a broad iron line. As for LMC X-3, without a broad line the relative deviation between the data and the model in the line region is $\approx$1 per cent. Again, the line region corresponds to the transition region between the disc blackbody and power-law/Comptonized emission components of the spectrum, so caution is warranted in interpreting the fit parameters of the line.

Our spectral parameter values are in general agreement with earlier data (Ebisawa et al. 1989; Schlegel et al. 1994), although our power-law index appears to be rather soft compared with the earlier measurements. As we show in Fig. 4, the soft ($\Gamma \sim 3$) power-law component dominates the observed flux above $\sim$7 keV, but also contributes an appreciable fraction of the total soft flux. Thus the lower energy channels are also in part determining the value of the fitted spectral index. In terms of the COMPPS Comptonization model, if we choose a purely thermal, slab-geometry corona with unity covering factor, we find similar coronal parameters as for LMC X-3; however, the disc temperature is somewhat lower so the observed spectrum is more dominated by Comptonized photons than that for LMC X-3. Again, purely non-thermal models are also permitted, indicating that the coronal geometry and parameters are not uniquely determined by these data.

Table 3. Results of spectral fitting to the LMC X-1 data.

$kT_{\rm in}$ (keV)	$A_{\rm disc}$	$A_{\rm compps}$ $\times 10^{-2}$	Γ	$A_{\rm PL}$ $\times 10^{-1}$	$kT_{\rm e}$ (keV)	$y_{\rm compps}$ $\times 10^{-2}$	σ (keV)	$A_{\rm Line}$ $\times 10^{-5}$	EW (eV)	χ^2/dof
$0.91^{+0.01}_{-0.01}$	$58.0^{+3.1}_{-3.0}$	…	$3.1^{+0.1}_{-0.1}$	$2.1^{+0.6}_{-0.6}$	…	…	*0.1*	7^{+4}_{-5}	38	71.8/41
$0.88^{+0.01}_{-0.01}$	$76.3^{+3.7}_{-6.0}$	…	$2.9^{+0.1}_{-0.1}$	$1.5^{+0.4}_{-0.5}$	…	…	$0.98^{+0.19}_{-0.15}$	32^{+10}_{-10}	195	46.4/40
$0.86^{+0.02}_{-0.02}$	…	$1.9^{+0.0}_{-0.3}$	…	…	68^{+7}_{-8}	$4.4^{+0.1}_{-0.3}$	$0.97^{+0.18}_{-0.14}$	33^{+10}_{-9}	207	48.5/40

See Table 2 for an explanation of the symbols. The interstellar equivalent column was fixed at $N_{\rm H} = 7.2 \times 10^{21}$ cm^{-2}. Parameters typeset in italics were frozen at the indicated value. Errors are at the 90 per cent confidence level for one interesting parameter ($\Delta\chi^2 = 2.71$).

Since our observations cover a larger energy range than many previous missions, they ensure that our best-fit models at least describe the spectral shape quite well. In accordance with Schlegel et al. (1994), we do not find evidence for a broad iron edge feature in the data. Such a feature might be artificially introduced in the data for instruments where the upper energy boundary is so low that the power-law index cannot be well constrained.

4 ARCHIVAL *ASCA* DATA

The High Energy Astrophysics Archive (HEASARC) contains one *ASCA* observation of LMC X-1 (1995 April 2) and two observations of LMC X-3 (1993 September 23, 1995 April 15). To the best of our knowledge, these observations have not been published previously. We extracted the data from all four instruments on *ASCA*, the two solid-state detectors (SIS0 and SIS1) and the two GIS detectors (GIS2 and GIS3); however, here we only discuss the SIS data, as the SIS has a more reliable low energy response and a better spectral resolution.

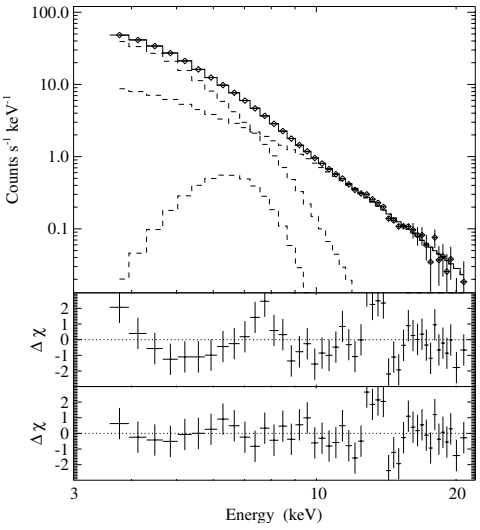

Figure 4. Same as Fig. 2 for the long observation of LMC X-1.

We used the SISCLEAN tools (Day et al. 1998), with the default values, to remove hot and flickering pixels. Furthermore, we filtered the data with the same cleaning criteria outlined by Brandt et al. (1996); however, we took the more conservative values of 10° for the minimum elevation angle and 7 GeV/c for the rigidity. We obtained background estimates by extracting source-free regions near the edges of the SIS chips. The spectra were rebinned so that each energy bin contained a minimum of 20 photons, and we only fitted SIS data in the 0.5 to 10 keV range. Cross-calibration uncertainties between the two SIS detectors were accounted for by introducing multiplicative constants (always found to be within $\lesssim$1 per cent of each other) for each detector in all fits.

Neutral hydrogen absorption of a disc blackbody spectrum (Mitsuda et al. 1984) provides a rough description of the *ASCA* data. Such models yielded reduced χ^2 values $\gtrsim$2 for LMC X-1 and $\approx$1 for LMC X-3. All three observations, however, exhibited evidence of excess emission at energies $\gtrsim$5 keV. Adding a power law (photon flux $\propto E^{-\Gamma}$, with $\Gamma \approx 2.2$–2.5) improved the reduced χ^2 to $\approx$1.1 and $\approx$0.7 for LMC X-1 and LMC X-3, respectively. As for the *RXTE* observations, we also were able to fit the COMPPS model; however, given that the *ASCA* data cuts off at 10 keV, there was not enough leverage to fit both kT_e and y_{compps}. We therefore froze the coronal electron temperature to 50 keV for all three observations. Results for these fits are presented in Table 4 and Fig. 5.

Both LMC X-3 observations are at very low flux values. We compared the 3–9 keV flux values from these observations with those obtained from our *RXTE* monitoring observations in Paper II. Using an SIS/PCA normalization ratio of 0.7, we estimate that the *ASCA* observations would correspond to ASM count rates of $\sim$1.3 and $\sim$0.6 cps. As discussed in Paper II, these low count rates occur near transitions from the soft to the hard state of LMC X-3. We note that the lower flux *ASCA* observation of LMC X-3 shows a significant drop in peak disc temperature, consistent with the trends seen in the state transitions discussed in Paper II.

Our main purpose for examining the *ASCA* data is to determine if there is evidence for an Fe line in the spectrum and an Fe–L complex near energies of $\approx$1 keV. Line features near 1 keV are a common occurrence in photoionized plasmas close to sources emitting hard X-rays (e.g. in eclipse in Vela X-1, Nagase et al. 1994). We would also expect such features in models of warped accretion discs with winds, similar to those of Schandl (1996), or in models of wind-driven limit cycles (Shields et al. 1986), as might be relevant for producing the long-term periodicity of LMC X-3 (Paper II). Such a line complex was also seen in the spectrally

Table 4. Results of fitting the LMC X-1 and LMC X-3 *ASCA* data.

Source	N_H ($\times10^{22}$ cm^{-2})	kT_e (keV)	A_{compps} $\times10^{-2}$	y_{compps} $\times10^{-2}$	kT_{ray} (keV)	A_{ray} $\times10^{-2}$	χ^2/dof
LMC X-1	$0.63^{+0.01}_{-0.01}$	$0.75^{+0.00}_{-0.01}$	$6.2^{+0.0}_{-0.0}$	$10.1^{+0.1}_{-0.4}$	…	…	498/464
(1995 Apr. 12)	*0.72*	$0.67^{+0.01}_{-0.01}$	$8.7^{+0.2}_{-0.3}$	$12.2^{+0.3}_{-0.3}$	…	…	924/465
	0.72	$0.71^{+0.01}_{-0.00}$	$7.2^{+0.2}_{-0.3}$	$10.9^{+0.4}_{-0.4}$	$0.82^{+0.02}_{-0.03}$	$2.5^{+0.2}_{-0.3}$	523/463
LMC X-3 (1995 Apr. 15)	$0.06^{+0.01}_{-0.00}$	$0.83^{+0.01}_{-0.00}$	$2.7^{+0.3}_{-0.0}$	$11.2^{+0.6}_{-0.5}$	…	…	295/429
LMC X-3 (1993 Sep. 23)	$0.03^{+0.00}_{-0.01}$	$0.70^{+0.01}_{-0.01}$	$2.0^{+0.3}_{-0.2}$	$11.9^{+1.1}_{-1.0}$	…	…	231/414

See Table 2 for an explanation of the symbols. kT_{ray}, A_{ray} are the temperature and normalization of the Raymond–Smith plasma component (Raymond & Smith 1977). Parameters typeset in italics were frozen at the indicated value. Errors are at the 90 per cent confidence level for one interesting parameter ($\Delta\chi^2 = 2.71$).

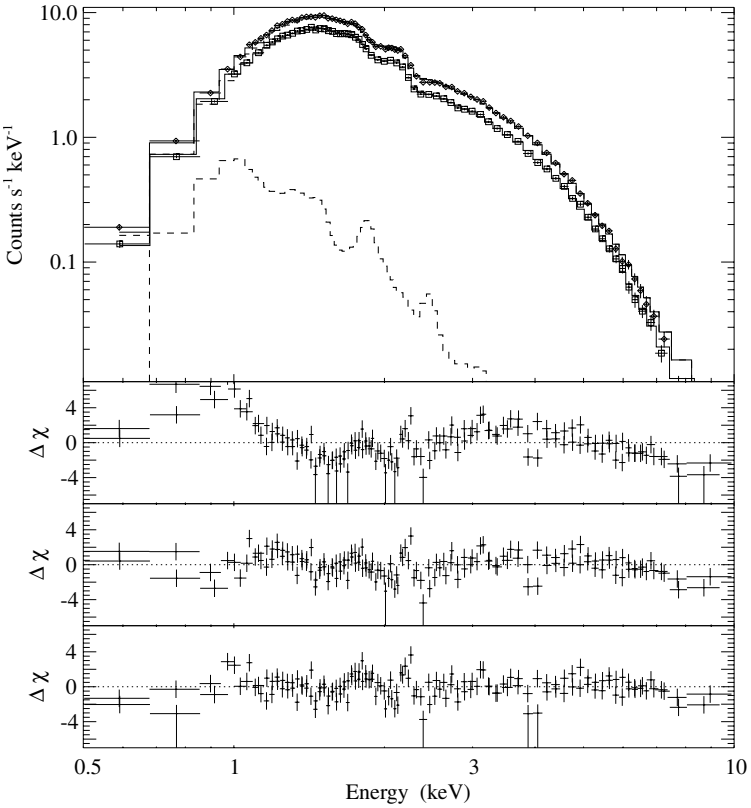

Figure 5. *ASCA* observations of LMC X-1. Top panel shows the COMPPS plus a Raymond–Smith plasma model fit to the data, with $N_{\rm H}$ fixed to 7.2×10^{21} cm^{-2}. Dashed lines show the individual model components folded through the response matrix of the SIS0 detector. Lower panels, from top to bottom, show data residuals for: COMPPS model with fixed $N_{\rm H}$ and no plasma component; COMPPS model with fixed $N_{\rm H}$ and a Raymond–Smith plasma component; and COMPPS model with free $N_{\rm H}$ and no plasma component.

very similar source V1408 Aql = 4U1957+11 (Nowak & Wilms 1999).

Starting with the COMPPS models, none of the three *ASCA* observations show evidence of an Fe line. If we freeze the line energy at 6.4 or 6.6 keV and the linewidth at 0.3 keV, we find an upper (90 per cent confidence) limit of 60 eV for the line equivalent width for the LMC X-1 observation. Narrower lines (down to the *ASCA* resolution of ~0.1 keV) produce more stringent equivalent width limits. For the slightly fainter 1995 April 15 and 1993 September 23 LMC X-3 observations, the equivalent width 90 per cent confidence limits are 90 and 320 eV, respectively.

The reduced χ^2 values with the COMPPS model are significantly less than 1 for both LMC X-3 observations, and therefore we do not attempt to fit a plasma component to these data. The COMPPS model fit to the LMC X-1 observation yields a reduced $\chi^2 \approx 1$; however, this fit requires an $N_{\rm H}$ value 12 per cent lower than the estimates of Staveley-Smith (private communication). Fixing the $N_{\rm H}$ column density to this value worsens the reduced χ^2 to ≈2 and yields significant residuals in the Fe–L complex region (Fig. 5). This residual can be removed and the reduced χ^2 value returned to ≈1 by adding a plasma component with $kT \sim 0.8$ keV (here modelled with the XSPEC RAYMOND model, after Raymond & Smith 1977). Thus the reality of any Fe–L complex is seen to depend strongly upon accurate modelling of the neutral hydrogen absorption of this source. Differing metal abundances in the LMC also could lead to errors in interstellar absorption models, adding further uncertainties to the level of any plasma component. If real, however, a plasma component at the levels allowed by the *ASCA* data with a fixed neutral hydrogen column would be readily detectable by the *X-ray Multiple Mirror Mission*, which would also resolve the complex into individual line components. (Note also that the residuals seen at ~1.7 and ~2.2 keV are likely related to well-known systematic features in the SIS responses matrices.)

5 TIMING ANALYSIS

We employed Fourier techniques, in the same manner as for our RXTE observations of Cyg X-1 (Nowak, Vaughan & Wilms 1999a), to study the short timescale variability of LMC X-1 and LMC X-3. Specifically, we used the same techniques for estimating deadtime corrections (Zhang et al. 1995; Zhang & Jahoda 1996) to the Power Spectral Density (PSD), and for estimating

uncertainties and the Poisson noise levels of the PSD (Leahy et al. 1983; van der Klis 1989). In the analysis discussed below, we use light curves with 2^{-7} s resolution constructed from the PCA top xenon layer data only. Furthermore, we subdivide the light curves into three energy channels: 0–3.3, 3.3–4.7 and 4.7–9.1 keV (absolute PCA channels 0–8, 9–12, 13–24, respectively). We chose these energy ranges as they are relatively background-free, and furthermore the three channels have roughly equal count rates. The lowest energy channel is dominated by the disc component, whereas the highest energy channel is sampling the power-law component (Section 3).

To maximize the signal-to-noise ratio, we created a single PSD in each energy channel that was averaged over the entire duration of our observations. We further averaged PSDs constructed from data segments of 1024 s duration (76 segments for LMC X-1, 65 segments for LMC X-3), and we logarithmically binned the PSD over frequencies $f \rightarrow 1.3f$. For the case of LMC X-3, weak variability with root-mean-square (rms) amplitude of 0.8 per cent of the mean was detected in the 10^{-3}–10^{-2}-Hz range. This is consistent with background fluctuations.

Significant variability above the noise, however, was detected in LMC X-1. Root-mean-square variabilities of 6.5, 6.3 and 7.1 per cent, lowest to highest energy channel, were found for the frequency range 7×10^{-4}–0.3 Hz. The PSDs for these energy channels are shown in Fig. 6. All three PSDs are approximately proportional to f^{-1} from 7×10^{-4}–0.2 Hz. The highest energy band PSD, however, shows evidence for a rollover at $\sim$0.2 Hz. Note that for this latter PSD there are only three or four points at frequencies higher than 0.2 Hz that sharply decline, followed by several points with a more gradual decline roughly proportional to $f^{-0.5}$. (Fig. 6 shows the PSD multiplied by frequency.) The $f^{-0.5}$ behaviour is also readily apparent at high frequencies in the PSD of the low energy channel as well as possibly in the PSD of the middle energy channel. An $f^{-0.5}$ proportionality is exactly that expected for positive noise residuals if the mean Poisson noise level was slightly underestimated (see Nowak et al. 1999a). The uncertainty in the noise level makes it difficult to assess the frequency-dependence of the rollover as a function of energy. The 4.7–9.1 keV energy band PSD values at frequencies 0.2–2 Hz, however, clearly lie below an extrapolation of the low-frequency PSD behaviour. Removing the break altogether would require that we *overestimated* the Poisson noise level, which seems doubtful given the $\propto f^{-0.5}$ behaviour of the noise-subtracted PSD residuals.

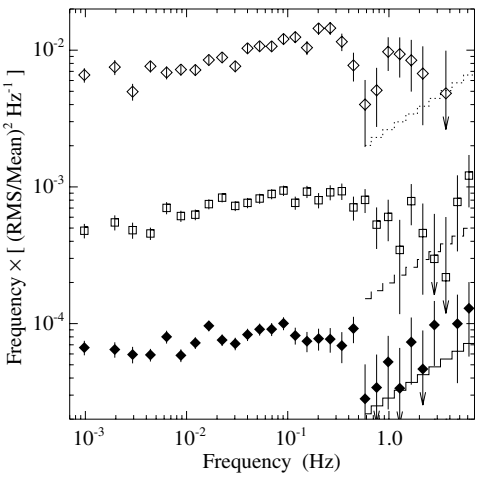

Figure 6. Fourier frequency times power spectral density (PSD) for LMC X-1 in the 0–3.3-keV (solid diamonds, lowered by a decade), 3.3–4.7-keV (clear diamonds), 4.7–9.1-keV (solid squares, raised by a decade) energy bands. PSD normalization is such that integrating over positive frequencies yields the mean square variability divided by the square of the mean for the light curve analysed. Lines represent the expected level of positive $1-\sigma$ noise residuals after subtracting Poisson noise from the PSDs.

These results for LMC X-1 are roughly consistent with the previous *RXTE* observations reported by Schmidtke et al. (1999) in terms of overall PSD amplitude and shape. However, Schmidtke et al. (1999) did not attempt any noise subtraction and did not search for breaks in any of the PSD. We do not find any evidence for a 0.08-Hz quasi-periodic oscillation as reported by Ebisawa et al. (1989), which is consistent with the results of Schmidtke et al. (1999). The 0.08-Hz QPO reported by Ebisawa et al. (1989), however, is nearly coincident with the expected level of the residuals after noise subtraction. Thus the previously reported QPO may have been an artefact of a misestimation of the Poisson noise level, as opposed to the lack of detection here and in the work of Schmidtke et al. (1999) being due to an intermitant nature of such low-frequency QPO.

Contrary to the results reported by Treves et al. (1988), we do not detect any variability from LMC X-3. We note, however, that the PSD reported by Treves et al. (1988) has the characteristic $f^{-0.5}$ shape and amplitude expected from noise residuals. We believe, therefore, that the results of Treves et al. (1988) are consistent with those reported here.

We further studied the temporal behaviour of LMC X-1 by computing the Fourier frequency-dependent time lags and variability coherence between the various energy bands (see Vaughan & Nowak 1997, and references therein). Owing to the low count rates, only weak 1-σ upper limits of $\gtrsim 2\,\mathrm{s}\ (f/10^{-2}\,\mathrm{Hz})^{-1}$ could be placed on the time lags between the lowest and highest energy channels over the frequency range 10^{-3}–0.3 Hz. We were able to measure the coherence among the variability in the various energy bands. As we have previously discussed (Vaughan & Nowak 1997; see also Bendat & Piersol 1986), the coherence function, $\gamma^2(f)$, which is always $\leqslant 1$, is a measure of the degree of linear correlation between two time series, or alternatively, it is a measure of how well one time series can be predicted from the other.

We present the coherence function for the LMC X-1 variability light curve, logarithmically binned over frequencies $f \rightarrow 2f$, in Fig. 7. The lowest and middle energy band light curves are fairly well-correlated and have a coherence function between them of $\gamma^2(f) \gtrsim 0.9$. Both of these light curves, however, are very incoherent with the highest energy band light curve, with $\gamma^2(f) \approx 0$ at 10^{-3} Hz and then rising approximately as $\propto \log(f)$. Owing to uncertainties in the Poisson noise level, there are additional systematic uncertainties above $\approx$0.3 Hz; however, the coherence is clearly below the near unity levels that we typically observe during the low/hard states of BHC such as Cyg X-1 and GX339−4 (Nowak et al. 1999a; Nowak, Wilms & Dove 1999b).

6 DISCUSSION

6.1 Variability of LMC X-1

The most obvious striking difference between LMC X-1 and LMC

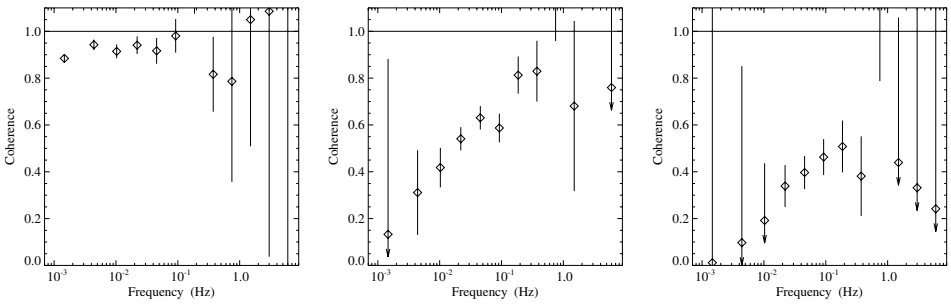

Figure 7. Coherence between the variability in the 0–3.3- and 3.3–4.7-keV energy bands (left), the 3.3–4.7- and 4.7–9.1-keV energy bands (middle), and the 0–3.3- and 4.7–9.1-keV energy bands (right).

X-3 is that the former shows moderate (7 per cent rms) variability whereas the latter shows essentially none (<0.8 per cent rms) on time-scales shorter than 1 ks, despite the fact that the X-ray spectra of these two objects are remarkably similar in terms of shape and overall flux. We hypothesize that the differences lie within their respective modes of accretion. As discussed by Cowley et al. (1983), van der Klis et al. (1983) and Cowley et al. (1994), LMC X-3 is consistent with accreting via Roche lobe overflow. One would therefore expect the accretion rate of LMC X-3 to be relatively steady (although see the discussion of the long-term periodicity presented in Paper II). LMC X-1, on the other hand, is most likely accreting partly via a wind with velocity $v_{\rm w} \gtrsim$ 600–1100 km s^{-1} (Hutchings, Crampton & Cowley 1983; Hutchings et al. 1987). This has a number of implications for the accretion flow.

Taking a presumed mass of 6 M$_\odot$ and a wind velocity of 600 km s^{-1} (Hutchings et al. 1987), the Hoyle–Lyttleton accretion radius (Hoyle & Lyttleton 1939; Bondi & Hoyle 1944) is then

$$R_{\rm HL} = \frac{2GM}{v_{\rm w}^2} \approx 4 \times 10^{11}\ {\rm cm} \left(\frac{M}{6\,{\rm M}_\odot}\right) \left(\frac{v_{\rm w}}{600\,{\rm km\,s^{-1}}}\right)^{-2}, \qquad (1)$$

which should be compared with the binary separation of $a \sim 2.2 \times 10^{12}$ cm given a 4.2 d period and a 20 M$_\odot$ companion (Hutchings et al. 1987). The 'circularization radius', however, will be much smaller, by a factor of the order $(v_{\rm orb}/v_{\rm w})^2$, where $v_{\rm orb} \sim$ 260 km s^{-1} is the orbital velocity. This estimate comes from assuming the accreted angular momentum per unit mass goes as $R_{\rm HL} \cdot v_{\rm orb}$, and then setting this value equal to the Keplerian value at the circularization radius. Thus, we expect a disc circularization radius of $\lesssim 8 \times 10^{10}$ cm $(v_{\rm w}/600\,{\rm km\,s^{-1}})^{-4}$. The disc is thus expected to be smaller than would be usual for Roche lobe overflow, perhaps substantially so. For $v_{\rm w} = 2000$ km s^{-1}, the expected circularization radius is $\sim 750\,GM/c^2$.

There is a long history of numerical simulations (Fryxell & Taam 1988; Taam & Fryxell 1988; Taam & Fryxell 1989; Benensohn, Lamb & Taam 1987; Ruffert 1997; Ruffert 1999) showing that wind dominated accretion inherently exhibits fluctuations in the net accretion rate onto the compact object. More recent 3-D numerical integrations (Ruffert 1997; Ruffert 1999) tend to show smaller amplitude fluctuations than earlier 2-D work (Benensohn et al. 1997); however, accretion-rate fluctuations of $\mathcal{O}$ (10 per cent), in rough agreement with the observed variability, are expected. LMC X-3, being Roche lobe fed, would not be expected to exhibit these fluctuations.

A disc with a truncated outer edge may also yield an explanation of the possible rollover in the high-energy band PSD seen at ~0.3 Hz. For $\alpha = 0.3$, $H/R \sim L/L_{\rm Edd} \sim 0.3$, $M = 6\,{\rm M}_\odot$, the viscous timescale at $R = 750\,GM/c^2$ is ~20 s, which is in rough agreement with the time scale of the possible rollover. This is consistent with the idea that any accretion-rate fluctuations on time-scales shorter than the viscous time scale at the circularization radius are smoothed out as they propagate into the inner X-ray emitting regions of the disc.

As discussed above, the low variability coherence values for LMC X-1 at $f > 10^{-3}$ Hz are unlike what we observed for the low/hard states of Cyg X-1 and GX 339−4 (Nowak et al. 1999a; Nowak, Wilms & Dove 1999b). We are aware of three possible ways of explaining such low values (Vaughan & Nowak 1997). First, the low and high energy bands may be completely unrelated to each other. This seems unlikely as all three energy bands exhibit a roughly $\propto f^{-1}$ PSD with comparable amplitudes. Second, the upper energy band PSD may be related to the lower energy band PSD via a non-linear transfer function. This is a viable option, given the complicated physics of 'coronal formation' and the fact that non-linear transfer functions couple power from frequencies f in one band to multiples of f in other bands (Bendat & Piersol 1986). This latter case is especially difficult to detect in the f^{-1} PSD because of its scale-free nature.

The third possibility is perhaps the most viable option. 'Mixing' of *independent* components with widely varying intrinsic time lags can lead to the loss of coherence (see the discussion presented by Nowak et al. 1999b). For example, if one component that shows a correlation between hard and soft X-rays (e.g. local dynamical time-scale disc fluctuations leading to an increase in both seed photons and, very slightly delayed, upscattered hard photons) is mixed with another, nearly equal in power *but independent* component with an anti-correlation between soft and hard X-rays (e.g. matter being transferred between disc and corona on thermal or viscous time-scales, with comparably long delays between soft and hard photons), then a strong loss of coherence is expected. In a simple two-component model the coherence function, $\gamma^2(f)$, is given by

$$\gamma^2(f) \approx \frac{R^2(f) + 2R(f)\cos(\theta_b - \theta_a)}{[R(f) + 1]^2}. \qquad (2)$$

Here $R(f)$ is the ratio of Fourier frequency-dependent cross correlation amplitudes for the two independent processes being considered (soft versus hard X-ray variability, process b over

process a), and θ_a, θ_b are the Fourier frequency-dependent phase delays between the hard and soft X-ray variability for the independent processes a and b, respectively (Vaughan & Nowak 1997; Nowak et al. 1999b). (Time delay, $\tau \equiv \theta/2\pi f$.) For the plots in Fig. 7, if $R(f) \approx 1$ and $\theta_b - \theta_a \approx \pi$ at $f = 10^{-3}$ Hz, then $\gamma^2(f) \approx 0$ there as well. The increase in coherence towards higher frequency could be due to a decrease of either $\theta_b - \theta_a$ or $R(f)$. The latter might be reasonably expected, for instance, if one process is happening predominantly on $\mathcal{O}(1000\,\mathrm{s})$ viscous time-scales (again, perhaps matter/energy transfer between disc and corona), whereas the other one is happening over a broader range of time-scales (fluctuations in the seed/Comptonized photons).

6.2 Spectroscopy of the soft state

The spectroscopy of LMC X-3 perhaps bears out the notion of there being an anti-correlation between the disc and coronal components on long time-scales, as shown in Fig. 3. A similar result can be obtained with the more phenomenological disc blackbody plus power-law models presented in Table 2. The photon flux in the 'disc component' ($\propto A_{\rm disc} kT_{\rm disc}^3$) is anti-correlated with the photon flux in the 'power-law component' ($\propto 3.6^{1-\gamma}/[1-\gamma]$) in an analogous way. The fastest variation occurs on time-scales of $\approx$0.4 d. Given $\alpha = 0.3$, $H/R \sim L/L_{\rm Edd} \sim 0.3$, and $M = 9\,{\rm M}_\odot$, this corresponds to a viscous time scale at a radius of $\sim 8 \times 10^{10}$ cm, approximately one quarter of the disc circularization radius. It is therefore more likely that this variation occurs on a thermal or dynamical time-scale closer towards the centre of the system. Thermal time-scale transfer of energy between disc and corona is again consistent with the results shown in Fig. 3.

Unfortunately, it is difficult to say much more about the spectrum other than it is well-fitted by a disc blackbody plus power-law model. Given a 70° inclination, 9 $\mathrm{M}_\odot$ black hole, and 50 kpc distance for LMC X-3, and a 30° inclination, 6 $\mathrm{M}_\odot$ black hole, and 50 kpc distance for LMC X-1, the disc normalizations in Tables 2 and 3 are roughly consistent with inner disc radii of $\sim 6\,GM/c^2$. This is quite remarkable, given the simplicity of the disc blackbody model (cf. Merloni et al. 1999). As regards the power-law tail, other soft state black-hole candidates exhibit evidence for non-thermal Comptonization in this tail (Gierliński et al. 1999). Here, however, as we were only able to go out to 50 and 20 keV for LMC X-3 and LMC X-1, respectively, we were able to describe the data completely adequately with pure thermal Comptonization.

The extent to which a strong, broad Fe line is required is likewise still somewhat uncertain. The $\approx$150-eV equivalent width, $\sigma \approx 1.4-$keV line is consistent with expectations from the basic picture outlined above: a disc extending down towards the black-hole horizon, with a large covering fraction corona sitting on top of it. (A slight Fe overabundance, or perhaps beaming of the coronal radiation towards the disc, might also be required for the implied equivalent widths.) However, as the Fe line occurs in a region where the two basic spectral components – soft disc spectrum and hard power-law/Comptonization spectrum – cross one another, the Fe line parameters are especially sensitive to our assumptions regarding the underlying continuum model. Again, this is in contrast to AGN where it is presumed that the underlying continuum in the Fe line/edge region is well-approximated by a simple power law.

7 SUMMARY

In this work, we have presented an analysis of long (170-ks) *RXTE* observations of LMC X-1 and LMC X-3, as well as an analysis of archival *ASCA* observations of these objects. The primary results of these analyses are as follows.

(i) Both LMC X-1 and LMC X-3 are well-fitted by a simple spectroscopic model consisting of a disc blackbody and a power law. The power law, which was seen out to 50 keV for LMC X-3, shows no obvious curvature. The data are consistent with exhibiting a broad Fe Kα line with equivalent width $\lesssim$150 eV; however, the line could in reality be narrower and weaker. *ASCA* observations do not reveal the presence of a narrow Fe Kα line, and the presence of any Fe–L complex in LMC X-1 is almost completely dependent upon the modelling of the neutral hydrogen column towards that source.

(ii) As a more physical interpretation of these results, the spectra are consistent with Comptonization of a disc spectrum by a corona with electron temperature $kT_{\rm e} \sim 60$ keV and $\tau_{\rm es} \sim 0.1$. These fits are not unique, however, as the data do not extend beyond 50 keV. Purely non-thermal Comptonization models are also permitted.

(iii) LMC X-3 shows no variability on $\lesssim$1-ks time-scales; however, it does show variability on half-day time-scales and longer. The time scale of these variations are slightly faster than the viscous time-scales of the outer disc. Spectral models of these variations are consistent with an anti-correlation between the disc and Compton corona components of the spectrum

(iv) LMC X-1 shows rms variability of a few per cent on faster than 1000-s time-scales. This variability, along with with a possible power spectrum rollover on time-scales $\lesssim$5 s, is consistent with accretion-rate variations in a wind-fed system where the disc is circularized at radii $\lesssim 1000\,GM/c^2$.

(v) The variability at energies $\lesssim$5 keV shows very low coherence with the variability at energies $\gtrsim$5 keV. Given the similarity of the PSD among the three energy bands, this low coherence is likely either due to a non-linear relationship between the soft and hard energy bands, or due to multiple variability components some with strong correlations between soft and hard variability and other others with strong anti-correlations.

ACKNOWLEDGMENTS

This research has been financed by NASA grants NAG5-3225, NAG5-4621, NAG5-4737, NSF grants AST95-29170, AST98-76887, DFG grant Sta 172/22, and a travel grant to JW and KP from the DAAD. L. Staveley-Smith provided us with the unpublished $N_{\rm H}$ values. MAN and JW would like to thank the Aspen Center for Physics for their hospitality and the participants of the 'X-ray Probes of Relativistic Astrophysics' workshop, especially J. Grindlay and R. Taam, for many useful discussions while this work was being completed. We thank the referee for comments that improved the clarity of this paper.

REFERENCES

Arnaud K. A., 1996, in Jacoby J. H., Barnes J., eds, Astronomical Data Analysis Software and Systems V, Astron. Soc. Pacific, Conf. Ser., Vol. 101. Astron. Soc. Pacific, San Francisco, p. 17

Bałucińska-Church M., McCammon D., 1992, ApJ, 400, 699

Bendat J., Piersol A., 1986, Random Data: Analysis and Measurement Procedures. Wiley, New York

Benensohn J. S., Lamb D. Q., Taam R. E., 1997, ApJ, 478, 723
Bondi H., Hoyle F., 1944, MNRAS, 104, 273
Bowyer S., Byram E. T., Chubb T. A., Friedman H., 1965, Science, 147, 394
Brandt W. N., Fabian A. C., Dotani T., Nagase F., Inoue H., Kotani T., Segawa Y., 1996, MNRAS, 283, 1071
Cowley A. P., Crampton D., Hutchings J. B., 1978, AJ, 83, 1619
Cowley A. P., Crampton D., Hutchings J. B., Remillard R., Penfold J. E., 1983, ApJ, 272, 118
Cowley A. P. et al., 1991, ApJ, 381, 526
Cowley A. P., Schmidtke P. C., Hutchings J. B., Crampton D., 1994, ApJ, 429, 826
Cowley A. P., Schmidtke P. C., Anderson A. L., McGrath T. K., 1995, PASP, 107, 145
Cui W., Zhang S. N., Focke W., Swank J. H., 1997, ApJ, 484, 383
Day C., Arnaud K., Ebisawa K., Gotthelf E., Ingham J., Mukai K., White N. E., 1998, The ASCA Data Reduction Guide. Technical Report, NASA Goddard Space Flight Center, Greenbelt, Md. Version 2.0
Dove J. B., Wilms J., Nowak M. A., Vaughan B. A., Begelman M. C., 1998, MNRAS, 298, 729
Ebisawa K., Mitsuda K., Inoue H., 1989, PASJ, 41, 519
Ebisawa K., Makino F., Mitsuda K., Belloni T., Cowley A. P., Schmidtke P. C., Treves A., 1993, ApJ, 403, 684
Fryxell B. A., Taam R. E., 1988, ApJ, 335, 862
Gierliński M., Zdziarski A. A., Poutanen J., Coppi P. S., Ebisawa K., Johnson W. N., 1999, MNRAS, 309, 496
Grebenev S. et al., 1993, A&AS, 97, 281
Hoyle F., Lyttleton R. A., 1939, Proc. Cam. Phil Soc., 35, 405
Hutchings J. B., Crampton D., Cowley A. P., 1983, ApJ, 275, L43
Hutchings J. B., Crampton D., Cowley A. P., Bianchi L., Thompson I. B., 1987, AJ, 94, 340
Jahoda K., Swank J. H., Giles A. B., Stark M. J., Strohmayer T., Zhang W., Morgan E. H., 1996, in Siegmund O. H., ed., EUV, X-ray and Gamma-ray Instrumentation for Astronomy VII. Proc. SPIE 2808. SPIE, Bellingham, WA, p. 59
Lampton M., Margon B., Bowyer S., 1976, ApJ, 208, 177
Leahy D. A., Darbro W., Elsner R. F., Weisskopf M. C., Kahn S., Sutherland P. G., Grindlay J. E., 1983, ApJ, 266, 160
Long K. S., Helfand D. J., Grabelsky D. A., 1981, ApJ, 248, 925
Merloni A., Fabian A. C., Ross R. R., 1999, MNRAS, 313, 193
Mitsuda K. et al., 1984, PASJ, 36, 741
Miyamoto S., Kitamoto S., Iga S. et al., 1994, ApJ, 435, 398
Nagase F., Zylstra G., Sonobe T., Kotani T., Inoue H., Woo J., 1994, ApJ, 436, L1
Nowak M. A., 1995, PASP, 107, 1207
Nowak M. A., Wilms J., 1999, ApJ, 522, 476
Nowak M. A., Vaughan B. A., Wilms J., Dove J. B., Begelman M. C., 1999a, ApJ, 510, 874
Nowak M. A., Wilms J., Dove J. B., 1999b, ApJ, 517, 355
Poutanen J., Svensson R., 1986, ApJ, 470, 249
Raymond J. C., Smith B. W., 1977, ApJS, 35, 419
Rothschild R. E. et al., 1998, ApJ, 496, 538
Ruffert M., 1997, AJ, 317, 793
Ruffert M., 1999, AJ, 346, 861
Schandl S., 1996, A&A, 307, 95
Schlegel E. M., Marshall F. E., Mushotzky R. F., Smale A. P., Weaver K. A., Serlemitsos P. J., Petre R., Jahoda K. M., 1994, ApJ, 422, 243
Schmidtke P. C., Ponder A. L., Cowley A. C., 1999, AJ, 117, 1292
Shields G. A., McKee C. F., Lin D. N. C., 1986, ApJ, 306, 90
Syunyaev R. A., Gil'fanov M., Churazov E. et al., 1990, Sov. Astron. Lett., 16, 55
Taam R. E., Fryxell B., 1988, ApJ, 327, L73
Taam R. E., Fryxell B., 1989, ApJ, 339, 297
Tanaka Y., Lewin W. H. G., 1995, Black-hole binaries, in Lewin W. H. G., van Paradijs J., van den Heuvel E. P. J., eds, X-ray Binaries, Ch. 3. Cambridge Univ. Press, Cambridge, p. 126
Treves A., Belloni T., Chiapetti L., Maraschi L., Stella L., Tanzi E. G., van der Klis M., 1988, ApJ, 325, 119
Treves A., Belloni T., Corbet R. H. D. et al., 1990, ApJ, 364, 266
van der Klis M., 1989, in Ögelman H., van den Heuvel E. P. J., eds, Timing Neutron Stars. NATO ASI C262, Astron. Soc. Pacific, Conf. Ser., Vol. 101. Kluwer, Dordrecht, p. 27
van der Klis M., Tjemkes S., van Paradijs J., 1983, A&A, 126, 265
Vaughan B. A., Nowak M. A., 1997, ApJ, 474, L43
Wilms J., Nowak M. A., Dove J. B., Fender R. P., di Matteo T., 1999a, ApJ, 522, 460
Wilms J., Nowak M. A., Dove J. B., Pottschmidt K., Heindl W. A., Begelman M. C., Staubert R., 1999b, in Aschenbach B., Freyberg M., eds, Highlights in X-ray Astronomy. MPE Report 272
Wilms J., Nowak M. A., Dove J. B., Pottschmidt K., Heindl W. A., Begelman M. C., Staubert R., 1999c, Astrophys. Lett. Comm., 38, 273
Wilms J., Nowak M. A., Pottschmidt K., Heindl W. A., Dove J. B., Begelman M. C., 2001, MNRAS, 320, 327 (Paper II, this issue)
Zhang W., Jahoda K., 1996, Deadtime Effects in the PCA. Technical Report. NASA GSFC, Greenbelt, MD
Zhang W., Jahoda K., Swank J. H., Morgan E. H., Giles A. B., 1995, ApJ, 449, 930
Zhang S. N., Cui W., Harmon B. A., Paciesas W. S., Remillard R. E., van Paradijs J., 1997, ApJ, 477, L95

This paper has been typeset from a TEX/LATEX file prepared by the author.

ANHANG D

Discovery of Recurring Soft to Hard State Transitions in LMC X-3

J. Wilms, M.A. Nowak, K. Pottschmidt, W.A. Heindl, J.B. Dove, M.C. Begelman

2001

Nachdruck aus

Monthly Notices of the Royal Astronomical Society
Vol. 320, S. 327–340

Mon. Not. R. Astron. Soc. **320**, 327–340 (2001)

Discovery of recurring soft-to-hard state transitions in LMC X-3

J. Wilms,[1★] M. A. Nowak,[2★] K. Pottschmidt,[1★] W. A. Heindl,[3★] J. B. Dove[4,5★] and M. C. Begelman[2,6★]

[1]*Institut für Astronomie und Astrophysik – Astronomie, Waldhäuser Str. 64, D-72076 Tübingen, Germany*
[2]*JILA, University of Colorado, Boulder, CO 80309-440, USA*
[3]*Center for Astronomy and Space Sciences, Code 0424, University of California at San Diego, La Jolla, CA 92093, USA*
[4]*Center for Astronomy and Space Astrophysics, University of Colorado, Boulder, CO 80309-389, USA*
[5]*Department of Physics, Metropolitan State College of Denver, C.B. 69, PO Box 173362, Denver, CO 80217-3362, USA*
[6]*Department of Astrophysics and Planetary Sciences, University of Colorado, Boulder, CO 80309, USA*

Accepted 2000 August 10. Received 2000 August 10; in original form 2000 January 17

ABSTRACT

We present the analysis of the approximately three-year long *Rossi X-ray Timing Explorerd* (*RXTE*) campaign for monitoring the canonical soft state black-hole candidates LMC X-1 and LMC X-3. In agreement with previous observations, we find that the spectra of both sources can be well-described by the sum of a multi-temperature disc blackbody and a power law. In contrast to LMC X-1, which does not exhibit any periodic spectral changes, we find that LMC X-3 exhibits strong spectral variability on time-scales of days to weeks. The variability pattern observed with the *RXTE* All Sky Monitor reveals that the variability is more complicated than the 99- or 198-d periodicity discussed by Cowley et al. For typical ASM count rates, the luminosity variations of LMC X-3 are due to changes of the phenomenological disc blackbody temperature, $kT_{\rm in}$, between $\sim$1 to $\sim$1.2 keV. During episodes of especially low luminosity (ASM count rates $\lesssim$0.6 counts s^{-1}; four such periods are discussed here), $kT_{\rm in}$ strongly decreases until the disc component is undetectable, and the power law significantly hardens to a photon index of $\Gamma \sim 1.8$. These changes are consistent with state changes of LMC X-3 from the soft state to the canonical hard state of galactic black holes. We argue that the long-term variability of LMC X-3 might be owing to a wind-driven limit cycle, such as that discussed by Shields et al.

Key words: accretion, accretion discs – black hole physics – binaries: spectroscopic – stars: individual: LMC X-1 – stars: individual: LMC X-3 – X-rays: stars.

1 INTRODUCTION

Long-term variability on time-scales of months to years is seen in many galactic black-hole candidates. By analogy with the 35-d cycle of Her X-1, the long-term variability of some objects has been identified with the precession of a warped accretion disc. Possible driving mechanisms for a warp include radiation pressure due to the luminous central X-ray source (Pringle 1996; Maloney et al. 1996; Maloney & Begelman 1997; Maloney et al. 1998), torques exerted by an accretion disc wind (Schandl & Meyer 1994; Schandl 1996), or tidal forces (Larwood 1998, and references therein).

In some sources, the long-term changes in the X-ray luminosity have been associated with state changes of the accretion disc. At low luminosities, these sources are usually observed in the hard state, in which the X-ray spectrum is dominated by a hard power-law component with a photon index of $\Gamma \sim 1.7$ and an exponential rollover at $\sim$150 keV. The hard-state spectrum is usually described in terms of thermal Comptonization (Sunyaev & Trümper 1979; Dove et al. 1997; and references therein). At higher luminosities, black-hole candidates exhibit a soft spectrum that can be characterized by a (multi-temperature) blackbody with a peak temperature of $kT \sim 1$ keV. In addition, a power law with a photon index of $\Gamma \sim 2.5$ or softer is present. Changes between the spectral states are typical for black holes as is evidenced by the 1996 soft state of Cygnus X-1 (Cui et al. 1997; Cui et al. 1998), and the frequent transitions seen in GX 339−4 (Makishima et al. 1986; Bouchet et al. 1993; Wilms et al. 1999a; Corbel et al. 2000). See Tanaka & Lewin (1995), Nowak (1995), and references therein for further details.

Prior to the observations discussed here, LMC X-1 and LMC X-3 were the only black-hole candidates that had always been seen in the soft state. Thus, both were ideal candidates for a

★ E-mail: wilms@astro.uni-tuebingen.de (JW); mnowak@rocinante.colorado.edu (MAN); katja@astro.uni-tuebingen.de (KP); biff@ucsd.edu (WAH); dove@casa.colorado.edu (JBD); mitch@rocinante.colorado.edu (MCB)

systematic study of the properties of the soft state. Although both sources were otherwise thought to be spectrally very similar, LMC X-1 had not shown signs of any periodic long-term variability, while LMC X-3 was known to be variable on a ∼100-d time-scale (Cowley et al. 1991; Cowley et al. 1994). We therefore initiated a two- (respectively, three-)year-long campaign to observe LMC X-1 (respectively, LMC X-3) with the *Rossi X-ray Timing Explorer* (*RXTE*). During the campaign we performed X-ray observations of roughly 10 ks length at approximately three-week intervals. The spacing and exposure time of the observations were chosen such that they would enable us to track spectral changes of the sources over any long-term variability pattern. The campaign was started in 1996 December with two long (∼170 ks) observations of the sources. The analysis of these observations is presented in a companion paper (Nowak et al. 2001, hereinafter Paper I). Preliminary results from the first year of this campaign, using earlier versions of the response matrix and background models, have been presented elsewhere (Wilms et al. 1999b; Wilms et al. 1999c), this paper is devoted to a discussion of the first two years of the campaign.

The remainder of this paper is structured as follows. In Section 2 we present the details of our data analysis procedure. Section 3 is devoted to the study of LMC X-3. Section 4 contrasts these observations with those from LMC X-1. In Section 5 we interpret our results in the context of current models of the soft state of galactic black hole candidates, and in the context of models of the long-term variability of X-ray binaries. We summarize our results in Section 6. Throughout this paper we assume a distance to the LMC of 50 kpc.

2 DATA ANALYSIS

Onboard *RXTE* are two pointed instruments – the proportional counter array (PCA) and the High-Energy X-ray Timing Experiment (HEXTE) – as well as the All-Sky Monitor (ASM). We used the standard *RXTE* data analysis software, FTOOLS 4.2, to examine the PCA and HEXTE data. Spectral modelling was done using XSPEC, version 10.00ab (Arnaud 1996). Owing to the short duration of the pointed observations, we use only the PCA data for this analysis. We used essentially the same data screening and analysis strategy as in Paper I, i.e. we used the PCA top xenon layer data only and ignored data taken within 30 min after passages through the south Atlantic anomaly and where the background count rate, as measured by the 'electron ratio', was comparatively large (see Paper I for details). Data from all PCUs was combined for the final analysis. Contrary to Paper I, the observations presented here are so short that the Poisson error dominates the uncertainty of the spectrum; therefore, no systematic error was applied to the data. For some of the observations, only part of the PCA detectors were turned on. These intervals were extracted separately and then combined. Response matrices were generated for each of these intervals. The response matrix for the final analysis was obtained from these individual matrices by adding the matrices weighted by the fraction of photons coming from each of the intervals. We analysed data taken in the energy band from 2.5 to 20 keV.

Since our data are background dominated above ∼5 keV, good background modelling is essential for our analysis. Background subtraction of the PCA data was performed using a model taking into account sky pointings of the PCA, and modelling the background variability using data from the Very Large Event (VLE) counter of the PCA or using the so-called 'Faint model', depending on the source count rate. To estimate the uncertainty of the background model, we compared the count rate measured in the PCA channels above 30 keV, where no source photons are detected, with the background model flux at these energies. In all cases the agreement between the background model and the measured background was within 2 per cent. We accounted for this fluctuation by renormalizing the background model flux, using the XSPEC 'corrfile' facility, such that χ^2 was minimized in our spectral fits. Note that this introduces a 'hidden' fitting parameter to the data analysis. This parameter was not taken into account in the number of degrees of freedom since we assume that it converges to the correct normalization of the background model, and therefore does not introduce an uncertainty into the spectral fitting process.

We used data from the ASM in order to be able to place our observations in the context of the long-term variability of the sources. This instrument, an array of shadow cameras scanning the whole sky visible from the spacecraft for five to ten times per day (Remillard & Levine 1997; Levine et al. 1996), provides almost uninterrupted information about the long-term behaviour of bright X-ray sources. We used the 'definitive one-dwell' data available from the Goddard Space Flight Center (GSFC) and only used flux solutions for which $\chi^2_{\rm red} < 1.1$.

3 LMC X-3: LONG-TIME-SCALE SPECTRAL VARIABILITY

3.1 Introduction

The black-hole candidate LMC X-3 was discovered during *UHURU* observations of the Large Magellanic Cloud (Leong et al. 1971). A summary of the early observational history has been given by Treves et al. (1988). Interest in LMC X-3 was heightened when it was realized that its X-ray spectrum is very similar to that of Cyg X-1 in the high state. White & Marshall (1984) therefore established the source as a potential black-hole candidate. Subsequent radial velocity measurements, resulting in a mass function of 2.3 $M_\odot$ (Cowley et al. 1983), as well as optical photometry (van der Klis et al. 1983; Kuiper et al. 1988; and references therein) of the B3V companion lead to a minimum mass of ∼4 $M_\odot$ (Mazeh et al. 1986), with a most probable mass of 9–10 $M_\odot$ (Cowley et al. 1983; Paczyński 1983) for the compact object. LMC X-3 thus almost certainly contains a black hole.

The luminosity of LMC X-3 can be as much as ∼30 per cent of the Eddington luminosity of a 9-$M_\odot$ black hole. The source has been known to be strongly variable since *Ariel V* and the *High Energy Astrophysics Observatory 1* (*HEAO 1*) discovered large (>5) intensity changes on time-scales of weeks to months (Griffiths & Seward 1977; Johnston et al. 1979). A first systematic study of its long-term periodicity was performed by Cowley et al. (1991), who, based on *Ginga* and *HEAO-1* data, found a long-term period of 98.9 or 197.8 d. In addition, optical photometry indicated a lag of ∼20 d between the optical and the X-rays (the optical leading the X-rays; Cowley et al. 1991). Later *Hubble Space Telescope* (*HST*) investigations revealed the presence of the periodicity also in the ultraviolet (Cowley et al. 1994), albeit the long-term trends were not as clear as in the earlier data. These *HST* observations and the shape of the X-ray light curve led Cowley et al. (1994) to prefer the ∼99-d period and to postulate that LMC X-3 might have gone through a low-luminosity state similar to the 'extended low' states that are seen in Her X-1 (Parmar et al. 1985).

Detailed spectral studies of the long-term variability were first performed by Ebisawa et al. (1993), who used data from *Ginga* LAC pointings, taken over a period of three years, that covered a large range of source luminosities. Ebisawa et al. showed that the X-ray spectra could be well-described with a multi-temperature disc blackbody model plus a power-law spectrum. Alternatively, optically thick ($\tau_e \gtrsim 20$) Comptonization could be used (see also Treves et al. 1988), but is not preferred due to the unphysical parameters resulting from the spectral fitting. In accordance with Cowley et al. (1991), Ebisawa et al. (1993) found that the soft spectral component hardens with increasing source luminosity (i.e. its temperature increases), while the power-law tail was found to be independent of the luminosity. One possible interpretation of this result is a varying mass accretion rate $\dot{M}$.

A major shortcoming of the earlier spectral observations is that it was impossible to put the observations in the context of the overall long-term variability of the source due to the lack of a real all-sky monitoring instrument. Furthermore, the relative inflexibility of the early X-ray satellites made it impossible to obtain an even sampling of X-ray spectra over the long time-scale changes observed. A satellite such as *RXTE*, which combines a broad spectral coverage with very flexible scheduling and an all-sky monitoring instrument, is therefore ideal to systematically study the long-term behaviour of sources such as LMC X-3. In the remainder of this section we discuss the *RXTE* ASM soft X-ray light curve (Section 3.2), describe our analysis of the pointed data (Section 3.3), and present the results of our campaign (Section 3.4).

3.2 Long-term variability of LMC X-3

In Fig. 1(c) we display the long-term light curve of the object as observed with the ASM, binned to a resolution of 3 d. Note the strong variability on time-scales of ~100 and ~250 d, which is well sampled by our monitoring (see Fig. 2). This variability had already been noted during the first year of ASM operations (Levine et al. 1996).

The variability pattern itself is very complicated. The analysis of the ASM light curve using the generalized periodogram of Lomb (1976) and Scargle (1982) reveals significant periodicities on long time-scales of ~100, ~160, ~190, and ~240 d (Fig. 1b). Epoch folding analysis (Leahy et al. 1983; Schwarzenberg-Czerny 1989; Davies 1990) independently verifies this result. No significant variability (using the full temporal resolution ASM light curve) is detected by these methods on the 1.7-d orbital time-scale of the system. This is consistent with earlier results (Weisskopf et al. 1983; Cowley et al. 1983; van Paradijs et al. 1987), but contrary to other high mass X-ray binaries, such as Cyg X-1 or Vela X-1, where a clear orbital modulation of the X-ray

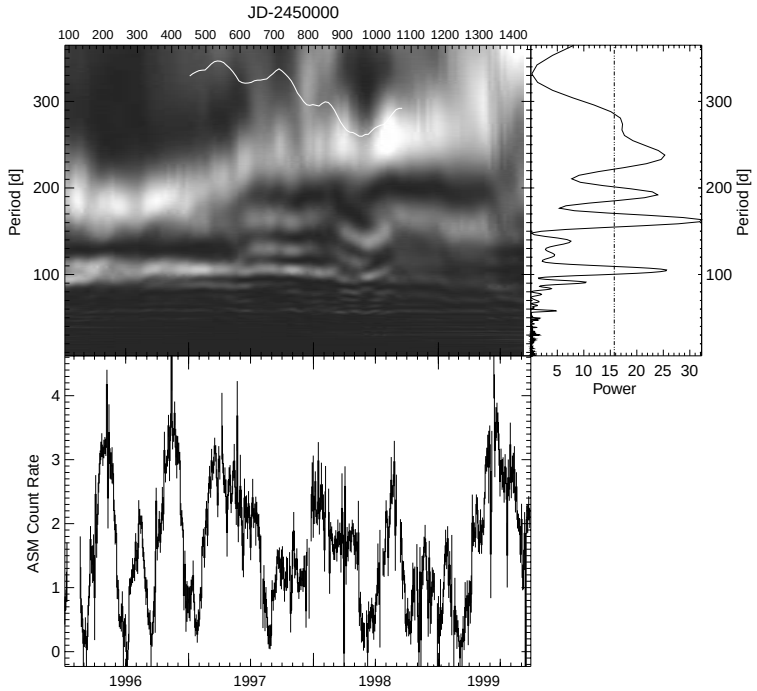

Figure 1. (a) *Upper left:* Dynamical PSD of LMC X-3 for the ASM data from 1996 through mid-1999. The white line displays the behaviour of the average ASM count rate (a period of 350 d corresponds to 4 ASM cps). (b) *Upper right:* Lomb–Scargle periodogram for the ASM data through 1999, the dashed line indicates a false alarm probability for periods at the 0.01 per cent level (for the definition of the false alarm probability, see Scargle 1982). (c) *Lower left:* ASM light curve of LMC X-3, binned to a temporal resolution of 3 d, and variation of the spectral parameters for our *RXTE* pointed observations. See text for explanations.

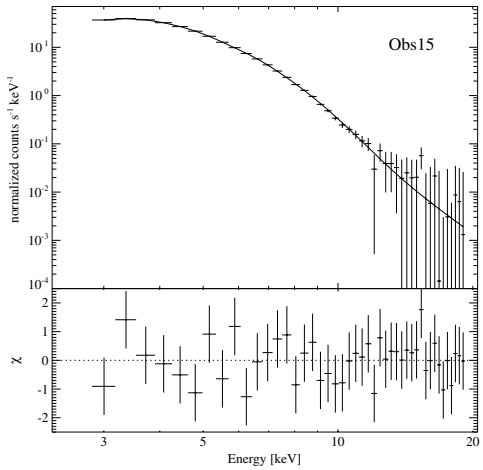

Figure 2. Temporal variability of the spectral parameters of LMC X-3.

flux is detected in the ASM. For these latter sources, this variation is most probably due to photoelectric absorption in the stellar wind (Wen et al. 1999). The lack of orbital variability in LMC X-3 can therefore be interpreted as a lack of a strong stellar wind from the companion star. This is not very surprising, considering that the companion is a B3 V star (Warren & Penfold 1975; Cowley et al. 1994).

Compared with sources with clear perioditicies such as Her X-1, the peaks in the Lomb–Scargle periodogram of Fig. 1(b) are quite broad. This can be a sign that the periods detected by this method are only quasi-periodic, i.e. they change with time or are not present during the whole time span covered. We therefore computed a dynamical Lomb–Scargle periodogram by taking slices of the ASM light curve (binned to a resolution of 3 d) with a length of 730 d each, and shifting these slices with a step size of 9 d over the whole ASM data range.[1] For each of these slices the Lomb–Scargle periodogram was computed for the period range from 6 to 365 d. To ensure that the periodograms are comparable, we normalized them such that

$$\frac{\sigma^2}{\mu} = \int_{f_{\min}}^{f_{\max}} \mathrm{PSD}(f)\,\mathrm{d}f, \qquad (1)$$

where $f_{\min}$ and $f_{\max}$ are the minimum and maximum frequency for which the Lomb–Scargle periodogram is computed, and where σ^2 is the variance and μ the mean ASM count rate of the 730-d light curve. The resulting periodogram was then gray scale coded and is displayed in Fig. 1(a), with each periodogram being displayed at the mid-time of the light curve for which it was computed.

Although the individual Lomb–Scargle periodograms are obviously not statistically independent, our approach is useful in revealing the long-term trends of the light curve. Fig. 1a shows clearly the origin of the individual peaks in the total periodogram of the source. Albeit with varying significance, the dynamical periodogram shows that a ∼100-d periodicity is present in all data segments analysed through the middle of 1998, confirming the periodicity discussed by Cowley et al. (1994). The ∼100-d periodicity is mainly attributable to the times of low (<0.5 ASM cps) source luminosity, that are, e.g. seen in 1996 July, 1997 January, and 1997 August (Fig. 1c). After mid-1998, the amplitude of the 100-d periodicity is seen to decrease; however, some of this reduction in amplitude can be attributed to the increasing inclusion of fake data in a given two-year periodogram. A possible shift in the distance between the light curve minima during mid 1998 through 1999 may lead to the additional time-scale of ∼160 d present in Fig. 1(b) (although see the discussion below). The ASM light curve for 1996 looks similar to the folded *HEAO 1* and *Ginga* light curve presented by Cowley et al. (1991). This might be an indication that the 'quasi-sinusoidial' variability of 1996 is not just a random event, but occurs frequently.

The peaks at lower frequency in the total Lomb–Scargle periodogram are due to long-term periodicities that are not fixed in period. The dynamical Lomb–Scargle periodogram shows a dominant periodicity on a time-scale of ∼190 d in 1996, which increases to ∼270 d for the 730-d light curve centred on 1997 December. These shifts in period can be attributed to the maxima of the ASM light curve, which behave quasi-sinusoidally in 1996 and then show an increase in period in 1997 and the first half of 1998, before (possibly) returning to a more periodic behaviour.[2] The strength of the individual peaks in the total periodogram (Fig.1b) can thus be seen as partly depending on the duration of the intervals in which each period dominated. It is also possible that the ∼160-d peak seen in the periodogram is the continuation of the ∼190-d period seen at the start of 1996, while the ∼240-d peak is due to the formation of a new periodicity beginning in late 1996 or early 1997. It is also interesting to note that the ∼100-d and ∼190-d periodicities that exist at the beginning of the ASM light curve have approximately the same period separation as the ∼160 and ∼240-d periods that exist at the end of the ASM light curve.

Although the ASM does in principle provide X-ray colour information, LMC X-3 is too weak to enable us to detect any statistically significant changes in the spectral shape during the three years of ASM coverage. Usable X-ray colours can only be computed after rebinning the data on ≳4-d intervals. These data indicate that the source might harden during lower ASM count rates. With the ASM, however, it is not possible to characterize these changes in greater detail. We therefore turn to our pointed monitoring observations to further describe these spectral trends.

3.3 Spectral modelling of LMC X-3 *PCA* data

Using the screening criteria of Section 2, we extracted the data from our 1997 and 1998 observations. A log of the observations is given in Table 1. Our conservative screening criteria reduce the effective usable exposure times from the scheduled 10 ks to the times shown in the table.

We modelled the *RXTE* spectra using the standard multi-temperature disc model (Mitsuda et al. 1984; Makishima et al.

[1] In order to extend the dynamical periodogram to the full length of time covered by the ASM data, we added Gaussianly distributed random data spanning one year before and after the ASM light curve. Each fake data set was chosen to have the same mean and variance of the first and last year, respectively, of the actual measured data set.

[2] Note that the determination of periods ≳250 d in the dynamical Lomb–Scargle periodogram is difficult since it is based on segments of 730-d length only. Since the long period shows up in the total periodogram of Fig. 1b, however, we believe the dynamical periodogram to represent at least the general trends in the period shifting behaviour.

Table 1. Observing log of the monitoring observations of LMC X-3.

Obs.	Date (y.m.d)	Exposure (s)	Count rate (count s^{-1})
01	1996.12.05	139800	390.1 ± 0.1
02	1996.12.29	7800	94.3 ± 0.1
03	1997.01.16	7600	83.6 ± 0.1
04	1997.02.07	9300	123.7 ± 0.1
05	1997.03.09	8000	352.2 ± 0.2
06	1997.03.21	7200	374.6 ± 0.2
07	1997.04.17	8500	318.5 ± 0.2
08	1997.05.05	5200	319.3 ± 0.3
09	1997.05.27	8400	289.4 ± 0.2
10	1997.06.18	8100	246.0 ± 0.2
11	1997.07.04	6200	234.8 ± 0.2
12	1997.08.03	5900	148.7 ± 0.2
13	1997.08.19	8100	35.9 ± 0.1
14	1997.09.09	9400	102.6 ± 0.1
15	1997.09.12	7900	113.3 ± 0.2
16	1997.09.19	8500	113.4 ± 0.1
17	1997.09.23	10300	153.7 ± 0.1
18	1997.10.11	7300	127.7 ± 0.2
19	1997.11.02	8400	152.3 ± 0.2
20	1997.11.23	8900	111.5 ± 0.1
21	1997.12.12	3300	166.8 ± 0.3
22	1998.01.06	8200	268.0 ± 0.2
23	1998.01.24	6100	254.0 ± 0.2
24	1998.02.20	9100	213.4 ± 0.2
25	1998.03.12	6600	182.4 ± 0.2
26	1998.04.06	9200	190.0 ± 0.2
27	1998.05.07	7600	169.0 ± 0.2
28	1998.05.29	9400	9.1 ± 0.1
29	1998.06.29	3400	42.5 ± 0.2
30	1998.07.20	9800	137.3 ± 0.1
31	1998.08.12	7700	133.6 ± 0.1
32	1998.09.02	4200	264.7 ± 0.3
33	1998.09.30	7600	33.2 ± 0.1

Exposure times shown are rounded to the closest 100 s. The count rate is background subtracted.

1986) plus an additional power law component. This is the traditional spectral model for describing the X-ray continuum of the soft state. We further discuss below the interpretation and possible shortcomings of this model (Section 5, see also Paper I). Our fits generally gave acceptable results. Several observations, however, showed evidence for deviations of the residuals in the Fe Kα band. Although these deviations are mainly in the 2σ range, adding a narrow ($\sigma = 0.1$ keV) Fe line to the model improved our fits. We therefore added a narrow Gaussian line feature at 6.4 keV to all of our fits. Although the presence of a line is consistent with our analysis from Paper I, we note that Fe-line studies with the PCA are complicated by the presence of systematic features in the PCA response matrix (Wilms et al. 1999a) and by the fact that the power-law and the disc model have comparable flux in the Fe-line region. The line parameters that we found here, therefore, should be seen as consistent with an upper limit of $\sim$60 eV for the equivalent width. We took the absorption in the intervening interstellar medium into account by fixing the equivalent hydrogen column to the value found from radio and *ASCA* observations $N_{\rm H} = 3.2 \times 10^{20}\,{\rm cm}^{-2}$ (Lister-Staveley, private communication; see also Paper I), using the cross sections of Bałucińska-Church & McCammon (1992). Using a fixed $N_{\rm H}$ is justified since preliminary modelling showed that none of the observations had the large $N_{\rm H}$ values that are detectable with the PCA energy range and spectral resolution ($N_{\rm H} \gtrsim 10^{22}\,{\rm cm}^{-2}$; Stelzer et al. 1999).

We list the results of our spectral modelling in Table 2, and a typical spectrum is shown in Fig. 3. Generally, the spectral model described the data satisfactorily with reduced χ^2 values of $\chi^2_{\rm red} \lesssim 2$. We note that especially for some brighter observations, the formal χ^2 values are influenced by systematic features in the response matrix. This can be examined, e.g. by comparing the ratio between the data and the best-fit model, with the ratio between an observation of the Crab pulsar and nebula and the best-fit power law to that observation (Wilms et al. 1999a). Visual inspection reveals that the deviations between the data and the model for all monitoring observations were comparable with or smaller than those seen in the Crab. Thus, although $\chi^2_{\rm red} > 1$ in these cases, adding additional spectral components to the model would only serve to model the response matrix features and not the observed spectrum. We are therefore confident that, given the spectral resolution of the PCA and the faint flux level of LMC X-3, we have found a satisfactory spectral description for all pointed observations.

We emphasize that the interpretation of the spectral components in terms of physical parameters, however, is hampered by the properties of the multi-temperature disc blackbody model. This discussion is necessitated by the result that the typical power law indices found in our data analysis are softer than those found by *Ginga* ($\Gamma \sim 2.2$; Ebisawa et al. 1993). A more detailed discussion can be found in Paper I. A problem associated with using the multi-temperature disc blackbody plus a power law for modelling the soft state is that especially for large Γ (i.e. soft power-law tail), the power law can have a non-negligible flux in the lowest pulse height analyser (PHA) channels so that the fit parameters of the power law are almost completely determined by these low channels. This effect is present in most of our fits for which $\Gamma \gtrsim 4$. We tried to limit the influence of the power law in the higher PHA channels with several other spectral models, e.g. by adding a heavily absorbed power-law to the disc blackbody, by using a modified multi-temperature disc blackbody which includes a high-energy power law tail only above a given energy, or by applying thermal Comptonization models. None of these models resulted in acceptable χ^2 values. In addition, using the multi-temperature disc blackbody and leaving the equivalent column $N_{\rm H}$ a free fit parameter always resulted in $N_{\rm H} \rightarrow 0\,{\rm cm}^2$.

The only model, apart from the one that we adopted here, which allowed us to describe the spectrum of LMC X-3 with similar or even better χ^2 values was a multi-temperature disc blackbody to which a low energy blackbody spectrum was added. Such a model has been successfully applied, e.g. also to the 1997 *RXTE* observations of GRO J1655$-$40 (Rothschild et al., in preparation). Although such a model works for those observations of LMC X-3 where we find $\Gamma \gtrsim 4$, the model fails to reproduce those observations where a harder power law component is clearly present in the data. We therefore decided to use the multi-temperature disc blackbody spectrum plus a power law in our analysis.

The significant contribution of the power law in the low-energy PHA channels has some effect on the determination of the characteristic disc temperature, $kT_{\rm in}$. As we noted in Paper I, the blackbody temperature obtained from *ASCA* data was systematically lower than the $kT_{\rm in}$ derived from the PCA data. We speculated that this was due to the significance of the power law in the low-energy PHA channels and the differing low-energy cut-offs between the two detectors. We further speculated that the *ASCA* fit temperature was more characteristic of the temperature for the 'seed photons' that are Compton upscattered to become the

Table 2. Results of spectral fitting to the LMC X-3 data.

Obs.	$kT_{\rm in}$ (keV)	$A_{\rm disc}$	Γ	$A_{\rm PL}$ $\times 10^{-1}$	$A_{\rm Line}$ $\times 10^{-5}$	EW (eV)	χ^2/dof
01	1.23 ± 0.01	33.9 ± 0.7	2.4 ± 0.2	$0.7^{+0.3}_{-0.2}$	$8.5^{+11.3}_{-8.5}$	14	59.5/47
02	0.92 ± 0.00	$35.9^{+0.8}_{-1.1}$	2.8 ± 0.2	0.5 ± 0.2	8.4 ± 2.2	88	72.7/42
03	0.91 ± 0.01	$29.7^{+1.6}_{-1.7}$	3.0 ± 0.1	1.4 ± 0.3	$6.7^{+2.0}_{-2.7}$	65	60.8/42
04	1.01 ± 0.01	$29.3^{+0.5}_{-0.8}$	4.3 ± 0.3	$3.6^{+1.8}_{-1.0}$	6.8 ± 2.4	51	19.3/41
05	$1.21^{+0.00}_{-0.01}$	$29.9^{+0.6}_{-0.7}$	3.1 ± 0.1	$3.4^{+0.5}_{-0.4}$	$11.6^{+4.1}_{-3.8}$	22	62.6/41
06	$1.22^{+0.00}_{-0.01}$	$31.8^{+0.4}_{-0.6}$	3.2 ± 0.1	3.3 ± 0.5	$20.5^{+4.1}_{-4.5}$	36	59.5/41
07	$1.23^{+0.01}_{-0.00}$	27.5 ± 0.4	4.1 ± 0.2	$5.3^{+1.5}_{-1.1}$	$7.5^{+4.1}_{-3.4}$	16	73.3/41
08	1.22 ± 0.01	29.5 ± 0.5	3.7 ± 0.2	$3.8^{+1.2}_{-0.9}$	$12.0^{+5.0}_{-4.7}$	25	46.4/41
09	$1.20^{+0.00}_{-0.01}$	29.0 ± 0.4	4.1 ± 0.2	$4.8^{+1.4}_{-1.1}$	$13.7^{+3.5}_{-3.7}$	32	49.9/41
10	$1.17^{+0.01}_{-0.00}$	$28.0^{+0.4}_{-0.5}$	$4.2^{+0.3}_{-0.2}$	$5.5^{+1.8}_{-1.3}$	$5.8^{+3.7}_{-3.2}$	17	58.3/41
11	1.16 ± 0.01	26.9 ± 0.5	$4.1^{+0.3}_{-0.2}$	$5.3^{+1.8}_{-1.3}$	10.1 ± 3.9	31	58.1/41
12	1.00 ± 0.01	$29.6^{+1.2}_{-1.6}$	3.1 ± 0.1	$2.1^{+0.6}_{-0.5}$	$8.2^{+2.9}_{-3.1}$	46	97.1/41
13	0.63 ± 0.02	$54.4^{+10.7}_{-8.7}$	2.8 ± 0.1	0.7 ± 0.1	$0.0^{+1.7}_{0.0}$	0	29.0/41
14	0.98 ± 0.01	$28.6^{+0.9}_{-0.7}$	$4.6^{+0.4}_{-0.3}$	$4.6^{+2.4}_{-1.2}$	$7.3^{+2.0}_{-2.5}$	71	34.4/41
15	1.00 ± 0.01	29.4 ± 0.9	4.2 ± 0.3	$3.0^{+1.6}_{-0.7}$	$6.7^{+2.4}_{-2.7}$	56	24.1/41
16	1.05 ± 0.01	$24.7^{+1.4}_{-1.1}$	4.6 ± 0.3	$6.9^{+2.9}_{-1.9}$	$5.3^{+2.5}_{-2.4}$	35	70.2/41
17	1.06 ± 0.01	$27.1^{+0.8}_{-1.4}$	4.0 ± 0.2	$4.6^{+1.1}_{-1.0}$	$2.5^{+2.6}_{-2.5}$	14	75.8/41
18	1.01 ± 0.01	$29.6^{+2.2}_{-1.0}$	$4.2^{+0.3}_{-0.2}$	$4.1^{+1.6}_{-1.1}$	$6.4^{+2.6}_{-3.0}$	46	26.5/41
19	1.06 ± 0.01	$28.6^{+1.0}_{-0.7}$	$4.4^{+0.3}_{-0.2}$	$5.5^{+1.9}_{-1.3}$	$7.5^{+2.5}_{-3.0}$	42	42.6/41
20	0.99 ± 0.01	$27.8^{+0.5}_{-0.8}$	$4.3^{+0.3}_{-0.2}$	$4.5^{+1.8}_{-1.1}$	$8.0^{+2.2}_{-2.7}$	70	17.2/41
21	1.08 ± 0.01	$28.3^{+2.3}_{-0.8}$	$4.3^{+0.5}_{-0.3}$	$4.9^{+3.3}_{-1.5}$	$11.9^{+4.7}_{-4.6}$	59	40.3/41
22	$1.19^{+0.01}_{-0.00}$	27.6 ± 0.4	4.3 ± 0.2	$7.4^{+1.9}_{-1.4}$	11.7 ± 3.6	31	43.8/41
23	1.18 ± 0.01	27.3 ± 0.5	4.2 ± 0.2	$7.4^{+2.1}_{-1.6}$	$11.2^{+3.9}_{-4.5}$	30	38.4/41
24	$1.13^{+0.01}_{-0.00}$	28.1 ± 0.4	$4.4^{+0.3}_{-0.2}$	$7.8^{+2.3}_{-1.6}$	$10.6^{+3.3}_{-2.9}$	38	42.3/41
25	1.10 ± 0.01	$27.3^{+0.3}_{-0.6}$	$4.6^{+0.4}_{-0.3}$	$8.4^{+3.3}_{-2.0}$	10.4 ± 3.4	45	35.2/41
26	1.11 ± 0.01	$27.5^{+0.5}_{-0.6}$	4.3 ± 0.2	$6.5^{+1.7}_{-1.4}$	$9.3^{+3.0}_{-2.9}$	38	55.8/41
27	1.05 ± 0.01	$25.0^{+1.1}_{-1.2}$	3.5 ± 0.1	$4.4^{+0.7}_{-0.6}$	5.8 ± 3.1	28	101.5/41
28			1.8 ± 0.0	0.1 ± 0.0	$1.2^{+1.1}_{-1.2}$	60	26.5/43
29	$0.56^{+0.05}_{-0.07}$	$80.1^{+80.5}_{-30.8}$	2.8 ± 0.1	$1.1^{+0.2}_{-0.3}$	$2.0^{+2.8}_{-2.0}$	33	22.7/41
30	1.04 ± 0.01	27.0 ± 0.6	$4.5^{+0.3}_{-0.2}$	$6.3^{+2.0}_{-1.5}$	$4.7^{+2.6}_{-2.5}$	30	38.1/41
31	1.16 ± 0.00	$24.8^{+0.6}_{-0.5}$	$5.5^{+0.8}_{-0.5}$	$27.7^{+18.7}_{-10.5}$	$7.0^{+3.9}_{-3.2}$	24	87.0/41
32	1.17 ± 0.01	$27.2^{+0.8}_{-0.9}$	3.8 ± 0.1	$7.7^{+1.4}_{-1.2}$	$11.4^{+5.2}_{-4.9}$	30	43.3/41
33	$0.66^{+0.02}_{-0.03}$	$57.0^{+10.7}_{-7.9}$	2.7 ± 0.1	1.0 ± 0.2	$4.9^{+2.3}_{-2.6}$	71	30.3/41

$T_{\rm in}$, $A_{\rm disc}$: peak multi-temperature disc temperature and normalization. Γ: photon index of the power law $A_{\rm PL}$: Power law normalization (photon $\mathrm{keV}^{-1}\,\mathrm{cm}^{-2}\,\mathrm{s}^{-1}$ at 1 keV). $A_{\rm Line}$: Line normalization (photon $\mathrm{cm}^{-2}\,\mathrm{s}^{-1}$ in the line), the Gaussian line was fixed at 6.4 keV with a width σ of 0.1 keV. EW: line equivalent width. Uncertainties are at the 90 per cent confidence level for one interesting parameter ($\Delta\chi^2 = 2.71$), the interstellar equivalent column was fixed at $N_{\rm H} = 3.2 \times 10^{20}\,\mathrm{cm}^{-2}$.

high-energy spectrum. As we further discuss below for our observations of LMC X-1 (Section 4.2), the presence of the power law may greatly affect the determination of the blackbody normalization, $A_{\rm disc}$.

3.4 Transitions between the soft and hard states

We now discuss the variations of the spectral parameters in terms of the long-term variability of LMC X-3. In Fig. 2 we display the spectral variation of LMC X-3 in the context of its ASM long-term light curve. The plot reveals a clear correlation between the total source luminosity, as expressed by the ASM count rate, and the parameters of the soft spectral component. During times of higher source luminosity, the temperature of the multi-temperature disc blackbody, $kT_{\rm in}$, increases. At the same time, the normalization of the disc blackbody stays remarkably constant (see also Fig. 4d). This effect is similar to that found in the soft-state of other galactic black holes (Tanaka & Lewin 1995). During episodes of comparatively low ASM count rate, however, the spectrum shows clear deviations from the typical pure soft state behaviour. During our campaign, there were four of these events: in 1997 January, 1997 August, 1998 June, and 1998 October. During these times $kT_{\rm in}$ decreased to $kT_{\rm in} \lesssim 0.5$ keV, while the photon index hardened (Fig. 4b). For the most extreme case, Obs28, no evidence for the soft component is seen, indicating that $kT_{\rm in} \ll 0.5$ keV, and the photon index is $\Gamma = 1.8$. These values are remarkably similar to the typical hard-state behaviour seen, e.g. in Cyg X-1. *We interpret the decreases in the ASM count rate as evidence for transitions from the normal soft state into the hard state of LMC X-3*.

In Fig. 5 we display the unfolded photon spectrum of Obs28, together with the spectra of the three subsequent monitoring observations, showing the transition from the pure hard-state spectrum back to the soft state. Obs28 is the only observation of our campaign in which there is no detectable evidence for the soft component. The occurrence of a pure hard state is thus either a

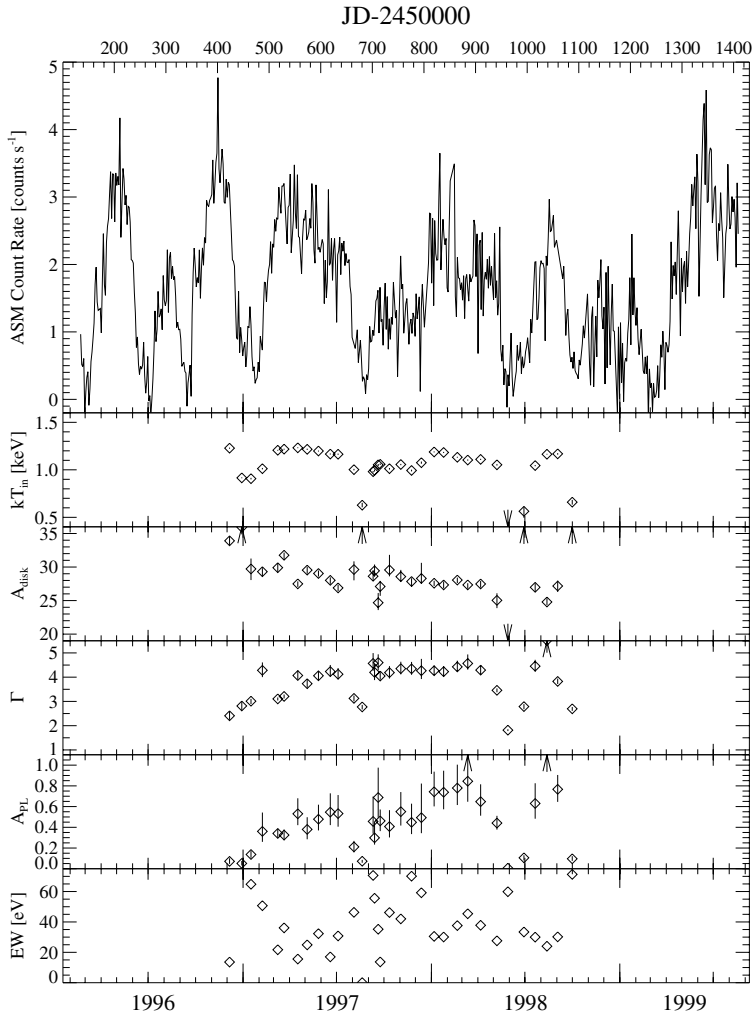

Figure 3. Typical fit of a multi-temperature disc spectrum and a power law to data from LMC X-3. The bottom panel shows the residuals in units of σ. The residuals are consistent with the remaining calibration uncertainty of the PCA.

very rare event for LMC X-3, or, if it is associated with each of the dips observed by the ASM, it is of relatively short duration. The data presented here represent the first observational detection of a pure hard state in LMC X-3. We speculate, however, that the data taken on *HEAO 1* day 461 and mentioned by White & Marshall (1984) might have been observed during one of the soft-to-hard state transitions. During this observation, however, the source was too faint for *HEAO 1* to obtain even a reliable measurement of the hardness ratio. Furthermore, during 2000 April another hard state was seen (Boyd & Smale 2000), with the timing behaviour being hard state like (Homan et al. 2000).

The hard-state observation Obs28 is the observation with the lowest PCA count rate of our campaign, it was also performed close to one of the lowest ASM fluxes seen so far. In Fig. 6 we display $kT_{\rm in}$ as a function of the ASM countrate averaged over 1-d worth of ASM dwellings centered on the observation. In the figure we have identified spectra for which $kT_{\rm in} < 0.8$ keV. All of these spectra also show a power law component which is relatively strong compared with the soft spectral component. These data indicate that for ASM count rates $\lesssim$0.6 cps a transition to the hard-state behaviour is probable. Therefore, it is possible to use the ASM count rate as a trigger for future systematic studies of the soft-to-hard transition in LMC X-3.

Our monitoring observations are too short to be able to characterize the variability of LMC X-3. We computed the average rms variability of the source from the background subtracted 16 s light curves. Although there is an apparent trend of the rms variability to increase with lower source flux, this trend

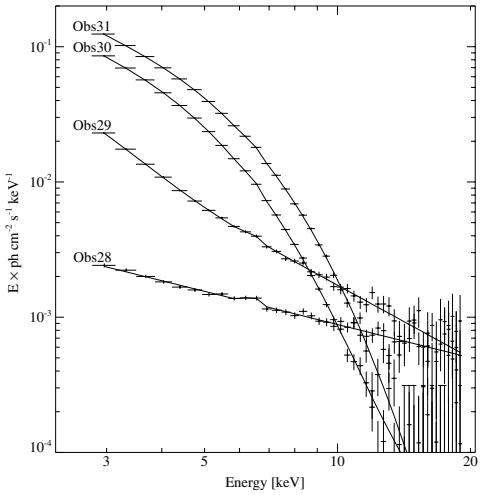

Figure 4. Correlation between the spectral parameters for LMC X-3. The dashed line in panel (d) denotes the proportionality $A_{\rm disc} \propto kT_{\rm in}^{-8/3}$ expected for $T_{\rm in} \propto r_{\rm in}^{-3/4}$ (see text).

is fully consistent with systematic variations due to PCA background model fluctuations at the 2 per cent level. This level is consistent with the uncertainty of the background model found in the time series analysis presented in Paper I, and also with the adjustments to the background flux found during the spectral modelling process. It is therefore impossible to check our interpretation of Obs28 being a hard state or an intermediate (Méndez & van der Klis 1997) state from its temporal characteristics. Much longer hard-state observations (>100 ks) are needed for this determination.

Outside of the hard states, LMC X-3 exhibits the standard behaviour of a classical soft state source. Fig. 4 displays several correlations between the spectral fit parameters. For power law indices $\Gamma \lesssim 4$ there is a clear correlation between the power law flux and Γ: the power law component hardens with decreasing power law flux (Fig. 4a). Such behaviour has been noted for GX 339−4 (Wilms et al. 1999a) and the Seyfert 1 galaxy NGC 5548 (Chiang et al. 2000), albeit in their hard spectral states. Figs 4b and c verify the results of Ebisawa et al. (1993) that during the soft state there is no strong correlation between the soft and the hard component. For $\Gamma \gtrsim 4$, Γ does not correlate with the accretion disc temperature, $kT_{\rm in}$. There is a slight trend for the power law flux and Γ to increase with $kT_{\rm in}$; however, the statistics of the data are not good enough to claim any firm correlation between these two parameters. In conjunction with the above spectral results for LMC X-3, in Paper I we noted that the Fourier frequency-dependent coherence function indicated that the soft and hard X-ray components were uncorrelated with each other for LMC X-1 (the variability of LMC X-3 was too weak to perform such an analysis).

Finally, we consider the behaviour of the soft spectral component. The normalization of the multi-temperature disc blackbody, $A_{\rm disc}$, is nearly constant throughout the monitoring observations (Fig. 4d), while $kT_{\rm in}$ strongly varies. A similar behaviour has been found in those soft state black-hole candidates where the luminosity is dominated by the soft component (Tanaka & Lewin 1995). If $A_{\rm disc}$ is interpreted literally, then $A_{\rm disc} \propto (r_{\rm in}/d)^2 \cos\theta$, where $r_{\rm in}$ is the innermost radius of the accretion disc, d is the distance of the source, and θ is the disc inclination angle. In Fig. 4(d) we display the values of $r_{\rm in}\cos^{1/2}\theta$ corresponding to our modelled values of $A_{\rm disc}$ on the upper x-axis. The parameters for $r_{\rm in}$ found here are typical for galactic black-hole candidates (Yaqoob et al. 1993). Interpreted in this framework, the constancy of $A_{\rm disc}$ for LMC X-3 could imply that the geometrical configuration of the accretion disc does not appreciably change during the soft state episodes of the object, and that all changes in the disc luminosity are accounted for via temperature changes. We also note that for disc blackbody temperatures $kT_{\rm in} \lesssim 0.9$ keV, the data approximately agree with the proportionality of $A_{\rm disc} \propto T_{\rm in}^{-8/3}$ which is expected if $T_{\rm in} \propto r_{\rm in}^{-3/4}$ and the inner disc radius moves outward, with relatively little bolometric luminosity change, during a soft-to-hard state transition (Fig. 4d, dashed line).

The literal interpretation of $A_{\rm disc}$ and $kT_{\rm in}$, however, is not without problems (Merloni et al. 2000). The innermost region of thin accretion discs is more complicated than assumed in the theory underlying the multi-temperature disc blackbody model. Even in simple α accretion disc models (Shakura & Sunyaev 1973), the inner region of the accretion disc is dominated by electron scattering. Thus the emerging spectrum is slightly Comptonized. As a result, the observed $kT_{\rm in}$ does not correspond to the temperature of the inner edge of the disc, but rather equals the colour temperature of the disc (Ebisawa et al. 1991; Shimura & Takahara 1995). Correcting for this effect is strongly model dependent, see, e.g. Shimura & Takahara (1995) and Merloni et al. (2000) for discussions. Furthermore, the presence of a hard spectral component can also influence $A_{\rm disc}$, as we mentioned above (see also Paper I and Section 4.2). We therefore consider it dangerous to use correlations between a (corrected) $kT_{\rm in}$ and $r_{\rm in}$ fit parameters to draw firm conclusions on the geometry or physical environment of the observed system. The apparent independency of the disc normalization from its characteristic (colour) temperature $kT_{\rm in}$, however, is striking in the case of LMC X-3. Any accretion disc theory attempting to model this object will have to explain this independency.

Finally, we note that no clear correlation is found between the equivalent width of the iron line and the other spectral parameters. This is consistent with our interpretation of the iron line parameters as upper limits.

4 LMC X-1: LONG TIME-SCALE SPECTRAL VARIABILITY

4.1 Introduction

Like LMC X-3, LMC X-1 was also discovered during the *UHURU* scans of the LMC. Its optical companion is a O(7–9)III star with a mass function of $0.144\,{\rm M}_\odot$ and an orbital period of 4.2 d (Hutchings et al. 1987; Hutchings, Crampton & Cowley 1983; Cowley et al. 1995) in a photoionized He II nebula (Bianchi & Pakull 1985; Pakull & Angebault 1986). The luminosity of LMC X-1 is about $2 \times 10^{38}\,{\rm erg\,s^{-1}}$ (Long et al. 1981) and was found to be quite constant (Syunyaev et al. 1990).

The X-ray spectrum of LMC X-1 is similar to that of LMC X-3 (Ebisawa, Mitsuda & Inoue 1989; Paper I and references therein), although the relative flux of the disc blackbody with respect to the power law is smaller. There is again evidence for a weak Fe emission line.

The long-term behaviour of LMC X-1 during 1996 as seen by

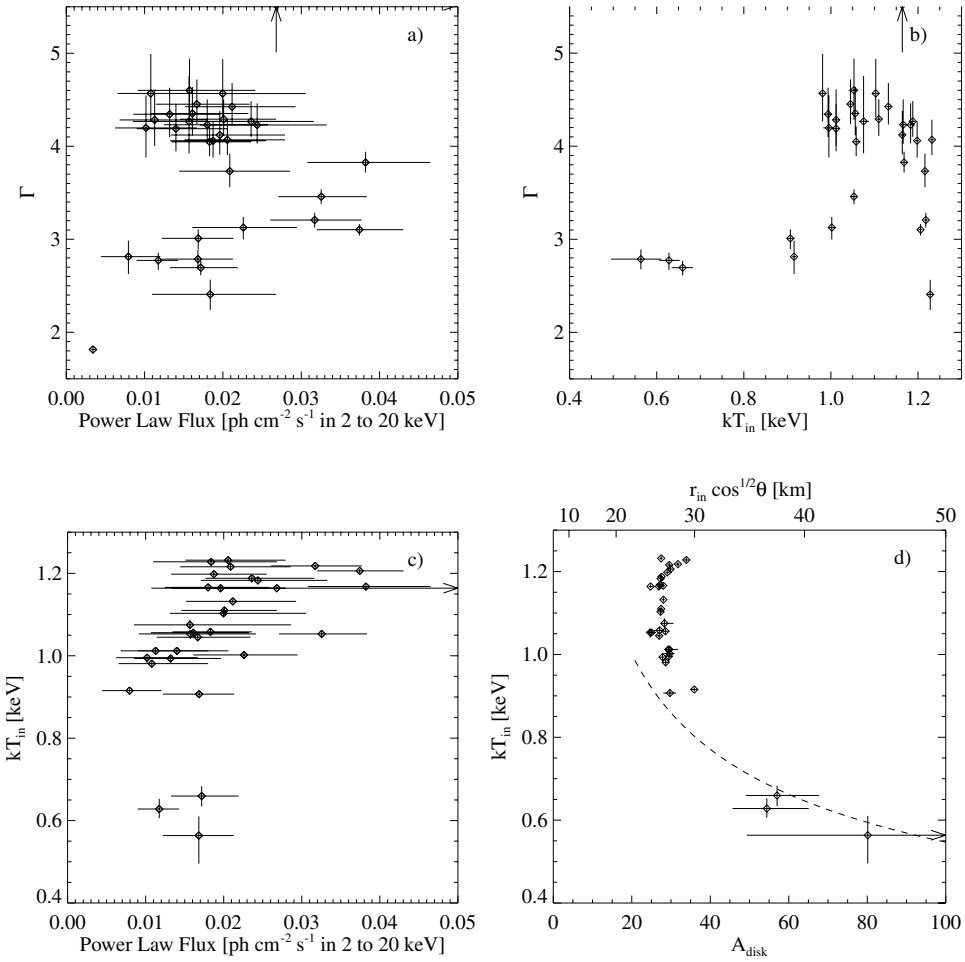

Figure 5. Spectral evolution of LMC X-3 from the hard state of Observation 28 to the normal soft state seen in Observations 30 and 31. Shown are the unfolded photon spectra, multiplied by photon energy, the lines denote the best-fitting model.

RXTE has been analysed by Schmidtke, Ponder & Cowley (1999). In agreement with previous observations these authors did not find evidence for any systematic variability on long timescales. We will, therefore, not re-analyse these data but concentrate rate in what follows on our monitoring data from 1997 and 1998.

4.2 Long-term variability of LMC X-1

The data of the monitoring observations of LMC X-1 were treated in the same way as those for LMC X-3. A log of the observations can be found in Table 3. During the campaign, the count rate of LMC X-1 was on average a factor of ∼2 smaller than that of LMC X-3. Again, we modelled the PCA data using a multi-temperature disc blackbody plus a power law and an iron line. We assumed an equivalent hydrogen column of $N_{\rm H} = 7.2 \times 10^{21}\,{\rm cm}^{-2}$ (Lister-Staveley, 1999, priv. comm., see also Paper I), as is appropriate from the radio measurements. The results of the spectral modelling are shown in Table 4.

As for LMC X-3, the LMC X-1 spectra are well-described by a phenomenological model consisting of a disc blackbody (with $kT_{\rm in} \approx 0.8$–1 keV) and a soft ($\Gamma \gtrsim 3.5$) power law component. Fig. 7 displays the correlations among the fit parameters for LMC X-1. The most striking aspect of Fig. 7 is the apparent strong correlation between the phenomenological disc blackbody temperature, $kT_{\rm in}$, and the disc blackbody normalization, $A_{\rm disc}$. Furthermore, there is a weaker correlation between the disc temperature and the 2–20 keV power law flux. These correlations are such that the disc temperature decreases by ∼20 per cent while its normalization increases by a factor of ∼4. This yields an overall increase of the blackbody flux by a factor of ∼1.6. There is at the same time, however, a decrease by a factor of ∼2 in the power law flux. In contrast to LMC X-3 the contribution of

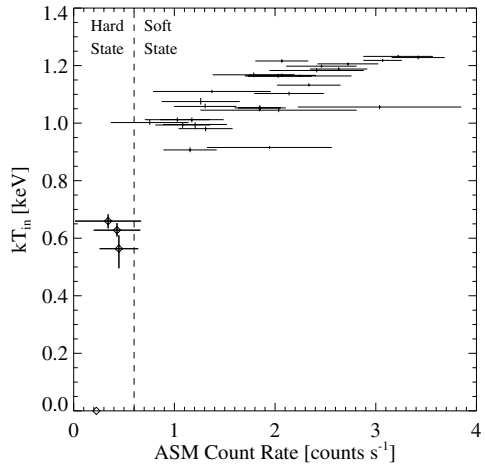

Figure 6. The disc blackbody temperature, $kT_{\rm in}$ as a function of the 1-d averaged ASM count rate. Spectra observed when the ASM count rate was less than about 0.6 count s^{-1} (indicated by the dashed line) exhibit signs for a transition to the hard state.

Table 3. Observing log of the monitoring observations of LMC X-1.

Obs.	Date (y.m.d)	Exposure (s)	Count rate (count s^{-1})
01	1996.12.06	128900	151.6 ± 0.0
02	1996.12.30	8600	146.7 ± 0.2
03	1997.01.18	8200	180.4 ± 0.2
04	1997.02.08	9300	149.4 ± 0.1
05	1997.03.09	3800	157.0 ± 0.2
06	1997.03.21	8200	160.8 ± 0.2
07	1997.04.16	10600	163.4 ± 0.1
08	1997.05.07	8600	163.6 ± 0.2
09	1997.05.28	7000	147.2 ± 0.2
10	1997.06.18	3600	161.9 ± 0.2
11	1997.07.04	3400	148.6 ± 0.3
12	1997.08.01	8500	157.1 ± 0.2
13	1997.08.20	7600	171.1 ± 0.2
14	1997.09.09	9600	138.9 ± 0.1
15	1997.09.12	8300	163.3 ± 0.2
16	1997.09.19	9100	120.8 ± 0.1
17	1997.10.10	9100	154.3 ± 0.2
18	1997.11.01	8800	157.0 ± 0.2
19	1997.11.23	6400	156.1 ± 0.2
20	1997.12.12	5100	160.7 ± 0.2
21	1998.01.04	8700	189.4 ± 0.2
22	1998.01.25	7100	168.0 ± 0.2
23	1998.02.20	9200	177.1 ± 0.2
24	1998.03.12	3300	173.9 ± 0.3
25	1998.04.07	9400	178.1 ± 0.2
26	1998.05.06	5500	154.0 ± 0.2
27	1998.05.28	8900	179.1 ± 0.2
28	1998.06.28	3700	178.1 ± 0.3
29	1998.07.19	9300	151.4 ± 0.2
30	1998.08.13	8000	181.2 ± 0.2
31	1998.09.02	5200	143.9 ± 0.2
32	1998.09.29	8600	112.7 ± 0.1

Exposure times shown are rounded to the closest 100 s. The count rate is background subtracted.

the power law makes up a greater fraction of the total 2–20-keV flux in LMC X-1; therefore, the decrease (increase) in disc temperature (normalization) corresponds to an overall decrease in 2–20-keV flux by only ≈20 per cent.

There are two possibilities to explain these spectral correlations. First, it is possible that, as in LMC X-3, the overall decrease in 2–20-keV flux corresponds to the beginnings of a transition to a low/hard state. Arguing against this notion, however, is that we do not see any corresponding hardening of the power law flux. Second, a more likely scenario is that we are seeing a complicated systematic interaction between the phenomenological disc component and power law component. For the soft photon indices seen in LMC X-1 there is a large contribution from the power law in the low-energy PHA channels. We therefore expect a strong systematic correlation between the power law flux, the disc temperature, and the disc normalization. In Fig. 8 we display the 99 per cent error contours computed for all spectra from the monitoring campaign. A strong correlation between the parameters that is consistent with the general trend seen in Fig. 7(d) is apparent. This correlation within the individual data sets strongly points towards our second argument, that at least part of the correlation is due to systematic errors in our model. We note, however, that the total variation of the parameters is much larger than the uncertainty of the individual data points. It is possible, therefore, that at least part of the $kT_{\rm in}$–$A_{\rm disc}$ correlation is indeed real. Observations with instruments with a lower energy boundary, however, are needed to verify this correlation.

Apart from a 50-d periodicity, which is seen in many weak ASM sources (Benlloch-García et al. 2000) and is likely due to the nodal precession of the *RXTE* orbit, no significant periodicity was found in the ASM data. The overall $\mathcal{O}$ (10 per cent) flux variability exhibited on the long time-scales of the ASM and our monitoring observations is comparable with the variability observed on time-scales of $\lesssim$1 ks, as discussed in Paper I. In Paper I we attributed the variability of LMC X-1 to accretion rate variations in a wind-fed accretion system.

5 THE SUPERORBITAL PERIOD OF LMC X-3

The 100–250-d periodicities seen in the ASM light curve of LMC X-3 are significantly longer than the measured orbital period of 1.7 d. For the case of Her X-1, the 35-d super-orbital period (Giacconi et al. 1973) was interpreted almost immediately as the result of periodic obscuration by a precessing accretion disc which is tilted with respect to the plane of the binary system (Katz 1973). The large amplitude of the X-ray flux (a factor of 30 between the ASM count rate during the 'main on' and the 'low state' is typical; see, e.g., Coburn et al. 2000), as well as numerous other observations (see Scott & Leahy 1999 and references therein), imply a near edge-on ($i \sim 85°$) disc. In addition, a fraction of the central X-ray flux of Her X-1 is likely scattered into our line of sight by an extended corona (Stelzer et al. 1999 and references therein). As discussed in the introduction, possible driving mechanisms for the disc-warp include radiation pressure due to the luminous central X-ray source (Pringle 1996; Maloney et al. 1996; Maloney & Begelman 1997; Maloney et al. 1998), torques exerted by an accretion disc wind (Schandl & Meyer 1994; Schandl 1996) or tidal forces (Larwood 1998, and references therein).

For the case of LMC X-3, if the super-orbital variability were also due to changes in the accretion disc geometry, we should be

Table 4. Results of spectral fitting to the LMC X-1 data.

Obs.	$kT_{\rm in}$ (keV)	$A_{\rm disc}$	Γ	$A_{\rm PL}$ $\times 10^{-1}$	$A_{\rm Line}$ $\times 10^{-5}$	EW (eV)	χ^2/dof
01	0.89 ± 0.00	63.8 ± 0.0	3.4 ± 0.0	4.1 ± 0.0	10.7 ± 0.0	63	80.8/41
02	0.96 ± 0.01	$33.0^{+1.6}_{-2.1}$	3.4 ± 0.0	5.9 ± 0.6	$10.8^{+3.0}_{-2.8}$	53	84.9/42
03	0.93 ± 0.01	$45.2^{+2.6}_{-1.8}$	$3.1^{+0.0}_{-0.1}$	4.5 ± 0.5	$19.2^{+3.0}_{-3.1}$	85	88.2/42
04	0.87 ± 0.01	$63.8^{+3.2}_{-4.1}$	3.5 ± 0.1	$7.8^{+1.2}_{-1.0}$	$13.1^{+3.0}_{-2.9}$	67	50.3/41
05	0.91 ± 0.01	$47.1^{+3.5}_{-4.2}$	3.7 ± 0.1	8.9 ± 1.8	$8.1^{+4.3}_{-4.0}$	47	37.5/41
06	0.88 ± 0.01	$61.3^{+2.6}_{-3.7}$	3.6 ± 0.1	6.7 ± 1.1	$8.6^{+3.1}_{-2.7}$	51	45.5/41
07	0.86 ± 0.01	$69.6^{+2.5}_{-4.0}$	3.6 ± 0.1	$7.5^{+1.2}_{-1.0}$	$11.6^{+2.6}_{-2.5}$	71	95.8/41
08	0.88 ± 0.01	$62.5^{+1.7}_{-3.2}$	3.6 ± 0.1	$7.4^{+1.1}_{-1.2}$	$11.3^{+2.7}_{-2.9}$	65	48.7/41
09	0.87 ± 0.01	$55.2^{+3.1}_{-4.2}$	3.7 ± 0.1	8.2 ± 1.4	$11.7^{+2.8}_{-2.9}$	76	52.7/41
10	0.85 ± 0.01	$67.5^{+6.1}_{-6.2}$	3.7 ± 0.1	$8.9^{+1.9}_{-2.0}$	$13.1^{+4.0}_{-4.4}$	78	32.4/41
11	0.83 ± 0.01	$77.6^{+5.9}_{-11.9}$	3.7 ± 0.1	$7.6^{+2.1}_{-2.0}$	6.6 ± 4.2	46	37.6/41
12	0.93 ± 0.01	$36.8^{+2.1}_{-2.7}$	3.5 ± 0.1	$7.7^{+1.0}_{-0.9}$	$10.2^{+2.8}_{-3.0}$	56	91.2/41
13	0.91 ± 0.01	$53.8^{+2.7}_{-3.2}$	3.7 ± 0.1	$8.8^{+1.2}_{-1.3}$	$9.3^{+3.1}_{-3.2}$	50	35.4/41
14	0.95 ± 0.01	$29.8^{+1.6}_{-2.4}$	3.6 ± 0.1	$8.6^{+1.0}_{-0.9}$	$9.4^{+2.9}_{-2.8}$	51	54.3/41
15	0.85 ± 0.01	$74.3^{+2.9}_{-5.3}$	3.8 ± 0.1	$9.0^{+1.6}_{-1.3}$	$8.6^{+2.9}_{-2.6}$	55	85.9/41
16	0.89 ± 0.01	$46.5^{+2.3}_{-3.7}$	3.7 ± 0.1	$8.0^{+1.3}_{-1.1}$	$11.5^{+2.8}_{-2.7}$	73	68.3/41
17	1.00 ± 0.01	$23.1^{+1.3}_{-1.8}$	$3.5^{+0.0}_{-0.1}$	8.0 ± 0.8	$10.5^{+3.0}_{-2.7}$	54	34.5/41
18	0.97 ± 0.01	$30.2^{+1.6}_{-2.1}$	3.5 ± 0.1	$7.3^{+0.9}_{-0.8}$	$11.0^{+2.7}_{-3.1}$	58	29.9/41
19	0.98 ± 0.01	$26.9^{+1.9}_{-2.4}$	3.6 ± 0.1	9.3 ± 1.1	$12.5^{+3.3}_{-3.7}$	63	47.0/41
20	0.88 ± 0.01	$63.7^{+3.5}_{-4.5}$	3.9 ± 0.1	$10.4^{+2.0}_{-1.8}$	$7.2^{+3.4}_{-3.5}$	45	36.9/41
21	0.96 ± 0.01	$38.1^{+2.1}_{-2.4}$	3.7 ± 0.0	$11.8^{+1.2}_{-1.1}$	$13.1^{+2.9}_{-3.2}$	59	66.0/41
22	0.98 ± 0.01	$29.6^{+1.8}_{-2.2}$	3.7 ± 0.1	9.9 ± 1.1	$10.9^{+3.3}_{-3.4}$	53	38.6/41
23	0.97 ± 0.01	$28.0^{+1.8}_{-2.3}$	3.6 ± 0.0	$10.4^{+0.9}_{-0.8}$	14.5 ± 3.0	66	90.9/41
24	0.90 ± 0.01	$52.5^{+4.7}_{-8.2}$	3.7 ± 0.1	9.9 ± 1.9	$7.7^{+4.5}_{-5.2}$	40	39.1/41
25	0.93 ± 0.01	$37.7^{+2.0}_{-3.0}$	3.7 ± 0.0	11.7 ± 1.1	$10.7^{+3.2}_{-2.7}$	52	40.9/41
26	0.87 ± 0.01	$58.1^{+3.7}_{-4.3}$	3.8 ± 0.1	$9.6^{+1.6}_{-1.8}$	$11.8^{+3.5}_{-3.6}$	73	46.4/41
27	0.90 ± 0.01	$46.8^{+3.6}_{-3.2}$	$3.7^{+0.0}_{-0.1}$	11.8 ± 1.2	$15.9^{+2.9}_{-3.0}$	79	44.2/41
28	$0.90^{+0.01}_{-0.02}$	$48.1^{+5.5}_{-4.9}$	3.7 ± 0.1	11.8 ± 1.9	$14.9^{+4.5}_{-4.7}$	75	59.5/41
29	0.87 ± 0.01	$55.8^{+2.9}_{-3.9}$	3.9 ± 0.1	$11.9^{+1.5}_{-1.4}$	$8.1^{+2.6}_{-2.8}$	54	34.5/41
30	0.94 ± 0.01	31.9 ± 2.8	3.6 ± 0.0	$11.9^{+1.1}_{-0.9}$	$16.9^{+3.0}_{-3.5}$	78	110.5/41
31	$0.91^{+0.02}_{-0.01}$	$35.9^{+3.2}_{-4.0}$	3.8 ± 0.1	$13.4^{+1.9}_{-1.6}$	$7.6^{+4.0}_{-3.7}$	43	45.7/41
32	$1.06^{+0.03}_{-0.02}$	$10.6^{+1.0}_{-1.4}$	3.7 ± 0.0	12.9 ± 0.9	$9.0^{+3.2}_{-2.9}$	48	71.7/41

See Table 2 for an explanation of the fit parameters. The interstellar equivalent column was fixed at $N_{\rm H} = 7.2 \times 10^{21}\,{\rm cm}^{-2}$.

able to observe strong variations in $N_{\rm H}$ as are observed for the turn-on of the Main-On state of Her X-1 (Kuster et al. 1999). Were the large intensity drops in LMC X-3 by a factor of more than five at 5 keV seen solely due to variations in $N_{\rm H}$, we would expect columns on the order of $N_{\rm H} > 5 \times 10^{23}\,{\rm cm}^{-2}$ blocking our line of sight. Although such columns are readily detectable with *RXTE*, they were not observed. Given the generally good model fits to the observed data and satisfactory residuals, only small changes of $N_{\rm H}$ above the interstellar value appear to be allowed by the data. We conclude that the strong intensity variations of LMC X-3 are not due to the accretion disc blocking our line of sight.

LMC X-3 is spectrally similar to the X-ray binary V1408 Aql (=4U1957+11), which also shows evidence of long-term (100–300-d) periodicities (Nowak & Wilms 1999). Coupled with evidence from recent optical observations (Hakala et al. 1999), we have argued that V1408 Aql also exhibits evidence of a warped precessing disc (Nowak & Wilms 1999). The ASM flux of V1408 Aql, however, varies only by a factor of $\lesssim 2$ (consistent with warp inclination angle changes of $\pm 20°$; Nowak & Wilms 1999), which is far less than the factor of $\gtrsim 5$ ASM flux variations seen for LMC X-3. Such large amplitude variations would be very difficult to achieve unless the inclination of the LMC X-3 system were comparable with that of Her X-1.[3] Given the lack of any strongly detected variability on the orbital time-scale in the ASM light curve of LMC X-3, this seems unlikely.

As discussed in Section 3.4, spectroscopy yields strong indications that LMC X-3 is periodically transitting into and out of the canonical low/hard X-ray spectral state of galactic black holes. Such transitions are typical for black holes as they drop below ~5 per cent of their Eddington luminosity (Nowak 1995; and references therein). If the peak ASM flux corresponds to ~30 per cent $L_{\rm Edd}$, then the observed transition flux threshhold of ~0.6 cps in the ASM is roughly consistent with 5 per cent of the Eddington luminosity. The question then arises of why LMC X-3 apparently shows evidence for large accretion rate variations, whereas LMC X-1 does not and V1408 Aql might not.[4]

[3] Van der Klis et al. (1983), however, argue for an inclination of LMC X-3 comparable to that which we inferred for V1408 Aql, i.e. $i \sim 70°$. Recent X-ray observations of LMC X-3 (Boyd, private communication) show tentative evidence of an orbital modulation. This might indicate some warping of at least the outer disc edge (see, for example, Dubus et al. 1999), in conjunction with the other long-term variability mechanisms discussed below.

[4] V1408 Aql historically has had far fewer X-ray observations than LMC X-3; therefore, the range of its X-ray spectral variations is far less certain.

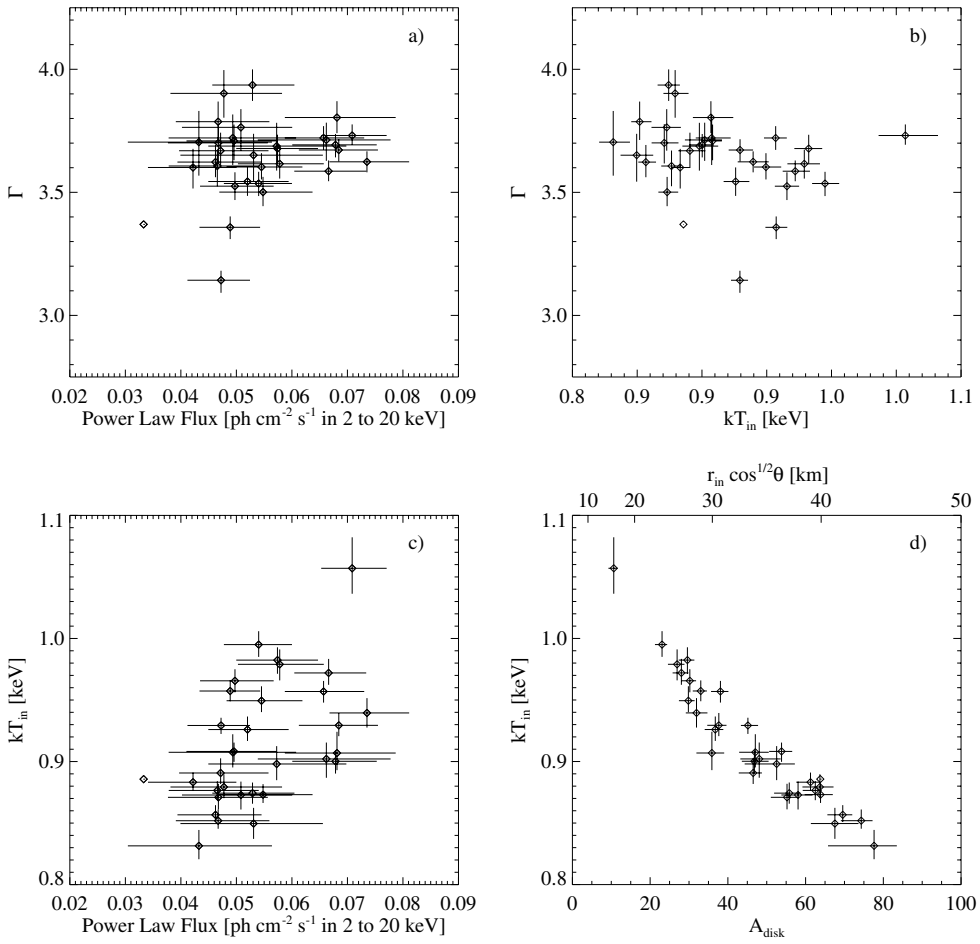

Figure 7. Correlation between the spectral parameters for LMC X-1. Note that the scales of the plots differ from those of Fig. 4!

One possible explanation for the periodic variability seen in LMC X-3 is a Compton heated accretion disc wind-driven limit cycle, as discussed by Shields et al. (1986). At large radii, in the optically thin upper atmosphere of the outer disc, the central X-ray source will heat the disc temperature to the inverse Compton temperature given by

$$4kT_{\rm IC} \equiv \int F_\nu h\nu \,{\rm d}\nu / \int F_\nu \,{\rm d}\nu, \tag{2}$$

where F_ν is the central source flux per unit frequency (Begelman et al. 1983; Begelman & McKee 1983; Shields et al. 1986; Schandl & Meyer 1994). If the sound speed for the inverse Compton temperature exceeds the escape velocity in the outer disc, a coronal wind can be driven off of the disc. For this to occur, the outer disc must have a radius

$$R_{\rm out} \geq 10^{11}\ {\rm cm} \left(\frac{3\,{\rm keV}}{kT_{\rm IC}}\right)\left(\frac{M}{{\rm M}_\odot}\right). \tag{3}$$

LMC X-1, which is likely a wind-fed accretion system (Paper I, and references therein), probably has a much smaller circularization radius than this value, perhaps substantially so, and therefore is not expected to be driving off a wind from its outer disc. V1408 Aql, assuming a $2\,{\rm M}_\odot$ primary and a $1\,{\rm M}_\odot$ companion, has a disc circularization radius of $\sim 4 \times 10^{10}$ cm, and also is not expected to be driving off a substantial wind (although it may show signs of a photoionized atmosphere; Nowak & Wilms 1999). For the measured system parameters of LMC X-3, the disc circularization radius is $\sim 1.6 \times 10^{11}$ cm, and therefore may be driving a substantial Compton-heated wind.

This opens up the possibility that the central X-ray source of LMC X-3 drives off a sufficiently strong wind such that it 'starves' itself of fuel. The mass accretion rate deficit then will propagate inwards on a viscous time-scale. The central source X-ray flux will decrease thereby shutting off the wind, and a limit-cycle can then occur on a viscous time-scale. This time-scale can be of order of 100 d if α, the usual disc viscosity parameter, is

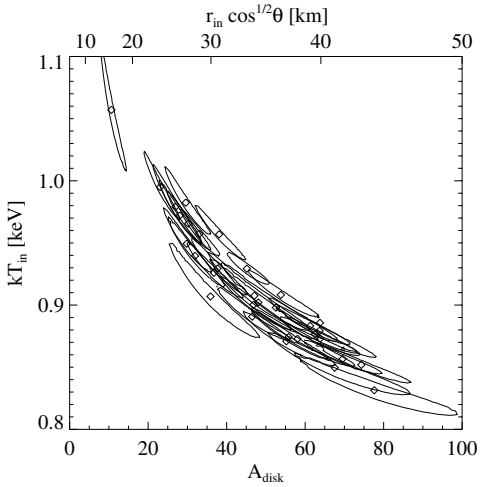

Figure 8. Same plot as Fig. 7d, but including 99 per cent error contours for each of the fits. The error contours indicate a strong *systematic* correlation between kT_{in} and A_{disc}.

$\approx 10^{-2}$ (Shields et al. 1986). One requirement of the instability discussed by Shields et al. is that at the peak mass flux of the wind, a large fraction, $\gtrsim$90 per cent, of the total accretion flow is expelled from the system. This is consistent with the large amplitude variability exhibited by LMC X-3 in the ASM light curve. As one expects the optical flux to come from large radii and the accretion rate fluctuations to propagate inwards from the outer disc, this picture is also consistent with the 20-d optical lead observed by Cowley et al. (1991).

To verify a picture such as discussed by Shields et al. (1986), one must verify that the low/hard flux periods of LMC X-3 truly correspond to a 'canonical' low/hard state. Additionally, one needs to search for signs of the X-ray heated wind. As regards the former possibility, sufficiently long *RXTE* observations during the hard state (>100 ks) should be able to detect the characteristically large amplitude variability of this state. Furthermore, it recently has been noted that low/hard states of galactic black holes, as opposed to high/soft states, typically show strong radio emission (Fender et al. 1999, Corbel et al. 1998, Zhang et al. 1997 and references therein). A previous radio survey of LMC X-1 and LMC X-3 at 3.5 and 6.3 cm did not result in the detection of these objects. The upper limits for the flux is 1.5 mJy for LMC X-1. For LMC X-3, an upper limit of 0.12 mJy at 3.5 cm and 0.18 mJy at 6.3 cm has been reported (Fender et al. 1998). These upper limits, however, were measured during the soft state of LMC X-3. The above flux limits do not apply during the recurring episodes of the hard state. Scaling from Cyg X-1, LMC X-3 should be observable at a flux of $\sim$0.05 mJy with a sensitive radio telescope during these phases.

6 SUMMARY

In this work, we have presented the analysis of an approximately two-year-long *RXTE* monitoring campaign of LMC X-3 and LMC X-1. The primary results of these analyses are as follows.

(i) Both LMC X-1 and LMC X-3 can usually be well-described by a phenomenological model consisting of a disc blackbody with $kT_{in} \sim 1$ keV and a soft ($\Gamma \gtrsim 3$) power law extending down to the lowest PHA channels.

(ii) LMC X-1 shows 2–20-keV energy flux variations with root-mean-square (rms) variability of $\mathcal{O}$(10 per cent) on time-scales of weeks to months. This is comparable with the rms variability exhibited on time-scales $\lesssim$1 ks, as discussed in Paper I. As elaborated upon in Paper I, we attributed the variability to accretion rate variations in a wind-fed accretion system.

(iii) Accompanying the flux variations in LMC X-1 are correlations among the phenomenological disc blackbody temperature, disc blackbody normalization, and power law flux. These correlations could be due to variations near a soft-state/hard-state transition region. A strong possibility, however, is that these correlations are due to a systematic dependence of the phenomenological fit components upon one another.

(iv) LMC X-3 shows far larger 2–20-keV flux variations than LMC X-1, i.e. a factor of $\mathcal{O}$(10) luminosity variations on 100–200-d time-scales. These fluctuations are quasi-periodic, albeit with time-varying periods. At the beginning of the timespan covered by the ASM light curve, $\sim$100 and $\sim$180-d periods are present, whereas at the end of the timespan covered by the ASM light curve, $\sim$160- and $\sim$240-d periods are present.

(v) The flux variations in LMC X-3 are correlated with clear spectral variations. At high ASM count rates, the flux variations are predominantly associated with variations of the phenomenological disc blackbody temperature, kT_{in}, while maintaining a relatively constant disc blackbody normalization, A_{disc}. As the ASM count rate drops below $\approx$0.6 cps, the disc blackbody temperature drops, the disc blackbody normalization increases, and the power law photon index hardens to $\Gamma \sim 1.8$.

(vi) The spectral variations in LMC X-3 are consistent with recurring state transitions between the canonical high/soft and low/hard X-ray states of galactic black holes. One possible mechanism for explaining the observed periodicities and spectral variations is a wind-driven limit-cycle, as discussed by Shields et al.(1986).

As discussed above, there are several ways of determining whether the low flux/hard spectral states do represent canonical low/hard states of galactic black holes. First, a relatively long (>100-ks) *RXTE* observation can determine whether the fast time-scale variability is that expected. Second, one can search for an increase of the radio flux concurrent with the transition to the low/hard state, as has been seen for GX 339-4 (Fender et al. 1999) and Cyg X-1 (Zhang et al. 1997). Evidence of a Compton-heated wind should also be searched for in LMC X-3. Sufficiently long observations with a sensitive X-ray spectroscopy instrument may reveal spectral evidence for a wind (e.g. emission lines in the 1-keV region) that may be driving a limit cycle in the LMC X-3 system.

ACKNOWLEDGMENTS

The research presented in this paper has been financed by NASA grants NAG5-3225, NAG5-4621, NAG5-4737, NSF grants AST95-29170, AST98-76887, DFG grant Sta 173/22, and a travel grant to JW and KP from the Deutscher Akademischer Austauschdienst. We thank Didier Barret, Omer Blaes, Włodzimierz Kluźniak, Phil Maloney, Chris Reynolds, Richard Rothschild, Greg Shields, and Ron Taam for helpful discussions. Lister Staveley-Smith provided us with the unpublished N_H values for

LMC X-1 and LMC X-3. MAN and JW acknowledge the hospitality of the Aspen Center for Physics and all participants of the Aspen 1999 summer workshop on 'X-ray Probes of Relativistic Astrophysics' for discussions.

REFERENCES

Arnaud K. A., 1996, in Jacoby J. H., Barnes J., eds, Astronomical Data Analysis Software and Systems V, Astron. Soc. Pacific, Conf. Ser., Vol. 101. Astron. Soc. Pacific, San Francisco, p. 17

Bałucińska-Church M., McCammon D., 1992, ApJ, 400, 699

Begelman M. C., McKee C. F., 1983, ApJ, 271, 89

Begelman M. C., McKee C. F., Shields G. A., 1983, ApJ, 271, 70

Benlloch S., Wilms J., Staubert R., Nowak M., 2000, Proc. 4th INTEGRAL Symposium. ESA-SP, in press

Bianchi L., Pakull M., 1985, A&A, 146, 242

Bouchet L. et al., 1993, ApJ, 407, 739

Boyd P., Smale A., 2000, IAU Circ. 7424,

Chiang J., Reynolds C. S., Blaes O. M., Nowak M. A., Murray N., Madejski G., Marshall H. L., Magdziarz P., 2000, ApJ, 528, 292

Coburn W. et al., 2000, ApJ, 543, 351

Corbel S., Fender R. P., Durouchoux P., Sood R. K., Tzioumis A. K., Spencer R. E., Campbell-Wilson D., 1997, in Dermer C. D., Strickman M. S., Kurfess J. D., eds, Proc. 4th Compton Symposium, AIP Conf. Proc. 410. AIP, Woodbury, p. 937

Corbel S., Fender R., Tzioumis A. K., Nowak M., McIntyre V., Durouchoux P., Sood R., 2000, A&A, 359, 251

Cowley A. P., Crampton D., Hutchings J. B., Remillard R., Penfold J. E., 1983, ApJ, 272, 118

Cowley A. P. et al., 1991, ApJ, 381, 526

Cowley A. P., Schmidtke P. C., Hutchings J. B., Crampton D., 1994, ApJ, 429, 826

Cowley A. P., Schmidtke P. C., Anderson A. L., McGrath T. K., 1995, PASP, 107, 145

Cui W., Heindl W. A., Rothschild R. E., Zhang S. N., Jahoda K., Focke W., 1997, ApJ, 474, L57

Cui W., Ebisawa K., Dotani T., Kubota A., 1998, ApJ, 493, L75

Davies S. R., 1990, MNRAS, 244, 93

Dove J. B., Wilms J., Nowak M. A., Vaughan B. A., Begelman M. C., 1998, MNRAS, 289, 729

Dubus G., Lasota J., Hameury J., Charles P., 1999, MNRAS, 303, 139

Ebisawa K., Mitsuda K., Inoue H., 1989, PASJ, 41, 519

Ebisawa K., Mitsuda K., Hanawa T., 1991, ApJ, 367, 213

Ebisawa K., Makino F., Mitsuda K., Belloni T., Cowley A. P., Schmidtke P. C., Treves A., 1993, ApJ, 403, 684

Fender R. P., Southwell K., Tzioumis A. K., 1998, MNRAS, 298, 692

Fender R. et al., 1999, ApJ, 519, L165

Giacconi R., Gursky H., Kellogg E., Levinson R., Schreier E., Tananbaum H., 1973, ApJ, 184, 227

Griffiths R. E., Seward F. D., 1977, MNRAS, 180, 75P

Hakala P. J., Muhli P., Dubus G., 1999, MNRAS, 306, 701

Homan J., Jonker P. G., van der Klis M., Kuulkers E., 2000, IAU Circ. 2425

Hutchings J. B., Crampton D., Cowley A. P., 1983, ApJ, 275, L43

Hutchings J. B., Crampton D., Cowley A. P., Bianchi L., Thompson I. B., 1987, AJ, 94, 340

Johnston M. D., Bradt H. V., Doxsey R. E., 1979, ApJ, 233, 514

Katz J. I., 1973, Nature, 246, 87

Kuiper L., van Paradijs J., van der Klis M., 1988, A&A, 203, 79

Kuster M., Wilms J., Blum S., Staubert R., Gruber D., Rothschild R., Heindl W., 1999, Astrophys. Lett. Commun., 38, 161

Larwood J., 1998, MNRAS, 299, L32

Leahy D. A., Darbro W., Elsner R. F., Weisskopf M. C., Kahn S., Sutherland P. G., Grindlay J. E., 1983, ApJ, 266, 160

Leong C., Kellogg K., Gursky H., Tananbaum H., Giacconi R., 1971, ApJ, 170, L67

Levine A. M., Bradt H., Cui W., Jernigan J. G., Morgan E. H., Remillard R., Shirey R. E., Smith D. A., 1996, ApJ, 469, L33

Lomb N. R., 1976, Ap&SS, 39, 447

Long K. S., Helfand D. J., Grabelsky D. A., 1981, ApJ, 248, 925

Makishima K., Maejima Y., Mitsuda K., Bradt H. V., Remillard R. A., Tuohy I. R., Hoshi R., Nakagawa M., 1986, ApJ, 308, 635

Maloney P., Begelman M. C., 1997, ApJ, 491, L43

Maloney P. R., Begelman M. C., Pringle J. E., 1996, ApJ, 472, 582

Maloney P. R., Begelman M. C., Nowak M. A., 1998, ApJ, 504, 77

Mazeh T., van Paradijs J., van den Heuvel E. P. J., Savonije G. J., 1986, A&A, 157, 113

Méndez M., van der Klis M., 1997, ApJ, 479, 926

Merloni A., Fabian A. C., Ross R. R., 2000, MNRAS, 313, 193

Mitsuda K. et al., 1984, PASJ, 36, 741

Nowak M. A., 1995, PASP, 107, 1207

Nowak M. A., Wilms J., 1999, ApJ, 522, 476

Nowak M. A., Wilms J., Heindl W. A., Pottschmidt K., Dove J. B., Begelman M. C., 2001, MNRAS, 320, 316 (Paper I, this issue)

Paczyński B., 1983, ApJ, 273, L81

Pakull M. W., Angebault L. P., 1986, Nat, 322, 511

Parmar A. N., Pietsch W., McKechnie S., White N. E., Trümper J., Voges W., Barr P., 1985, Nat, 313, 119

Pringle J. E., 1996, MNRAS, 281, 357

Remillard R. A., Levine A. M., 1997, in Matsuoka N., Kawai N., eds, All-sky X-ray Observations in the Next Decade, Astron. Soc. Pacific, Conf. Ser., Vol. 101. Riken, Tokyo, p. 29

Scargle J. D., 1982, ApJ, 263, 835

Schandl S., 1996, A&A, 307, 95

Schandl S., Meyer F., 1994, A&A, 289, 149

Schmidtke P. C., Ponder A. L., Cowley A. P., 1999, AJ, 117, 1292

Schwarzenberg-Czerny A., 1989, MNRAS, 241, 153

Scott D. M., Leahy D. A., 1999, ApJ, 510, 974

Shakura N. I., Sunyaev R., 1973, A&A, 24, 337

Shields G. A., McKee C. F., Lin D. N. C., Begelman M. C., 1986, ApJ, 306, 90

Shimura T., Takahara F., 1995, ApJ, 445, 780

Stelzer B., Wilms J., Staubert R., Gruber D., Rothschild R. E., 1999, A&A, 342, 736

Sunyaev R. A., Trümper J., 1979, Nat, 279, 506

Syunyaev R. A. et al., 1990, Sov. Astron. Lett., 16, 55

Tanaka Y., Lewin W. H. G., Black-hole binaries, 1995, in Lewin W. H. G., van Paradijs J., van den Heuvel E. P. J., eds, X-ray Binaries. Cambridge Astrophysics Series 26. Cambridge Univ. Press, Cambridge, Ch. 3, p. 126

Treves A., Belloni T., Chiapetti L., Maraschi L., Stella L., Tanzi E. G., van der Klis M., 1988, ApJ, 325, 119

van der Klis M., Tjemkes S., van Paradijs J., 1983, A&A, 126, 265

van Paradijs J. et al., 1987, A&A, 184, 201

Warren P. R., Penfold J. E., 1975, MNRAS, 172, 41P

Weisskopf M. C., Darbro W. A., Elsner R. F., Williams A. C., Kahn S. M., Grindlay J. E., Naranau S., Sutherland P. G., 1983, ApJ, 274, L65

Wen L., Cui W., Levine A. M., Bradt H. V., 1999, ApJ, 525, 958

White N. E., Marshall F. E., 1984, ApJ, 281, 354

Wilms J., Nowak M. A., Dove J. B., Fender R. P., di Matteo T., 1999a, ApJ, 522, 460

Wilms J., Nowak M. A., Dove J. B., Pottschmidt K., Heindl W. A., Begelman M. C., Staubert R., 1999b, in Aschenbach B., Freyberg M., eds, Highlights in X-ray Astronomy. MPE Report 272, p. 98

Wilms J., Nowak M. A., Dove J. B., Pottschmidt K., Heindl W. A., Begelman M. C., Staubert R., 1999c, Astrophys. Lett. Comm., 38, 273

Yaqoob T., Ebisawa K., Mitsuda K., 1993, MNRAS, 264, 411

Zhang S. N., Mirabel I. F., Harmon B. A., Kroeger R. A., Rodriguez L. F., Hjellming R. M., Rupen M. P., 1997, in Dermer C. D., Strickman M. S., Kurfess J. D., eds, Proc. 4th Compton Symposium, AIP Conf. Proc. 410. AIP, Woodbury, p. 141

This paper has beeen typeset from a TEX/LATEX file prepared by the author.

ANHANG E

On the Enigmatic X-ray Source V1408 Aql (=4U 1957+11)

M.A. Nowak, J. Wilms

1999

Nachdruck aus

The Astrophysical Journal
Vol. 522, S. 476–486

THE ASTROPHYSICAL JOURNAL, 522:476–486, 1999 September 1

ON THE ENIGMATIC X-RAY SOURCE V1408 AQUILAE (=4U 1957+11)

MICHAEL A. NOWAK[1] AND JÖRN WILMS[2]
Received 1998 December 14; accepted 1999 April 14

ABSTRACT

Models for the characteristically soft X-ray spectrum of the compact X-ray source V1408 Aql (=4U 1957+11) have ranged from optically thick Comptonization to multicolor accretion disk models. We critically examine the X-ray spectrum of V1408 Aql via archival *Advanced Satellite for Cosmology and Astrophysics* (*ASCA*) data, archival *Röntgensatellit* data, and recent *Rossi X-Ray Timing Explorer* (*RXTE*) data. Although we are able to fit a variety of X-ray spectral models to these data, we favor an interpretation of the X-ray spectrum as being due to an accretion disk viewed at large inclination angles. Evidence for this hypothesis includes long-term (117, 235, 352 day) periodicities seen by the *RXTE* All Sky Monitor, which we interpret as being due to a warped precessing disk, and a 1 keV feature in the *ASCA* data, which we interpret as being the blend of L fluorescence features from a disk atmosphere or wind. We also present a timing analysis of the *RXTE* data and find upper limits of 4% for the rms variability between $f = 10^{-3}$ and 16 Hz. The situation of whether the compact object is a black hole or neutron star is still ambiguous; however, it now seems more likely that an X-ray–emitting, warped accretion disk is an important component of this system.

Subject headings: accretion, accretion disks — black hole physics — stars: individual (V1408 Aquilae) — stars: neutron

1. INTRODUCTION

The low-mass X-ray binary (LMXB) V1408 Aql (=4U 1957+11, 3U 1956+11) was detected during scans of the Aquila region by *Uhuru* in 1973 (Giacconi et al. 1974), and it was subsequently identified with an 18.7 mag star having a strong blue excess (Margon, Thornstensen, & Bowyer 1978). The object is situated in a region of relatively small extinction ($N_{\rm H} \approx 1.3 \times 10^{21}$ cm^{-2}; Dickey & Lockman 1990; Stark et al. 1992). A_V measurements place the source at a distance greater than 2.5 kpc, and comparisons of its X-ray and optical luminosity to Sco X-1 place it at a distance of $\sim$7 kpc (Margon et al. 1978).

Little is known about the nature of the system. Optical spectra of V1408 Aql reveal a power-law continuum with Hα, Hβ, and He II 4686 Å emission lines (Cowley, Hutchings, & Crampton 1988; Shahbaz et al. 1996), typical for an accretion disk–dominated system. Thorstensen (1987) reported a nearly perfectly sinusoidal V-band luminosity modulation with 10% amplitude and a 0.389 day (=9.33 hr) period, which he interpreted as being due to X-ray heating of the companion. In recent multicolor photometry a more complex light curve with 30% modulation amplitude was observed. Hakala, Muhli, & Dubus (1999) interpret this change in the shape of the light curve as evidence for a disk with a large outer rim, possibly because of a warped disk, seen close to edge-on (Hakala et al. 1999; see also § 4). This interpretation is also consistent with the shape of the infrared spectrum (Smith, Beall, & Swain 1990). The short orbital period is indicative of a late-type main-sequence star of $M \sim 1\ M_\odot$ as the donor star. The absence of X-ray eclipses and the assumption that the donor star fills its Roche lobe yield an upper limit on the orbital inclination of $i \sim 70°$–$75°$, consistent with the models for the optical variability (Hakala et al. 1999).

V1408 Aql is one of the less well studied possible black hole candidates (BHCs). Identification as either a BHC or a neutron star–low-mass X-ray binary (NS-LMXB) is usually made by analogy with the spectral and timing behavior of better observed sources. V1408 Aql has been a BHC since 1984, when *EXOSAT* X-ray observations revealed that V1408 Aql has a very soft X-ray spectrum, similar to those of other BHCs. In color-color diagrams, V1408 Aql lies halfway between the BHC GX 339−4 (in its high/soft state) and the neutron-star LMXBs Cyg X-2 and LMC X-2 (White & Marshall 1984; Schulz, Hasinger, & Trümper 1989). This color identification of V1408 Aql as a BHC, however, is not definitive.

Previous narrowband observations have not characterized the X-ray spectrum in a consistent manner. The analysis of 1983 and 1985 *EXOSAT* observations of V1408 Aql led to contradictory results. While Singh, Apparao, & Kraft (1994) succeeded in fitting a Comptonization spectrum to these data and interpreted this as an indication that V1408 Aql is a BHC, Ricci, Israel, & Stella (1995) interpreted the same data as being similar to that observed from NS-LMXBs. Observations with *Ginga*, with its larger spectral range and effective area, have shed more light on the nature of V1408 Aql (Yaqoob, Ebisawa, & Mitsuda 1993). The values of the normalizations of multicolor disk models (MCDs) (Mitsuda et al. 1984), i.e., $(r_{\rm in}/d)^2 \cos i$, where $r_{\rm in}$ is the inner disk radius, d is the distance to the source, and i is the inclination, have been used to distinguish between BHCs and NS-LMXBs (Tanaka & Lewin 1995). In the case of V1408 Aql, $r_{\rm in} \cos^{1/2} i \approx 2$ km assuming $d = 7$ kpc, which is more characteristic of sources containing neutron stars. Additionally, the *Ginga* observation showed evidence of a hard tail (1–18 keV) making up $\sim$25% of the inferred flux for this system at that time. The best-fit power-law photon indices for the hard component ranged from $\Gamma \approx 2$ to 3.

The *EXOSAT* observations of Ricci et al. (1995) indicate the presence of an iron fluorescence line with an equivalent

[1] JILA, University of Colorado, Campus Box 440, Boulder, CO 80309-0440; mnowak@rocinante.colorado.edu.
[2] Institut für Astronomie und Astrophysik, Abt. Astronomie, Waldhäuser Strasse 64, D-72076 Tübingen, Germany; wilms@astro.uni-tuebingen.de.

width of 90 eV or smaller and a line energy of 7.06 keV (i.e., highly ionized). Other values in the literature range from nondetection (e.g., Yaqoob et al. 1993) to 200 eV (White & Marshall 1984), the uncertainty being mainly due to the difference in the assumed spectral continua and the different sensitivities of the instruments.

Except for one observation, which hints toward a weak red noise ($f^{-\alpha}$) component between 10^{-4} and 10^{-3} Hz, all *EXOSAT* observations are consistent with the absence of any periodic features (Ricci et al. 1995). The *Ginga* observations have yet to have their short timescale variability analyzed; however, they do show evidence of significant flux and color changes on long timescales ($\gtrsim 10^4$ s). The *Vela 5B* satellite did not detect any long-term X-ray variability from this source (Priedhorsky & Terrell 1984); however, the upper limits to the variability were not particularly strong.

If the published spectral models are accepted at face value, then the *relative* energetics of the disk blackbody and power-law components, as well as the slope of the high-energy power law, are very similar to those seen in BHCs such as LMC X-1 (Ebisawa, Mitsuda, & Inoue 1989; Wilms et al. 1998b), LMC X-3 (Treves et al. 1988; Wilms et al. 1998b), and in the soft state of GX 339−4 (Miyamoto et al. 1991; Grebenev et al. 1991). However, at luminosities as low as that of V1408 Aql, BHCs tend to show hard tails with no evidence of a disk or thermal component. On the other hand, NS-LMXBs that exhibit soft disk spectra also tend to show an additional $\sim$2 keV blackbody component, while showing little hard flux (Miyamoto 1994 and references therein). Furthermore, low-luminosity NS-LMXBs *also* tend to be dominated by hard emission.

Thus, there are good arguments that point toward V1408 Aql being a neutron star and also toward it being a black hole; however, none of the arguments are truly conclusive. In either case, V1408 Aql would still be a unique object, being either an unusually soft low-luminosity BHC, an unusually soft low-luminosity neutron star, or a soft neutron star with an unusually energetic hard tail. With the advent of X-ray detectors with much larger effective areas than *EXOSAT* and *Ginga*, as well as with the availability of detectors of higher energy resolution, such as those on the *Advanced Satellite for Cosmology and Astrophysics* (*ASCA*), a critical reexamination of the X-ray spectrum of V1408 Aql has become possible. In this paper we present the results from our analysis of a 30 ks pointed observation with the *Rossi X-Ray Timing Explorer* (*RXTE*), as well as archival data from *ASCA* and the *Röntgensatellit* (*ROSAT*). In § 2 we present the results from the spectral analysis. We discuss the timing analysis in § 3 and the long-term variability of the source in § 4, and we discuss our results in § 5. The details of the data extraction are described in the Appendix.

2. SPECTRAL ANALYSIS

V1408 Aql was observed with *RXTE* in 1997 November in three observing blocks for a total on-source time of 27 ks. A log of the observations is given in Table 1. Since the spectral shapes of the three observing blocks are identical, the data were analyzed together. Spectral and temporal data were extracted using the methods outlined in the Appendix § A1. Spectral analysis was performed with XSPEC, version 10.0s (Arnaud 1996).

The *RXTE* spectrum of V1408 Aql is very soft. The Proportional Counter Array (PCA) did not detect any flux above $\sim$20 keV, and the High Energy X-ray Timing Experiment (HEXTE) count rates are consistent with zero: the background-subtracted count rates were 0.4 ± 0.2 and 0.0 ± 0.2 counts s^{-1}, for HEXTE clusters A and B, respectively. The residual flux in cluster A is most probably due to a slight overestimation of the HEXTE background dead time, as the spectrum seen is similar to the HEXTE background. Therefore, we do not consider V1408 Aql to be detected with HEXTE and will not further discuss these data.

To describe the PCA spectrum we use the spectral models traditionally applied to V1408 Aql: an exponentially cut off power law, a multicolor disk blackbody (Mitsuda et al. 1984), and a Comptonization model after Titarchuk (1994). Because of the low sensitivity of the PCA to the low absorbing column toward V1408 Aql (see Stelzer et al. 1999 for a discussion of the sensitivity of the PCA to $N_{\rm H}$), we fixed $N_{\rm H}$ to the Dickey & Lockman (1990) value of $N_{\rm H} = 1.3 \times 10^{21}$ cm^{-2}. The results of our spectral fits are given in Table 2, while the PCA spectrum and the residues are displayed in Figure 1. All three models roughly describe the observational data. Note that we do not see any evidence for a high-energy power-law tail as that seen in previous observations. The 90% confidence level upper limit to the 3–20 keV flux from a power law is 8×10^{-12} ergs cm^{-2} s^{-1}, which is less than 2% of the observed 3–20 keV flux.

The best description of the PCA data is given by the Comptonization model ($\chi^2_{\rm red} = 0.82$ for 29 dof), while the residues of the MCD model and the exponentially cut off power law show structure in excess of that expected from calibration uncertainties of the PCA. These residues are especially apparent in the low-energy channels of the PCA, below the characteristic feature of the Xe L-edge at $\sim$5 keV (a region of very uncertain detector calibration; see the discussion by Wilms et al. 1998a). Inspection of our best-fit

TABLE 1

OBSERVING LOG FOR V1408 AQL[a]

Date	On-Source Time (ks)	Instrument	Count Rate (counts s^{-1})
1997 Nov 26.02–26.45	21.2	*RXTE*-PCA	230
1997 Nov 27.08–27.17	4.7	*RXTE*-PCA	229
1997 Nov 29.08–29.15	1.5	*RXTE*-PCA	233
1994 Oct 31.13–31.93	21.6	*ASCA* SIS0	9.8
		ASCA SIS1	7.0
		ASCA GIS2	19.4
		ASCA GIS3	21.5
1992 May 08.39–11.14	14.6	*ROSAT* PSPC	19.2

[a] Count rates given are background subtracted.

TABLE 2

RESULTS OF SPECTRAL FITTING

Model	Detector	Parameters	χ^2/dof
cutoffpl[a]	PCA	$\Gamma = -0.26 \pm 0.06$, $A_{\rm PL} = 0.21 \pm 0.01$, $E_{\rm fold} = 1.44 \pm 0.02$	60.2/30
	SIS	$\Gamma = 0.43 \pm 0.04$, $A_{\rm PL} = 0.200 \pm 0.002$, $E_{\rm fold} = 2.30 \pm 0.07$, $N_{\rm H} = 1.4 \pm 0.01$	559/501
	GIS	$\Gamma = 0.56 \pm 0.02$, $A_{\rm PL} = 0.267 \pm 0.001$, $E_{\rm fold} = 2.44 \pm 0.03$	1630/1342
power[b]	PSPC	$\Gamma = 1.54 \pm 0.05$, $A_{\rm PL} = 0.148 \pm 0.004$, $N_{\rm H} = 1.8 \pm 0.1$	56.7/21
diskbb[c]	PCA	$kT_{\rm in} = 1.319 \pm 0.003$, $A_{\rm diskbb} = 15.7 \pm 0.26$	42.0/31
	SIS	$kT_{\rm in} = 1.530 \pm 0.001$, $A_{\rm diskbb} = 8.7 \pm 0.2$, $N_{\rm H} = 1.32 \pm 0.04$	628/502
	GIS	$kT_{\rm in} = 1.487 \pm 0.004$, $A_{\rm diskbb} = 12.2 \pm 0.1$	2148/1343
	PSPC	$kT_{\rm in} = 1.0$, $A_{\rm diskbb} = 30.3$, $N_{\rm H} = 1.0$	104/22
compTT	PCA	$kT_0 = 0.338^{+0.08}_{-0.337}$, $kT_e = 1.17 \pm 0.01$, $\tau = 10.7 \pm 0.3$, norm $= 0.33^{+2.5}_{-0.05}$	23.8/29
	SIS	$kT_0 = 0.32 \pm 0.01$, $kT_e = 1.28^{+0.03}_{-0.02}$, $\tau = 12.2^{+0.2}_{-0.1}$, norm $= 0.239 \pm 0.003$, $N_{\rm H} = 0.37^{+0.16}_{-0.14}$	580/500
	GIS	$kT_0 = 0.27 \pm 0.01$, $kT_e = 1.24 \pm 0.01$, $\tau = 12.9 \pm 0.2$, norm $= 0.333 \pm 0.005$	1371/1341
	PSPC	$kT_0 = 0.176 \pm 0.030$, $kT_e = 2.40^{+20.}_{-1.0}$, $\tau = 9.8^{+5.5}_{-3.2}$, norm $= 0.15^{+0.11}_{-0.07}$, $N_{\rm H} = 1.07 \pm 0.30$	29.5/29
cutoffpl + ray.....	PCA	$\Gamma = -0.69^{+0.25}_{-0.19}$, $A_{\rm PL} = 0.12^{+0.01}_{-0.02}$, $E_{\rm fold} = 1.35 \pm 0.06$, $kT_{\rm ray} = 1.17 \pm 0.19$, $A_{\rm ray} = 44^{+23}_{-20}$	17.4/28
	SIS	$\Gamma = 0.36 \pm 0.05$, $A_{\rm PL} = 0.196 \pm 0.003$, $E_{\rm fold} = 2.21 \pm 0.07$, $kT_{\rm ray} = 1.08^{+0.06}_{-0.08}$, $A_{\rm ray} = 6.7^{+1.7}_{-1.8}$, $N_{\rm H} = 1.4 \pm 0.01$	507/499
	GIS	$\Gamma = 0.35 \pm 0.03$, $A_{\rm PL} = 0.251 \pm 0.002$, $E_{\rm fold} = 2.16 \pm 0.04$, $kT_{\rm ray} = 0.55^{+0.02}_{-0.09}$, $A_{\rm ray} = 32^{+9}_{-3}$	1303/1340
power + ray	PSPC	$\Gamma = 1.2 \pm 0.1$, $A_{\rm PL} = 0.12 \pm 0.01$, $N_{\rm H} = 1.3 \pm 0.02$, $kT_{\rm ray} = 1.09^{+0.06}_{-0.09}$, $A_{\rm ray} = 12.6^{+4.8}_{-5.2}$	19.1/20
diskbb + ray[c].....	PCA	$kT_{\rm in} = 1.33 \pm 0.01$, $A_{\rm diskbb} = 14.2^{+1.9}_{-0.7}$, $kT_{\rm ray} = 1.68^{+0.65}_{-0.19}$, $A_{\rm ray} = 100^{+56}_{-48}$	17.3/29
	SIS	$kT_{\rm in} = 1.55 \pm 0.01$, $A_{\rm diskbb} = 8.3 \pm 0.2$, $N_{\rm H} = 1.46 \pm 0.06$, $A_{\rm ray} = 8.6^{+3.6}_{-1.5}$, $kT_{\rm ray} = 1.13^{+0.16}_{-0.03}$	542/500
	GIS	$kT_{\rm in} = 1.58 \pm 0.01$, $A_{\rm diskbb} = 9.14 \pm 0.26$, $A_{\rm ray} = 67^{+9}_{-8}$, $kT_{\rm ray} = 1.64^{+0.14}_{-0.19}$	1276/1341
	PSPC	$kT_{\rm in} = 1.43^{+0.24}_{-0.15}$, $A_{\rm diskbb} = 8.5 \pm 3.6$, $N_{\rm H} = 0.8 \pm 0.1$, $A_{\rm ray} = 12.7^{+10}_{-4}$, $kT_{\rm ray} = 1.1 \pm 0.1$	23.2/20

NOTE.—The absorbing column, $N_{\rm H}$, has been fixed at 1.3×10^{21} cm^{-2} for the PCA data, while it was fixed at the value found from the SIS data in the case of the GIS data. In all other cases it was a free parameter (measured in 10^{21} cm^{-2}). The normalization of the SIS1 detector with respect to the SIS0 detector was 0.987 ± 0.006, while that of the GIS3 with respect to the GIS2 was found to be 1.043 ± 0.004 in all cases. The uncertainties given are at the 90% level for one interesting parameter.

[a] Exponentially cut off power law of the form $A_{\rm PL}\, E^{-\Gamma} \exp(-E/E_{\rm fold})$, where E is the photon energy and $E_{\rm fold}$ is the folding energy, both measured in keV.

[b] Power law of the form $A_{\rm PL}\, E^{-\Gamma}$, where the symbols have the same meaning as for the cutoffpl model.

[c] MCD model after Mitsuda et al. 1984; $kT_{\rm in}$ is the temperature at the inner edge of the disk measured in keV [$T(r) \propto r^{-3/4}$, where r is the radius], and the normalization constant is $A_{\rm diskbb} = (r_{\rm in}/d)^2 \cos i$, where $r_{\rm in}$ is the inner disk radius measured in kilometers, d is the source distance, measured in units of 10 kpc, and i is the disk inclination.

[d] Comptonization model after Titarchuk 1994 for a disk geometry; kT_0 is the temperature of the Wien-like seed photon input spectrum measured in keV, kT_e is the plasma temperature, measured in keV, and τ is the plasma optical depth.

[e] Optically thin emission spectrum after Raymond & Smith 1977, where $kT_{\rm ray}$ is the plasma temperature in keV. The normalization constant is $A_{\rm ray} = 10^{-17}(4\pi D^2)^{-1} \times \int n_e n_{\rm H}\, dV$, integrating over the emitting volume, where n_e and $n_{\rm H}$ are the electron and hydrogen particle densities, respectively, and D is the distance in cm.

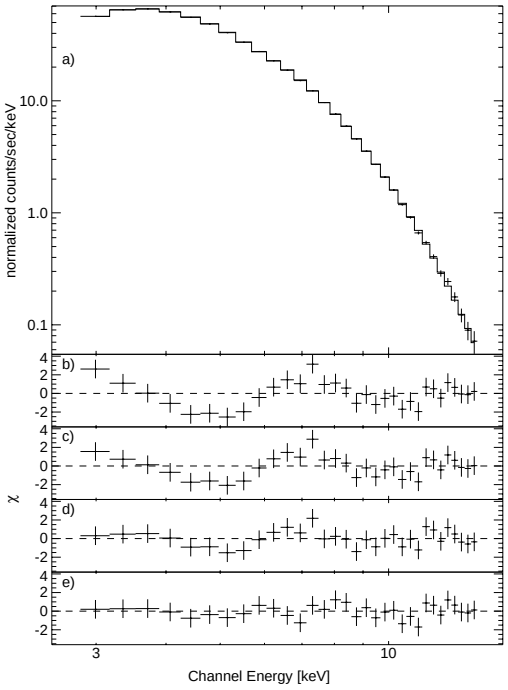

FIG. 1.—Spectral modeling of the PCA data. Residues are shown as the contribution to χ. (*a*) Count rate spectrum and the best-fit MCD model with an optically thin plasma spectrum. (*b*) Residues of the best-fit exponentially cut off power law, (*c*) residues of the best-fit MCD model, (*d*) residues of the best-fit Comptonization model, and (*e*) residues of the best-fit MCD plus optically thin plasma spectrum.

values in Table 2 shows that the Comptonization model results in such a good fit because the seed photon temperature of the model, taken here as a Wien spectrum with best-fit temperature $kT_0 = 0.34$ keV, is uncharacteristically large. This is also evident in the very asymmetric confidence contour indicated in Table 2. Setting kT_0 to a small value yields residues that more resemble those seen in the MCD and exponentially cut off models. We conclude that there is unambiguous evidence for the presence of an additional soft excess below ~ 5 keV. Since the low-energy cutoff of the PCA is at ~ 2 keV, this instrument cannot be used to further constrain the nature of this soft excess. We therefore turned to archival data from observations of V1408 Aql made with *ASCA* and *ROSAT*.

The High Energy Astrophysics Archive contains one *ASCA* observation of V1408 Aql, made in 1994 October (Table 1). A preliminary analysis of these data has been presented by Ricci et al. (1996). We extracted the data from all four instruments on *ASCA*, the two solid state detectors (SIS0 and SIS1) and the two GIS detectors (GIS2 and GIS3). Because of the uncertainty in the intercalibration of the instruments, the GIS and the SIS detectors were analyzed separately. We describe the data extraction process in the Appendix § A2.

In Table 2 we list the results from modeling the data with the standard models for the SIS and the GIS, respectively. The data and residues for the models are shown in Figure 2. Note that because of our extraction procedure the model normalizations differ between the detectors. It is only possible to compare the spectral shapes (see the Appendix § A2). As with the *RXTE*-PCA data, both the exponentially cut off power law and the MCD model provide a rough description of the data. Because of the higher spectral resolution of the *ASCA* detectors, however, the causes for the spectral deviations are now apparent and include a strong deviation at ~ 1 keV. We interpret this feature as evidence for the presence of line emission at this energy, which might come from the iron L complex or emission features from other metals such as Kα lines from highly ionized neon or magnesium (see Nagase et al. 1994). Modeling the feature with the addition of a simple Gaussian line does not result in a markedly improved fit. In contrast, including an optically thin thermal plasma spectrum after Raymond & Smith (1977) in the spectral modeling process results in a dramatic improvement of the fit ($\Delta\chi^2_{\rm red} = 0.65$ for the MCD model). The best-fit parameters for the thermal plasma are similar to the disk temperature found with the MCD model, and the emission-line spectrum is dominated by emission around 1 keV.

In order to further check whether the 1 keV feature is always present in the X-ray spectrum of V1408 Aql, we turned to archival *ROSAT* position sensitive proportional counter (PSPC) data. The observing log for this observation is given in Table 1, and the data extraction procedure is described in the Appendix § A3. As can be seen from our fit results in Table 2, the *ROSAT* data give results similar to the *ASCA* data. In fact, the *ROSAT* data *require* the presence of the line emission component to provide satisfactory fits (see also Fig. 3).

We note that the PCA data show weak residuals in the region of an Fe line. An MCD model with a weak power-law tail, for example, admits the inclusion of a 6.6 keV line with width 0.8 keV and equivalent width 80 eV. Such a weak, broad line, however, is comparable to the remaining uncertainties in the PCA response matrix, and we therefore cannot be confident of its significance nor of its parameters. Adding an Fe line (with energies ranging from 6.4 to 7.1 keV) to the models of the *ASCA* data also does not significantly improve the fits. Limits to the equivalent width of any line in this region were of O(10 eV), which is comparable to the equivalent width of the Fe line present in the best-fit Raymond-Smith models. We note that contrary to the *EXOSAT* and *Ginga* data, the *ASCA* data also do not show strong evidence of a hard tail. The upper limit to the flux from a power-law tail was 12% of the 2–10 keV flux in the cutoff power-law model of the *ASCA* GIS data. The upper limits for the MCD models and for the SIS models were 3–20 times lower. We therefore cannot rule out the possibility that the 7.06 keV line claimed by Ricci et al. (1995) was associated with the presence of a hard tail.

3. TIMING ANALYSIS

We employed Fourier techniques, in the same manner as for our *RXTE* observations of Cyg X-1 (Nowak et al. 1999a) and GX 339−4 (Nowak et al. 1999b) to study the short timescale variability of V1408 Aql. We use the same techniques for estimating dead-time corrections (Zhang et al. 1995; Zhang & Jahoda 1996) to the power spectral density (PSD) and for estimating uncertainties and the Poisson noise levels of the PSD (Leahy et al. 1983; van der

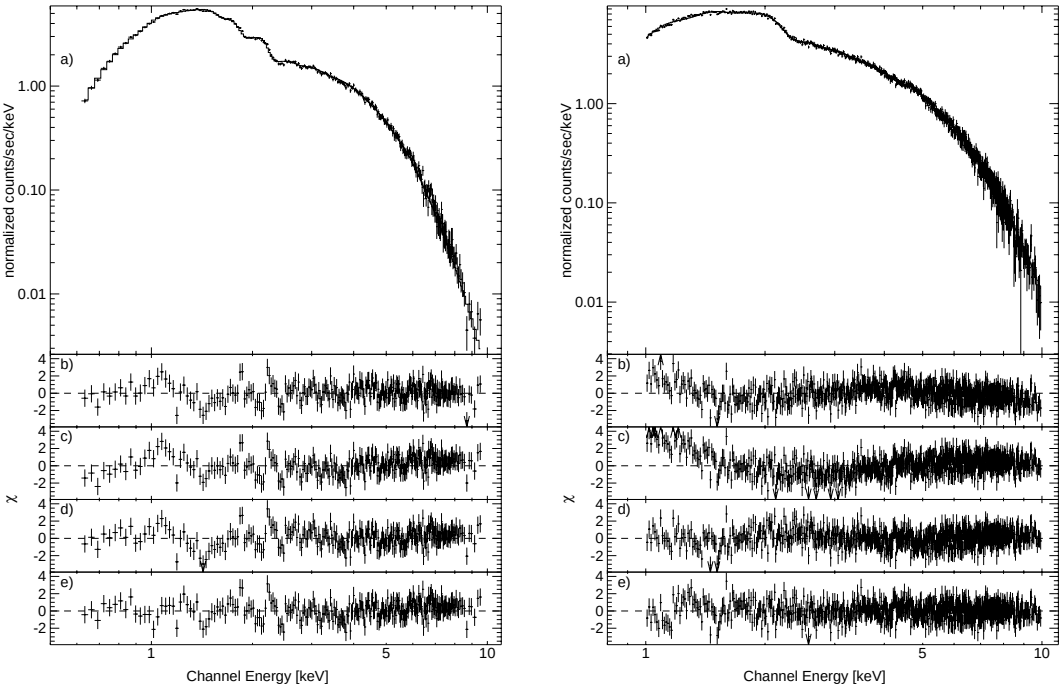

FIG. 2.—Same as Fig. 1, but for the *ASCA* data. *Left-hand panel:* SIS data. *Right-hand panel:* GIS data. Residuals at 1.7 and 2.2 keV are well-known *ASCA* response features.

Klis 1989) as in our previous *RXTE* analyses. We use light curves with 2^{-5} s resolution, from the PCA top layer data only, over the energy range $\approx$1–7.2 keV (absolute PCA channels 1–20), in the analysis discussed below. We also searched 2^{-11} s light curves over the same energy range for high-frequency features, but none was found above the Poisson noise limits.

As the source intensity did not appear to vary over the course of the observation, we created a single PSD. The results are presented in Figure 4 for a normalization where integrating over positive frequency yields the mean square variability (see Belloni & Hasinger 1990; Miyamoto et al. 1992). Note that above $f = 10^{-2}$ Hz the power is completely consistent with Poisson noise. We estimate that the background contributes 13 counts s^{-1} to the light curves, compared with 210 counts s^{-1} for the signal. Based on these count rates and from calculating the PSD of the background light curve generated using the *RXTE* software, we find that the PSD observed between $f = 10^{-3}$ and 10^{-2} Hz is consistent with background fluctuations. We find that the upper limit to the root mean square (rms) variability between 10^{-3} and 16 Hz is 4%.

4. LONG-TERM VARIABILITY

We used data from the All Sky Monitor (ASM) on *RXTE* to study the long-term behavior of V1408 Aql. The ASM is an array of three shadow cameras combined with position sensitive proportional counters that provide for a quasi-continuous coverage of the sky visible from *RXTE* (Levine et al. 1996; Remillard & Levine 1997). Light curves in three energy bands—1.3–3.0, 3.0–5.0, and 5.0–12.2 keV—as well as over the whole ASM band are publically available from the ASM data archives (Lochner & Remillard 1997[3]). Typically, there are several 90 s measurements available for each day.

In Figure 5 we present the ASM data of V1408 Aql that were available as of 1998 November 20. The date of our pointed *RXTE* observation is indicated by an arrow in this figure. Several features are immediately apparent in these data. The count rate light curve shows significant variability with fluctuations up to $O(50\%)$ of the mean. These fluctuations occur on $O(100$ day) timescales. The color light curve (we show the 1.3–3.0 keV light curve divided by the 5.0–12.2 keV light curve) shows significantly less variability, with peaks in the softness of the source occurring on $O(400$ day) timescales. Furthermore, the peaks in the softness of the source seem to be correlated with dips in the intensity of V1408 Aql. The features in the light curve appear to be associated with possible long-term periodicities.

We determined the significance of these possible long-term periodicities by computing the Lomb-Scargle periodogram (Lomb 1976; Scargle 1982) for the 1.3–12.2 keV band for 6 day averages of the ASM light curves. We averaged data where the best fit to the source position and flux in an ASM observation had a $\chi^2_{\rm red} \leq 1.5$ (see Lochner &

[3] See also ASM Data Products Guide, Version Dated 1997 August 27, http://heasarc.gsfc.nasa.gov/docs/xte/asm_products_guide.html.

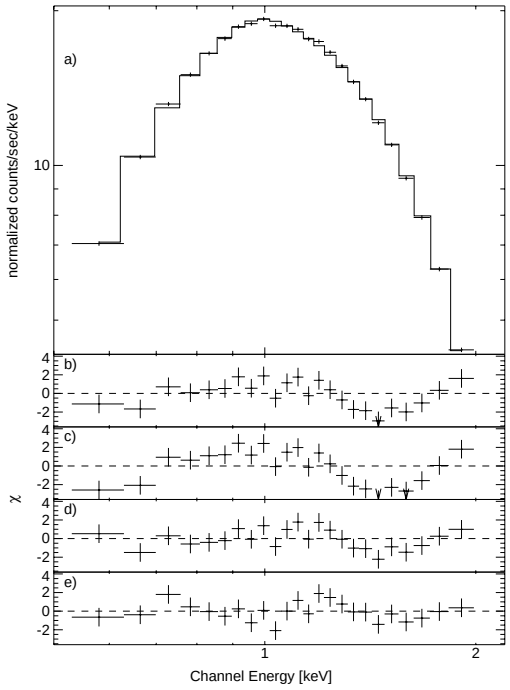

FIG. 3.—Same as Fig. 1, but for the *ROSAT* PSPC data

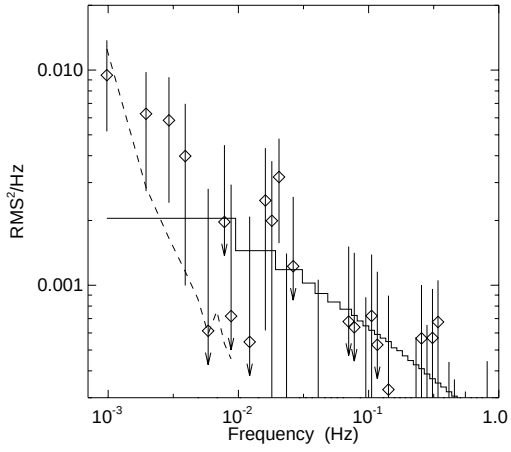

FIG. 4.—Power spectral density for 1–7.2 keV, logarithmically binned in frequency over $f \rightarrow 1.08f$ and normalized as by Belloni & Hasinger (1990) and Miyamoto et al. (1992). The solid line is the effective Poisson noise level for noise-subtracted data (see van der Klis 1989; Nowak et al. 1999a). The dashed line is our estimate of the contribution from *RXTE* background fluctuations.

Remillard 1997[3]) in *each* of the three ASM energy channels. The periodogram presented in Figure 5 shows evidence of a 117, 235, and 352 day periodicity. Each of these periodicities is significant at greater than the 95% level, as determined by the methods of Horne & Baliunas (1986). We note that the Lomb-Scargle periodogram does not assume the presence of harmonics; this is a result of the analysis. Epoch folding (see Leahy et al. 1983; Schwarzenberg-Czerny 1989; Davies 1990) of the ASM light curves also shows evidence of these periodicities, although each period has uncertainties of approximately ± 10 days. The evidence for a periodicity in the color light curve is somewhat weaker. Only the longest period appears, with an approximately 370 day period and then only at the 50% significance level in a Lomb-Scargle periodogram.

Figure 5 shows the result of fitting three harmonically spaced sinusoids to the count rate and color light curves. In these fits, the periods were constrained to be within a few days of the periods found in the Lomb-Scargle periodogram of the count rate light curve; however, the phases of the sinusoids were left completely free. For the count rate light curve, the amplitudes of the sinusoids are 0.32, 0.26, and 0.41 counts s^{-1} for the fundamental, first harmonic, and second harmonic. For the color light curve, the respective amplitudes are 0.1, 0.05, and 0.01. Furthermore, the phases of the sinusoids are displaced from those of the count rate light curves by $O(\pi)$. In Figure 5 we also show the light curves folded on the 117 day period. Note that the folded color light curve indeed exhibits very little variation on this timescale. The count rate light curve shows significantly more periodic structure. The low flux points, however, display the most variations from phase bin to phase bin. This could be partly due to interference from the 235 and 352 day periods. Additionally, if this periodicity is due to inclination effects in a warped disk, as we further discuss below, the low flux points come at times when the disk is at its greatest inclination to our line of sight. The light curve is most sensitive at these times to small changes in disk thickness and/or shape.

Long timescale periodicities and quasi periodicities are relatively common in ASM observations of binary sources (R. A. Remillard 1997, private communication). Evidence for a 294 day periodicity in Cyg X-1 has been previously reported (Kemp et al. 1983; Priedhorsky, Terrell, & Holt 1983) and is readily apparent in the ASM data during the hard state. A 198 day periodicity also has been observed in LMC X-3 (Cowley et al. 1991; Wilms et al. 1998b), and a possible 240 day periodicity appears in ASM data of the low/hard state of GX 339−4 (Nowak et al. 1999b).

5. DISCUSSION—THE NATURE OF V1408 Aql

To summarize, our spectral analysis has provided evidence for a very soft spectrum which can be satisfactorily modeled with any of the three traditional models used here, namely, the exponentially cut off power law, the MCD model, and Comptonization. We did not see any evidence for a hard power-law tail similar to that seen in previous observations. We have also found evidence for a spectral feature at ~ 1 keV, which we interpret as emission from the iron L complex or as Kα lines from highly ionized metals. No short-term variability in excess of the noise was detected from the source, and the upper limit to the rms variability between 10^{-3} and 16 Hz is 4%. On long timescales, we found evidence for periodic variability on a timescale of

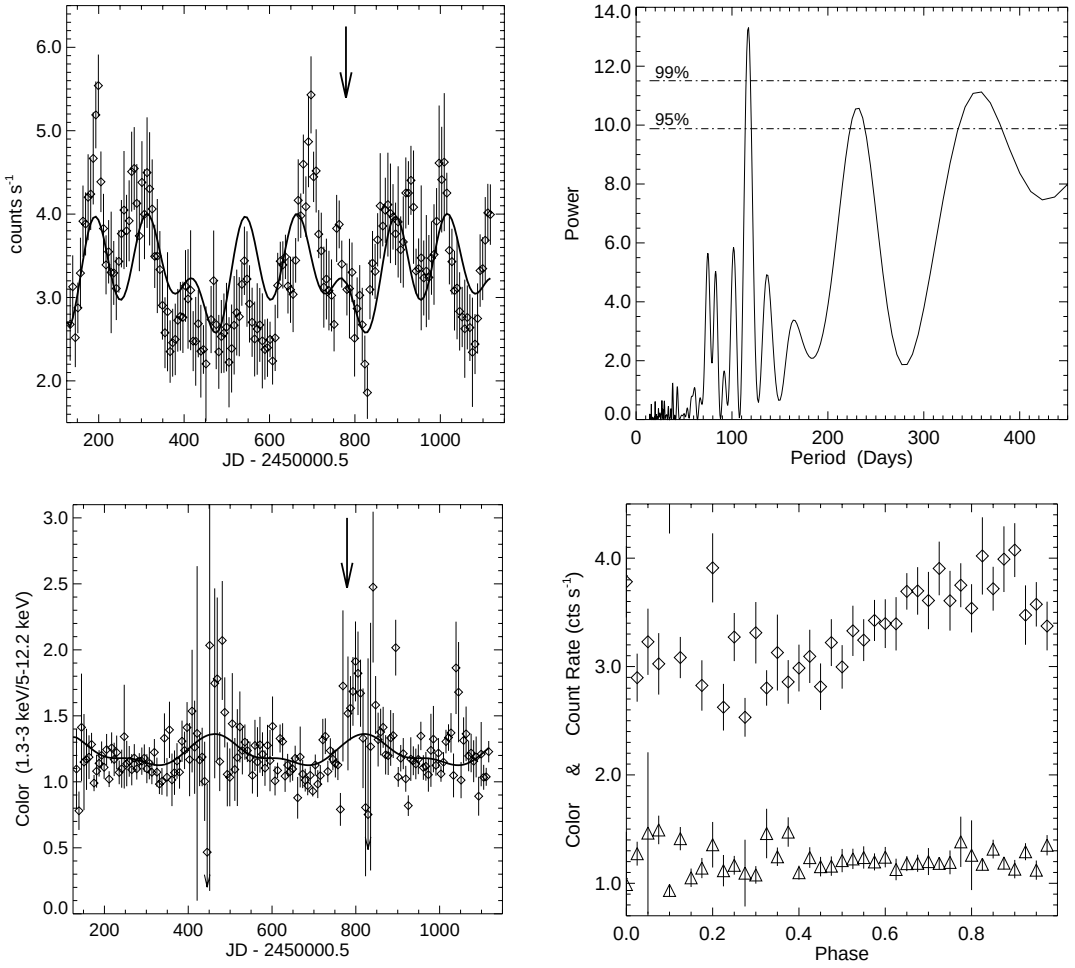

FIG. 5.—*Top left:* *RXTE*-ASM count rate light curve for V1408 Aql, 6 day binning, with sinusoids fit at periods of 117, 235, and 352 days. *Bottom left:* *RXTE*-ASM color light curve (1.3–3.3 keV count rate divided by the 5–12.2 keV count rate), 6 day binning, with sinusoids fit at periods of 117, 235, and 352 days. *Top right:* Lomb-Scargle Periodogram for *RXTE*-ASM count rate light curve binned at 6 days. Lines are the 95% and 99% significance levels. *Bottom right:* Count rate light curve (*diamonds*) and color light curve (channel 1/channel 3; *triangles*) folded on a 117 day period. Arrows in left-hand panels denote the date of our *RXTE* observation.

about 117 days in the soft X-ray luminosity and evidence for a periodic softening of the X-ray spectrum on a 350–400 day timescale. Below we discuss interpretations of these results.

5.1. *Spectral Considerations*

Although the Comptonization model appears to provide the best fit to our broadband *RXTE* data, we do not regard it as likely that Comptonization is indeed the physical process responsible for producing the X-ray spectrum. As we have shown in § 2, part of the small $\chi^2_{\rm red}$ obtained for Comptonization is attributable to the comparably high speed photon temperature, $kT_0 = 0.34$ keV, which mimics the soft excess seen in the *RXTE* data. Also, the best-fit parameters hint at a very cold and optically thick Comptonizing plasma with an optical depth of almost 10. Commonly assumed models for Compton coronae, such as advection-dominated accretion flows (Esin, McClintock, & Narayan 1997) or other "sphere plus disk" coronal models (Dove et al. 1997), have considered only hot, optically thin to moderately optically thick coronae. It is not clear whether a cool and very optically thick corona can be made energetically self-consistent, nor is it clear what physical processes would lead to such a configuration. We therefore

conclude that Comptonization is an improbable physical mechanism for producing the observed soft spectrum.

The accretion disk spectrum and the exponentially cut off power law both provided similar quality fits and yielded almost indistinguishable residues. The MCD model, however, seems the better phenomenological representation of the underlying physical mechanism for producing the observed spectrum. The best-fit parameters for the exponentially cut off power law span a wide range (including a negative photon index in the *RXTE* spectrum) and in many ways appear to be "mimicking" the features of the MCD model. The MCD models, on the other hand, have best-fit spectral parameters that are all similar for each of the independent observations. More importantly, optical and infrared observations (Cowley et al. 1988; Shahbaz et al. 1996; Hakala et al. 1999) provide independent evidence for the presence of an extended accretion disk in V1408 Aql. As we discuss further below, additional independent evidence for the assumption that the X-rays are dominated by the accretion disk comes from the presence of the long-term spectral variability.

We note that the line features apparent in the *ASCA* and *ROSAT* data are also consistent with an accretion disk picture. Line features around 1 keV are a common occurrence in photoionized plasmas close to sources emitting hard X-rays (e.g., in eclipse in Vela X-1; Nagase et al. 1994). We would also expect such features in models with warped accretion disks similar to those of Schandl (1996) (see discussion below). Iron L features and Kα lines from Mg and Ne are also predicted in models for reflection off ionized accretion disks (Ross & Fabian 1993) and are in fact observed in several NS-LMXBs such as Cygnus X-2 (Vrtilek et al. 1986; Kallman, Vrtilek, & Kahn 1989), although the complexity of the observed line shapes makes a direct comparison between the data and the models difficult. See Kallman et al. (1996) for a detailed discussion of these features.

5.2. *Long-Term Variability*

The timescales of the periodicities observed with the ASM are comparable to the timescales expected from precessing accretion disk warps, whether they are driven by the radiation pressure instability discovered by Pringle (1996) (see also Maloney, Begelman, & Pringle 1996; Maloney & Begelman 1997; Maloney, Begelman, & Nowak 1998), or by an X-ray–heated wind as for models of Her X-1 (Schandl 1996). As radiation pressure must typically strongly dominate gas pressure before a wind can be launched, the former mechanism may dominate (Maloney & Begelman 1997), at least for warps large enough that the outer disk is effectively illuminated by the X-ray flux from the inner disk. This radiation pressure–driven instability is fairly generic and is expected to cause a radiatively efficient (i.e., non–advection dominated) accretion disk to warp and precess on O(100 day) timescales. The observed ratio between the precession period and the orbital period in V1408 Aql is too long to be explained by a tidally forced precession of the accretion disk (Larwood 1998).

In a warped disk scenario, the long-term modulations could be due to a combination of the flux varying as the cosine of the inclination angle, as well as due to obscuration of the inner disk by the outer disk. For the former effect, we note that if the inclination of V1408 Aql is 70°–75° as suggested by Hakala et al. (1999), then relatively modest inclination variations of $\pm 10°$ can yield the observed X-ray luminosity variations. The softening of the spectrum observed on the 352 day timescale could be due to a warp periodically obscuring the central regions of the accreting system, which would explain why we do not detect the hard power-law tail seen by the previous observations. In analogy to other soft sources such as LMC X-3 (Wilms et al. 1998b), we can assume that this tail is produced in a small and comparably cold accretion disk corona close to the compact object which is then obscured by the precessing warp. A prediction of this scenario, therefore, is that a long-term monitoring campaign with an instrument capable of detecting the hard power-law tail (e.g., *RXTE* or *BeppoSAX*), will detect a *periodic* change in the flux level of the power law, including a periodic disappearance of this tail.

One alternative explanation is that the corona is covered by the rim of a (geometrically thick) accretion disk. Unlike the warped disk scenario where the relative inclination of the disk to our line of sight does not change on orbital timescales (see Fig. 6), in a disk rim scenario the rim is caused by interaction of the accretion stream with the outer edge of the disk. Our relative view through the rim therefore changes on orbital timescales (see Hakala et al. 1999 and references therein). This seems to be less likely than the warp scenario, however, since contrary to the optical and infrared data there appears to be no evidence for a modulation of the X-ray spectrum on orbital timescales. The warped disk picture could also explain the observed change in the *optical* light curve recently discovered by Hakala et al. (1999) as a precession of a warp on long timescales.

5.3. *Short-Term X-Ray Variability*

Although we only have upper limits for the amplitude of the 10^{-3}–16 Hz variability, these limits are consistent with the few observations of BHCs and some NS-LMXBs in nearly "pure" soft states (Miyamoto 1994). For examples of BHC high/soft states, with little or no discernible hard tail wherein short-term variability is presented, see Grebenev et

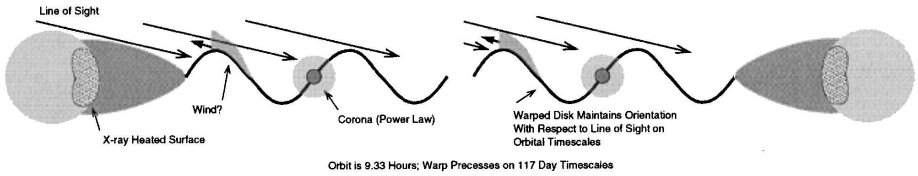

FIG. 6.—Possible model for the behavior of V1408 Aql (not to scale). Optical modulation is due to partial eclipsing of a warped disk. Long-term X-ray variations are due to the changing orientation of the warp. The X-ray power law is due to Comptonization within a corona. The $\sim$1 keV plasma component is due to a wind or possibly due to a disk atmosphere.

al. (1991) for an observation of GX 339−4, Treves et al. (1988) for an observation of LMC X-3, Ebisawa et al. (1989) for an observation of LMC X-1, and Miyamoto et al. (1994) for observations of Nova Muscae. The PSD presented in these works typically have a PSD level of $(\mathrm{rms})^2/\mathrm{Hz} \approx 10^{-3}$ at 0.01 Hz, which decreases as $f^{-0.7}$ for higher Fourier frequencies and an rms variability of $\approx 3\%$ in the 10^{-2}–30 Hz range. This is slightly below the upper limits presented in Figure 4.

The "normal branch" of the NS-LMXB GX 5+1 also has a similar amplitude and shape PSD as described above for high/soft state BHC; however, its energy spectrum consists of both a 1 keV MCD component and a 2 keV blackbody spectral component (Miyamoto 1994 and references therein). The high/soft state of Cir X-1 has been similarly modeled (Miyamoto 1994 and references therein). If V1408 Aql had weak 1–10 Hz variability comparable to that discussed by Miyamoto (1994) for Cir X-1, our observations would have detected it. Other soft neutron star sources with luminosities of $O(10\%)$ Eddington (the approximate luminosity of V1408 Aql, if it were a 1.4 $M_\odot$ neutron star given our hypothesis of a highly inclined disk), especially the bright atoll sources such as GX 13+1, GX 3+1, GX 9+1, and GX 9+9, can also exhibit "very low frequency noise" with approximately 5% rms variability (Hasinger & van der Klis 1989). The 10^{-4}–100 s low-amplitude variability in the light curves of these sources has been interpreted as intermittent, slow nuclear burning on the surface of the neutron star (Bildsten 1993, 1995). Low-frequency variability at such a level is absent in V1408 Aql. Furthermore, bright atoll sources often show a 0.1–10 Hz power spectrum in excess of the upper limits discussed here (Hasinger & van der Klis 1989). The level of the 0.1–10 Hz PSD seen in GX 13+1 (Homan et al. 1998), for example, also would have been easily detected in the PSD of V1408 Aql, yet it was not.

5.4. *Black Hole or Neutron Star?*

The nature of the compact object as of now is not clear. The general picture outlined above is similar to that seen in neutron star X-ray binaries such as Sco X-1, Cyg X-2, and others. Yaqoob et al. (1993) pointed out that the normalization of the best-fit MCD model appears to indicate that the compact object is a neutron star. This argument, however, strongly relies on the assumed distance to V1408 Aql, for which no compelling measurement exists (a lower limit of 2.5 kpc comes from the fact that *ASCA*- and *ROSAT*-measured N_{H}-values are consistent with the full Galactic column) and also relies on the assumption that the accretion disk is seen closer to *face-on*. The recent optical and soft X-ray variability measurements, however, make a large inclination more probable.

Taking these points into account and assuming for the sake of argument a source distance of 7 kpc, then the overall flux of V1408 Aql is comparable to that of the high state of the BHC GX 339−4, which is a very plausible BHC. The upper limits to the high-frequency variability discussed above are consistent with previously observed BHC power spectra in high/soft states. If transitions from the hard state to the soft state occur at 5%–10% of the Eddington luminosity (see Nowak 1995), then the compact object in V1408 Aql is consistent with being a 2–3 $M_\odot$ black hole. Thus, although there is no compelling evidence that V1408 Aql contains a black hole, there also is no compelling evidence that V1408 Aql is a neutron star.

5.5. *Conclusions*

X-ray spectroscopy and the study of both the long-term and the short-term variability of V1408 Aql make a system geometry as that depicted in Figure 6 seem likely. A low-mass main-sequence star serves, via Roche lobe overflow, as the donor for a compact object which is surrounded by a large accretion disk which in turn dominates the system at all wavelength ranges. The accretion disk is surrounded by an optically thin plasma, in the form of either an accretion disk wind or a stationary accretion disk photosphere, which emits the observed X-ray line radiation. A small hot corona directly surrounding the compact object produces the hard X-ray power law. The whole accretion disk precesses on a timescale of about 117 days, obscuring the central region and causing the power-law tail to periodically disappear and reappear. Also on these long timescales, the changing view of the warp causes the orbital modulation of the optical light curve (because of partial obscuration of the outer accretion disk) to vary from sinusoidal (Thorstensen 1987) to a more complex pattern (Hakala et al. 1999).

The nature of the compact object in V1408 Aql is still ambiguous. We have put forth a hypothesis, however, that might explain the observed phenomenology and makes predictions that are observationally testable. X-ray monitoring over the 117 day period with an instrument like *RXTE* or *BeppoSAX* should reveal whether the X-ray power-law tail really does periodically disappear and reappear as predicted by our model. Furthermore, if the source is at 10% L_{Edd} and contains a neutron star, then about one "Type I" microburst per day might be expected (Bildsten 1995). This should be easily observable during such a campaign. One might also hope to find "kilohertz QPOs" (van der Klis 1998), as are often associated with atoll sources. For these latter two possibilities, however, we note that some of the brighter atoll sources such as GX 13+1 have yet to exhibit kilohertz QPOs (Homan et al. 1998 and references therein) and rarely exhibit Type I bursts (see, for example, Matsuba et al. 1984 and references therein). Finally, high spectral resolution observations as will be provided by the upcoming new generation of X-ray instruments, such as the gratings on the *Advanced X-Ray Astronomy Facility* and the *X-Ray Multiple Mirror Mission*, will provide the spectral resolution necessary for resolving and studying the Fe L complex. This will allow the application of plasma spectroscopic diagnostics (e.g., Liedahl et al. 1992) to the study of this fascinating source.

We thank Neil Brandt and Christopher Reynolds for valuable advice concerning the *ASCA* data analysis. We would also like to acknowledge useful correspondence with Lars Bildsten and Rob Fender. Ingo Kreykenbohm made some literature references available to us. We thank Erik Kuulkers for pointing out to us additional references. Rudy Wijnands provided invaluable advice concerning the timing analysis. This work has been financed by NASA grants NAG 5-3225, NAG 5-4737, and NAG 5-7024. J. W. was also supported by a travel grant from the Deutscher Akademischer Austauschdienst. This research has made use of data obtained through the High Energy Astrophysics Science Archive Research Center Online Service, provided by the NASA Goddard Space Flight Center, and the *ROSAT* archive at the Max-Planck-Institut für Extraterrestrische Physik in Garching bei München.

APPENDIX A

DATA ANALYSIS METHODOLOGY

A1. *RXTE* DATA ANALYSIS

Our *RXTE* data were analyzed using the same procedure as that for our analysis of the spectrum of GX 339−4 (Wilms et al. 1998a). The screening criteria for the selection of good on-source data were that the source elevation be larger than 10° and data measured within 30 minutes of passages of the South Atlantic Anomaly or during times of high particle background (as expressed by the "electron ratio" being greater than 0.1) were ignored. Using these selection criteria, a total exposure time of 27 ks was obtained. To increase the signal-to-noise level of the data, we restricted the analysis to the first anode layer of the proportional counter units (PCUs) where most source photons are detected (the particle background is almost independent of the anode layer), and we combined the data from all five PCUs.

To take into account the calibration uncertainty of the PCA we applied the channel-dependent systematic uncertainties described by Wilms et al. (1998a). These uncertainties were determined from a power-law fit to an observation of the Crab Nebula and pulsar taking into account all anode chains; however, they also do provide a good estimate for the first anode layer only since most of the photons are detected in this layer.

Since V1408 Aql has a comparably small count rate we are able to use the new background model for the PCA that was made available by the *RXTE* Guest Observers Facility in 1998 June. The quality of this model was checked by looking at high detector channels which are completely background dominated. Although the measured count rate of V1408 Aql was at the high end of the applicability of the new background model, the agreement between the model and the measured background was good. This is in part due to the fact that V1408 Aql is a very soft source which allows greater latitude in using the background model for faint sources. Remaining background residuals were minimized by using the XSPEC CORFILE facility which renormalizes the background flux to decrease the best-fit $\chi^2_{\rm red}$. The corrections applied to the background flux were on the order of $\lesssim$1.5%, indicating that at least for this source the background model provides a good background estimate. Since the spectrum is completely background dominated above 20 keV, and because of the calibration uncertainty below 3 keV, we restricted the spectral analysis to the range from 3 to 20 keV.

For the timing analysis we generated light curves from the GoodXenon data. Note that although there are short data gaps of 1–4 s duration that are flagged by commensurate jumps in the value of the time coordinate from one data bin to the next, there are occasional data gaps where the extraction software generates a continuous series of time bins despite the data losses. These data gaps *do not* appear in light curves generated from the STANDARD2F data (which is processed by a different event analyzer on-board *RXTE*). These gaps can be recognized, however, in the high time resolution data by searching for any sequence, 1 s or greater in length, of time bins with zero count rate. Four such unflagged sequences, with 16 s duration each, were found in our data. (Aside from these four 16 s sequences, there were a few instances where two 1/32 s time bins in a row would have zero detected counts. The lack of counts in these bins was consistent with counting statistics, and we did not consider these to be data gaps.) The power spectra that we presented in Figure 4 were made from continous data segments without internal data gaps. If we include data segments with the unflagged data gaps in the calculation of the PSD, we obtain a low-amplitude (5% rms) PSD that is flat from 10^{-3} to 10^{-2} Hz and is exponentially cut off at higher Fourier frequencies. In fact, the presence of unflagged data gaps can be deduced from such a characteristic PSD shape (R. Wijnands 1999, private communication).

A2. *ASCA* DATA ANALYSIS

We extracted data from the two solid state detectors (SIS0, SIS1) and the two gas detectors (GIS2, GIS3) on board *ASCA* by using the standard FTOOLS as described in the *ASCA* Data Reduction Guide (Day et al. 1998). The data extraction regions were limited by the fact that all the observations were in 1-CCD mode and that the source was placed close to the chip edge. To maximize the extraction regions, we chose rectangular regions of $6' \times 8'$ and $6' \times 7'$ for SIS0 and SIS1, respectively. Choosing a rectangular region does not affect the shape of the extracted spectrum; however, the ASCAARF ancillary response matrix generator assumes a circular region, so the flux normalization is slightly off (hence the $\approx$30% normalization differences between the SIS and GIS detectors in Table 2). For the GIS detectors we chose circular regions centered on the source each with a radius of 13′.

The SIS count rate for V1408 Aql is large enough that the central regions of the CCD suffer from pileup (i.e., two or more events being registered as a single event). Estimates of the amount of this pileup can be found in the appendix presented by Ebisawa et al. (1996). Based on our measured spectrum and these estimates, we chose to exclude from analysis central rectangular regions with dimensions of $4' \times 3'$ and $3' \times 3'$ for SIS0 and SIS1, respectively. With these exclusions, we estimate that pileup will contribute less than 1% of the counts at 10 keV.

We used the SISCLEAN and GISCLEAN tools (Day et al. 1998), with the default values, to remove hot and flickering pixels. As the spectrum of V1408 Aql is very similar to the low flux level of Cir X-1 described by Brandt et al. (1996), we filtered the data with the same cleaning criteria outlined in that work; however, we took the slightly larger values of 10° for the minimum elevation angle and 7 GeV/c for the rigidity. Also, similar to the work of Brandt et al. (1996), we formed background estimates by extracting a circular region of radius 5′ near the edge of the detector for the GIS observations. For the SIS observations, we chose L-shaped regions near the corner of the chip opposite from the source. Background, however, contributes relatively little to the observations.

We rebinned the spectral files so that each energy bin contained a minimum of 20 photons. We retained SIS data in the 0.6–10 keV range and GIS data in the 1–10 keV range. The cross-calibration uncertainties among the instruments were

accounted for by introducing a multiplicative constant for each detector in all of our fits. As discussed above, the resulting data files showed reasonable agreement between all four detectors.

A3. *ROSAT* DATA ANALYSIS

The extraction of the *ROSAT* spectrum was performed using the standard *ROSAT* PSPC data analysis package, the Extended X-Ray Scientific Analysis System (Zimmermann et al. 1998), following the procedures described by Brunner et al. (1997). Source counts were extracted from a circular region centered on the position of V1408 Aql with a radius of 2′, while the background was extracted from an annulus centered on the source from which source counts from detected background sources were removed. A correction for the telescope vignetting was applied to the standard *ROSAT* response matrix. The spectrum was then rebinned into 26 channels of $\sim$10,000 counts each to ensure an even signal-to-noise ratio over the whole *ROSAT* energy band. As for *RXTE* and *ASCA*, the spectral analysis of the extracted data was then performed with XSPEC, ignoring data measured below 0.5 keV and above 2.5 keV.

REFERENCES

Arnaud, K. A. 1996, in ASP Conf. Ser. 101, Astronomical Data Analysis Software and Systems V, ed. J. H. Jacoby & J. Barnes (San Francisco: ASP), 17
Belloni, T., & Hasinger, G. 1990, A&A, 230, 230
Bildsten, L. 1993, ApJ, 418, L21
———. 1995, ApJ, 438, 852
Brandt, W. N., Fabian, A. C., Dotani, T., Nagase, F., Inoue, H., Kotani, T., & Segawa, Y. 1996, MNRAS, 283, 1071
Brunner, H., Müller, C., Friedrich, P., Dörrer, T., Staubert, R., & Riffert, H. 1997, A&A, 326, 885
Cowley, A. P., Hutchings, J. B., & Crampton, D. 1988, ApJ, 333, 906
Cowley, A. P., et al. 1991, ApJ, 381, 526
Davies, S. R. 1990, MNRAS, 244, 93
Day, C., Arnaud, K., Ebisawa, K., Gotthelf, E., Ingham, J., Mukai, K., & White, N. 1998, The *ASCA* Data Reduction Guide, Tech. Rep., (Greenbelt: NASA GSFC), v.2.0
Dickey, J. M., & Lockman, F. J. 1990, ARA&A, 28, 215
Dove, J. B., Wilms, J., Maisack, M. G., & Begelman, M. C. 1997, ApJ, 487, 759
Ebisawa, K., Mitsuda, K., & Inoue, H. 1989, PASJ, 41, 519
Ebisawa, K., Ueda, Y., Inoue, H., Tanaka, Y., & White, N. E. 1996, ApJ, 467, 419
Esin, A. A., McClintock, J. E., & Narayan, R. 1997, ApJ, 489, 865
Giacconi, R., Murray, S., Gursky, H., Kellogg, E., Schreier, E., Matilsky, T., Koch, D., & Tananbaum, H. 1974, ApJS, 27, 37
Grebenev, S. A., Sunyaev, R., Pavlinsky, M. N., & Dekhanov, I. A. 1991, Soviet Astron. Lett., 17, 413
Hakala, P. J., Muhli, P., & Dubus, G. 1999, MNRAS, submitted
Hasinger, G., & van der Klis, M. 1989, A&A, 225, 79
Homan, J., Klis, M. V., Wijnands, R., Vaughan, B., & Kuulkers, E. 1998, ApJ, 499, L41
Horne, J. H., & Baliunas, S. L. 1986, ApJ, 302, 757
Kallman, T. R., Liedahl, D., Osterheld, A., Goldstein, W., & Kahn, S. 1996, ApJ, 465, 994
Kallman, T. R., Vrtilek, S. D., & Kahn, S. M. 1989, ApJ, 345, 498
Kemp, J. C., et al. 1983, ApJ, 271, L65
Larwood, J. 1998, MNRAS, 299, L32
Leahy, D. A., Darbro, W., Elsner, R. F., Weisskopf, M. C., Sutherland, P. G., Kahn, S., & Grindlay, J. 1983, ApJ, 266, 160
Levine, A. M., Bradt, H., Cui, W., Jernigan, J. G., Morgan, E. H., Remillard, R., Shirey, R. E., & Smith, D. A. 1996, ApJ, 469, L33
Liedahl, D. A., Kahn, S. M., Osterheld, A. L., & Goldstein, W. H. 1992, ApJ, 391, 306
Lomb, N. R. 1976, Ap&SS, 39, 447
Maloney, P. R., & Begelman, M. C. 1997, ApJ, 491, L43
Maloney, P. R., Begelman, M. C., & Nowak, M. A. 1998, ApJ, 504, 77, in press
Maloney, P. R., Begelman, M. C., & Pringle, J. E. 1996, ApJ, 472, 582
Margon, B., Thornstensen, J. R., & Bowyer, S. 1978, ApJ, 221, 907
Matsuba, E., Dotani, T., Mitsuda, K., Asai, K., Lewin, W. H. G., van Paradijs, J., & van der Klis, M. 1995, PASJ, 47, 575
Mitsuda, K., et al. 1984, PASJ, 36, 741
Miyamoto, S. 1994, Time-Variation from X-Ray Stars, Tech. Rep. RN 548 (Tokyo: ISAS)
Miyamoto, S., Kimura, K., Kitamoto, S., Dotani, T., & Ebisawa, K. 1991, ApJ, 383, 784
Miyamoto, S., Kitamoto, S., Iga, S., Hayashida, K., & Terada, K. 1994, ApJ, 435, 398
Miyamoto, S., Kitamoto, S., Iga, S., Negoro, H., & Terada, K. 1992, ApJ, 391, L21
Nagase, F., Zylstra, G., Sonobe, T., Kotani, T., Inoue, H., & Woo, J. 1994, ApJ, 436, L1
Nowak, M. A. 1995, PASP, 107, 1207
Nowak, M. A. Vaughan, B. A., Wilms, J., Dove, J., & Begelman, M. C. 1999a, ApJ, 510, 874
Nowak, M. A., Wilms, J., & Dove, J. B. 1999b, ApJ, 517, 355
Priedhorsky, W. C., & Terrell, J. 1984, ApJ, 280, 661
Priedhorsky, W. C., Terrell, J., & Holt, S. S. 1983, ApJ, 270, 233
Pringle, J. E. 1996, MNRAS, 281, 357
Raymond, J. C., & Smith, B. W. 1977, ApJS, 35, 419
Remillard, R. A., & Levine, A. M. 1997, in All-Sky X-Ray Observations in the Next Decade, ed. N. Matsuoka & N. Kawai (Tokyo: Riken), 29
Ricci, D., Asai, K., Israel, G. L., Mereghetti, S., Mitsuda, K., Parmar, A. N., & Stella, L. 1996, Mem. Soc. Astron. Italiana, 67, 1039
Ricci, D., Israel, G. L., & Stella, L. 1995, A&A, 299, 731
Ross, R. R., & Fabian, A. C. 1993, MNRAS, 261, 74
Scargle, J. D. 1982, ApJ, 263, 835
Schandl, S. 1996, A&A, 307, 95
Schulz, N. S., Hasinger, G., & Trümper, J. 1989, A&A, 225, 48
Schwarzenberg-Czerny, A. 1989, MNRAS, 241, 153
Shahbaz, T., Smale, A. P., Naylor, T., Charles, P. A., van Paradijs, J., Hassall, B. J. M., & Callanan, P. 1996, MNRAS, 282, 1437
Singh, K. P., Apparao, K. M. V., & Kraft, R. P. 1994, ApJ, 421, 753
Smith, H. A., Beall, J. H., & Swain, M. R. 1990, AJ, 99, 273
Stark, A. A., Gammie, C. F., Wilson, R. W., Bally, J., Linke, R. A., Heiles, C., & Hurwitz, M. 1992, ApJS, 79, 77
Stelzer, B., Wilms, J., Staubert, R., Gruber, D., & Rothschild, R. 1999, A&A, in press
Tanaka, Y., & Lewin, W. H. G. 1995, in X-Ray Binaries, ed. W. H. G. Lewin, J. van Paradijs, & E. P. J. van den Heuvel (Cambridge: Cambridge Univ. Press), 126
Thorstensen, J. R. 1987, ApJ, 312, 739
Titarchuk, L. 1994, ApJ, 434, 570
Treves, A., Belloni, T., Chiapetti, L., Maraschi, L., Stella, L., Tanzi, E. G., & van der Klis, M. 1988, ApJ, 325, 119
van der Klis, M. 1989, in Timing Neutron Stars, ed. H. Ögelman & E. P. J. van den Heuvel (Dordrecht: Kluwer), 27
———. 1998, in Proc. Third William Fairbank Meeting, in press (astro-ph/9812395)
Vrtilek, S. D., Kahn, S. M., Grindlay, J. E., Seward, F. D., & Helfand, D. J. 1986, ApJ, 307, 698
White, N. E., & Marshall, F. E. 1984, ApJ, 281, 354
Wilms, J., Nowak, M. A., Dove, J. B., Fender, R. P., & di Matteo, T. 1998a, ApJ, in press
Wilms, J., Nowak, M. A., Dove, J. B., Pottschmidt, K., Heindl, W. A., Begelman, M. C., & Staubert, R. 1998b, in Highlights in X-Ray Astronomy, ed. B. Aschenbach & M. Freyberg, in press
Yaqoob, T., Ebisawa, K., & Mitsuda, K. 1993, MNRAS, 264, 411
Zhang, W., & Jahoda, K. 1996, Deadtime Effects in the PCA, Tech. Rep. (Greenbelt: NASA GSFC)
Zhang, W., Jahoda, K., Swank, J. H., Morgan, E. H., & Giles, A. B. 1995, ApJ, 449, 930
Zimmermann, U., Boese, G., Becker, W., Belloni, T., Döbereiner, S., Izzo, C., Kahabka, P., & Schwentker, O. 1998, EXSAS User's Guide, 5th ed., Tech. Rep. (Garching: Max-Planck-Institut für Extraterrestrische Physik)

ANHANG F

On the Absorption of X-rays in the Interstellar Medium

J. Wilms, A. Allen, R. McCray

2000

Nachdruck aus

The Astrophysical Journal
Vol. 542, S. 914–924

THE ASTROPHYSICAL JOURNAL, 542:914–924, 2000 October 20

ON THE ABSORPTION OF X-RAYS IN THE INTERSTELLAR MEDIUM

J. WILMS
Institut für Astronomie und Astrophysik, Abteilung Astronomie, Waldhäuser Strasse 64, D-72076 Tübingen, Germany; wilms@astro.uni-tuebingen.de
AND
A. ALLEN AND R. MCCRAY
JILA, University of Colorado, Campus Box 440, Boulder, CO 80309-0440; allenu@super.colorado.edu, dick@jila.colorado.edu
Received 1999 July 13; accepted 2000 May 23

ABSTRACT

We present an improved model for the absorption of X-rays in the interstellar medium (ISM) intended for use with data from future X-ray missions with larger effective areas and increased energy resolution such as *Chandra* and the *X-Ray Multiple Mirror* mission, in the energy range $\gtrsim 100$ eV. Compared with previous work, our formalism includes recent updates to the photoionization cross section and revised abundances of the interstellar medium, as well as a treatment of interstellar grains and the H_2 molecule. We review the theoretical and observational motivations behind these updates and provide a subroutine for the X-ray spectral analysis program XSPEC that incorporates our model.

Subject headings: atomic data — dust, extinction — ISM: abundances — X-rays: ISM

1. INTRODUCTION

Precise knowledge of the modification of X-ray radiation in the interstellar medium (ISM) is of crucial importance for the understanding of X-ray spectra from cosmic sources since the observed X-ray spectra have to be corrected for this modification before interpreting the observed data. The current state of the art in the computation of the energy-dependent photoionization cross section of the ISM, $\sigma_{\rm ISM}$, has been summarized by Bałucińska-Church & McCammon (1992, hereafter BM92). These authors greatly improved[1] the precision in the computation of $\sigma_{\rm ISM}$ compared with previous implementations (Strom & Strom 1961; Brown & Gould 1970; Fireman 1974; Ride & Walker 1977; Morrison & McCammon 1983, hereafter MM83) by allowing the assumed abundances of the ISM to be adjusted and by using polynomial fits to the photoionization cross sections of Henke et al. (1982).

Although the BM92 model provides sufficient precision for data analysis with current instruments, the advent of X-ray missions with instruments of high energy resolution and large effective areas, such as *Chandra* or the *Newton X-ray Multiple Mirror* mission (*XMM-Newton*), will result in large improvements in the precision of X-ray astronomical measurements. It is therefore necessary to have tools at hand that reflect the current understanding of the physics of the interaction of X-rays with the ISM at the percent level.

In this paper we improve on the models of BM92 by incorporating recent improvements in the photoionization cross sections and by taking into account the physics of the interstellar dust and the molecular phase of the interstellar medium. Section 2 describes the formalism employed to compute $\sigma_{\rm ISM}$. We describe the atomic physics data (§ 2.2) and explain our choices of elemental and molecular abundances (§2.3) as well as dust grain parameters (§ 2.4). We summarize the model, compare it with previous models, and point out its remaining shortcomings in § 3. In the appendices, we derive the influence of dust on $\sigma_{\rm ISM}$ (Appendix A) and describe the implementation of our model into XSPEC (Appendix B).

The intended readership of this paper consists of users of the new missions, many of whom do not intend to become specialists on the ISM. We have therefore attempted to include sufficient information to make this paper self-contained and have chosen a review-like style.

2. MODELING THE X-RAY ABSORPTION IN THE ISM

2.1. *X-Ray Absorptivity in the ISM*

The total photoionization cross section of the ISM, $\sigma_{\rm ISM}$, is obtained by summing over the contributions of the astrophysically relevant elements. Taking into account the phases of the ISM, $\sigma_{\rm ISM}$ can be written as

$$\sigma_{\rm ISM} = \sigma_{\rm gas} + \sigma_{\rm molecules} + \sigma_{\rm grains} \, . \tag{1}$$

As is common for X-ray applications, we normalize $\sigma_{\rm ISM}$ to the total hydrogen number density (i.e., in molecular, neutral, or ionized form), $N_{\rm H}$, so that the observed X-ray spectrum of a source, $I_{\rm obs}$, is given by

$$I_{\rm obs}(E) = e^{-\sigma_{\rm ISM}(E) N_{\rm H}} I_{\rm source}(E) \, , \tag{2}$$

where $N_{\rm H}$ is measured in atoms cm^{-2} and $I_{\rm source}(E)$ is the X-ray spectrum as emitted by the X-ray source. We drop the explicit energy dependence of $\sigma_{\rm ISM}$ for the rest of the paper.

The contribution of the gaseous, nonmolecular cold and warm phases of the ISM to $\sigma_{\rm ISM}$ is obtained by summing the photoionization cross sections of the individual atoms and ions in these phases, weighting their contributions by the abundances. Hence,

$$\sigma_{\rm gas} = \sum_{Z,i} A_Z \times a_{Z,i} \times (1 - \beta_{Z,i}) \times \sigma_{\rm bf}(Z, i) \, , \tag{3}$$

where we use the notation pioneered by Ride & Walker (1977), in which $A_Z = N(Z)/N({\rm H})$ is the abundance in number of element Z with respect to hydrogen, $a_{Z,i} = N(Z, i)/N(Z)$ is the fraction of ions of element Z that are in ionization stage i, and $\sigma_{\rm bf}(Z, i)$ is the total photoionization cross section of element Z in ionization stage i. The deple-

[1] When referring to the cross sections of BM92 we use their subroutines as implemented as the "phabs" model in XSPEC, version 10.0z (Arnaud 1996). This implementation contains improvements compared to the original publication. Starting with XSPEC, version 11.0, other cross sections are used in the computation of this model (see § 2.2 below).

tion of the elements into grains is taken into account through the "depletion factor" $1 - \beta_{Z,i}$.

For the molecular phase of the ISM, only molecular hydrogen needs to be taken into account because of its large abundance ($\sim$20% of the hydrogen might be molecular, see § 2.3). Therefore,

$$\sigma_{\rm molecules} = A_{\rm H_2}\,\sigma_{\rm bf}({\rm H_2})\ . \tag{4}$$

For material in the grain phase of the ISM, several complications arise. Since the X-ray optical depth of a large grain can be much greater than 1 (see Fig. 2), most of the X-ray absorption will occur on its surface. Consequently, the contribution of material "within" the grain to $\sigma_{\rm ISM}$ is small. Thus, the net effect of this shielding is that the presence of grains *reduces* the effective absorptivity of the ISM relative to the absorptivity of a completely gaseous medium. As we show in Appendix A, the total optical depth for grains with a size distribution $dn_{\rm gr}(a)/da$ is given by

$$\begin{aligned}\tau_{\rm grains} &= \sigma_{\rm grains}\,N_{\rm H}\\ &= N_{\rm H}\,\xi_g \int_0^\infty \frac{dn_{\rm gr}(a)}{da}\,\sigma_{\rm geom}\\ &\quad\times [1 - \exp\,(-\langle\sigma\rangle\langle N\rangle)]da\ .\end{aligned} \tag{5}$$

In the derivation of equation (5) we assume that the grains are of chemically homogeneous composition with an average photoabsorption cross section $\langle\sigma\rangle$ and can be approximated as spheres with radius a and average column density $\langle N\rangle$ (measured in atoms cm^{-2}). Since the grains are partly transparent to X-rays, their absorption cross section is smaller than the grain geometrical cross section, $\sigma_{\rm geom} = \pi a^2$. Finally, the number of grains per hydrogen atom along the line of sight is ξ_g. We discuss the validity of these assumptions in § 2.4 and give explicit formulae for all parameters of equation (5) in Appendix A.

In the following sections we describe the data used for evaluating equations (1) and (5) in greater detail.

2.2. *Atomic Physics*

Despite decades of effort, the knowledge of elemental photoionization cross sections in the X-ray regime is still uncertain. In many cases, therefore, one has to rely on either theoretical work or interpolation along the isoelectronic sequence to obtain usable cross sections and then use compilations of experimental data to gauge the precision of these theoretical computations. In what follows we will describe the basis of the photoionization cross sections used here, focusing on the region $E \gtrsim 100$ eV. The emphasis is on the choice of cross sections that are good for instruments with a resolution comparable to the CCDs on *Chandra* or *XMM-Newton*. Therefore, we will not make an attempt to include the resonances that are important close to the absorption edges that might well be important for the grating instruments aboard these satellites.

For the computation of the photoionization cross section of H, we use the fitting formula of Band et al. (1990), which provides a very good approximation of the exact, analytic cross section but is much faster to evaluate. The maximum deviation between the Band et al. (1990) formula and the analytical cross section (e.g., Bethe & Salpeter 1957, eq. [71.7], divided by 2) is $\sim$1.5% at energies below 2 keV.

The cross section for helium is taken from the recent theoretical evaluation of Yan, Sadeghpour, & Dalgarno (1998). Autoionization resonances occur at energies less than 0.08 keV, and the four strongest resonances are included here (as in BM92), using values from Oza (1986) and Fernley, Taylor, & Seaton (1987). For energies between 0.1 and 1 keV, the helium cross section is *smaller* by a factor of $\sim$0.9–$\sim$0.6 than that assumed in the subroutine used by BM92, which is based on theoretical work of Chen, Cooper, & Brion (1991) and on experimental data by Marr & West (1976). The Yan et al. (1998) cross section, however, agrees with other more recent theoretical computations (e.g., those of Verner & Yakovlev 1995) and is in agreement with more recent experimental data (Yan et al. 1998, and references therein). It also has the correct $E^{-3.5}$ asymptote required by nonrelativistic quantum theory (Bethe & Salpeter 1957). For implications of this smaller He cross section on studies of the ISM, see, e.g., Arabadjis & Bregman (1999).

For all other elements we use the photoionization cross sections as originally published by Verner et al. (1993) and later updated by Verner & Yakovlev (1995) and which are used in XSPEC version 11.0. These authors fitted the results from Hartree-Dirac-Slater computations of $\sigma_{\rm bf}$ for individual subshells to a semiempirical fitting formula. The major advantage of this semiempirical fitting formula over previous fitting formulae (such as, e.g., polynomial fits) is that it requires only a small number of fitting parameters to express $\sigma_{\rm bf}$ to high accuracy while preserving the correct asymptotical properties. A comparison between the experimental data and these cross sections is presented by Verner & Yakovlev (1995), who focus on the overall agreement throughout the electromagnetic spectrum. In addition, we compared the total photoionization cross sections computed from the fitting formula with the compilation of data presented by Henke, Gullikson, & Davis (1993) for the range from 0.1 to 10 keV. Except for energies close to the K and L shell edges, our comparisons indicate maximum relative deviations between these cross sections on the order of 5% above 1 keV.

In their determination of $\sigma_{\rm bf}$ close to the K and L shell edges, Henke et al. (1993) used a linear interpolation through the resonances to the edge energy. Since this edge energy was obtained from experimental data, it includes the effects of energy shifts in the solid state and thus is not representative of the true edge energy for the gaseous state of the materials. Indeed, the difference in edge energy between the solid and the gaseous states can be up to several tens of eV (see, e.g., Nicolosi, Jannitti, & Tondello 1991, for an illustrative experimental example). In many cases, Henke et al. also do not consider the different subshell threshold energies. On the other hand, the Verner & Yakovlev (1995) cross sections are based on quantum mechanical computations that include the resonances, and the edge energy is unaffected by solid-state effects. We have checked the precision of the Verner & Yakovlev edge energies by comparing them with the computations of Gould & Jung (1991), which are more appropriate for our work than the Henke et al. (1982, 1993) values since they assume the elements to be in the gas phase. For $Z > 8$ the edge energies of Verner & Yakovlev (1995) agree on the 10 eV level with those of Gould & Jung (1991). For C, N, and O, the edge energies adopted by Verner & Yakovlev (1995) are between those of Henke et al. (1993) and Gould & Jung (1991). We therefore decided to adopt the Verner & Yakovlev edge energies for this work. Note, however, that these differences in the edge energy are relevant only for instruments with

extremely high resolution and are irrelevant for most other work.

For molecular hydrogen we adopt the cross sections reported by Yan et al. (1998) for energies above 85 eV. These cross sections are claimed to be accurate to about 5% and have the correct $E^{-3.5}$ asymptotics. Albeit outside of our formal energy range ($E \gtrsim 100$ eV), we note that the fit formula given by equation (18) of Yan et al. (1998) for energies below 85 eV has significant deviations with respect to the tabulated cross sections of Samson & Haddad (1994), on which the Yan et al. values are based. Furthermore, the fit formula is noncontinuous at 85 eV. For energies between 30 and 85 eV we find that the cross section can be represented by

$$\sigma_{\mathrm{bf,H_2}}(x) = \sum_{i=0}^{5} a_i x^{-i}, \qquad (6)$$

where $x = E/15.4$ eV and where σ_{bf} is given in megabarns ($=10^{-18}$ cm^2). The fit coefficients a_i are given in Table 1. The maximum deviation between the fit and the tabulated data is less than 1%. We note that the photoabsorption cross section of H_2 is $\sim 2.85\sigma_{\mathrm{H}}$, which results in an increase over previous estimates of σ_{ISM} for regions where molecular hydrogen is an important contributor to the total absorptivity (i.e., below ~ 1 keV). Molecular effects were not included in the earlier models, so essentially these models assumed $\sigma_{\mathrm{bf,H_2}} = 2\sigma_{\mathrm{bf,H}}$.

TABLE 1

FIT COEFFICIENTS a_i TO EQUATION (6) FOR THE H_2 PHOTOABSORPTION CROSS SECTION

a_0	a_1	a_2	a_3	a_4	a_5
0.664	−11.768	78.118	−231.339	368.053	−189.953

2.3. *Abundances*

Naturally, the assumed elemental abundances are of crucial importance for the computation of σ_{ISM}. While many measurements of gas-phase abundances have been made, measurement of the total gas plus dust abundance of the ISM is very difficult. As a result, solar abundances, i.e., abundances determined from analysis of the solar photosphere or (carbonaceous) meteorites, have generally been used as the reference abundance for the ISM (Anders & Ebihara 1982; Grevesse & Anders 1989; Anders & Grevesse 1989; Shull 1993, and references therein). For reference, we list in Table 2 what we consider to be the best estimates of these "local" ISM abundances. We list the logarithmic abundances by number, normalized to a hydrogen abundance of $\log A_{\mathrm{H}} = 12$, based on the meteoritic abundances of Anders & Grevesse (1989). We updated the abundances of C and N using the results of Grevesse et al. (1991) and Grevesse & Noels (1993), respectively. The solar abundance of iron has been the subject of several discussions in recent years (Raassen & Uylings 1998; Kostik, Shchukina, & Rutten 1996; Biémont et al. 1991, and references therein). We adopted $\log A_{\mathrm{Fe}} = 7.50 \pm 0.05$ as recently determined

TABLE 2

MOLECULAR WEIGHT, K EDGE ENERGIES, ABUNDANCES, AND DEPLETION FACTORS $1 - \beta_Z$ FOR THE ABUNDANT ELEMENTS

Element	μ_Z (amu)	E_K[b] (keV)	$12 + \log A_Z$ Solar[c]	$12 + \log A_Z$ ISM[d]	$1 - \beta_Z$[e] This Paper	$1 - \beta_Z$[e] MM83	$1 - \beta_Z$[e] Ride77
1 H	1	...	12.00	12.00	1.0	1.0	1.0
2 He.....	4	...	10.99	10.99	1.0	1.0	1.0
6 C	12	0.29	8.60	8.38	0.5	0.0	0.2
7 N	14	0.41	7.97	7.88	1.0	0.0	0.5
8 O	16	0.54	8.93	8.69	0.6	0.75	0.5
10 Ne	20	0.87	8.09	7.94	1.0	1.0	1.0
11 Na	23	1.08	6.31	6.16	0.25	0.0	...
12 Mg.....	24	1.31	7.59	7.40	0.2	0.0	0.2
13 Al	27	1.57	6.48	6.33	0.02	0.0	...
14 Si.....	28	1.85	7.55	7.27	0.1	0.0	0.5
15 P	31	2.15	5.57	5.42	0.6	...	...
16 S	32	2.48	7.27	7.09	0.6	0.0	0.7
17 Cl	35	2.83	5.27	5.12	0.5	0.0	...
18 Ar	40	3.20	6.56	6.41	1.0	1.0	0.5
20 Ca	40	4.04	6.34	6.20	0.003	0.0	...
22 Ti	48	4.97	4.93	4.81	0.002	...	...
24 Cr	52	5.97	5.68	5.51	0.03	0.0	...
25 Mn.....	55	6.55	5.53	5.34	0.07	...	...
26 Fe	56	7.12	7.50	7.43	0.3	0.0	0.2
27 Co	59	7.73	4.92	4.92	0.05	...	...
28 Ni	59	8.35	6.25	6.05	0.04	0.0	...

[a] Molecular weight.

[b] K edge energy (rounded after Verner & Yakovlev 1995).

[c] Solar abundance (see also § 2.3; Anders & Grevesse 1989; Grevesse et al. 1991; Grevesse & Noels 1993).

[d] Adopted abundance of the ISM based on Snow & Witt 1996, Cardelli et al. 1996, and Meyer et al. 1997, 1998; see § 2.3.

[e] Ratio of gas abundance to total ISM abundance, $1 - \beta_Z$, using our adopted abundances (§ 2.4) and, for comparison, the older values of Morrison & McCammon 1983 (MM83) and Ride & Walker 1977 (Ride77).

by Grevesse & Sauval (1999) in a critical reevaluation of the available data on Fe I lines. The uncertainty of the solar abundances in Table 2 is ~ 0.06 dex or smaller with the exception of log $A_{\rm Ne}$ and log $A_{\rm Ar}$, for which the uncertainty is 0.1 dex.

As more abundance measurements have been made outside our solar system, it has become apparent that the total gas plus dust ISM abundances are actually lower than the solar abundances (Sofia, Cardelli, & Savage 1994; Savage & Sembach 1996, and references therein). Studies of the carbon abundance reviewed by Snow & Witt (1995) strongly indicate a subsolar abundance of carbon in the ISM, with a probable value of $\sim 70\%$ solar. Similar reductions of 20%–30% with respect to solar abundances are also indicated for the other metals (Snow & Witt 1996; Savage & Sembach 1996). This trend is consistent with new measurements of the gas-phase abundance of O, C, and N obtained with the Goddard High Resolution Spectrograph (GHRS) on the *Hubble Space Telescope* (Meyer, Jura, & Cardelli 1998; Meyer, Cardelli, & Sofia 1997; Cardelli et al. 1996).

Possible differences between solar and ISM abundances had been noted already at the time of publication of previous models for $\sigma_{\rm ISM}$, and the previous computations of $\sigma_{\rm ISM}$ closely reflect the historical changes in the understanding of these local abundances. Ride & Walker (1977), for instance, used abundances that were greater than solar abundances in order to better represent abundance values in an ISM assumed to be chemically enriched by Galactic evolution, and the model of BM92 was specifically designed to allow adjustments to the assumed abundances.[2] Now that a consistent picture of lower ISM abundance seems to have emerged, the cosmic abundance needs to be revised in models of $\sigma_{\rm ISM}$. To that end we adopt default recommended abundances for the ISM. These abundance values are listed in Table 2 and refer to the *total* abundance of the elements in either the gaseous or grain phase of the ISM. For C, N, and O, we use the values of Cardelli et al. (1996) and Meyer et al. (1997, 1998), respectively, while for all other elements we use the abundances given by Snow & Witt (1996; Mg, Si, S, Ca, Ti, Cr, Fe, Ni), or, where no value was recommended by these authors, we assume an abundance of 70% with respect to our adopted solar abundances.

We are aware that these abundances are still very much uncertain; the uncertainties in the general ISM abundances are still on the order of 0.1 dex or higher and also strongly depend on the line of sight. However, we feel that it has been adequately established that solar abundances are enriched with respect to the ISM and that for most astronomical work using the ISM abundances in Table 2 is preferable. Since one may anticipate the need for further revision of the interstellar abundances, we have also included an option to change these default abundances in the XSPEC implementation of our model (Appendix B), as BM92 did.

Because of the appreciable difference in the X-ray cross sections for molecular and neutral hydrogen (§ 2.2), it is necessary to include the contribution of molecular hydrogen. About one-half of the hydrogen in the Galaxy as a whole is molecular; however, it is not uniformly distributed (Shull & Beckwith 1982). Surveys of low Galactic latitudes indicate that the ratio between H_2 and H I is strongly dependent on the radial distance from the Galactic center (Brinks 1990; Bronfman et al. 1988). UV observations of H_2 absorption lines with *Copernicus* and with the orbiting and retrievable far- and extreme-ultraviolet spectrometer (*ORFEUS II*) echelle spectrograph indicate that about 20%– 25% of the hydrogen is in H_2 in the local ISM (Savage et al. 1977; W. Gringel et al. 2000, in preparation). These results are very line-of-sight dependent, though, with some lines of sight being completely free of H_2. Because of these large fluctuations in the H_2/H I ratio, it is thus difficult to choose a "typical value." In order to include the effect of molecular hydrogen on $\sigma_{\rm ISM}$ we therefore choose to use the value of 20% as the default value. To more accurately account for the opacity of molecular hydrogen, however, we strongly recommend that this ratio be set to that corresponding to the line of sight to the source. The abundances of other molecules are much smaller, so their inclusion is necessary only for work along lines of sight with very high $N_{\rm H}$ and hence not within the scope of this paper.

2.4. *Grain Physics*

Evidence for the presence of dust grains in the ISM comes from the observed interstellar extinction (Fitzpatrick 1999; Mathis 1990), as well as from the fact that the observed abundances of the elements in the ISM are generally less than the abundances assumed for the ISM (Savage & Sembach 1996). The ratio between the observed and the assumed abundances is called the "depletion," β_Z, of the elements. It is generally assumed that the depletion indicates the presence of dust in the ISM, especially since the most depleted elements, C, O, and Si, are thought to be good candidates for the formation of solids in the ISM (Sofia et al. 1994; Snow & Witt 1995; Mathis 1996, and references therein).

We have adopted a simplified grain model that assumes spherical grains in a Mathis, Rumpl, & Nordsieck (MRN) size distribution (Mathis, Rumpl, & Nordsieck 1977),

$$\frac{dn_{\rm gr}(a)}{da} \propto a^{-3.5}, \quad \text{where} \quad a_{\rm min} \le a \le a_{\rm max}, \qquad (7)$$

where typically grain size ranges from 0.025 to 0.25 μm (Draine & Lee 1984). While the grain composition and structure is still a matter of debate (Mathis 1996; Dwek 1997; Smith & Dwek 1998; Wolff, Clayton, & Gibson 1998), here, we assume composite ("fluffy") grains, consisting of vacuum inclusions in solids. Thus, the grain density in our model ($\rho = 1$ g cm^{-3}) is less than the $\rho = 2$ g cm^{-3} used in previous models (Fireman 1974; Ride & Walker 1977; MM83).

We assume chemically homogeneous grains consisting of silicates, graphites, and oxides. We list the adopted chemical composition of the grains in Table 2 in terms of the "depletion factor" $1 - \beta_Z$, the ratio between the *gas* abundance and the *total* interstellar abundance of the elements. Table 2 is based on the compilation of measurements given by Shull (1993), which is in general agreement with later GHRS measurements (Savage & Sembach 1996). Contrary to Shull, we do not assume N to be depleted into grains as is suggested by the observational evidence (Savage & Sembach 1996; Meyer et al. 1997). As recommended by Sofia et al. (1994), we also assume a larger abundance of Fe

[2] The abundances available in XSPEC are those of Anders & Grevesse (1989), Feldman (1992), and Anders & Ebihara (1982); in addition, user-specified abundances are possible. The BM92 model allows the user to vary the abundances with respect to these default abundances.

in grains than that assumed by Shull (1993). For cobalt the values determined by Mullman et al. (1998) are used.

To illustrate the large uncertainties associated with the grain composition, we also list in Table 2 the depletions used by Ride & Walker (1977) and MM83, the previous works that included grains in the computation of $\sigma_{\rm ISM}$. The depletion factors of Ride & Walker (1977), as shown in Table 2, are based on gas-abundance measurements using *Copernicus* data. Only one of the depletion factors of MM83 is based on observation, that for oxygen (de Boer 1979, 1981); for the rest, MM83 considered elements to be either completely depleted into grains or entirely in gas form. This simplifying assumption represents the maximum effect of grains on the ISM opacity.

We note that grains are included here partly for completeness and partly to indicate how changes to the current ISM grain model might affect observations made with the more recent X-ray observatories and not as an attempt to model the solid state in the interstellar medium. While a "perfect" grain model meeting all abundance and observational requirements remains elusive, our grain model at least adequately reproduces the observed extinction, emission features, and depletions of the diffuse ISM (Mathis 1996). For more detailed work, the assumption of spherical grains must be modified (Mathis 1990).

3. CONCLUSIONS AND SUMMARY

3.1. *Results*

Using equation (1) and the assumptions described above, we compute $\sigma_{\rm ISM}$. The results are shown in Figure 1, where we display the X-ray absorptivity as $\sigma_{\rm ISM} E^3$ to emphasize deviations from the E^{-3} proportionality of $\sigma_{\rm bf}$. By reading the plot as a "bar diagram," it is easy to estimate the relative importance of the contributors to $\sigma_{\rm ISM}$. For energies above the oxygen K edge at $\sim$0.5 keV (see Table 2), the X-ray opacity is dominated by the metals and H and He are relatively unimportant. Below 1 keV, C, N, O, and Ne are the important absorbers, while above 1 keV, Si, S, and Fe are important.

Also clear from Figure 1 is that the effect of grains on $\sigma_{\rm ISM}$ is small for a standard MRN distribution. The effect of grains is found to be less than previous estimates such as MM83 in part because our grain model consists of lower density porous grains and in part because we calculate $\sigma_{\rm grains}$ for an MRN distribution of grain sizes rather than by choosing an average grain size such as 0.3 μm as used by Fireman and others. Thus, the greatest number of grains lies in very small grains with $\tau \ll 1$ above $\sim$1 keV, so self-shielding is not important in these grains. Consequently, for an MRN distribution there are only small differences between the optical depth of an entirely gas-phase ISM and the optical depth for an ISM in which some of the gas atoms have been depleted into grains. This is illustrated in Figure 2, where we plot the grain optical depth as a function of energy for grains of radius 0.25 and 0.025 μm, as well as for an MRN distribution of grains. These optical depths are calculated using Appendix A and considering a hydrogen column density $N_{\rm H}$ of 1.0×10^{20} cm^{-2}. The total mass in grains is the same for all three grain models shown. Clearly, the self-blanketing factor affects the opacity more for low energies and larger grain sizes. Since the change in grain

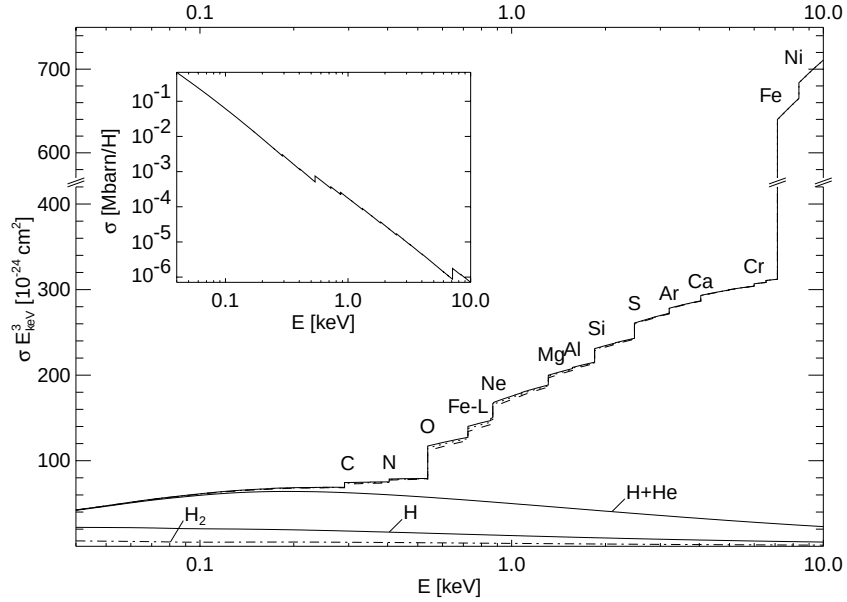

FIG. 1.—Absorptivity per hydrogen atom of the ISM using the assumptions described in the text. The dotted line is the absorptivity including grains with an MRN distribution, and the dashed line is the absorptivity assuming that all grains are of radius $a = 0.3$ μm. The inset shows the cross section without the multiplication by E^3. We also illustrate the contribution of hydrogen and hydrogen plus helium to the total cross section. The contribution of the H_2 cross section to the total hydrogen cross section is indicated by the dot-dashed line.

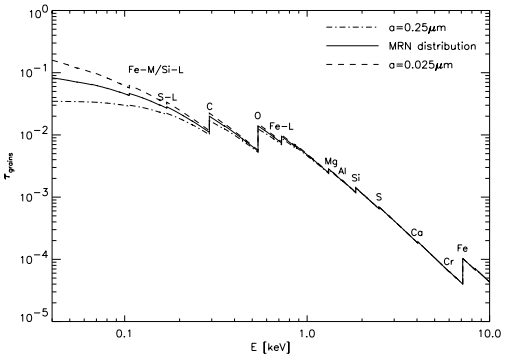

FIG. 2.—Optical depth of grains for a hydrogen column $N_H = 1.0 \times 10^{20}$ cm^{-2} (see Appendix A) and for grains of radius $a = 0.25$ μm (*dot-dashed line*) and $a = 0.025$ μm (*dashed line*) as a function of X-ray energy. The total mass in grains is constant. The shielding reduces the optical depth at low energies and for large grain sizes. The labels denote the K edges of the elements indicated.

optical depth for the MRN distribution is quite small, grains only slightly modify the absorptivity of the ISM.

We stress, however, that the grain model as used here applies to the diffuse ISM rather than to dense regions such as inner molecular clouds or young stellar objects, where grains might play a much more important role (Mathis 1990). By changing the range of grain sizes from the range adopted here for the diffuse ISM to a grain distribution with larger grains, our formalism (including the XSPEC routine described in Appendix B) can be used to treat these regions as well. As an example, we show in Figure 1 the influence of grains with $a = 0.3$ μm. In this case, X-ray observations will allow the detection of the grains because of the large influence of self-shielding, even with instruments that do not have the high energy resolution to see the solid-state resonance effects close to the absorption edges.

3.2. *Comparison with Previous Models*

As we outlined in §§ 2.2 and 2.3, the major differences between this model and the previous models are the updates to the atomic cross sections and the assumed abundances. With the use of simulated observations, we can examine the impact of an updated σ_{ISM} on the interpretation of observations.

In order to demonstrate the effect of the updates to the cross sections, we compare our values of σ_{ISM} with those of MM83 and BM92. In Figure 3*a* we show the relative deviation between our formulation and that of the earlier models, using our adopted cross sections and the assumed abundances of the MM83 and BM92 models, respectively. Thus, the figure shows the cumulative effect of the updated cross sections. The differences between the models at photon energies below 0.3 keV are mainly a result of the uncertainty in the He cross section. Additional peaks at the K and L shell edges are due to $\sim$10 eV discrepancies in the assumed edge energy between these models (§ 2.2) and are not relevant for practical work with moderate-resolution instruments. The difference in the values of σ_{bf} produces the curvature of the relative deviation. The missing subshell absorption edges in the MM83 model are also readily apparent.

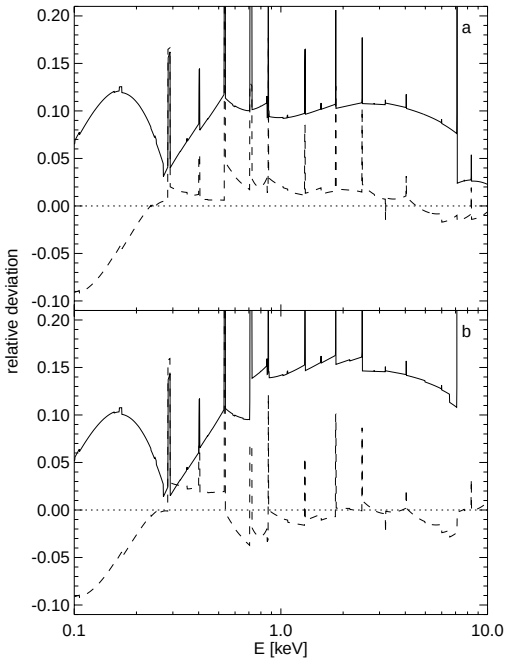

FIG. 3.—Relative deviation of the cross sections of BM92 (*solid lines*) and MM83 (*dashed lines*) from the model described here. The relative computation is given as $(\sigma_i - \sigma)/\sigma$, where σ_i = the value of BM92 or MM83 and where σ is our formulation. The spikes at the K and L absorption edges are due to slight differences in the assumed edge energies. (*a*) Relative deviation computed using the abundances of BM92 and MM83, respectively. This panel highlights the effect of the change in the cross sections. (*b*) Relative deviation from our model, computed using the solar abundances of Table 2, illustrating the cumulative effect of using different default solar abundances and changing cross sections. See § 2.2 for further discussion.

In Figure 3*b*, we again show the relative deviation between our model and the earlier models but this time using our default *solar* abundance (Table 2) for the abundances in our model, including the additional elements not contained in the MM83 and BM92 models, as well as the H_2 molecule (important especially below $\sim$300 eV). In this figure, all models are with "solar" abundances, but the disagreement between the "solar" abundances used by the different authors results in 10% of the difference between the three models compared in Figure 3. However, the difference resulting from different values of the "solar" abundance is small compared with the difference that results from using our default abundance values, which are reduced with respect to solar abundances. The discrepancy in σ_{ISM} that results from the use of our default ISM abundances instead of the solar abundances indicated in Table 2 is shown in Figure 4.

In order to illustrate the observable changes introduced by our updated model of σ_{ISM}, we studied these effects using simulations of observations. We simulated the observation of a bright X-ray source that has a pure power-law spectrum with photon index $\Gamma = -1.7$ and a normalization of $A_{PL} = 2$ photons cm^{-2} s^{-1} keV^{-1} at 1 keV. Such a source

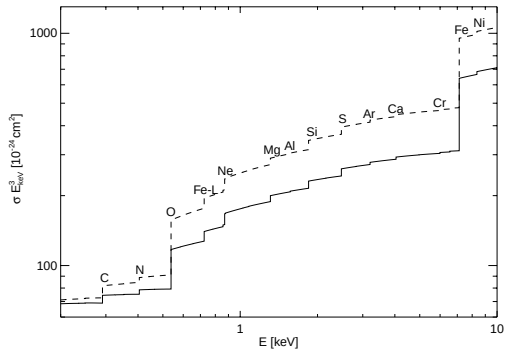

FIG. 4.—Absorptivity per hydrogen atom of the ISM for our adopted ISM abundances (*solid line*) and for the solar abundances of Table 2 (*dashed line*). For clarity, the cross section has been multiplied by E^3; however, the *y*-axis is logarithmic here, not linear as in Fig. 1. The revised abundances produce changes in σ_{ISM} of up to 30% with respect to the solar abundances.

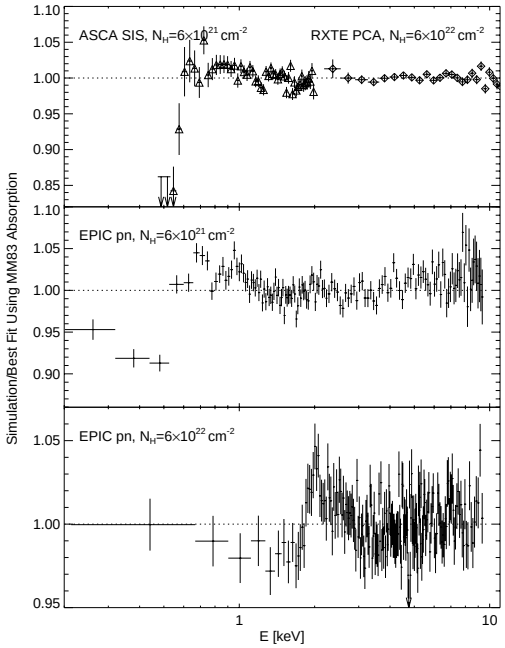

FIG. 5.—Ratio of simulated X-ray data absorbed with our model for σ_{ISM} to the best-fit model using a power-law model and the MM83 models, for the *ASCA* SIS (*triangles*), *RXTE* PCA (*diamonds*), and the *XMM-Newton* EPIC pn CCDs. The *ASCA* SIS simulation with our model is shown for energies below 2 keV. In all cases, the error bars represent Poisson noise. While older models produce adequate fits for the current instruments (with the exception at the O edge, see text), differences of ~5%–10% are found with the EPIC pn simulations.

spectrum is characteristic, e.g., of Cygnus X-1 in the hard state (Dove et al. 1998). We then used two values of hydrogen column, $N_H = 6 \times 10^{21}$ cm^{-2} and $N_H = 6 \times 10^{22}$ cm^{-2}, to produce the absorbed spectrum using our model for σ_{ISM}, using our assumed interstellar abundances. The two values for N_H are necessary to illustrate the effects of N_H both in the low-energy band (small N_H) and in the high-energy band (large N_H). We simulated an observation by folding the photon spectrum through the detector response matrix and adding Poisson noise. To ensure comparable signal-to-noise ratios in all simulated observations, the exposure times were chosen such that 10^6 photons were contained in the resulting spectrum. The detectors we chose to represent current instruments were SIS on the *Advanced Satellite for Cosmology and Astronomy* (*ASCA*) for the low-N_H simulation and the Proportional Counter Array (PCA) on the *Rossi X-Ray Timing Explorer* (*RXTE*) for the large-N_H simulation. The detector chosen to represent the quality and energy resolution of the future missions is the European Photon Imaging Camera (EPIC) pn-CCD on *XMM-Newton*. In neither case did we take photon pileup or other instrumental effects such as a saturation of the telemetry bandwidth into account.

The resulting simulated photon spectrum was rebinned and analyzed using the MM83 and the BM92 models for σ_{ISM}. In Figure 5 we present the ratio between the data and the resulting best-fit model using the MM83 model (the BM92 model without varying the abundances gave qualitatively the same results). For the PCA and the SIS, the fits with the MM83 model gave an acceptable description of the data. Our low-N_H simulation shows that the *ASCA* SIS is able to detect the discrepancy in the oxygen abundance between the solar and the ISM values. The other abundance differences are not measurable in reasonable amounts of observing time. We note in passing that Ebisawa et al. (1996) indeed found residuals in an observation of the black hole candidate Cygnus X-1 that are very similar to those shown in Figure 5, which points toward an oxygen abundance of ~80% solar in the direction to Cyg X-1.

For the large-N_H simulation, the fit to the simulated *RXTE* PCA spectrum recovered the input parameters for Γ and for A_{PL} to two significant digits and found a hydrogen column of $N_H = 4 \times 10^{22}$ cm^{-2}. The residuals shown in Figure 5 show some structure below 3 keV that is caused by underestimating N_H, which results in the nonoptimal χ^2 value of the fit ($\chi^2_{red} = 1.7$). However, the PCA has significant systematic uncertainties in this region (Wilms et al. 1999), and the deviation seen in our simulation would probably go undetected in a real observational situation.

Although we have not done an exhaustive search of the whole N_H space, the above result convinces us that, for most applications using the current moderate-resolution instruments, the models of MM83 and BM92 are sufficient. The physical cause for the underestimate of N_H is that, for energies above 1 keV, σ_{ISM} is dominated by the metals. Since the abundance ratios of the metals are a result of stellar nucleosynthesis, reducing the metal abundance with respect to hydrogen from the MM83 or BM92 values to our values can be compensated for by assuming a different (lower) hydrogen column. Nor does the slightly different shape of σ_{bf} that results from the updated cross sections produce a noticeable effect in the PCA simulations; the energy resolution of the PCA is insensitive to a difference of this magnitude.

Our simulations for the EPIC pn camera, on the other hand, show deviations on the 5% level when fitted with the MM83 and BM92 models (Fig. 5). These changes are clearly

due to the update of the abundances and cross sections. It is for instruments such as the EPIC pn camera that we recommend that our model be used. The EPIC observation simulated here is quite short (the raw EPIC pn count rate of Cygnus X-1 will be ~ 2400 counts s^{-1}, so the spectrum used for modeling here has an exposure time of only 4 ks, shorter than the minimum *XMM-Newton* observing time of 5 ks), and the ratio plots in Figure 5 already show the characteristic curvature due to the deviation in the shape of the cross section assumed in the MM83 models. We note that a similar behavior is also present when fitting the simulated spectrum with the BM92 data. When using the BM92 cross sections, however, it is possible to obtain a good description of the overall absorption by treating the abundances as free parameters. In this case the "wavy" residual structure still remains, although the relative abundances found for the elements do come close to the abundances that we assumed in our modeling of $\sigma_{\rm ISM}$. As a result, we recommend using our model whenever high-precision work on the 1%–2% level is necessary, as well as in cases when the absorbing column resulting from the spectral fitting process is to be physically interpreted (i.e., when comparing X-ray $N_{\rm H}$ values with radio data or when modeling an observed X-ray spectrum for which the $N_{\rm H}$ value is known by other means).

3.3. *Caveats*

While we feel that the model for $\sigma_{\rm ISM}$ as presented in the previous sections is well suited for most X-ray astronomical work, several astronomical or physical issues had to be neglected in the modeling process. In particular, our model does not include the effects of the warm phase or of the ionized phase of the ISM. In addition, we ignore Thomson scattering, which becomes important at moderate to high Thomson optical depths and $E \gtrsim 4$ keV. These effects have not been included largely because they are negligible for most situations in which our model is likely to be used. Furthermore, the model assumes that there is no variation of the abundances along the line of sight. Finally, we note that energy-dependent scattering by dust grains has not been considered here since an XSPEC routine ("dust") already exists to treat it.

The warm and ionized phases of the ISM have been neglected here for a number of reasons. Large parts of the ISM are assumed to be (moderately) ionized, and a good model for $\sigma_{\rm ISM}$ should in principle include the ionized phase. However, there is even less agreement on the ionization state of the ISM as a whole than there is on the grain phase, which was discussed in § 2.4. The major reason for this disagreement is a good one: the ionization of the ISM depends strongly on the line of sight, so any general model for the ionization structure of the Galaxy is prone to fail. It appears, however, that most of the warm phase of the ISM is only moderately ionized, so our model will still be applicable except for photon energies close to the K edges. For oxygen, e.g., the K edge energy increases from 0.54 keV for O I to 0.61 keV for O IV, and the photoionization cross section is also dependent on the ionization stage. It should be noted, though, that the ionization of hydrogen will strongly influence $\sigma_{\rm ISM}$ for energies below 0.1 keV. For instance, in their study of soft X-ray emission from other galaxies, Cui et al. (1996) assumed the ratio between H I and H II to be 1. Using the code presented in Appendix B, this effect may be taken into account by changing the relative abundances of He and the metals with respect to hydrogen.

Similar line-of-sight effects also hold true for the abundances. In the Galaxy, measurement of abundances in H II regions and planetary nebulae has suggested the existence of a radial abundance gradient, particularly at small Galactic radii (Rana 1991; Kaufer et al. 1994, and references therein). When one computes the absorption of any background object through such a medium with varying abundances, the abundances measured in the X-rays will be the average of the abundance variations along the line of sight. Since the abundances in our model are allowed to vary, it is possible to take this effect into account. Obviously, in such a case the assumed abundance set with respect to which the relative abundances are measured is a matter of taste, and using the solar abundances of Table 2 as a baseline instead of the ISM abundances might be a better choice.

Our model also ignores the influence of Thomson scattering because for many observations it will not make a substantial contribution. This is not to say that it is always negligible; Thomson scattering is the dominant physical process for the attenuation of X-rays above ~ 10 keV. As a rough guideline, Thomson scattering should always be included in the modeling process when $N_{\rm H} \gtrsim 10^{22}$ cm^{-2} (see, e.g., Stelzer et al. 1999). Detailed instructions based on Monte Carlo modeling of Thomson scattering in moderately optically thick media are given by Yaqoob (1997). Note, however, that Yaqoob assumes the electrons to be free. When the electrons are bound, it is more appropriate to consider incoherent scattering, i.e., Compton scattering, off the bound electrons. The cross sections for incoherent scattering and the Klein-Nishina cross section are slightly different (on the percent level), which should be taken into account. Analytical estimates for this effect have been given by Gorshkov, Mikhailov, & Sherman (1973) for the H atom; for other elements tables are available (Hubbell et al. 1975; Henke et al. 1993). For most work, however, these corrections are negligible.

Finally, we also stress that our model, like its predecessors MM83 and BM92, is *not* well suited for extremely high precision work, e.g., high signal-to-noise ratio spectra with the grating spectrometers on *XMM-Newton* and *Chandra*. The energy resolution of these very high resolution instruments is so high that the X-ray absorption fine structure (XAFS) within grains and molecules might become relevant, as well as resonance effects close to the absorption edges in the absorption cross section itself. For the inclusion of the resonances much higher resolution cross sections than those available here are required. XAFS effects become noticeable especially in regions of large $N_{\rm H}$ where grains are an important ingredient. For these studies, dedicated modeling codes are being devised, which should be used instead. See Forrey, Woo, & Cho (1998), Woo, Forrey, & Cho (1997), Woo (1995), and the references therein for further details.

3.4. *Summary and Outlook*

We have presented an improved model for the X-ray absorption in the interstellar medium valid above ~ 100 eV by updating the relevant photoionization cross sections and by including the effect of the H_2 molecule and a revised set of recommended elemental abundances for the interstellar medium. Since the abundances of the metals are smaller than previously estimated, our values of $\sigma_{\rm ISM}$ are generally smaller than those used previously. We have shown that these updates will be relevant for instruments to be avail-

able as this paper goes into print. We have also reconsidered the effect of grains in the ISM by improving the grain model and the calculation of $\tau_{\rm grains}$, taking into account recent studies of the physical properties of interstellar dust grains. Our results show that the change in opacity due to grains on $\sigma_{\rm ISM}$ for realistic grain models and realistic chemical composition of the grains is small. As described in Appendix B, our calculation of $\sigma_{\rm ISM}$ is available as a subroutine that can be used with X-ray data analysis packages such as XSPEC.

This work highlights the point made by Shull (1993) and others: that great uncertainties remain in much of the atomic physics data needed to interpret X-ray astronomical observations. The effective areas and energy resolutions of instruments recently launched will be more sensitive than the available atomic data for the X-ray energy range can accommodate, and the situation is even worse for possible future instruments such as *Constellation-X* or the *X-Ray Evolving Universe Spectroscopy Mission* (*XEUS*). The differences between the currently available cross sections discussed in § 2.2 are still at the 5% level. We hope that the advent of the new instruments will also initiate new attempts to more accurately determine the atomic data on which X-ray astronomy can rely. We will therefore continue over the next years to update the database of the computations presented here and periodically release new versions of the code presented in Appendix B that will incorporate the improvements in the abundances or the atomic physics.

This work has been partially financed by NASA grants NGT 5-80, NAG5-7339, and NAG5-7340 and by a National Physical Science Consortium Fellowship grant (to A. A.). J. W. acknowledges the hospitality of the high-energy astrophysics groups at JILA and at the University of California at San Diego, where part of this work was done. We thank the referee Dan McCammon for his comments, which greatly improved the presentation of this paper, and for providing the code for the helium autoionization resonances. We also thank Laurie Kovalenko, Phil Maloney, Katja Pottschmidt, Richard Rothschild, Rüdiger Staubert, Klaus Werner, and Svet Zhekov for useful comments.

APPENDIX A

SELF-SHIELDING IN THE GRAINS

To derive the optical depth of the grains (eq. [5]), we consider a population of grains of homogeneous chemical composition with size a, geometrical cross section $\sigma_{\rm geom}$, column density $\langle N\rangle$, and average photoionization cross section $\langle\sigma\rangle$ (per atom). For grains of realistic shape, $\langle N\rangle$ is a complicated function of a. Since the influence of grains on $\sigma_{\rm ISM}$ is small, however, for simplicity we can assume that the grains are spheres with radius a so that

$$\langle N\rangle = \frac{4\rho a}{3\mu} = \frac{4na}{3}\,, \tag{A1}$$

where ρ is the mass density of the grain, n the number density of the grain, and μ the mean molecular weight of the grain's constituents. Using the notation of § 2.1, μ is given by

$$\mu = \sum_Z A_Z \times \beta_Z \times \mu_Z \Big/ \sum_Z A_Z \times \beta_Z\,. \tag{A2}$$

Here, μ_Z is the molecular weight of element Z (Table 2). For the default abundances and depletions of Table 2, $\mu = 18.2$ amu $= 3.0 \times 10^{-23}$ g atom^{-1}. Assuming $\rho = 1$ g cm^{-3}, the grain number density is $n = 3.3 \times 10^{22}$ atoms cm^{-3}. Ignoring solid-state effects, the photoionization cross section of the grain material is given by

$$\langle\sigma\rangle = \sum_Z A_Z \times \beta_Z \times \sigma_{\rm bf}(Z) \Big/ \sum_Z A_Z \times \beta_Z\,. \tag{A3}$$

For a column density $N_{\rm grains}$ of grains of a *single size* along the line of sight, the optical depth for photoabsorption of the grains is the product between the geometrical optical depth of the grains, $N_{\rm grains}\sigma_{\rm geom}$, and the fraction of photons that encounter the grain and are absorbed:

$$\tau_{\rm grains} = N_{\rm grains}\sigma_{\rm geom}[1 - \exp\,(-\langle\sigma\rangle\langle N\rangle)]\,. \tag{A4}$$

In computing $\sigma_{\rm ISM}$ for grains of a single size it is sometimes convenient to express $\tau_{\rm grains}$ in terms of the optical depth that would be observed if the constituents of the grain were in the gaseous phase, $\tau_{\rm grains} = fN_{\rm gas}\langle\sigma\rangle$. Hence,

$$f = \frac{N_{\rm grains}\sigma_{\rm geom}}{N_{\rm gas}\langle\sigma\rangle}\,[1 - \exp\,(-\langle\sigma\rangle\langle N\rangle)] = \frac{1 - \exp\,(-\langle\sigma\rangle\langle N\rangle)}{\langle\sigma\rangle\langle N\rangle}\,, \tag{A5}$$

since the column density of the grain is $N_{\rm gas}/(N_{\rm grains}\sigma_{\rm geom})$. This factor is called the self-blanketing factor (Fireman 1974).

For the general case that the grains have a *size distribution* $dn_{\rm gr}(a)/da$, where

$$\int_0^\infty \frac{dn_{\rm gr}}{da}\,da = 1\,, \tag{A6}$$

a similar derivation shows that

$$\tau_{\rm grains} = N_{\rm H}\,\xi_g \int_0^\infty \frac{dn_{\rm gr}(a)}{da}\,\sigma_{\rm geom}[1 - \exp\,(-\langle\sigma\rangle\langle N\rangle)]da\,, \tag{A7}$$

where ξ_g is the number of grains per hydrogen atom along the line of sight. For spherical grains,

$$\xi_g = \sum A_Z \times \beta_Z \times \mu_Z \Big/ \int \frac{dn_{\rm gr}}{da} \times \rho \times \frac{4}{3}\,\pi a^3 \times da\,. \tag{A8}$$

For a power-law size distribution, $dn_{\rm gr}(a)/da = ka^{-p}$, where $a_{\rm min} \le a \le a_{\rm max}$, we can express $\tau_{\rm grains}$ in terms of special functions. Inserting $\sigma_{\rm geom} = \pi a^2$ into equation (A7) and performing a partial integration, we obtain for $p < 4$

$$\tau_{\rm grains} = N_{\rm H}\,\xi_g\,\frac{\pi k}{p-3}\left\{\frac{1}{a_{\rm min}^{p-3}}\,(1 - e^{-4\langle\sigma\rangle n a_{\rm min}/3}) - \frac{1}{a_{\rm max}^{p-3}}\,(1 - e^{-4\langle\sigma\rangle n a_{\rm max}/3})\right.$$
$$\left. + (4\langle\sigma\rangle n/3)^{p-3}[\gamma(4-p,\,4\langle\sigma\rangle n a_{\rm max}/3) - \gamma(4-p,\,4\langle\sigma\rangle n a_{\rm min}/3)]\right\}, \tag{A9}$$

where the incomplete gamma function is given by (§ 6.5 of Abramowitz & Stegun 1964)

$$\gamma(\alpha,\,x) = \int_0^x e^{-t}t^{\alpha-1}\,dt \tag{A10}$$

and can be evaluated using algorithms presented by § 6.2 of Press et al. (1992).

APPENDIX B

IMPLEMENTATION INTO XSPEC

Using the formalism and data described in § 2, we have written subroutines that can be used in conjunction with the popular X-ray data analysis package XSPEC (Arnaud 1996).[3]

Given the uncertainty of many of the parameters entering the model, there are several interfaces to the subroutine. The main spectral model, "tbabs," is intended as a replacement for the earlier "wabs" and "phabs" models, as well as their redshifted versions. This model assumes the abundances and depletion factors of Table 2. A subroutine "ztbabs" for modeling redshifted absorption is also available. The latter subroutine does not account for the dust component, as X-ray observations with a measurable dust influence will most probably include only observations of Galactic objects, at least within the next decade.

In addition, the XSPEC model "tbvarabs" provides a full interface to the X-ray absorption model presented in § 2 and allows the user to change all abundances, depletion factors, and grain properties. We stress that this model is very powerful and therefore prone to misuse. Caution is required when fitting data with too many free parameters.

REFERENCES

Abramowitz, M., & Stegun, I. A. 1964, Handbook of Mathematical Functions (Washington: U.S. Government Printing Office)
Anders, E., & Ebihara, M. 1982, Geochim. Cosmochim. Acta, 46, 2363
Anders, E., & Grevesse, N. 1989, Geochim. Cosmochim. Acta, 53, 197
Arabadjis, J. S., & Bregman, J. N. 1999, ApJ, 510, 806
Arnaud, K. A. 1996, in Astronomical Data Analysis Software and Systems V, ed. J. H. Jacoby & J. Barnes (San Francisco: ASP), 17
Bałucińska-Church, M., & McCammon, D. 1992, ApJ, 400, 699 (BM92)
Band, I. M., Trzhaskovskaya, M. B., Verner, D. A., & Yakovlev, D. G. 1990, A&A, 237, 267
Bethe, H. A., & Salpeter, E. E. 1957, Quantum Mechanics of One- and Two-Electron Atoms (Berlin: Springer)
Biémont, E., Baudoux, M., Kurucz, R. L., Ansbacher, W., & Pinnington, E. H. 1991, A&A, 249, 539
Brinks, E. 1990, in The Interstellar Medium in Galaxies, ed. H. A. Thronson & J. M. Shull (Dordrecht: Kluwer), 39
Bronfman, L., Cohen, R. S., Alvarez, H., & Thaddeus, P. 1988, ApJ, 324, 248
Brown, R. L., & Gould, R. J. 1970, Phys. Rev. D, 1, 2252
Cardelli, J. A., Meyer, D. M., Jura, M., & Savage, B. D. 1996, ApJ, 467, 334
Chen, W. F., Cooper, G., & Brion, C. E. 1991, Phys. Rev. A, 44, 186
Cui, W., Sanders, W. T., McCammon, D., Snowden, S. L., & Womble, D. S. 1996, ApJ, 468, 102
de Boer, K. S. 1979, ApJ, 229, 132
———. 1981, ApJ, 244, 848
Dove, J. B., Wilms, J., Nowak, M. A., Vaughan, B., & Begelman, M. C. 1998, MNRAS, 289, 729
Draine, B. T., & Lee, H. M. 1984, ApJ, 285, 89
Dwek, E. 1997, ApJ, 484, 779
Ebisawa, K., Ueda, Y., Inoue, H., Tanaka, Y., & White, N. E. 1996, ApJ, 467, 419
Feldman, U. 1992, Phys. Scr., 46, 202
Fernley, J. A., Taylor, K. T., & Seaton, M. J. 1987, J. Phys. B, 20, 6457
Fireman, E. L. 1974, ApJ, 187, 57
Fitzpatrick, E. L. 1999, PASP, 111, 63
Fogel, M. E., & Leung, C. M. 1998, ApJ, 501, 175
Forrey, R. C., Woo, J. W., & Cho, K. 1998, ApJ, 505, 236
Gorshkov, V. G., Mikhailov, A. I., & Sherman, S. G. 1973, Zh. Eksp. Teor. Fiz., 64, 1128 (Sov. Phys.–JETP, 37, 572)
Gould, R. J., & Jung, Y.-D. 1991, ApJ, 373, 271
Grevesse, N., & Anders, E. 1989, in AIP Conf. Proc. 183, Cosmic Abundances of Matter, ed. C. Waddington (New York: AIP), 1
Grevesse, N., Lambert, D. L., Sauval, A. J., van Dishoeck, E. F., Farmer, C. B., & Norton, R. H. 1991, A&A, 242, 488
Grevesse, N., & Noels, A. 1993, in Origin and Evolution of the Elements, ed. N. Prantzos, E. Vangioni-Flam, & M. Casse (Cambridge: Cambridge Univ. Press), 15
Grevesse, N., & Sauval, A. J. 1999, A&A, 347, 348
Henke, B. L., Gullikson, E. M., & Davis, J. C. 1993, At. Data Nucl. Data Tables, 54, 181 (http://cindy.lbl.gov/optical_constants/)

[3] These subroutines are available at http://astro.uni-tuebingen.de/nh/.

Henke, B. L., Lee, P., Tanaka, T. J., Shimabukuro, R. L., & Fujikawa, B. K. 1982, At. Data Nucl. Data Tables, 27, 1
Hubbell, J. H., et al. 1975, J. Phys. Chem. Ref. Data, 4, 471
Kaufer, A., et al. 1994, A&A, 289, 740
Kostik, R., Shchukina, N. G., & Rutten, R. J. 1996, A&A, 305, 325
Marr, G. V., & West, J. B. 1976, At. Data Nucl. Data Tables, 18, 497
Mathis, J. S. 1990, ARA&A, 28, 37
———. 1996, ApJ, 472, 643
Mathis, J. S., Rumpl, W., & Nordsieck, K. H. 1977, ApJ, 217, 425
Meyer, D. M., Cardelli, J. A., & Sofia, U. J. 1997, ApJ, 490, L103
Meyer, D. M., Jura, M., & Cardelli, J. A. 1998, ApJ, 493, 222
Morrison, R., & McCammon, D. 1983, ApJ, 270, 119 (MM83)
Mullman, K. L., Lawler, J. E., Zsargó, J., & Federman, S. R. 1998, ApJ, 500, 1064
Nicolosi, F., Jannitti, E., & Tondello, G. 1991, J. Phys. IV, C1, 89
Oza, D. H. 1986, Phys. Rev. A, 33, 824
Press, W. H., Teukolsky, S. A., Vetterling, W. T., & Flannery, B. P. 1992, Numerical Recipes in FORTRAN (2d ed.; Cambridge: Cambridge Univ. Press)
Raassen, A. J. J., & Uylings, P. H. M. 1998, A&A, 340, 300
Rana, N. C. 1991, ARA&A, 29, 129
Ride, S. K., & Walker, A. B. C., Jr. 1977, A&A, 61, 339
J. A. R., & Haddad, G. N. 1994, J. Opt. Soc. Am. B, 11, 277
Savage, B. D., Bohlin, R. C., Drake, J. F., & Budich, W. 1977, ApJ, 216, 291
Savage, B. D., & Sembach, K. R. 1996, ARA&A, 34, 279
Shull, J. 1993, Phys. Scr., T47, 165
Shull, J. M., & Beckwith, S. 1982, ARA&A, 20, 163
Smith, R. K., & Dwek, E. 1998, ApJ, 503, 831
Snow, T. P., & Witt, A. N. 1995, Science, 270, 1455
———. 1996, ApJ, 468, L65
Sofia, U. J., Cardelli, J. A., & Savage, B. D. 1994, ApJ, 430, 650
Stelzer, B., Wilms, J., Staubert, R., Gruber, D., & Rothschild, R. 1999, A&A, 342, 736
Strom, S. E., & Strom, K. M. 1961, PASP, 73, 43
Verner, D. A., & Yakovlev, D. G. 1995, A&AS, 109, 125
Verner, D. A., Yakovlev, D. G., Band, I. M., & Trzhaskovskaya, M. B. 1993, At. Data Nucl. Data Tables, 55, 233
Wilms, J., Nowak, M. A., Dove, J. B., Fender, R. P., & di Matteo, T. 1999, ApJ, 522, 460
Wolff, M. J., Clayton, G. C., & Gibson, S. J. 1998, ApJ, 503, 815
Woo, J. W. 1995, ApJ, 447, L129
Woo, J. W., Forrey, R. C., & Cho, K. 1997, ApJ, 477, 235
Yan, M., Sadeghpour, H. R., & Dalgarno, A. 1998, ApJ, 496, 1044
Yaqoob, T. 1997, ApJ, 479, 184

ANHANG G

Broad Iron Lines in Active Galactic Nuclei:
A Possible Test of the Kerr Metric?

J. Wilms, R. Speith, C.S. Reynolds

1998

Nachdruck aus

Black holes: theory and observation
Hrsg. F.W. Hehl, R.J.K. Metzler, C. Kiefer
Lecture Notes in Physics
Vol 514, S. 69–79
Berlin, Heidelberg, New York: Springer Verlag

Broad Iron Lines in Active Galactic Nuclei: A possible test of the Kerr Metric?

Jörn Wilms[1], Roland Speith[2], and Christopher S. Reynolds[3]

[1] Institut für Astronomie und Astrophysik, Abt. Astronomie, Waldhäuser Str. 64, D-72076 Tübingen, Germany
[2] Institut für Astronomie und Astrophysik, Abt. Theoretische Astrophysik, Auf der Morgenstelle 10, D-72076 Tübingen, Germany
[3] JILA, University of Colorado, C. B. 440, Boulder, CO 80309-0440, U.S.A.

Abstract. The broad lines in Active Galactic Nuclei (AGN) discovered recently have been interpreted as evidence for emission close to the central black hole. We briefly describe the physical processes leading to the line emission, describe the computational methods used to compute the emerging line profiles, and summarize the qualitative behavior of these lines. We present the observational evidence for the relativistic lines, concentrating on the properties of the line in MCG −6-30-15, where the line profile shows strong indications that a Kerr black hole is present in the object. Finally, we show how future X-ray missions will help in deepening our understanding of the emission of broad iron lines from AGN.

1 Introduction

As reviewed in several chapters of this volume, there is ample evidence for the presence of optically thick accretion disks in Active Galactic Nuclei (AGN) and in Galactic black hole candidates. While the high luminosity of AGN is a good indicator for the presence of a deep potential well, the evidence for the geometry of the accretion process has to rely mainly on indirect evidence from the UV, X-ray, and γ-ray spectrum. The ultraviolet excess seen in most AGN, the "big blue bump", and (probably) also the soft X-ray excess below 1 keV are usually assumed to originate in the accretion disk. At energies above 1 keV the spectrum of AGN can be roughly described by a power-law with a photon index of 1.7 and, at least in Seyfert galaxies, an exponential cutoff above 100 or 200 keV. The current physical interpretation of this X-ray and γ-ray power-law component is that of Comptonization of the soft photons in a hot electron plasma, usually called an accretion disk corona, situated geometrically close to the accretion disk [6, 13, 12]. See [26] for a review of the radiation processes around AGN. Although the geometry of the X-ray producing region is still unclear, with possibilities ranging from "standard" thin accretion disks to more complicated accretion geometries as the advection dominated flows and the solutions proposed by Chakrabarti in this volume, there is general agreement that the high temperatures necessary for the production of the hard radiation are only possible in the close vicinity of the black hole, closer than about 100 Schwarzschild radii, where relativistic effects are important. The X-ray and γ-ray radiation

from Seyfert galaxies, therefore, should exhibit signatures that allow us to directly probe this region and perhaps even to find physical processes enabling us to directly measure parameters of the black hole as its mass or its angular momentum.

The availability of high sensitivity X-ray and γ-ray satellites in the past ten years has allowed the observational study of the broad band spectrum of AGN to search for such processes. Recently, extremely broad Iron fluorescence lines have been observed in several Seyfert galaxies. The most convincing interpretation for these lines is that they are produced in a geometrically thin accretion disk close to the central black hole. If this interpretation is correct, the line profiles are the best evidence for the existence of black holes known so far. In this review, we give a brief introduction to the field. In §2 we describe the physical processes leading to line emission close to the black hole, i.e. Compton reflection and fluorescent line emission (§2.1), followed by a description of the computational methods used to calculate the emerging line profiles (§2.2), and a summary of the qualitative behavior of the emitted lines (§2.3). In §3, we describe the observational evidence for the relativistic lines and give a summary of possible future observations. A recommended review of the subject stressing the observational material has recently been published by Fabian [7].

2 Line Emission Close to the Black Hole

2.1 Compton Reflection and Reprocessing

One direct consequence of the Accretion Disk Corona model is that it requires the presence of a hot electron plasma with a temperature of a few 100 keV in the close vicinity of the cold accretion disk, which has a temperature of less than 10^6 K (~ 0.1 keV). Due to the proximity of the cold material, hard X-rays emitted from the corona interact with the cold material, leading to observable spectral features. In a gas with $kT \lesssim 0.2$ keV, only Hydrogen and Helium are fully ionized. Most metals, i.e. elements with a nuclear charge number $Z > 2$, are only moderately ionized [24]. Since the cross-section for photo-absorption is $\sigma_{\rm bf} \propto E^{-3}$, most of the irradiating soft X-rays (i.e. photons with $E \lesssim 10$ keV) get photo-absorbed within the accretion disk. On the other hand, the cross-section for Compton scattering is almost equal to the Thomson cross section $\sigma_{\rm T}$ (a constant), so that photons with high energies predominantly Compton scatter off the electrons in the disk. The threshold energy above which Compton scattering dominates is about 15 keV. Since the electrons in the accretion disk have low thermal velocities, Compton scattered X-ray photons with $E \gg 15$ keV lose energy. The result of these two processes, photoabsorption and Compton scattering, is a "hump" of radiation in the spectrum emerging from the disk, peaking at about 30 keV(Fig. 1; see also [18, 10, 19] and references therein]. Such humps have indeed been found in many Seyfert galaxies, proving the presence of cold matter in these objects [21].

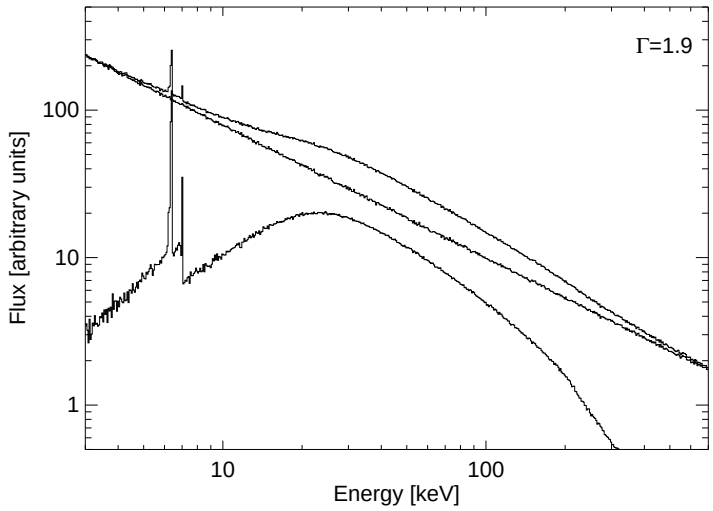

Fig. 1: Reflection spectrum for a cold disk irradiated with a power-law with photon-index $\Gamma = 1.9$. From top to bottom, the plot shows the total emerging spectrum, the incident power-law, and the reflection spectrum. Note the strong Iron K_α line at 6.4 keV and the Iron K_β line and Iron K edge at 7.1 keV. The spectrum was generated with our Monte Carlo code (Wilms, 1996, unpublished), using the cosmic abundances given by Grevesse [11], photo-absorption cross-sections from Verner et al. [29], and fluorescence yields from Kaastra & Mewe [15].

In addition to the reflection hump, the reprocessing of the irradiated X-rays within the accretion disk also leads to the production of emission lines in the X-ray spectrum below 10 keV. The absorption of an X-ray photon by the K-shell of an atom can lead to the emission of a K_α fluorescence photon. For astronomical objects, features of Iron are especially abundant, since Iron has a high cosmic abundance and high fluorescence yield (Fig. 1). Consistent with this picture, Iron features have been found in most Seyfert galaxies [22].

2.2 Radiative Transfer in the Kerr Metric

Since the spectrum is emitted close to the black hole, an observer at infinity will see the spectrum of Fig. 1 "distorted" by relativistic effects, namely Doppler boosting and gravitational red-shift. In this section, we briefly show how to take care of these effects. Due to space limitations, we can only sketch the important physics, for the details we refer to the literature referenced.

The specific flux F_{ν_o} at frequency ν_o as seen by an observer at infinity is defined as the (weighted) sum of the observed specific intensities I_{ν_o} from all

parts of the accretion-disk,

$$F_{\nu_\mathrm{o}} = \int_\Omega I_{\nu_\mathrm{o}} \cos\theta \,\mathrm{d}\Omega, \tag{1}$$

where Ω is the solid angle subtended by the accretion disk as seen from the observer and θ is the angle between the direction to the disk and the direction of the observed photon. Since the black hole (=AGN) is assumed to be very far away from the observer (=us), we can safely set $\cos\theta = 1$. Thus, we "only" have to compute the specific intensity I_{ν_o} at infinity from the spectrum emitted on the surface of the accretion disk, I_{ν_e}. In an axisymmetric accretion disk, I_{ν_e} is a function of the radial distance of the point of emission from the black hole, r_e, and of the inclination angle, i_e, of the emitted photon, measured with respect to the normal of the accretion disk.

Due to Doppler boosting and gravitational red-shift, the observed frequency ν_o is related to the emitted frequency ν_e by

$$g = \frac{\nu_\mathrm{o}}{\nu_\mathrm{e}} = \frac{1}{1+z}, \tag{2}$$

where z is the red-shift of the photon. According to Liouville's theorem, the phase-space density of photons, proportional to I/ν^3, is constant along the path of propagation of the photon (the null-geodesic). It is therefore possible to express eq. (1) in terms of the emitted specific flux on the accretion disk:

$$F_{\nu_\mathrm{o}} = \int_\Omega \frac{I_{\nu_\mathrm{o}}}{\nu_\mathrm{o}^3}\nu_\mathrm{o}^3 \,\mathrm{d}\Omega = \int_\Omega \frac{I_{\nu_\mathrm{e}}}{\nu_\mathrm{e}^3}\nu_\mathrm{o}^3 \,\mathrm{d}\Omega = \int_\Omega g^3 I_{\nu_\mathrm{e}}(r_\mathrm{e}, i_\mathrm{e}) \,\mathrm{d}\Omega. \tag{3}$$

In other words, the computation of the emerging spectrum breaks down to the computation of the "red-shift" g. In the weak field limit, when $r/M \gg 3$ in geometric units, and in the Schwarzschild metric, g and therefore the line profile emitted by the accretion disk, can be evaluated analytically. Profiles computed this way have been presented, e.g., by Fabian et al. [9] for the Schwarzschild case, and by Chen & Halpern [4] in the weak field limit. In most cases, however, the computation has to be done in the Kerr metric since the accreting black hole will be sped up by the accreted material [28].

The "brute force" approach to the computation of g in the Kerr metric is the direct integration of the trajectory of the photon in the Kerr metric [3, 16]. This approach allows the computation of exact line profiles even in the case of very complicated geometries, like thick accretion disks, but is very expensive: The computation of one line profile takes several hours on a typical workstation, and several tens of minutes on a supercomputer (Bromley, Chen & Miller [3] quote a computation time of 15 minutes on a Cray T3D with 128 nodes for the computation of one line profile). It is clear, therefore, that ray-tracing is not suitable for the analysis of X-ray observations, where a direct comparison between the measured data and the theory is to be made using a χ^2 minimization method.

The second way to compute the observed flux was first used by Cunningham [5] who noted that the observed flux from eq. (3) can be expressed by

$$F_{\nu_o} = \int T(i_e, r_e, g) I_{\nu_e}(r_e, i_e)\, \mathrm{d}g\, r_e\, \mathrm{d}r_e, \tag{4}$$

where the integration is carried out over all possible "red-shifts" g and over the whole surface of the accretion disk. This form is well suited for fast numerical evaluation. All relativistic effects are hidden in the *transfer-function* T. We refer to [5], [17], [25], and the references in these works for the technical details. Numerical values for T from the computations of [17] are available in FITS-format as part of the popular X-ray analysis package XSPEC [1]. For detailed studies, a `FORTRAN 77` code is available [25]. This code needs about 5 minutes on a DEC Alpha machine (233 MHz) to compute T for one value of i_e. The evaluation of the line profile afterwards takes almost no time.

2.3 The Emerging Line Profile

In Figs. 2 to 4 we illustrate the relativistic effects on the emerging line profile. Due to its astrophysical importance, we chose the Iron fluorescence line at 6.4 keV for our examples. To facilitate the translation to other lines, we indicate the red-shift on the upper abscissa of the figures. All line profiles have been computed with the code of Speith, Riffert & Ruder [25].

In our computations we assumed a geometrically thin, but optically thick Keplerian accretion disk to be the source of the line radiation. We note that our adopted velocity profile is different from the profiles resulting from the thick accretion disks presented by Chakrabarti elsewhere in this volume. The local emissivity of the line on the disk was parameterized as

$$I_{\nu_e}(r_e, i_e) \propto (1 + a\mu)\mu^b \cdot r^{-\alpha}, \tag{5}$$

where a, b, and α are free parameters, and where $\mu = \cos i_e$. This parameterization is sufficient for most practical work [2]. For optically thick material, $a, b = 0$, for the optically thin case, $a = 0$, $b = -1$, and for general limb-darkening, $a \neq 0$, $b = 0$. In our computations, the disk was assumed to be optically thick. For realistic accretion disks, the coefficient for the radial emissivity, α, ranges from 2 to 3 (the comparison with observations, §3, indicates $\alpha \approx 3$).

Common to all line profiles is a characteristic double-horned shape (Fig. 2). This shape is due to the Doppler effect, with the line emitted from material receding from the observer being red-shifted, and the line emitted from material moving towards the observer being blueshifted. Contrary to accretion-disks around normal stars, the emitted line profile is not symmetric: relativistic boosting causes the blue wing of the line to be much stronger than the red wing (it is customary in astronomy to call lower energies "red" and higher energies "blue", even when talking about lines in other energy bands than the optical). In addition to the Doppler boosting, the line is also red-shifted due to the gravitational

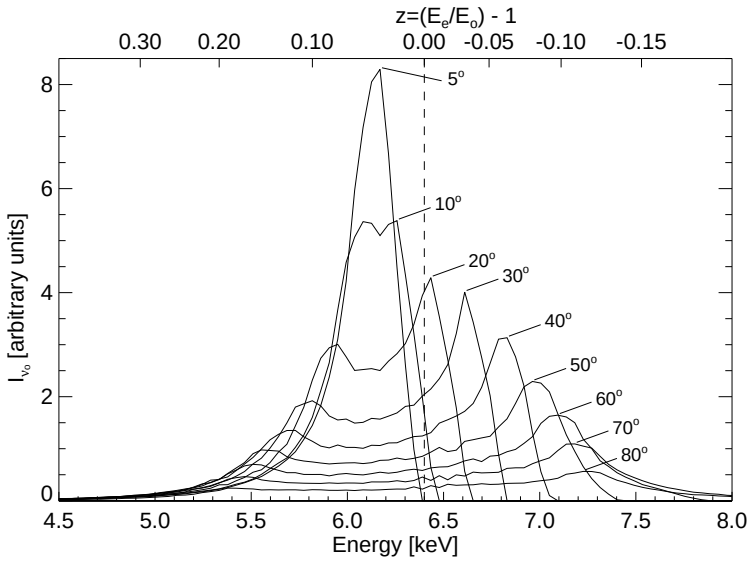

Fig. 2: Line profile as a function of the inclination angle i_o for $a = 0.9981$ and $\alpha = 0.5$.

red-shift. The influence of both effects on the line profile depends on the observers' inclination angle i_o: For a disk seen almost face on (i.e. i_o close to 0°), the gravitational red-shift dominates. With larger and larger i_o, Doppler effects become dominant.

The broadest parts of the profile are due to material emitted very close to the black hole, as is evident from Fig. 3, where line profiles for different emissivity coefficients α are shown. For large α, most of the line emission takes place close to the last stable orbit, so that these profiles are the broadest. Note that for values of $\alpha \gtrsim 2$ the red wing of the profile gets weaker until it is almost undetectable.

For the same emissivity coefficient α, the blue wings of lines emitted from disks around Schwarzschild and Kerr black holes are almost indistinguishable (Fig. 4), the red wings, however, are very different since in the Kerr case the radius of marginal stability, i.e. the inner edge of the accretion disk, is closer to the black hole than in the Schwarzschild case. Therefore, the red wing of the line can extend to much lower energies than in the Schwarzschild case. These effects from regions close to the last stable orbit, are the most promising for measuring general relativistic effects around Kerr black holes [17].

3 Observational Evidence for Broad Iron Lines

3.1 The Case of MCG −6-30-15

The rapid evolution of moderate resolution X-ray detectors in the past decade finally made the discovery of relativistically broadened Iron lines possible. The

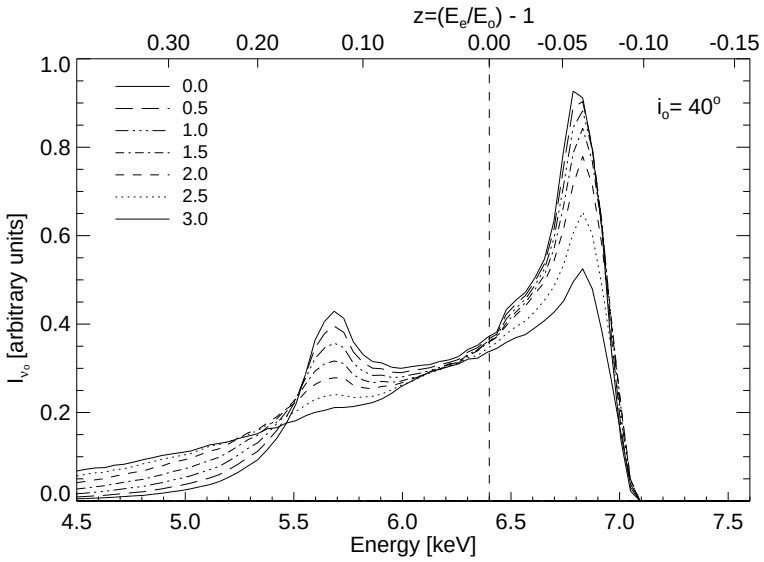

Fig. 3: Line profile as a function of the coefficient of radial emissivity, α, where the emitted intensity profile is $I_{\nu_e} \propto r^{-\alpha}$ (eq. (5)), for a black hole with $a = 0.5$. To emphasize the different profiles, the lines have been flux-normalized.

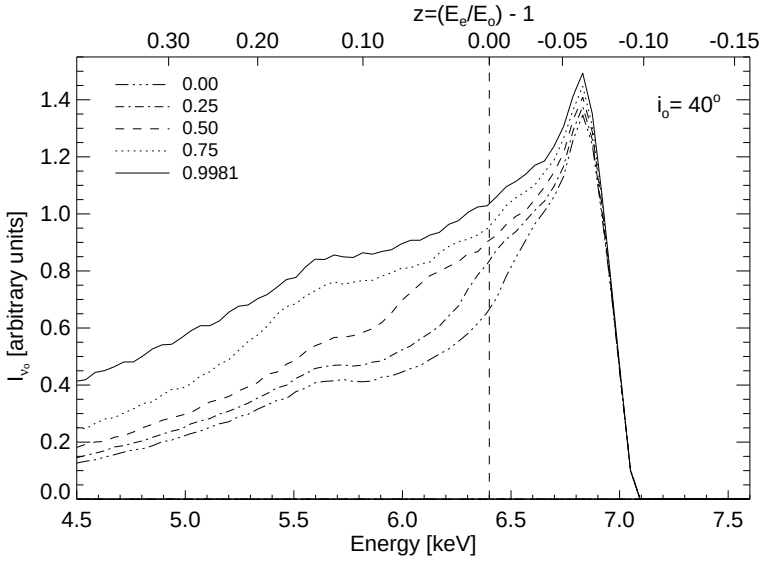

Fig. 4: Line profile for different angular momenta $a = J/M$ of the Kerr black hole for an inclination of $i_o = 40^\circ$ and $\alpha = 3$.

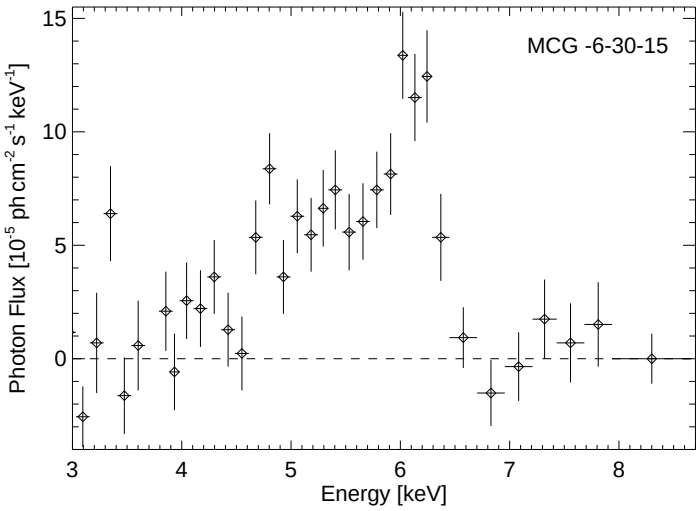

Fig. 5: Average line profile of MCG −6-30-15, as observed with ASCA. The best-fit power-law continuum has been subtracted [27].

best candidate for such a line is the Seyfert galaxy MCG −6-30-15. Here, the Japanese Advanced Satellite for Cosmology and Astrophysics (ASCA) discovered a strongly broadened Iron feature, with a full width at zero intensity of 100 000 km/sec [27]. Comparing Fig. 5 with Fig. 2 shows that such a profile has to come from a disk that is seen close to face-on, since the blue-wing of the line is still very close to the rest-frame energy of the line. Fitting the data with the theoretical line models shows that the observed line profile is consistent with that emitted by an accretion disk seen at an inclination of $30 \pm 3°$ [27]. As we showed in the last section, the line profiles from Schwarzschild and Kerr black holes are very similar, with the main difference being in the very red parts of the line. For determining the type of the black hole, therefore, a more careful analysis of the observation of MCG −6-30-15 has to be done. Iwasawa et al. [14] looked at the temporal changes of the Iron line profile during the 4.5 days of the ASCA observation and correlated the profile with the observed variability of MCG −6-30-15. They were able to find three distinct "states" of the line: when MCG −6-30-15 was close to its average flux (Fig. 6b), the profile is similar to the average profile shown in Fig. 5, at times where the flux was very large (Fig. 6a), the line profile is very narrow and centered at 6.4 keV. Finally, when the source intensity was very small (Fig. 6c), the line is very broad and extends down to about 4 keV. This large width is only possible if the line is emitted from material inside six gravitational radii, i.e. inside the marginally stable orbit for a Schwarzschild black hole. Such an emission is only possible if the central object is a Kerr black hole where the disk can extend to smaller radii.

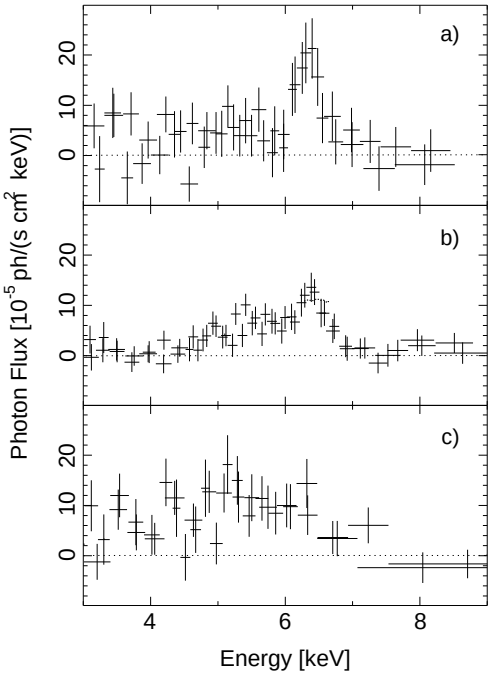

Fig. 6: Variability of the fluorescent iron line in MCG −6-30-15, the different panels show the line profile for phases with high flux (a) down to phases where the continuum flux was very small [14]

If this interpretation of the line variability is true, then the observations present the first *direct* evidence for rotating black holes. Although various objections have been raised against the interpretation of the line as a relativistic line, most objections can be rejected on physical grounds [8][1].

There is strong evidence that the broad Iron line of MCG −6-30-15 is not a special case, but that broad Iron lines are a common phenomenon. In a recent study, Nandra et al. [20] analyzed ASCA observations of 18 Seyfert 1 galaxies. They find evidence for broad lines with a strong asymmetry of the profiles to the red in all 14 objects in which they could detect a line. Nandra et al. [20] were able to explain these lines with relativistic line profiles, but due to the poor signal to noise ratio they could not distinguish between lines from Kerr or Schwarzschild black hole accretion disks.

3.2 The Future: AXAF, XMM, and Such

Although the ASCA results are very exciting and have undoubtfully opened the door to directly observing relativistic effects in AGN, more detailed observations

[1] See, however, the objections by Reynolds & Begelman [23] that could weaken the result for the angular momentum of the central black hole.

are needed.

With the currently planned next generation X-ray missions, the American *Advanced X-ray Astrophysics Facility* (AXAF; launch 1998), the Russian Spectrum-X/γ (SXG, launch 1998), the European *X-ray Multiple Mirror mission* (XMM; launch 1999), and the US-Japanese Astro E (launch 2000), we will be able to use X-ray instruments with a much higher energy resolution and larger effective areas than presently available. The huge effective area of XMM will allow us to probe for temporal variability in the line on much smaller time-scales than presently possible: With XMM we might be able to study the time-delay between fluctuations in the continuum and the reaction of the line to these fluctuations, allowing us to directly probe the geometry of the accretion flow. The large energy resolution of AXAF and Astro E will enable us to measure line profiles with a much higher resolution than ever before, which should help us to distinguish without doubt between the current relativistic models for the broad line emission. In the framework of the European EPIC consortium for XMM, two of us (J.W. and C.S.R.) have proposed an uninterrupted 100 ksec observation of MCG −6-30-15. The signal to noise ratio of such an observation will be much higher than that of Fig. 6, making the study of the line variability on short time-scales possible. Our future ability to observe relativistic effects happening on a large scale close to $10^8\,M_\odot$ black holes look very positive indeed.

Acknowledgments J.W. thanks Prof. N. Straumann for his enthusiastic suggestion to write this review and to Prof. F. W. Hehl for his invitation to include the review in these proceedings. We thank J. Dove, I. Kreykenbohm, K. Pottschmidt, T. Rauch, and R. Staubert for helpful discussions.

Bibliography

[1] Arnaud, K. A., 1996, in Astronomical Data Analysis Software and Systems V, ed. J. H. Jacoby, J. Barnes, (San Francisco: Astron. Soc. Pacific), 17

[2] Bao, G., Hadravana, P., Østgaard, E., 1994, ApJ, 435, 55

[3] Bromley, B. C., Chen, K., Miller, W. A., 1997, ApJ, 475, 57

[4] Chen, K., Halpern, J. P., 1989, ApJ, 344, 115

[5] Cunningham, C. T., 1975, ApJ, 202, 788

[6] Dove, J. B., Wilms, J., Begelman, M. C., 1997, ApJ, 487, 747

[7] Fabian, A., 1997, Astron. Geophys., 38, 10

[8] Fabian, A. C., et al., 1995, MNRAS, 277, L11

[9] Fabian, A. C., et al., 1989, MNRAS, 238, 729

[10] George, I. M., Fabian, A. C., 1991, MNRAS, 249

[11] Grevesse, N., Anders, E., 1989, in Cosmic abundances of matter, ed. C. Waddington, (New York: AIP Conf. Proc.), 1

[12] Haardt, F., Maraschi, L., Ghisellini, G., 1994, ApJ, 432, L95

[13] Hua, X.-M., Titarchuk, L., 1995, ApJ, 449, 188

[14] Iwasawa, K., et al., 1996, MNRAS, 282, 1038

[15] Kaastra, J. S., Mewe, R., 1993, A&AS, 97, 443

[16] Karas, V., Vokrouhlický, D., Polnarev, A. G., 1992, MNRAS, 259, 569

[17] Laor, A., 1991, ApJ, 376, 90

[18] Lightman, A. P., White, T. R., 1988, ApJ, 335, 57

[19] Magdziarz, P., Zdziarski, A. A., 1995, MNRAS, 273, 837

[20] Nandra, K., et al., 1997, ApJ, 477, 602

[21] Nandra, K., Pounds, K. A., 1994, MNRAS, 268, 405

[22] Pounds, K. A., et al., 1989, MNRAS, 240, 769

[23] Reynolds, C. S., Begelman, M. C., 1997, ApJ, 488, 109

[24] Shull, J. M., Van Steenburg, M., 1982, ApJS, 48, 95

[25] Speith, R., Riffert, H., Ruder, H., 1995, Comput. Phys. Commun., 88, 109

[26] Svensson, R., 1996, A&AS, 120, C475

[27] Tanaka, Y., et al., 1995, Nature, 375, 659

[28] Thorne, K. S., 1974, ApJ, 191, 507

[29] Verner, D. A., et al. , 1993, Atomic Data Nucl. Data Tables, 55, 233

ANHANG H

XMM-EPIC observation of MCG−6-30-15: direct evidence for the extraction of energy from a spinning black hole?

J. Wilms, C.S. Reynolds, M.C. Begelman, J. Reeves, S. Molendi, R. Staubert, E. Kendziorra

2001

Nachdruck aus

Monthly Notices of the Royal Astronomical Society
Vol. 542, 328, S. L27–L31

Mon. Not. R. Astron. Soc. **328,** L27–L31 (2001)

XMM-EPIC observation of MCG–6-30-15: direct evidence for the extraction of energy from a spinning black hole?

Jörn Wilms,[1]★ Christopher S. Reynolds,[2,3]† Mitchell C. Begelman,[3,4] James Reeves,[5] Silvano Molendi,[6] Rüdiger Staubert[1] and Eckhard Kendziorra[1]

[1]*Institut für Astronomie und Astrophysik, Abt. Astronomie, Universität Tübingen, Sand 1, D-72076 Tübingen, Germany*
[2]*Department of Astronomy, University of Maryland, College Park, MD 20742, USA*
[3]*JILA, Campus Box 440, University of Colorado, Boulder, CO 80309, USA*
[4]*Department of Astrophysical and Planetary Sciences, University of Colorado, Boulder, CO 80309, USA*
[5]*X-Ray Astronomy Group, Department of Physics and Astronomy, Leicester University, Leicester LE1 7RH*
[6]*Istituto di Fisica Cosmica, CNR, via Bassini 15, I-20133 Milano, Italy*

Accepted 2001 October 22. Received 2001 October 22; in original form 2001 August 24

ABSTRACT

We present *XMM-Newton* European Photon Imaging Camera (EPIC) observations of the bright Seyfert 1 galaxy MCG–6-30-15, focusing on the broad Fe Kα line at ~ 6 keV and the associated reflection continuum, which is believed to originate from the inner accretion disc. We find these reflection features to be *extremely* broad and redshifted, indicating an origin in the very central regions of the accretion disc. It seems likely that we have caught this source in the 'deep minimum' state first observed by Iwasawa et al. The implied central concentration of X-ray illumination is difficult to understand in any pure accretion disc model. We suggest that we are witnessing the extraction and dissipation of rotational energy from a spinning black hole by magnetic fields connecting the black hole or plunging region to the disc.

Key words: accretion, accretion discs – black hole physics – galaxies: individual: MCG–6-30-15 – galaxies: Seyfert – X-rays: galaxies.

1 INTRODUCTION

X-ray spectra of Seyfert 1 galaxies commonly show an iron Kα emission line at ~ 6 keV. The line is often extremely broad, with a velocity width of $> 70\,000\,\mathrm{km\,s^{-1}}$. Furthermore, the asymmetries in the line profiles are well explained by relativistic effects. Both of these facts suggest that the line is emitted from the surface layers of the accretion disc within a few gravitational radii $r_\mathrm{g} = GM/c^2$ of the black hole (BH) itself. It is now widely believed that this spectral feature is a relatively clean probe of the immediate environments of supermassive BHs (see Fabian et al. 2000, and references therein).

One of the best-studied broad iron line sources is the nearby bright Seyfert 1 galaxy MCG–6-30-15 ($z = 0.008$). This was the first active galactic nucleus (AGN) for which a relativistic iron line disc profile was measured. In their *Advanced Satellite for Cosmology and Astrophysics* (*ASCA*) observations, Tanaka et al. (1995) found that the iron line profile could be explained by emission from an accretion disc around a non-rotating (Schwarzschild) BH. In a detailed reanalysis, however, Iwasawa et al. (1996) found a much broader line during a period of low continuum X-ray flux, the so-called 'deep minimum state'. The line becomes so broad that disc models require emission from within $6r_\mathrm{g}$, suggesting either a rotating (Kerr) BH, with its marginally stable orbit at $r_\mathrm{ms} < 6r_\mathrm{g}$ (Iwasawa et al. 1996; Dabrowski et al. 1997), or iron fluorescence from material spiralling into the BH at $< r_\mathrm{ms}$ (Reynolds & Begelman 1997). Such a broad line was later confirmed, e.g. by Guainazzi et al. (1999) and Lee et al. (1999).

Using the new generation of X-ray satellites such as *XMM-Newton* with their improved collecting area and X-ray CCD spectral resolution, the Fe line of Seyferts can be studied in greater detail than was possible before. In this Letter, we present data from a 100 ks *XMM-Newton* observation of MCG–6-30-15.

2 INSTRUMENTATION AND DATA REDUCTION

Our observation covered most of orbit 108 of *XMM-Newton*, on 2000 June 11/12, and was simultaneous with the *Rossi X-ray Timing Explorer* (*RXTE*). Here, we report on data from the European Photon Imaging Cameras (EPIC) on board *XMM-Newton* (Strüder et al. 2001; Turner et al. 2001). To prevent photon pile-up, the EPIC-pn camera was operated in its small-window mode (using the medium thick filter to prevent optical light contamination), and the EPIC MOS-1 camera was operated in its timing mode. The MOS-2 camera was operated in full-frame

★E-mail: wilms@astro.uni-tuebingen.de
† Hubble Fellow while at the University of Colorado.

mode to study the field surrounding MCG−6-30-15. Although we primarily rely on the pn data here, the pile-up in the MOS-2 data can be reduced to < 5 per cent when using single events only. Therefore we can use the MOS-2 data to check for the instrument-independence of our results.

As of 2001 August, the official version of the *XMM-Newton* Science Analysis Software (SAS) contained only a preliminary model for the charge transfer efficiency (CTE) of the pn-chips. Therefore, we used an internal SAS version implementing an improved model for the EPIC-pn CTE (Haberl, private communication). To avoid remaining response matrix uncertainties, we concentrate on the energy range from 0.5 to 11 keV. To produce EPIC-pn source and background spectra, we collected events from two circles of radius 10 pixels on and off the source for those times when the source count rate was below 14 counts s^{-1}. This upper limit of the count rate is necessary to avoid phases where the core of the MCG−6-30-15 point spread function was slightly piled up. The total resulting EPIC integration time was 54 ks. We checked the background light curve for periods of severely increased background, but none was found.

For spectral modelling, response matrices appropriate for the improved CTE model and appropriate for the source position on the EPIC chip were used. Furthermore, we corrected the exposure time in the spectra for the ∼71 per cent live time of the pn small-window mode (Kuster et al. 1999) and performed simultaneous fits with single and double events. We estimate that the overall uncertainties in the spectral calibration and flux calibration owing to these procedures are at most a few per cent.

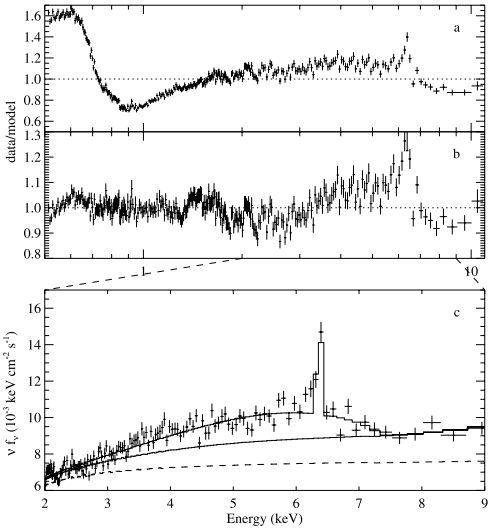

Figure 1. (a) Ratio between data and model from fitting a power law to the 0.5–11 keV data. (b) Ratio from fitting a power law and the empirical warm absorber model (see text). (c) Deconvolved spectrum of the Fe Kα band, showing the total LAOR model and the continuum with and without (dashed) the reflection component for a model with reflection from an ionized disc. For clarity, the data have been rebinned and only the single-event data points are shown.

3 THE IRON LINE PROFILE AND ACCRETION DISC FITS

Fig. 1(a) shows the ratio of the 0.5–11 keV EPIC-pn data to a spectral model consisting of a pure power law (fitted in the 2–11 keV band) modified by Galactic absorption ($N_{\rm H} = 4.1 \times 10^{20}\,{\rm cm}^{-2}$, using the XSPEC PHABS model with cross-sections similar to those described by Wilms, Allen & McCray 2000). Below ∼2 keV, there is significant spectral complexity which is due to a warm absorber (Nandra & Pounds 1994; Reynolds & Fabian 1995; Lee et al. 2001), possibly superposed with a complex of relativistically broadened soft X-ray recombination lines (Branduardi-Raymont et al. 2001). At 3–7 keV, a broad hump in the spectrum suggests the identification with disc reflection signatures and, especially, the broad iron Kα line.

The putative broad iron line is more apparent once the soft X-ray spectral complexity has been modelled. This is not a trivial exercise since the physical nature of this complexity is still a matter of debate. To start with, we consider a warm absorber scenario (this will be generalized to include soft X-ray relativistic emission lines below). We assume that the continuum consists of a power law modified by Galactic absorption. We also allow for the possibility of intrinsic neutral absorption in MCG−6-30-15 (although the best-fitting column density is always consistent with zero). By fitting the high-resolution X-ray spectrum from the Reflection Grating Spectrograph (RGS), we construct an empirical warm absorber model (based on Lee et al. 2001) with absorption edges of C V, O VII, O VIII and Ne X (at 392, 740, 870 and 1362 eV, respectively, with best-fitting optical depths at threshold of $\tau = 0.34$, 0.87, 1.17 and 0.10), a Gaussian absorption feature below the O VII and O VIII edges to crudely model blended resonance absorption lines, and four moderately broad and weak Gaussian emission features at observed energies of 0.885, 0.935, 0.995 and 1.06 keV, which are merely included to fit the RGS data; we do not attempt to make a physical identification of these features. After applying this empirical model to the data, the soft X-ray residuals are reduced to less than 10 per cent, and the broad iron line feature is much more obvious (Fig. 1b). The best-fitting photon index is $\Gamma = 1.87 \pm 0.01$ (goodness of fit $\chi^2/{\rm dof} = 2625/1719$, all uncertainties are quoted at the 90 per cent level for one interesting parameter, $\Delta\chi^2 = 2.71$).

We now consider the nature of the hard spectral complexity. While it may be tempting to model the hump-like feature as pure broad iron line emission, this is not a physically consistent model. The equivalent width of this feature (measured relative to the continuum at the iron Kα rest-frame energy) is ∼1 keV, and it would be impossible to obtain such a broad iron line without also observing the X-ray continuum photons that have been back-scattered from the accretion disc. Consequently, we will not present pure broad iron line models and jump, instead, to more physically motivated spectral models which include both iron line fluorescence and the backscattered 'reflection' continuum. Within the framework of such models, the 3–7 keV hump is a combination of iron line fluorescence and backscattered continuum photons (with the Fe K edge responsible for some fraction of the drop in flux at ∼7 keV).

We construct a spectral model appropriate for the case of reflection from the Keplerian regions of an accretion disc around a near-extremal Kerr BH ($a = 0.998$). The inner edge of the X-ray reprocessing region is taken to be the radius of marginal stability, $r_{\rm ms} = 1.23 r_{\rm g}$, and the outer edge is taken to be $r_{\rm out} = 400 r_{\rm g}$. We fix the inclination of the inner disc to be $i = 30°$ (Tanaka et al. 1995) and note that our results below only slightly depend on the value of

i chosen. We assume that the reflected emission has an emissivity profile $\epsilon \propto r^{-\beta}$ and leave β as a free parameter. The reflection continuum is described using the PEXRIV model of XSPEC and normalized to the case where the accretion disc intercepts half of the X-ray power-law continuum photons (i.e. $R = 1$). Both the iron line profile and the reflection continuum are then relativistically smeared [using the model of Laor (1991) as the kernel]. Here, and throughout the rest of the spectral modelling discussed in this paper, we also include a narrow (unresolved) Gaussian line at 6.4 keV with equivalent width $W_{\mathrm{K}\alpha,\mathrm{N}}$ to model the obvious narrow-line core. This component presumably originates from distant material such as the putative molecular torus of Seyfert unification schemes, and has recently be seen in several other AGN [e.g. in NGC 5548 (Yaqoob et al. 2001) or in Mrk 205 (Reeves et al. 2001)].

First, we consider the case of a fairly cold accretion disc (rest-frame iron line energy of 6.4 keV, disc ionization parameter $\xi = 1$, and $R = 1$). The resulting best-fitting parameters are $\Gamma = 2.09 \pm 0.01$, $\beta = 3.6 \pm 0.1$, $W_{\mathrm{K}\alpha,\mathrm{N}} = 38$ eV and $W_{\mathrm{K}\alpha,\mathrm{B}} = 805$ eV (χ^2/dof = 2383/1717). However, this model fails to explain the data as well as possessing an unphysically large broad-line equivalent width. Significant residuals (up to ~ 20 per cent) remain in the 3–11 keV band. The pattern of residuals suggests that the model is failing to produce the red wing of the 3–7 keV hump, and is underestimating the flux in the blueward edge of this feature. A hard tail above 8 keV suggests that we are also underestimating the strength of the high-energy reflection continuum. If we allow the relative normalization of the reflection continuum, R, to be a free parameter, the fit converges to a very large value of R ($R = 7.6^{+1.8}_{-1.3}$, also $\Gamma = 2.35 \pm 0.05$ and $\beta = 4.4 \pm 0.2$, χ^2/dof = 2055/1716). Despite the slightly better χ^2, large residuals around $\sim$7 keV remain.

Ionization of the accretion disc surface is another way of increasing the amount of reflection continuum. To model this (with the relative normalization of the reflection continuum fixed to $R = 1$), we allow the ionization parameter of the disc ξ, the temperature of the disc T and the energy of the iron line E to be free parameters (E is constrained to lie in the range of allowable Fe Kα energies: 6.40 to 6.97 keV). The resulting best fit has $\Gamma = 2.00 \pm 0.02$, $\beta = 3.29^{+0.12}_{-0.11}$, $E = 6.40^{+0.05}_{-0}$ keV, $\xi = 1380^{+570}_{-190}$, $T > 6.0 \times 10^5$ K, $W_{\mathrm{K}\alpha,\mathrm{N}} = 41$ eV and $W_{\mathrm{K}\alpha,\mathrm{B}} = 235$ eV (χ^2/dof = 2051/1714). This leads to a significantly better fit with the higher iron edge/line energies explaining the residual at $\sim$7 keV. However, significant residuals still exist in the 3–5 keV range (suggesting that we are still under-predicting the flux in the red wing of the reflection feature) and above 8 keV.

Detailed examination of this last spectral model shows that features in the *soft* X-ray band below 1.5 keV determine the best-fitting ionization parameter and temperature. Consequently, such fits must be viewed with suspicion – there are a number of physical processes that are not included in this reflection model but which may well contribute to the soft X-ray spectrum (most notably, the recombination line and edge emission from C, N, O and Ne). It would also not be surprising if our empirical warm absorber model left small soft X-ray residuals which may then be mistakenly fitted by ionized reflection models.

First, we can consider the ionized reflection fits ignoring all data below 1.5 keV. Refitting the ionized disc model (including the empirical warm absorber) to the 1.5–11 keV band results in a good fit with no clear residuals. The best-fitting parameters are $\Gamma = 1.94 \pm 0.02$, $\beta = 4.6 \pm 0.3$, $E = 6.95^{+0}_{-0.15}$ keV, $W_{\mathrm{K}\alpha,\mathrm{N}} = 51$ eV and $W_{\mathrm{K}\alpha,\mathrm{B}} = 582$ eV (χ^2/dof = 1506/1312). T and ξ are unconstrained by the data, while the relative normalization of the reflection continuum is constrained to be $R < 4.7$. During the fitting R is anti-correlated with $W_{\mathrm{K}\alpha,\mathrm{B}}$. These quantities are physically consistent with each other (i.e. the iron line has the appropriate strength for that value of R and ξ) when $R \sim 1.5$–2 (corresponding to $W_{\mathrm{K}\alpha,\mathrm{B}} \sim 300$–400 eV).

This spectral modelling suggests that the accretion disc may be ionized. Consequently, the Kα line need not be intrinsically narrow as we have assumed so far, but might be Compton-broadened in the hot skin of the accretion disc [note that Compton broadening alone cannot explain the large line width (Reynolds & Wilms 2000)]. We examine this possibility by relaxing our assumption of a narrow intrinsic line and, instead, model the *intrinsic* iron line with a Gaussian profile of width σ. Using the 1.5–11 keV data, the best-fitting value is $\sigma = 0$ (with other parameters as above). Even if we force the line to be very broad (e.g. $\sigma = 1$ keV, at the expense of reducing the goodness of fit by $\Delta\chi^2 = 13$), the data still require $\beta > 3.9$.

The second approach for handling the soft X-ray spectrum is to model explicitly the recombination K lines of C, N, O and Ne. Qualitatively, this model is the same as the mixed emission-line model of Branduardi-Raymont et al. (2001) with the presence of additional warm absorption. The best-fitting parameters are $\Gamma = 1.96 \pm 0.01$, $\beta = 4.70^{+0.25}_{-0.27}$, $E = 6.97^{+0}_{-0.10}$ keV, $W_{\mathrm{K}\alpha,\mathrm{N}} = 53$ eV, $\xi > 130$ and $W_{\mathrm{K}\alpha,\mathrm{B}} = 546$ eV (χ^2/dof = 1907/1704). Again, the relative reflection normalization is poorly constrained by these data, but self-consistency is achieved for $R \sim 1.5$–2 and $W_{\mathrm{K}\alpha,\mathrm{B}} \sim 300$–400 eV. We conclude that the parametrization of the soft energy spectrum does not qualitatively change the results for the broadened Fe Kα line.

We note that the PEXRIV reflection model employed here is also incomplete because of the neglect of Compton smearing of the absorption edges. We do not expect this to seriously compromise our results since the observed smearing is much greater than that expected from Compton effects. However, we will examine these effects using improved models (Ballantyne, Iwasawa & Fabian 2001; Nayakshin & Kallman 2001) in a future publication. Preliminary investigations show our current conclusions to be robust. Finally, to check the dependence of these result on possible remaining calibration uncertainties, we used the data from the MOS-2 camera. The best-fitting parameters that we find are consistent to within the error bars, with slight deviations at the Si edge which are a known calibration issue. We conclude that our results are independent of any remaining calibration issues with the EPIC instruments.

To summarize, our physically motivated best-fitting model consists of reflection from an ionized accretion disc that emits H-like iron Kα fluorescence with a relative reflection fraction of $R \approx 1.5$–2 and a broad iron line equivalent with of $W_{\mathrm{K}\alpha,\mathrm{B}} \approx 300$–400 eV. The 2–10 keV flux of $F_{2-10} = 2.3 \times 10^{-11}$ erg s^{-1} cm^{-2} is comparable with the 'deep minimum state' found by Iwasawa et al. (1996, $F_{2-10} = 2.0 \times 10^{-11}$ erg s^{-1} cm^{-2}). *The most interesting feature of these spectral models is that a very steep emissivity profile $\beta = 4.3$–5.0 for the iron-line/reflection features is required*. We address the implications of this result in the next section.

Finally, we note that if r_{in} is allowed to vary, the data require $r_{\mathrm{in}} < 2.1 r_{\mathrm{g}}$ in order to model the red wing of the 3–8 keV hump. We explicitly note that the data cannot be adequately described by any reflection model with an inner radius of $r_{\mathrm{in}} = 6 r_{\mathrm{g}}$, the radius of marginal stability around a Schwarzschild BH. Thus models in which the X-ray reflection occurs in the Keplerian part of accretion

discs around a non-rotating BH cannot explain these data. In principle, there can be X-ray reflection inside the radius of marginal stability (Reynolds & Begelman 1997). However, as discussed below, the extremely steep emissivity index β required by our data is very hard to understand in the context of Schwarzschild geometry.

4 DISCUSSION

Very steep emission profiles are required in all of our good fits to the Fe Kα line and reflection continuum. Here, we explore the implications of this result, assuming that the reflected flux (including the iron line) from a local patch of the disc is proportional to the X-ray continuum flux (at the iron K-shell edge) irradiating that patch. We will assume that a fixed fraction f of the energy released locally in the body of the accretion disc is transported into an accretion disc corona and then radiated in the X-ray band. Studies of such coronae suggest that $f \sim 1$ in order to produce the observed continua (Haardt & Maraschi 1993; Dove et al. 1997). Thus, while our assumption may not be true in detail, it must be approximately true across a wide range of disc radii.

4.1 Accretion disc models

Can standard BH accretion disc models (Novikov & Thorne 1973; Riffert & Herold 1995) explain the observed emissivity profiles? With the assumptions described above, this question reduces to an examination of the radial distribution of energy dissipation in such disc models. For a disc around an $a = 0.998$ BH, the flux emitted from the disc per unit proper area of the disc, $\mathcal{E}(r)$, peaks at $r \sim 1.6 r_{\rm g}$ and then gradually steepens to approach $\mathcal{E}(r) \propto r^{-3}$. At no point does $\mathcal{E}(r)$ become as steep as $r^{-4.5}$, as required by our iron line observations. This is true for any assumed BH spin. Also, as noted above, the emissivity profile is steeper than accretion disc models even if one accounts for intrinsic broadening of the iron line via Comptonization.

We note that there are two complications that may be relevant to real discs, even though they go beyond the realm of standard disc models. First, magnetic fields might couple material within $r = r_{\rm ms}$ to the rest of the disc, thereby permitting continued energy extraction from this material (Gammie 1999; Krolik 1999; Agol & Krolik 2000, hereafter AK00). Non-relativistic accretion disc simulations employing pseudo-Newtonian potentials suggest that the stresses and presumably the dissipation remain fairly flat within this region (Hawley & Krolik 2001; Armitage, Reynolds & Chiang 2001). Hence it would seem that the required emissivities are difficult to achieve through such effects for discs around Schwarzschild holes. Secondly, X-rays produced away from the equatorial plane might be gravitationally focused into the central regions of the disc. However, using the method of Petrucci & Henri (1997), we find that such effects cannot produce the observed emissivity profile unless the X-ray source is already situated in the very central regions of the disc.

We conclude that the disc has to be irradiated in a more centrally concentrated manner than predicted by current pure accretion disc models. In other words, we require some additional X-ray source that is both powerful and very centrally concentrated. There is one obvious candidate: *X-rays that are associated with the magnetic extraction of BH spin energy.*

4.2 Magnetic extraction of BH spin energy

Here, we explore the suggestion that the central X-ray source is associated with the extraction of BH spin energy, focusing on scenarios in which the BH spin is extracted via magnetic fields that pierce the (stretched) event horizon (Blandford & Znajek 1977). An alternative class of models in which the magnetic fields do not pierce the horizon will be addressed below. In order to produce the required steep irradiation profile, the X-ray production must occur close to the disc itself with a production rate that is a steeply declining function of radius. Thus we are led to consider models in which the magnetic field lines connect the rotating event horizon to the accretion disc and/or disc corona. For definiteness, we will consider the canonical near-extremal Kerr BH.

In models in which the magnetic field lines are strongly coupled to the body of the accretion disc, the magnetic field transmits a retarding couple to the BH if the BH rotates faster than the magnetically connected region of the disc where the extracted rotational energy will be deposited. In order to power the observed X-ray source, the field strength close to the BH needs to be $B \sim 10^4\,{\rm G}(M/10^7\,{\rm M}_\odot)^{-1}$ (Blandford & Znajek 1977). This is not an impossibly high field; the corresponding magnetic pressure is still substantially below the ram pressure of the accretion flow within $r_{\rm ms}$ and so can be confined to the BH region.

If a ring within the disc of width δr is connected to the event horizon with magnetic flux $\delta\Psi$, then the power dumped into the ring is (setting $GM_{\rm BH} = c = 1$)

$$\delta P = \frac{(\delta\Psi)^2 \Omega_{\rm D}(\Omega_{\rm H} - \Omega_{\rm D})}{4\pi^2 \delta r(-{\rm d}Z_{\rm BH}/{\rm d}r)}, \qquad (1)$$

where $\Omega_{\rm D}(r) = (r^{3/2} + a)^{-1}$ is the angular velocity of the accretion disc, and the angular velocity of the event horizon is $\Omega_{\rm H} = 0.479$ (Li 2000). The BH resistance, $Z_{\rm BH}$, is a function of disc radius, r, defined by a map from the BH horizon to the accretion disc along the magnetic field lines. Viscous forces then transport this energy *outwards* by some distance before it is dissipated and radiated. AK00 and Li (2000) examine this process in detail and compute the radial dependence of the energy dissipation when the magnetic field connects to the accretion disc at one particular radius. We can use the formulae of AK00 (also see Li 2000) as the Green's function for computing the more general case.

It is beyond the scope of this Letter to address the detailed distribution of the hole-threading magnetic field across the disc surface, $B(r)$, or the nature of $Z_{\rm BH}(r)$. If all of the extracted spin energy is dumped into a ring at $r = r_{\rm ms}$, the emissivity is very steep ($\beta > 6$) within $r < 1.8 r_{\rm g}$ and gradually flattens to $\mathcal{E} \propto r^{-3.5}$ at large radius (Li 2000). More generally, the spin energy will be deposited into a range of radii, flattening this profile. We will assume ${\rm d}Z_{\rm BH}/{\rm d}r \propto r^{-\nu}$ and ${\rm d}\Psi/{\rm d}r \propto r^{-\mu}$ ($\mu = 2$ corresponds to a dipole field for $r \gg 1$). For $\nu = 1$ and $\mu = 2$, $\mathcal{E} \propto r^{-3}$ at $r = 2r_{\rm g}$ and is flatter inside that radius. To produce emission profiles as extreme as those required by our data (i.e. $\beta \sim 4.5$ at $r \sim 1.5 r_{\rm g}$), field configurations must be as concentrated as $\mu \sim 3$–4 (with some dependence on ν). Such conditions could be achieved, for example, if the field were 'pinned' on to the BH by the ram pressure of the accretion flow.

We note that the models addressed by AK00 do not employ the Blandford–Znajek effect but, instead, magnetically torque the disc via coupling to *matter* deep within the plunging region. For parameters relevant to our discussion, the extra energy source is provided by the BH spin via the Penrose effect occurring within the

radius of marginal stability (but outside the stretched horizon). In this case, all of the extra torque is provided at the inner edge of the disc (rather than across a range of radii as addressed above) and so a steep emissivity profile is a natural outcome.

Finally, we note that the large self-consistent value of $R \sim 1.5-2$ may have its origin in general relativity. Some fraction $f_{\rm ret} < 0.5$ of the upwardly directed disc emission will be bent by the strong gravity and strike the disc again ('returning radiation': Cunningham 1975; Speith, Riffert & Ruder 1995; AK00), further enhancing $W_{\rm K\alpha,B}$. This can enhance the relative amount of reflection by up to a factor of 2. Further computations are required to assess the effect of returning radiation on the emissivity profile in a self-consistent manner.

5 CONCLUSIONS

We have presented *XMM-Newton*-EPIC observations of MCG−6-30-15 containing a spectral feature that is best described as an extremely broad and redshifted X-ray reflection feature. On the basis of both the extreme spectrum and the source flux, it seems likely that we have caught MCG−6-30-15 in the peculiar 'deep minumum' state first noted by *ASCA* (Iwasawa et al. 1996). The extreme nature of the line profile leads us to conclude that it originates from the most central parts of the accretion disc. Standard accretion disc models cannot produce an emissivity profile that is centrally concentrated enough to produce the observed feature. It also seems unlikely that gravitational focusing of the continuum X-rays or magnetic coupling of the plunging region to the rest of the disc can ameliorate this conclusion. Therefore we suggest that, during the deep minimum state, X-rays associated with the magnetic extraction of the spin energy of the black hole are dominating the emission, producing a sufficiently compact source to explain our observations. Our results thus confirm the suggestion of Iwasawa et al. (1996) and Dabrowski et al. (1997) that MCG−6-30-15 possesses a rapidly rotating black hole.

In a forthcoming paper, we will present a more detailed analysis of our observation, including simultaneous fits with the *RXTE* Proportional Counter Array, a study of the time dependence of the reflection features and the X-ray continuum, and fits using a larger and more detailed set of continuum and reflection models.

ACKNOWLEDGMENTS

We thank A. C. Fabian, F. W. Haberl, J. H. Krolik and M. Kuster for useful conversations, and the referee, Chris Done, for her very prompt reply and useful comments. We acknowledge support from DLR grant 50 OX 0002 (JW, RS, EK), Hubble Fellowship grant HF-01113.01-98A (CSR) and NSF grant AST 98-76887 (CSR, MCB). This work is based on observations obtained with *XMM-Newton*, an ESA science mission with instruments and contributions directly funded by ESA Member States and the USA (NASA).

REFERENCES

Agol E., Krolik J. H., 2000, ApJ, 528, 161, (AK00)
Armitage P. J., Reynolds C. S., Chiang J., 2001, ApJ, 548, 868
Ballantyne D. R., Iwasawa K., Fabian A. C., 2001, MNRAS, 323, 506
Blandford R. D., Znajek R. L., 1977, MNRAS, 179, 433
Branduardi-Raymont G., Sako M., Kahn S. M., Brinkman A. C., Kaastra J. S., Page M. J., 2001, A&A, 365, L140
Cunningham C. T., 1975, ApJ, 202, 788
Dabrowski Y., Fabian A. C., Iwasawa K., Lasenby A. N., Reynolds C. S., 1997, MNRAS, 288, L11
Dove J. B., Wilms J., Maisack M. G., Begelman M. C., 1997, ApJ, 487, 759
Fabian A. C., Iwasawa K., Reynolds C. S., Young A. J., 2000, PASP, 112, 1145
Gammie C. F., 1999, ApJ, 522, L57
Guainazzi M. et al., 1999, A&A, 341, L27
Haardt F., Maraschi L., 1993, ApJ, 413, 507
Hawley J. F., Krolik J. H., 2001, ApJ, 548, 348
Iwasawa K. et al., 1996, MNRAS, 282, 1038
Krolik J. H., 1999, ApJ, 515, L73
Kuster M., Benlloch S., Kendziorra E., Briel U. G., 1999, in Siegmund O. H., Flanagan K. A., eds, EUV, X-ray and Gamma-Ray Instrumentation for Astronomy X. SPIE, Bellingham, WA, p. 673
Laor A., 1991, ApJ, 376, 90
Lee J. C., Fabian A. C., Brandt W. N., Reynolds C. S., Iwasawa K., 1999, MNRAS, 310, 973
Lee J. C., Ogle P. M., Canizares C. R., Marshall H. L., Schulz N. S., Morales R., Fabian A. C., Iwasawa K., 2001, ApJ, 554, L13
Li L.-X., ApJ,2000, submitted (astro-ph/0012469)
Nandra K., Pounds K. A., 1994, MNRAS, 268, 405
Nayakshin S., Kallman T. R., 2001, ApJ, 546, 406
Novikov I. D., Thorne K. S., 1973, in DeWitt C., DeWitt B., eds, Black Holes – Les Astres Occlus. Gordon and Breach, New York, p. 345
Petrucci P. O., Henri G., 1997, A&A, 326, 99
Reeves J. N. et al., 2001, A&A, 365, L134
Reynolds C. S., Begelman M. C., 1997, ApJ, 487, 109
Reynolds C. S., Fabian A. C., 1995, MNRAS, 274, 1167
Reynolds C. S., Wilms J., 2000, ApJ, 533, 812
Riffert H., Herold H., 1995, ApJ, 450, 508
Speith R., Riffert H., Ruder H., 1995, Comput. Phys. Commun., 88, 109
Strüder L. et al., 2001, A&A, 365, L18
Tanaka Y. et al., 1995, Nat, 375, 659
Turner M. J. L. et al., 2001, A&A, 365, L27
Wilms J., Allen A., McCray R., 2000, ApJ, 542, 914
Yaqoob T., George I. M., Nandra K., Turner T. J., Serlemitsos P. J., Mushotzky R. F., 2001, ApJ, 546, 759

This paper has been typeset from a TEX/LATEX file prepared by the author.